# Microwave Remote Sensing Algorithms for Cirrus Clouds and Precipitation

By
K. Franklin Evans and Graeme L. Stephens

Department of Atmospheric Science
Colorado State University
Fort Collins, Colorado

Research was supported by NASA grant NAG 5-1592S

Colorado State University

Department of Atmospheric Science

Paper No. 540

# MICROWAVE REMOTE SENSING ALGORITHMS FOR CIRRUS CLOUDS AND PRECIPITATION

K. Franklin Evans and Graeme L. Stephens

Research supported by NASA grant NAG-5-1592S

Principal Investigator: Graeme L. Stephens

Department of Atmospheric Science

Colorado State University

Fort Collins, CO 80523

November 1993

Atmospheric Science Paper No. 540

## ABSTRACT

The global distribution of ice mass in cirrus clouds is very poorly known, but important for validating climate models that predict cirrus ice content. In this work theoretical modeling is carried out to investigate the feasibility of and possible techniques for high frequency microwave sensing of cirrus clouds from satellite. The discrete dipole approximation is used to compute the scattering properties for horizontally oriented ice crystals at frequencies of 85, 157, 220, and 340 GHz. Five particle shapes (solid columns, hollow columns, plates, planar rosettes, and spheres) and 18 gamma size distributions are considered. Upwelling brightness temperatures are computed with a polarized radiative transfer model. The brightness temperature depression ($\Delta T_b$), relative to clear sky, is proportional to the ice water path (IWP), but the relationship depends strongly on the characteristic particle size and also on the crystal shape (typical range is a factor of two). Multiple frequencies and polarizations are shown to be useful for determining particle size and shape. Moderate IWP is detectable, e.g. 30 g/m$^2$ produces $\Delta T_b = 3$°K at 340 GHz for a typical distribution.

A multichannel passive microwave precipitation retrieval algorithm is also developed in this work. Bayes theorem is used to combine statistical information from numerical cloud models with forward radiative transfer modeling. A multivariate log-normal prior probability distribution contains the covariance information about hydrometeor distributions that resolves the nonuniqueness inherent in the inversion process. Hydrometeor profiles are retrieved by maximizing the posterior probability density for each vector of observations. Theoretical tests with brightness temperatures simulated from cloud model data show that a five layer structure with variable rain, graupel, and cloud water is as effective as more complex structures. The hydrometeor profile retrieval method is tested with four channel (10 to 85 GHz) aircraft-based microwave radiometer data from convection over ocean and land in Florida. Multiparameter radar data is used to verify the retrieved profiles. The results show that the method generally works, but that more research needs to be done to improve the use of cloud model information.

## ACKNOWLEDGEMENTS

We are very grateful to Dr. Joe Turk of CSU for providing the AMPR microwave and CP-2 radar data and his radar hydrometeor retrievals in a very convenient form for the precipitation retrieval validation experiment. We thank Dr. Wei-Kuo Tao for providing the 2D GATE cloud model simulation output. We acknowledge Takmeng Wong for running the Florida RAMS simulations. Dr. Tim Cornwell of the National Radio Astronomy Observatory introduced one of us to Bayesian inversion many years ago. Dr. J. Vivekanandan provided the EBCM oblate spheroid scattering results for comparison with the DDA. Hans Liebe provided his MPM92 code for computing microwave atmospheric absorption. Financial support for this research was provided by the National Aeronautics and Space Administration under Grant NAG-5-1592S.

CONTENTS

LIST OF FIGURES

LIST OF TABLES

# Chapter 1

# INTRODUCTION

The advance of microwave radiometer technology for satellite instrumentation has led to increased opportunities for microwave remote sensing of clouds and precipitation. The increase in radiometer frequencies to the submillimeter range allows the sensing of lower concentrations and smaller sizes of cloud hydrometeors so that remote sensing of cirrus clouds is now possible. High precision radiometers operating with multiple frequencies and polarizations such as the Special Sensor Microwave/Imager (SSM/I) instrument have increased interest in the development of multichannel precipitation retrieval algorithms. This dissertation examines, through modeling and algorithm development, two areas of passive microwave remote sensing important to understanding the climate system. The first area uses theoretical modeling to explore the feasibility of and possible methods for high frequency microwave (> 100 GHz) sensing of cirrus clouds from high altitude aircraft and satellite. The second area involves the development and testing of a multichannel microwave precipitation measuring algorithm that uses output from numerical cloud modeling to help constrain the retrieval of hydrometeor profiles.

## 1.1 The Importance of Cirrus and Precipitation Measurement

Because of their large areal coverage cirrus clouds exert a strong radiative influence on the global climate. A ground based cloud climatology (Warren et al., 1986; Warren et al., 1988) has a globally averaged cirrus cloud fraction of 23% over land and 13% over ocean. A climatology by Woodbury and McCormick (1983) from SAGE (Stratospheric Aerosol and Gas Experiment) reports high cloud (above 70 percent of tropopause height or 8 km, whichever is greater) fractions from 25% in the subtropics to 50% in the tropics and midlatitudes. While the satellite based solar occultation method of SAGE gives it a coarser spatial resolution and also includes deep convection, it does not have the low cloud fraction bias for high thin clouds that a ground based climatology has.

The high altitudes of cirrus clouds, combined with their relatively low optical depth, endows them with radiative properties rather distinct from other types of clouds. The cold temperatures of cirrus clouds means they emit much less infrared radiation to space than clear sky, thus trapping energy and warming the lower troposphere in a "greenhouse" effect. Of course, cirrus clouds also reflect solar radiation back to space giving a cooling

effect. Numerical studies have shown that whether cirrus warms or cools the surface depends on the optical thickness of the cloud, with thinner cirrus having a warming effect (Stephens and Webster, 1981; Platt, 1981; Liou, 1986). There is also radiative heating inside cirrus clouds, especially in the tropics where there is a large cloud to surface temperature contrast (Stackhouse and Stephens, 1991).

Because of the prevalence and large radiative effect of cirrus clouds it is important to model these clouds in climate models such as general circulation models in order to predict climate change. To do so successfully requires several types of global measurements of cirrus clouds. The spatial and temporal distribution of cirrus is needed for validating GCM output of high cloudiness. This type of global distribution is currently being provided by the International Satellite Cloud Climatology Project (ISCCP) (Rossow and Schiffer, 1991). ISCCP uses several geostationary and polar orbiting satellites that measure clouds with visible and thermal infrared channels. From these two channels the clouds are detected and categorized using cloud top height and optical depth, which are derived using radiative models and a number of assumptions. GCMs are beginning to improve their modeling of clouds by using parameterizations that have cloud ice mass as a prognostic variable (Fowler et al., 1993). Measurements of the ice water content (IWC) of cirrus clouds, which ISCCP cannot provide accurately, is needed for validation of these new cloud modeling parameterizations.

The radiative properties of cirrus clouds are key for GCM prediction. The development of cirrus radiative parameterizations for GCMs requires observations of optical and microphysical properties of the clouds. The optical properties of ice clouds, in turn, depend on ice crystal shapes and size distributions. Because of the high altitude of cirrus clouds it has been difficult to perform in situ measurements of these microphysical quantities, hence they are rather poorly known on a global scale. In addition, the nonspherical shapes of the ice particles has greatly complicated the interpretation of in situ and remotely sensed observations. It is thus highly desirable to develop remote sensing techniques that will aid the measurement of cirrus characteristics such as integrated ice mass, characteristic particle size and shape, simultaneously with optical properties such as solar reflectance and infrared emissivity.

In the tropics, most cirrus clouds are produced by high level detrainment from deep convection. Another hydrological result of tropical convection is large amounts of rainfall. The latent heat release associated with precipitation in the Intertropical Convergence Zone is the primary energy source driving the ascending branch of the Hadley cell (Riehl and Malkus, 1958). On a regional scale latent heating is important in the forcing of tropical circulations (Webster, 1972; Gill, 1982). The tropical circulation is also sensitive to the vertical distribution of latent heating (Hartmann et al., 1984; DeMaria, 1985). The difference between precipitation and evaporation from the surface determines the net

latent heat flux, which, in most places on the globe, is the majority of the non-radiative energy transfer between the Earth and the atmosphere.

Precipitation also represents fresh water input into the ocean. This salinity sink has a large impact on the thermodynamics of the mixed layer and affects the ocean circulation. Through its effect on temperature the salinity modulates the ocean to atmosphere energy fluxes. Of the processes making up the hydrological cycle (evaporation, water vapor transport, and precipitation), precipitation is the least understood. Most of the precipitation on Earth results from complex convective-scale and mesoscale circulations that are difficult to model.

The detailed global distribution of precipitation, both the amount and variability, is inadequately known. The high temporal and spatial variability of precipitation makes it very difficult to measure over most of earth's surface, especially the oceans. An accurate global climatology of precipitation is important for validating general circulation models (GCMs). Most precipitation processes are below the grid resolution of GCMs and simple parameterization are used. Better global precipitation measurements will hasten the improvement of these parameterizations and aid in the verification of the circulations predicted by GCMs. Short term climate modeling, for example of the El Nino-Southern Oscillation (ENSO), will also be helped by improved precipitation climatologies. ENSO causes dramatic longitudinal shifts in precipitation over the Pacific Basin with intense human impacts. To address the need for improved precipitation measurements the Global Precipitation Climatology Project is using satellite infrared and microwave observations to produce a long term climatology of monthly precipitation in 2.5° areas.

## 1.2 Advantages of Satellite Microwave Remote Sensing

The most important advantage of using satellites to observe cirrus clouds and precipitation is the global coverage. For measuring these and other components of the climate system it is crucial to sample the entire globe in a timely fashion, which only satellite-borne instruments can do. There is still a temporal sampling issue with satellites because in sun synchronous orbit a given area will be sampled typically only twice a day, depending on the swath width. Geosynchronous orbit can achieve high temporal sampling, but so far it has been too technically demanding and expensive to put adequate resolution microwave instruments in that orbit (Vonder Haar et al., 1986). Remote sensing instruments and methods developed for satellites are typically first tested on high flying aircraft such as NASA's ER-2. NASA's Millimeter-wave Imaging Radiometer (MIR) with channels at 89, 150, 183$\pm$1,3,7, 220, and 325$\pm$1,3,9 GHz (Gasiewski, 1992) and the Advanced Microwave Precipitation Radiometer (AMPR) with channels at 10.7, 19.35, 37.1, 85.5 GHz (Spencer et al., 1993) are examples of instruments currently being flown on the ER-2. This mode of operation is especially useful for intensive field campaigns where a number of remotely sensed and in situ observations can be made of particular atmospheric phenomena.

Microwave remote sensing offers a number of potential advantages for measuring cirrus ice water path (IWP) as compared to visible and infrared techniques. Visible methods require a number of gross assumptions about ice particle shape, size distribution and cloud spatial homogeneity to convert from radiance to optical depth to ice water path. Thermal infrared techniques in addition require accurate knowledge of cloud temperature. Microwave radiation, to the contrary, interacts with ice particles primarily through scattering so emission and cloud temperature are relatively unimportant. Furthermore, microwave radiative transfer will usually be the linear regime so the signal is directly proportional to IWP and cloud inhomogeneity effects are less important. While the effects of particle shape and size distribution are also important for microwave remote sensing of cirrus, they are more amenable to calculation because the particle sizes are comparable to and smaller than the wavelength. Microwave methods are complementary to visible and IR methods in that microwave radiation is sensitive to larger ice crystals and thicker cirrus whereas visible/IR radiation is more sensitive to smaller particles and lower IWP.

The most direct way to measure precipitation is with a rain gauge. Due to the large spatial variability of rainfall, however, there are substantial errors in rainfall even in regions with rather dense networks of gauges (Thiele, 1987). In sparsely inhabited land regions and over the oceans rain gauges are nearly non-existent. Well calibrated radars can improve rainfall measurements, but the errors are still significant because of uncertainties such as the drop size distribution. Furthermore, the rainfall measurements are limited to areas with expensive radar networks. Of the various options for satellite remote sensing of precipitation, microwave techniques are the most promising. Rainfall retrieval algorithms based on geosynchronous infrared data have been in used for a number of years (Arkin, 1979; Adler and Negri, 1988) but have low accuracy and are only useful for large area/long time averages. IR methods are usually based on the area of very cold cirrus anvils which is rather indirectly related to the precipitation process.

Microwave remote sensing is much more directly related to the precipitation process. For the range of frequencies used in precipitation retrieval, microwave radiation penetrates through the clouds and interacts directly with the precipitation-sized ice and water hydrometeors. Furthermore, multiple microwave frequencies probe different levels of hydrometeor structure. For example, 85 GHz is affected primarily by scattering from precipitation sized ice particles high in the cloud, while 10 GHz is sensitive to integrated rain and the surface below. In addition to retrieving rainfall, multichannel microwave observations can give information about the vertical distribution of hydrometeors. Of course, spaceborne precipitation radars offer rather better measurements of hydrometeor distribution, but have not yet been flown and only now are being considered.

The Tropical Rain Measuring Mission (TRMM) (Simpson et al., 1988), to be launched in 1997, has a goal of determining monthly mean rainfall over $5° \times 5°$ boxes for latitudes equatorward of 35°. A major component instrument is the TRMM Microwave Imager

(TMI) that contains dual polarized channels (except horizontal at 21 GHz) for 10.7, 19.4, 21.3, 37.0, and 85.5 GHz. A 14 GHz precipitation radar (covering only part of the swath) and visible and infrared channels are included as well. The low orbit (around 350 km) will give the TMI relatively high resolution ($\approx$ 5 km at 85 GHz). A number of precipitation retrieval algorithms that use single and multiple TMI channels, some in combination with radar data, are currently under development for TRMM.

### 1.3 Scientific Objectives

The overall goal of this work is to increase the understanding of the interaction of microwave radiation with clouds and precipitation and use this knowledge to aid in the improvement of microwave remote sensing techniques for cirrus clouds and precipitation. The specific objectives are:

1. Develop a capability for modeling single scattering and radiative transfer for non-spherical particles.

2. Determine how ice particle shape and size affect scattering properties over a range of microwave frequencies.

3. Determine the range of ice water path detectable at particular microwave frequencies for realistic distributions of cirrus ice particles.

4. Examine the effects of particle shape and size distributions on microwave remote sensing of cirrus and develop methods that overcome the uncertainties associated with these effects.

5. Develop a multichannel microwave precipitation algorithm that retrieves hydrometeor profiles using information from numerical cloud models in a mathematically sound way.

6. Test the precipitation retrieval algorithm to learn how the assumed hydrometeor structure and combination of frequencies affects the accuracy of the retrieval.

7. Perform a preliminary validation of the algorithm with aircraft microwave radiometer data.

A particle scattering model using the Discrete Dipole Approximation and a polarized radiative transfer model are developed for this work and described in Chapter 2. Chapter 3 explains how the scattering properties for 18 gamma size distributions and five particle shapes are computed for 85, 157, 220, and 340 GHz. Radiative transfer calculations are carried out and the resulting brightness temperatures at several angles and polarizations

are analyzed to determine how the brightness temperature depression is related to IWP. How multiple frequencies and polarizations can be used to help determine particle size and shape are examined.

Chapter 4 describes the new microwave precipitation retrieval algorithm that uses Bayes theorem to combine prior information about hydrometeor profiles from cloud models with a forward radiative transfer model to retrieve optimal profiles. Chapter 5 describes a number of theoretical tests that are carried out using brightness temperatures modeled from a 2D simulation of a tropical squall line. These tests include examinations of the effect of different assumed hydrometeor profile structures, the effect of using different information from the cloud model, the result of various assumptions about the hydrometeor size distributions, and the effect of using several combinations of microwave frequencies in the retrieval. A limited validation study using AMPR data from the Convective and Precipitation/Electrification experiment (CaPE) is described. Hydrometeor profiles from a sea breeze simulation using the RAMS numerical cloud model is used for prior information. The retrieved profiles are then compared with data obtained with the NCAR CP-2 multiparameter radar.

## Chapter 2

# INTERACTION OF RADIATION WITH IRREGULAR PARTICLES

The interaction of radiation with particles in the atmosphere is conveniently divided into two parts. The first part considers how an electromagnetic wave scatters from and is absorbed by particles. The second part considers how radiation is transferred through the atmosphere including the effects of multiple scattering. This chapter explains how the scattering and radiative transfer calculations are performed in order to compute upwelling brightness temperatures from distributions of ice particles in cirrus clouds.

## 2.1 The Discrete Dipole Approximation

The first step in computing the transfer of microwave radiation through cirrus particles is to model the electromagnetic scattering properties of ice crystals. Scattering from ice particles in the atmosphere is most often modeled by assuming that the particles can be approximated by spheres so that Lorenz-Mie theory may be used. For most, if not all, types of cirrus particles this is a poor approximation, both because the basic scattering properties are incorrectly computed and because there is then no difference between horizontally and vertically polarized radiation. In much of the microwave portion of the spectrum the wavelengths are large compared to the particle sizes so the Rayleigh approximation for nonspherical particles may be used (e.g. van de Hulst, 1981). At the microwave wavelengths considered here (down to 0.088 cm) the Rayleigh condition is not valid for larger ice crystals, so more complicated scattering methods must be considered. The extended boundary condition method (EBCM) (Barber and Yeh, 1975), also known as the T-matrix method, has been used in the engineering and radar meteorology fields for computing the scattering properties from oblate and prolate spheroids. While theoretically applicable to any shape that can be expanded in a spherical harmonic type series, in practice there are limitations that prevent its use for particles that are very thin (axial ratios $< 0.1$) or have sharp edges. The EBCM has been applied in an atmospheric context to particles defined by a surface of revolution that is a Chebyshev polynomial (Mugnai and Wiscombe, 1986).

In this work the electromagnetic scattering computations are accomplished with the discrete dipole approximation (DDA), first described by Purcell and Pennypacker (1973). DDA is very general in that it applies to any particle shape, although computer limitations

restrict the size of the particle relative to the wavelength. The basic concept behind the DDA is to divide the particle into a number of subunits whose size is small compared to the incident wavelength of radiation. These small subunits behave as dipoles in terms of their response to an applied electro-magnetic field. Each dipole responds to a sum of the incident plane wave and the fields from all the other dipoles, and in turn generates a field which affects the other dipoles. The DDA is also called the coupled dipole method because of this mutual interaction among the subunits. The DDA solves for the polarization of the dipoles for a given incident plane wave, and computes the resulting far field scattering amplitudes from which the desired scattering properties may be derived.

Over the past 20 years the DDA method has been applied to a variety of fields and improved in a number of ways. Yung (1978) improved upon Purcell and Pennypacker's simple iterative solution scheme with a conjugate gradient type method derived with a variational principle. Yung's method requires the particle to be symmetric around the incident beam direction and under interchange of dipoles. Singham et al. (1986) developed an analytical method for computing the particle orientation averaged scattering results directly, i.e. without solving for many incident directions. Singham and Bohren (1987) used an order of dipole scattering approach to solve the coupled dipole system. Draine (1988) used the conjugate gradient method to solve the DDA system for any type of particle and the applied the method to light scattering from interstellar grains. Goedecke and O'Brien (1988) used a different, but equivalent, formalism to derive the DDA method, and then applied it to microwave scattering by snow crystals (O'Brien and Goedecke, 1988). Flatau (1990) exploited the block Toeplitz structure of the dipole interactions to develop a fast solution method for rectangular particles. Evans and Vivekanandan (1990) used the DDA to investigate the multiparameter radar and passive microwave radiometer signatures of various shapes of ice crystals. Dungey and Bohren (1993) modeled the backscattering of several ice particle shapes with the DDA for application to radar remote sensing.

### 2.1.1 DDA theory

The following mathematical discussion of the DDA method uses a Greens function approach and follows closely a paper by Goedecke and O'Brien (1988). Starting from Maxwell's equations it can be shown that the solution for the electric field $\mathbf{E}(\mathbf{r})$ everywhere in space resulting from the scattering of an incident field $\mathbf{E}^{\text{in}}(\mathbf{r})$ from a dielectric particle may be expressed as an integral over the particle volume of the Greens function $G$ multiplied by the dielectric polarization $\mathbf{p}(\mathbf{r})$. The solution is

$$\mathbf{E}(\mathbf{r})\,[1 + 4\pi\chi(\mathbf{r})/3] = \mathbf{E}^{\text{in}}(\mathbf{r}) + \int d^3r' G(\mathbf{r} - \mathbf{r}') \cdot \mathbf{p}(\mathbf{r}') \; . \tag{2.1}$$

The polarization at points inside the particle is related to the field by $\mathbf{p}(\mathbf{r}) = \chi\mathbf{E}(\mathbf{r})$ where $\chi$ is the susceptibility ($\chi = (1/4\pi)[m^2 - 1]$) and $m$ is the complex index of refraction. The

Greens function is the field due to a single harmonically oscillating dipole, and depends only on the position relative to the dipole ($R$):

$$G_{ij}(\mathbf{R}) = \frac{1}{R}\exp(-ikR)\left[k^2\left(\delta_{ij} - \hat{R}_i\hat{R}_j\right) - \left(\delta_{ij} - 3\hat{R}_i\hat{R}_j\right)\left(\frac{1}{R^2} + \frac{ik}{R}\right)\right] , \qquad (2.2)$$

where the subscripts $i$ and $j$ refer to the Cartesian components of the fields and the direction vector $\hat{R}$, and $k = 2\pi/\lambda$ is the wavenumber for the free-space wavelength $\lambda$.

Dividing the particle into dipoles is equivalent to discretizing the field and Greens function over the volume of the particle. In the current model the particle is divided into cubes of size $d$. Discretizing equation 2.1 and rearranging gives

$$E^{\text{in}}_{\alpha i} = \left[\chi_\alpha^{-1} + 4\pi/3(1-\Gamma)\right] p_{\alpha i} \; - \; d^3 \sum_{\beta\neq\alpha}\sum_{j} G_{ij}(r_\alpha - r_\beta) p_{\beta j} \qquad (2.3)$$

where $\alpha$ and $\beta$ are indices of the dipoles. The small but nonzero volume of a dipole contributes to the integral in equation 2.1, giving rise to a "self interaction" term $\Gamma$. The self-term is modeled by Goedecke and O'Brien as

$$\Gamma = (3/4\pi)^{2/3}(kd)^2 - i(kd)^3/2\pi \; . \qquad (2.4)$$

The small imaginary part of $\Gamma$ is necessary to satisfy the optical theorem. Equation 2.3 is a coupled linear system which may be solved for the dipole polarizations $\mathbf{p}_\alpha$ for a given incident field $\mathbf{E}^{\text{in}}$. The incident plane wave field with direction $\hat{k}'$ is evaluated at the $\alpha$'th dipole according to

$$\mathbf{E}^{\text{in}}_\alpha(\hat{\mathbf{k}}') = \mathbf{E_0}\exp(-ik\hat{\mathbf{k}}'\cdot\mathbf{r}_\alpha) \; . \qquad (2.5)$$

$\mathbf{E_0}$ is either vertically or horizontally polarized and has unit amplitude ($|\mathbf{E_0}| = 1$).

The coordinate system for the electric field polarization is in terms of the plane defined by the propagation direction $\hat{k}$ and the vertical $z$ axis. The vertical unit vector $\hat{V}$ is in the meridional plane perpendicular to the propagation direction and has a positive $z$ component. The horizontal unit vector $\hat{H}$ is perpendicular to the plane such that $\hat{V}\times\hat{H} = \hat{k}$.

The scattered electric field far away from the particle is an outgoing spherical wave with components given by the scattering amplitude matrix multiplied by the incident field vector. In terms of $V$ and $H$ components this is expressed by,

$$\begin{bmatrix} E_{vs} \\ E_{hs} \end{bmatrix} = \frac{\exp(-ikr)}{ikr}\begin{pmatrix} F_{vv} & F_{vh} \\ F_{hv} & F_{hh} \end{pmatrix}\begin{bmatrix} E_{vi} \\ E_{hi} \end{bmatrix} , \qquad (2.6)$$

which can be taken as the definition of the scattering amplitudes $F$. The scattering amplitudes represent a linear transformation of the incident electric field vector with propagation direction $\hat{k}'$ into the scattered electric field with direction $\hat{k}$. The scattering amplitudes are easily found from the dipole polarizations using eq. 2.2 with $R\to\infty$, giving

$$F_i(\hat{k}) = \sum_j(\delta_{ij} - \hat{k}_i\hat{k}_j)\; i(kd)^3\sum_\alpha \exp(ik\hat{k}\cdot\mathbf{r}_\alpha)\; \mathbf{p}_{\alpha j} \qquad (2.7)$$

This form explicitly shows that the scattering amplitude vector is perpendicular to the propagation direction as required. The Cartesian components $F_i$ are projected onto the polarization directions $\hat{V}$ and $\hat{H}$ for each of the two incident polarizations to generate the four scattering amplitudes $(F_{vv}, F_{vh}, F_{hv}, F_{hh})$. The set of scattering amplitudes for all incident and outgoing directions contain the complete information about the far-field aspects of the scattering process.

### 2.1.2 Using DDA for radiative transfer

The radiative transfer calculations require that the radiation field and scattering properties be expressed in terms of power or intensity rather than amplitude. This is a result of using incoherent averaging over particle ensembles which is valid when the particles making up the medium are sufficiently far apart and are randomly positioned. The standard Stokes parameters $(I, Q, U, V)$ are used to completely characterize the polarization state of the radiation. The scattering process is then expressed with 4 × 4 Stokes parameter scattering and extinction matrices. While the DDA model computes the scattering properties for all four Stokes parameters, there is a simplification that is used for the modeling in this work. In a thermally emitting atmosphere with a plane- parallel geometry and no preferred azimuthal orientation of particles the radiation field is azimuthally symmetric and the $U$ and $V$ Stokes parameters are zero. In terms of the electric field the two remaining Stokes parameters are $I = |E_v|^2 + |E_h|^2$ and $Q = |E_v|^2 - |E_h|^2$.

For an azimuthally symmetric system the relevant scattering properties can be expressed with 2 × 2 matrices. The scattering matrix is computed from the scattering amplitudes according to

$$M = \frac{1}{2k^2} \sum_l n_l \begin{pmatrix} |F_{vv}|^2 + |F_{vh}|^2 + |F_{hv}|^2 + |F_{hh}|^2 & |F_{vv}|^2 - |F_{vh}|^2 + |F_{hv}|^2 - |F_{hh}|^2 \\ |F_{vv}|^2 + |F_{vh}|^2 - |F_{hv}|^2 - |F_{hh}|^2 & |F_{vv}|^2 - |F_{vh}|^2 - |F_{hv}|^2 + |F_{hh}|^2 \end{pmatrix}, \tag{2.8}$$

where $n_l$ is the number concentration of particles and $\sum_l$ indicates the incoherent sum over an ensemble of particles. There is a scattering matrix for each combination of incident and outgoing directions. Similarly, the extinction matrix is defined in terms of the forward scattering amplitudes according to the fundamental extinction formula, as

$$K = \frac{2\pi}{k^2} \sum_l n_l \begin{pmatrix} \mathrm{Re}(F_{vv} + F_{hh}) & \mathrm{Re}(F_{vv} - F_{hh}) \\ \mathrm{Re}(F_{vv} - F_{hh}) & \mathrm{Re}(F_{vv} + F_{hh}) \end{pmatrix}. \tag{2.9}$$

There is an extinction matrix for each incident direction. Both the scattering and extinction matrices have units of inverse length. The full 4 × 4 Stokes parameter representation for the scattering and extinction matrices was given in Evans and Vivekanandan (1990), but with scattering amplitudes $f$ defined so that $F = ikf$.

A simpler, though entirely equivalent, basis for the polarization state of the radiation field is $I_V = |E_v|^2$ and $I_H = |E_h|^2$. In this basis the scattering and extinction matrices are

$$M = \frac{1}{k^2} \sum_l n_l \begin{pmatrix} |F_{vv}|^2 & |F_{vh}|^2 \\ |F_{hv}|^2 & |F_{hh}|^2 \end{pmatrix} , \tag{2.10}$$

and

$$K = \frac{2\pi}{k^2} \sum_l n_l \begin{pmatrix} \mathrm{Re}(F_{vv}) & 0 \\ 0 & \mathrm{Re}(F_{hh}) \end{pmatrix} . \tag{2.11}$$

There are two ways to compute absorption by the particle. One is to subtract the integral of the scattering matrix over outgoing directions from the extinction matrix:

$$\begin{aligned} \sigma_I &= K_{II}(\hat{k}') - \int M_{II}(\hat{k}', \hat{k}) \, d\hat{k} , \\ \sigma_Q &= K_{IQ}(\hat{k}') - \int M_{IQ}(\hat{k}', \hat{k}) \, d\hat{k} . \end{aligned} \tag{2.12}$$

The second method is to integrate the power dissipated in the particle for each incident polarization:

$$\begin{aligned} A_{v/h} &= -4\pi k \sum_\alpha d^3 |\mathbf{E}_\alpha|^2 \mathrm{Im}(\chi_\alpha) , \\ \sigma_I &= A_v + A_h , \\ \sigma_Q &= A_v - A_h . \end{aligned} \tag{2.13}$$

The absorption/emission coefficient computed by these two methods is compared. This provides a check that enough outgoing angles have been selected for the scattering matrix.

For interfacing with the radiative transfer computations the scattering matrix, extinction matrix, and emission vector are computed for a set of incident zenith angles given by Gaussian or Lobatto quadrature formulae. If the particle shape is symmetric around the horizontal plane, then only one hemisphere of incident zenith angles is computed, and the other half is filled in by symmetry. Since the particles are assumed to have no preferred azimuthal orientation, averaging may be done over a number of incident azimuth angles in the appropriate range (typically $0, \pi$) for shapes that are not already azimuthally symmetric. The outgoing azimuth angles are evenly spaced in $(0, 2\pi)$. For the convenience of the radiative transfer computation the scattering matrix is expressed as a Fourier series in the difference in azimuth angle between the incident and outgoing directions. For an azimuthally symmetric situation such as the one here, only the lowest Fourier mode is needed, which is simply the average over the outgoing azimuth angles.

The set of dipole positions $\mathbf{r}_\alpha$ and susceptibilities $\chi_\alpha$ defines the particle for the DDA computations. The model used here uses a uniform rectangular grid of dipoles. The geometrical center of the particle is set at the origin, and the grid location is adjusted in each dimension so that an integral number of dipoles fits across the particle. The shapes of particles is specified with simple geometrical formulae (e.g. for spheres, cylinders,

hexagonal plates, rectangular solids, etc.). The portion of the volume of each cube that lies within the geometrical definition of a particle is computed by laying down a subgrid of typically 1000 points per coarse grid cell. This volume fraction determines whether the cube becomes a dipole making up the particle, and also may be used to adjust the susceptibility of the dipole. The susceptibility of the partially filled dipoles is adjusted using Lorentz-Lorenz mixing rule, by

$$\frac{\chi_{eff}}{4\pi\chi_{eff}+3} = V_f \frac{\chi}{4\pi\chi+3} \ , \tag{2.14}$$

where $\chi_{eff}$ is the reduced susceptibility and $V_f$ is the volume fraction. Typically it is dipoles on the edge of a particle that are partially filled, and reducing the susceptibility of these dipoles in effect attempts to better approximate the particle shape. Using the mixing rule on the edge dipoles dramatically improves the accuracy of the scattering properties for smaller particles.

The size of the dipoles $d$ is governed by the requirement that the electric field be relatively constant in the dipole cell. This means that the phase variation across a dipole must be small or $|m|kd \ll 1$. Goedecke and O'Brien suggest $|m|kd < 1/3$ for high accuracy, but as shown below $|m|kd < 1$ can give adequate accuracy. Another reason to use dipoles as small as possible is to better approximate smooth particle shapes with discrete arrays of dipoles. For this purpose it is the number of dipoles across a particle that matters rather then their size relative to the wavelength. How well an array of dipoles approximates a particle depends, of course, on the particular shape involved.

### 2.1.3 DDA solution methods

Two methods are used to solve the coupled linear system (eq. 2.3) for the dipole polarizations $\mathbf{p}_\alpha$. The first method treats eq. 2.3 as a $3N \times 3N$ complex matrix equation $Ap = E^{\text{in}}$ and solves for the $p$ vector using matrix inversion. The diagonal part of the matrix $A$ contains the dipole susceptibilities and the self terms, while the off-diagonal part has the dipole-dipole interaction terms. The inversion solution method first computes the LU decomposition of $A$ and then rapidly solves for $p$ for each incident direction $E^{\text{in}}$. The computer storage requirements for the inversion method go as $N^2$ while the CPU time goes as $N^3$, where $N$ is the number of dipoles which is proportional to the particle volume. Computer memory rather quickly becomes the limiting factor, for example 600 dipoles requires nearly 26 megabytes of storage.

The second solution method takes into account that equation 2.3 contains a convolution sum that can be carried out efficiently with a fast Fourier transform (FFT). The equation is solved by using the conjugate gradient method to iterate the $p$ vector until the residuals of the equation are suitably small (see appendix A for a full description of the method). This FFT method was also used for solving the DDA problem by Goodman

et al. (1991). Each convolution involves an FFT of the dipole polarizations, multiplication by the precomputed transform of the Greens function, followed by an inverse FFT. In order to avoid aliasing the FFT's for the convolutions must be done on a uniform 3-D grid of twice the particle extent in each dimension. The main advantage of the FFT method is that the DDA may be solved rapidly for large numbers of dipoles. The number of conjugate gradient iterations is virtually independent of the number of dipoles, ranging from a few tens to a few hundreds of iterations depending on the problem. Since FFT's take of order $N \log^2 N$ operations the running time for the FFT DDA method basically goes as $N$, the number of dipoles. There is, however, a rather large factor in front of the order $N$, because of the number of iterations required and because the FFT's must be done on an array at least eight times larger than the number of dipoles in the particle. Nevertheless the FFT method makes DDA with hundreds of thousands of dipoles feasible whereas before at most a few thousand dipoles were practical. One disadvantage of the FFT method is that each incident direction must go through the lengthy conjugate gradient iteration procedure. For radiative transfer computations, where the DDA system must be solved for many incident directions, the inversion solution method is superior for less than about 1000 dipoles, assuming the required computer storage is available.

### 2.1.4 Tests of the DDA model

To validate the DDA model and illustrate the accuracy typically achieved, a comparison was carried out for spherical and oblate spheroidal ice particles. For spheres the reference method was Mie theory; for oblate spheroids, with a 0.25 axial ratio, the reference method was the EBCM (Barber and Yeh, 1975). The scattering comparison was made at 340 GHz ($m = 1.781 - 0.0033i$) which is the highest frequency considered for this work. The computations were run for a range of particle sizes from 0.06 mm to 2.00 mm (to 1.00 mm for spheres). The dipole sizes used in these calculations were the same as those used below for column shaped cirrus particles. The DDA computations used just one incident azimuth angle, and the other parameters were similar to those used for the cirrus particle calculations below. The dipole sizes and total number of dipoles for the various test shapes are shown in Table 2.1.

The comparisons were made for the part of the Stokes scattering and extinction matrices relevant for the radiative transfer considered here, i.e. for $I$ and $Q$. For scattering the RMS difference over the incident and outgoing quadrature zenith angles was computed for the azimuthally averaged scattering matrix, while for extinction the RMS difference was computed over the incident zenith angles. A fractional RMS difference was made by dividing the absolute RMS difference by the maximum matrix value encountered over all the angles.

Figure 2.1 shows the fractional RMS difference in extinction and scattering as a function of particle size for spheres and oblate spheroids. The graph shows that the

Table 2.1: Dipole sizes and number used in the DDA/Mie/EBCM test.

| Particle Size (mm) | Dipole Size (mm) | Sphere Dipoles | Spheroid Dipoles |
|---|---|---|---|
| 0.060 | .006 | 720 | 248 |
| 0.120 | .011 | 967 | 303 |
| 0.250 | .022 | 1064 | 344 |
| 0.500 | .032 | 2536 | 760 |
| 1.000 | .0375 | 11531 | 3287 |
| 2.000 | .0725 | - | 3592 |

discrete dipole approximation can calculate the scattering properties of different shapes with adequate accuracy. The maximum fractional difference in extinction and scattering (not shown) is typically around 3% for the sphere cases and ranges from 3% to 12% for the oblate spheroid cases. The accuracy of the DDA improves as the particle size increases. The reason for this is that the larger number of dipoles used for the bigger particle sizes better approximate the true shape of the test particles. This also explains why the DDA is poorer for oblate spheroids than the spheres. The oblate spheroids have less dipoles, and the smaller sizes are especially poorly represented with only about 2.5 dipoles across the thickness of the spheroid.

These tests, at the shortest wavelength considered, indicate that the DDA error due to the approximation of the particle shape is probably larger that the error due to the nonzero size of the dipoles for the scattering computations done below. There are some reasons to believe that the accuracy implied by these test results is somewhat conservative. The dipole sizes used for the test are optimized for approximating columns and not for the test shapes considered here. Also the cirrus particle shapes modeled below are relatively more angular than the spheres and spheroids considered in these tests, and hence will be more faithfully modeled by assemblages of dipoles.

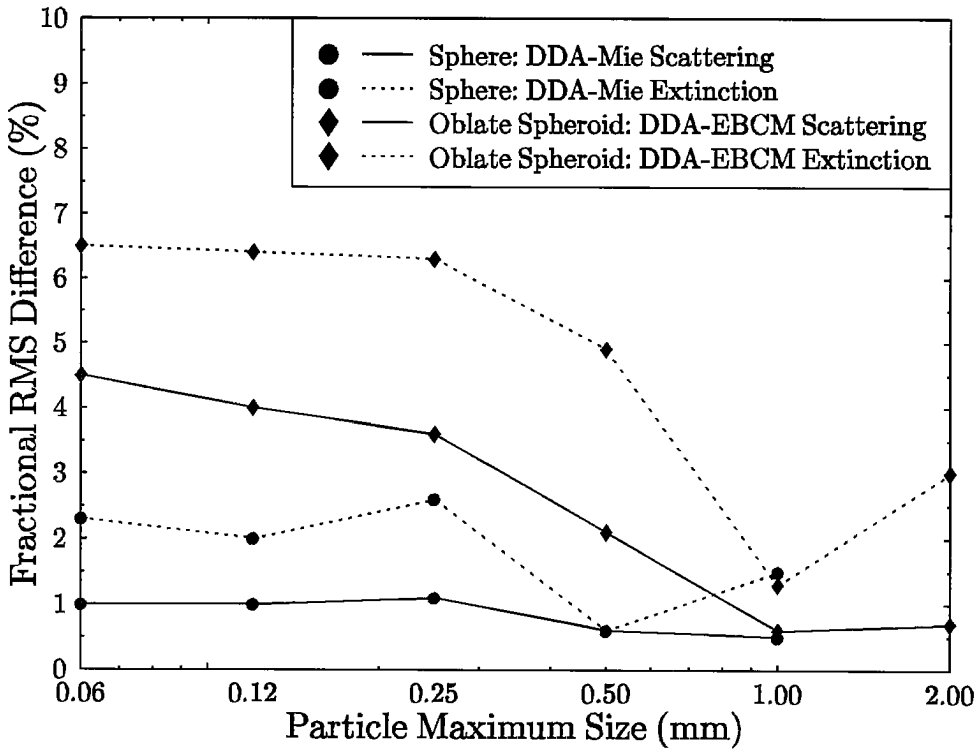


Figure 2.1: Fractional RMS difference between DDA and Mie/EBCM results for spheres and 0.25 axial ratio oblate spheroids. RMS difference is computed for extinction and scattering matrices at all angles for ice particles at 340 GHz.

## 2.2 Polarized Radiative Transfer

Upwelling microwave brightness temperatures from cirrus clouds are computed with a radiative transfer model developed to calculate the outgoing monochromatic polarized radiation from oriented nonspherical particles. This radiative transfer model requires two types of information about the atmosphere: 1. the microwave scattering properties of ice particles distributions computed by the discrete dipole approximation, and 2. the profile of temperature and gaseous absorption at the specified microwave frequency.

### 2.2.1 Microwave atmospheric absorption

In the microwave portion of the spectrum the primary gaseous absorbers in the atmosphere are molecular oxygen and water vapor. The absorption by oxygen is due to its magnetic dipole moment and occurs in a band between 50 and 60 GHz, an isolated line at 118.75 GHz, and weaker lines above 350 GHz. Water vapor has rotational lines due to its electric dipole moment at 22.235, 183.31, 325.15, and 380.20 GHz and several of increasing strength above 400 GHz. In addition, water vapor has a continuum absorption presumably from the far wings of many high frequency lines.

The absorption of microwaves by liquid cloud droplets can be combined with that from oxygen and water vapor. Cloud droplets, with diameters smaller than 50 microns, are very small compared to microwave wavelengths, and so are in the Rayleigh regime. For highly absorbing material, such as liquid water at these frequencies, Rayleigh scattering is negligible compared with absorption. The amount of absorption is proportional to the droplet volume and hence the microwave attenuation is proportional to the liquid water content ($W$ in g/m$^3$) of the cloud:

$$K = \left(\frac{6\pi}{\rho_\ell \lambda}\right) \mathrm{Im}\left[-\frac{m^2-1}{m^2+2}\right] W \ , \tag{2.15}$$

where $\rho_\ell$ is the density of water and $\lambda$ is the wavelength.

The absorption from oxygen, water vapor, and liquid cloud droplet is computed by the MPM92 (Millimeter-wave Propagation Model 1992) developed by Liebe (Liebe and Hufford, 1993). This model was adapted for this project into a routine that computes the attenuation at a specified frequency for a given temperature, total pressure, water vapor pressure, and liquid water content. The MPM92 models 44 oxygen lines and 30 water vapor lines with the Van Vleck-Weisskopf line shape with Rosenkranz modifications for line overlap. A two frequency Debye formula is used to fit the index of refraction of water. The water vapor continuum is fit empirically with terms proportional to the water vapor pressure and its square. Compared with an earlier version (Liebe, 1985) MPM92 has as much as 30% decrease in absorption in the microwave window regions.

### 2.2.2 Adding-doubling polarized radiative transfer model

The radiative transfer model used here is a modification of the model described in Evans (1990) and Evans and Stephens (1991), originally developed for randomly oriented nonspherical particles. This model was modified to apply to oriented particles. In this context the term "oriented particles" means that the scattering properties depend on the incident zenith angle, but not the incident azimuth angle, i.e. particles are still randomly oriented azimuthally. Counterintuitively, this actually simplifies things considerably since one does not have to translate the input scattering information and polarization reference frame from the scattering plane to the meridional plane used in the radiative transfer model. The DDA model computes and outputs the scattering matrix in terms of the meridional plane (defined by the z-axis and the direction of travel). Another difference between the two radiative transfer models is that the one for oriented particles does not support a solar direct beam source of radiation, which, anyway, is not needed for the microwave transfer problem considered here. The direct beam was removed because oriented particles polarize the direct radiation thereby complicating the source of diffuse radiation.

The radiative transfer model is monochromatic, meaning only one frequency is computed at a time. This is appropriate because the particle scattering and atmospheric absorption properties are fairly constant across typical radiometer bandpasses for the window channels considered here. The model also assumes a plane-parallel, or horizontally homogeneous, geometry. In contrast to the usual situation, this is a good approximation for computing microwave transfer in cirrus clouds. The small optical depth of cirrus clouds at microwave frequencies means that the inhomogeneities present in the clouds are averaged out over the footprint of the sensor. If thermal emission is the only source of radiation in a plane-parallel geometry then the the radiation field is azimuthally symmetric and of the four Stokes parameters that describe the polarization state of the radiation only $I$ and $Q$ are non-zero. Use of the vertical/horizontal polarization basis is more common in the field of microwave radiometry. The two polarization bases are simply related by

$$I_V = I + Q \qquad I_H = I - Q \ . \tag{2.16}$$

The $I$ Stokes parameter is the total intensity of radiation, and $Q$ is proportional to the difference between the vertical and horizontal polarizations.

The Planck function relates the emission from a blackbody to its temperature,

$$B(T) = \frac{c_1}{\lambda^5 \left[\exp\left(c_2/\lambda T\right) - 1\right]} \ , \tag{2.17}$$

where $B(T)$ has units of W m$^{-2}$ ster$^{-1}$ $\mu$m$^{-1}$, $T$ is the temperature in Kelvin, $\lambda$ is the wavelength in cm, $c_1 = 2hc^2 = 1.1911 \times 10^{-12}$ W m$^{-2}$ cm$^5$, and $c_2 = \frac{hc}{k} = 1.43388$ K cm.

In the microwave radiative transfer field the Rayleigh-Jeans approximation is often used. This approximation relates the Planck function linearly to the temperature,

$$B(T) \approx \frac{c_1}{c_2 \lambda^4} T \ , \tag{2.18}$$

and allows the radiative transfer to be done directly in terms of the brightness temperature. In this work the Rayleigh-Jeans approximation is *not* used, because of the high frequencies involved, and the radiative transfer is carried out in terms of radiance (W $m^{-2}$ $ster^{-1}$ $\mu m^{-1}$).

After the radiative transfer computation the $I$ and $Q$ radiances are converted to vertical and horizontal polarizations and expressed in terms of brightness temperatures. There are two ways to convert from a radiance ($I_\lambda$) to a brightness temperature. One is to invert the Planck function,

$$T_{EBB} = \frac{c_2 \lambda^{-1}}{\log\left[1 + c_1 / \lambda^5 I_\lambda\right]} \ , \tag{2.19}$$

giving the equivalent blackbody temperature. The other way is to use the Rayleigh-Jeans approximation,

$$T_{RJ} = \frac{c_2}{c_1} \lambda^4 I_\lambda \ . \tag{2.20}$$

These two different ways of computing the brightness temperature may be related by expressing the equivalent blackbody brightness temperature in terms of the Rayleigh-Jeans brightness temperature as

$$T_{EBB} \approx T_{RJ} + \frac{c_2}{2\lambda} - \frac{1}{3}\left(\frac{c_2}{2\lambda}\right)^2 \frac{1}{T_{RJ}} \ . \tag{2.21}$$

This means that to first order the difference between equivalent blackbody and Rayleigh-Jeans brightness temperature is a constant that depends on $\lambda$. For the frequencies considered here this constant offset varies from 2.05 K at 85.5 GHz to 8.21 K at 340 GHz. The discrepancy between $T_{EBB}$ and $T_{RJ}$ in the microwave is insignificant when dealing with brightness temperature differences. For example at 340 GHz and $T_{RJ} = 250$ K, the fractional difference between $\Delta T_{EBB}$ and $\Delta T_{RJ}$ is 0.00036. For this work the more accurate equivalent blackbody brightness temperatures will be used exclusively.

The monochromatic plane-parallel polarized radiative transfer equation with azimuthal symmetry is

$$\mu \frac{d\mathbf{I}(z,\mu)}{dz} = K(z,\mu)\mathbf{I}(z,\mu) \ - 2\pi \int_{-1}^{1} M(z,\mu,\mu') \ \mathbf{I}(z,\mu') d\mu' - \sigma(z,\mu) B\left[T(z)\right] \tag{2.22}$$

where,

- **I** is the vector of $I$ and $Q$ Stokes parameters,
- $M$ is the $2 \times 2$ scattering matrix,
- $K$ is the $2 \times 2$ extinction matrix,
- $\sigma$ is the emission vector,
- $B(T)$ is the Planck function of temperature,
- $z$ is the height coordinate, and
- $\mu$ is the cosine of the zenith angle ($\mu > 0$ downward).

The scattering matrix $M$, extinction matrix $K$, and the emission vector $\sigma$ for particles are computed by the DDA code. These three quantities should be related by

$$K(\mu) = 2\pi \int_{-1}^{1} M(\mu, \mu') d\mu' \; + \sigma(\mu) \; , \tag{2.23}$$

and this normalization condition is checked. For a gaseous absorption coefficient $k_g$, the extinction matrix is diagonal ($K_{II}(\mu) = K_{QQ}(\mu) = k_g$), the emission vector is unpolarized ($\sigma_I(\mu) = k_g$, $\sigma_Q = 0$), and the scattering matrix is zero. For layers containing both particles and gaseous absorption the corresponding extinction matrices and emission vectors are added together.

The angular aspects of the radiance field are represented by discrete angles chosen according to Gaussian or Lobatto quadrature schemes. The polarized radiative transfer equation then becomes

$$\begin{aligned} \pm\mu_j \tfrac{d\mathbf{I}(z,\pm\mu_j)}{dz} &= K(\pm\mu_j)\mathbf{I}(z,\pm\mu_j) - \sigma(z,\pm\mu)B(T) \qquad (2.24) \\ -2\pi \; \textstyle\sum_{j'=1}^{N} w_{j'} \; & [M(\pm\mu_j, +\mu_{j'}) \; \mathbf{I}(z,+\mu_{j'}) + M(\pm\mu_j, -\mu_{j'}) \; \mathbf{I}(z,-\mu_{j'})] \quad j = 1,\ldots,N \; , \end{aligned}$$

where there are $N$ quadrature angles per hemisphere ($0 < \mu_j < 1$), and the $w_j$'s are the quadrature weights. The scattering matrix, extinction matrix, and emission vector are computed by DDA for a particular set of quadrature angles that the radiative transfer program then uses. At each $z$ level the radiance field for one hemisphere of angles can be represented by vector $I = (\mathbf{I}_1, \ldots, \mathbf{I}_N) \; = (I_1, Q_1, \ldots, I_N, Q_N)$. In this notation $I^+$ is the downwelling radiance, and $I^-$ is the upwelling radiance.

The doubling and adding method is used to integrate the radiative transfer equation. This method requires the atmosphere to be broken down into a number of layers each with vertically uniform scattering and absorption properties. The temperature of the layer is given by the temperatures of its top and bottom, and a linear gradient in Planck function is assumed. The doubling/adding method was developed by van de Hulst (1963) and Grant and Hunt (1969). The starting point for discussion of the doubling/adding method is the interaction principle, which relates the radiation outgoing from a layer to the radiation incident upon the layer and radiation generated internally. In terms of matrix notation this is expressed as

$$\begin{aligned} I_b^+ &= T^+ I_t^+ + R^+ I_b^- + S^+ \\ I_t^- &= T^- I_b^- + R^- I_t^+ + S^- \; , \end{aligned} \tag{2.25}$$

where $T$ is the transmission matrix, $R$ is the reflection matrix, and $S$ is the source vector. $I_b^-$ is the radiation incident on the bottom of the layer, and $I_t^+$ is the radiation incident on the top of the layer. The goal of the doubling and adding method is to compute $T$, $R$, and $S$ for the whole atmosphere, and hence find the upwelling radiance.

The interaction principle may be used to find the properties $(T, R, S)$ of the combination of two adjacent layers in terms of the individual layer properties. This adding formula is derived by eliminating the intervening level radiances from the interaction principle equations for the two layers, to get

$$\begin{aligned} R_T^- &= R_1^- + T_1^- \Gamma^- R_2^- T_1^+ \,, \\ T_T^- &= T_1^- \Gamma^- T_2^- \,, \qquad \Gamma^- = \left[1 - R_2^- R_1^+\right]^{-1} \,, \\ S_T^- &= S_1^- + T_1^- \Gamma^- (S_2^- + R_2^- S_1^+) \,. \end{aligned} \tag{2.26}$$

The formulae for the downwelling properties are equivalent.

The properties of each homogeneous input layer are computed with the doubling algorithm. The doubling method is just the adding method applied multiple times to layers with the same properties. Starting with an infinitesimally thin layer, each step doubles the thickness of the layer until the desired thickness is reached. For $n$ doubling steps the infinitesimal layer thickness is $\delta z = 2^{-n} \Delta z$, where $\Delta z$ is the final layer thickness. The infinitesimal layer properties are related to the scattering matrix $M$, extinction matrix $K$, and emission vector $\sigma$ by

$$\begin{aligned} |T^{\pm}|_{iji'j'} &= \left[\delta_{ii'}\delta_{jj'} - \frac{\delta z}{\mu_j}\left(\delta_{jj'}|K(\pm\mu_j)|_{ii'} - 2\pi w_{j'}|M(\pm\mu_j, \pm\mu_{j'})|_{ii'}\right)\right] \\ |R^{\pm}|_{iji'j'} &= 2\pi \frac{\delta z}{\mu_j} w_{j'} |M(\pm\mu_j, \mp\mu_{j'})|_{ii'} \\ |S^{\pm}|_{ij} &= \frac{\delta z}{\mu_j} |\sigma(\pm\mu_j)|_i B(T_t) \,, \end{aligned} \tag{2.27}$$

where the $j$'s are the quadrature angle index and the $i$'s are the Stokes parameter index ($i = 1, 2$ for $I$ and $Q$). This defines the initialization of the doubling method, and these particular formulae are called the infinitesimal generator initialization.

Since it is desirable to have the thermal source (i.e. temperature) vary with depth within a homogeneous layer, the simple doubling formula for sources cannot be used. Instead an extension due to Wiscombe (1976) for sources that vary linearly with height is used. The complete doubling formulae used here for relating the $2^{k+1}\delta z$ thick layer to the $2^k \delta z$ thick layer are

$$\begin{aligned} R_{k+1}^+ = R_k^+ + T_k^+ \Gamma^+ R_k^+ T_k^- \quad &, \quad R_{k+1}^- = R_k^- + T_k^- \Gamma^- R_k^- T_k^+ \\ T_{k+1}^+ = T_k^+ \Gamma^+ T_k^+ \quad &, \quad T_{k+1}^- = T_k^- \Gamma^- T_k^- \\ \Gamma^+ = \left[1 - R_k^+ R_k^-\right]^{-1} \quad &, \quad \Gamma^- = \left[1 - R_k^- R_k^+\right]^{-1} \,, \end{aligned}$$

$$\begin{aligned} S_{k+1}^+ &= (S_k^+ + 2^k \alpha C_k^+) + T_k^+ \Gamma^+ \left[S_k^+ + R_k^+ (S_k^- + 2^k \alpha C_k^-)\right] \\ S_{k+1}^- &= S_k^- + T_k^- \Gamma^- \left[(S_k^- + 2^k \alpha C_k^-) + R_k^- S_k^+\right] \end{aligned}$$

$$
\begin{aligned}
C_{k+1}^{+} &= C_k^{+} + T_k^{+}\Gamma^{+}\left[C_k^{+} + R_k^{+}C_k^{-}\right] \\
C_{k+1}^{-} &= C_k^{-} + T_k^{-}\Gamma^{-}\left[C_k^{-} + R_k^{-}C_k^{+}\right] \\
\alpha &= \left(\frac{B(T_b)}{B(T_t)} - 1\right) 2^{-n} \,,
\end{aligned} \tag{2.28}
$$

where $T_t$ is the temperature of the top of the layer, and $T_b$ is the temperature at the bottom. The $C$ vector is initialized the same as the $S$ vector. If a layer has no scattering then doubling is bypassed by directly computing the $T, R, S$ properties of the layer.

The doubling algorithm computes the reflection and transmission matrices and the source vectors for the homogeneous layers, which are then successively combined, from the top down, with the adding method. The surface boundary is treating as a layer with a transmission of unity, the appropriate reflection, and no source term. The radiation emitted from the surface is then the incident radiation on the lower boundary. The model incorporates two types of surfaces: Lambertian and Fresnel. The Lambertian surface emits and reflects isotropic and unpolarized radiation. The Lambertian reflection matrix and emitted radiance vector are

$$
|R_g|_{jj'ii'} = 2(1-\epsilon) w_{j'} \mu_{j'} \delta_{i,1} \quad , \quad |I_g^{-}|_{ji} = \epsilon B(T) \delta_{i,1} \,. \tag{2.29}
$$

where $\epsilon$ is the surface emissivity. The Fresnel surface is use to model flat water surfaces at microwave frequencies. The incident radiation is reflected specularly such that the incident zenith angle equals the reflected zenith angle. The horizontal polarization is reflected differently than the vertical polarization. The Fresnel reflection formulae for a vacuum/dielectric interface are

$$
\begin{aligned}
R_V(\mu) &= \frac{m^2\mu - \sqrt{m^2 + \mu^2 - 1}}{m^2\mu + \sqrt{m^2 + \mu^2 - 1}} \\
R_H(\mu) &= \frac{\mu - \sqrt{m^2 + \mu^2 - 1}}{\mu + \sqrt{m^2 + \mu^2 - 1}} \,,
\end{aligned} \tag{2.30}
$$

where $\mu$ is the cosine of the incident zenith angle and $m$ is the complex index of refraction of the dielectric surface. The reflection matrix is then

$$
|R_g|_{jj'} = \begin{pmatrix} \frac{1}{2}(|R_V|^2 + |R_H|^2) & \frac{1}{2}(|R_V|^2 - |R_H|^2 \\ \frac{1}{2}(|R_V|^2 - |R_H|^2) & \frac{1}{2}(|R_V|^2 + |R_H|^2 \end{pmatrix} \delta_{jj'} \,, \tag{2.31}
$$

where the reflection coefficients are at the angles $\mu = \mu_{j'}$ The thermal radiation emitted by a semi-infinite absorbing Fresnel surface is polarized and angle dependent

$$
|I_g^{-}|_j = \begin{pmatrix} 1 - \frac{1}{2}(|R_v|^2 + |R_h|^2) \\ -\frac{1}{2}(|R_v|^2 - |R_h|^2) \end{pmatrix} B(T) \,. \tag{2.32}
$$

This polarized radiative transfer model for oriented particles was tested by comparison with the model for randomly oriented particles. The comparison was made for a three

layer atmosphere containing a layer of spherical ice particles and a layer of spherical water drops. The Legendre series representation of the phase function computed by Mie theory was converted to the form required by this model (scattering matrices, extinction matrices, and emission vectors) using the procedure developed for the randomly oriented particle model (Evans and Stephens, 1991). The resulting upwelling brightness temperatures were identical between the two models. The radiative transfer model was not specifically tested for oriented particles.

# Chapter 3

# THEORY OF PASSIVE MICROWAVE REMOTE SENSING OF CIRRUS

## 3.1 Overview of Satellite Remote Sensing of Cirrus

Most methods previously proposed for remote sensing of cirrus have been aimed at determining the location, optical depth, or particle effective radius. Perhaps the most important of these methods is the one used for ISCCP (Rossow et al., 1985). This uses the standard visible and thermal infrared channels on operational geostationary and polar orbiting satellites to detect cloud and retrieve optical depth and cloud top pressure. The visible reflectance is converted to optical depth using a radiative transfer model that assumes a homogeneous cloud made up of water spheres with a fixed size distribution. The visible optical depth is divided by 3 to produce an infrared optical depth that is used to derive an emissivity for retrieving cloud top temperature. Recently, Minnis et al. (1993a, 1993b) have developed a radiative parameterization for hexagonal ice particles and showed that the resulting retrieved cirrus heights are much closer to lidar measured heights than when using the water droplet assumption.

Barton (1983) used solar reflection data from two channels in the 2.7 $\mu$m absorption band to detect high clouds and measure their height, producing a cirrus cloud climatology. The advantage of this method is that the strong absorption prevents radiation reflected by the surface or lower clouds to interfere with the detection of clouds above 6 km. Woodbury and McCormick (1986) derived a cirrus climatology from the limb scanning solar occultation technique employed in the Stratospheric Aerosol and Gas Experiment (SAGE). These two methods are effective for determining if cirrus is present, but cannot determine the mass or optical properties of the cirrus.

Recently near infrared reflection has also been used to estimate effective particle size in cirrus by relying on the single scattering albedo dependence on particle size. Wielicki et al. (1990) used Landsat observation at 0.83, 1.65, and 2.21 $\mu$m to retrieve effective particle size as well as visible optical depth. The near IR reflectance, for example at 1.6 $\mu$m, can also be used to distinguish water from ice clouds (Pilewskie and Twomey, 1987).

A number of techniques have been developed that use the brightness temperature difference between 11 and 12 $\mu$m to detect thin cirrus or retrieve cirrus emissivity and cloud temperature (Inoue, 1985; Wu, 1987; Prabhakara et al., 1988; Parol et al., 1991).

Plots of the brightness temperature difference (BTD) vs. the brightness temperature at 11 $\mu$m shows an arch pattern due to small cloud particles. The height of the arch is related to the effective particle size (smaller particles causing a larger BTD). A related method developed by Smith et al. (1993) matches high resolution IR interferometer spectra with output from a high spectral resolution radiative transfer model to retrieve effective particle size and ice water content. A lidar is used to determine cloud top and base height and spherical particles and homogeneous clouds are assumed. Ou et al. (1993) developed a method using AVHRR 3.7 and 10.9 $\mu$m channels to retrieve optical depth, effective particle size, and cloud temperature. They used scattering from hexagonal ice crystals to compute emissivity, but relied on a parameterization by Heymsfield and Platt (1984) to get the size distribution from the cloud temperature.

Lidar remote sensing has been used extensively for cirrus research over the past two decades. Lidar is excellent for determining cloud base and top and internal structure of cirrus (e.g., Sassen et al., 1990). Airborne lidar systems (e.g., Spinhirne and Hart, 1990) allow much greater coverage for intensive field campaigns than do ground base systems. The depolarization of the lidar return from nonspherical ice crystals allows determination of the water phase (Sassen, 1974; Platt et al., 1978). The determination of optical depth, ice mass, particle size, or shape is rather limited due to the difficulties of large and nonspherical particles which cause unknown backscattering to extinction ratios and large optical depths which cause multiple scattering back into the lidar return. Techniques that combine lidar with IR radiometers (Platt, 1979) offer a way to measure the backscattering to extinction ratio.

Another active remote sensing technique that has been recently applied to cirrus clouds is that of high frequency radar. Kropfli et al. (1993) have developed a method to infer ice water content, particle size, and shape from 8 mm Doppler radar by using average measured fallspeed/reflectivity relationships. A technique that combines radar and thermal infrared radiometry data to retrieve ice water content and characteristic particle size has been described by Matrosov et al. (1992). Even lidar and radar have been combined to infer cirrus cloud effective radius (Intrieri et al., 1993).

The survey above touches on just some of the many schemes to remotely sense cirrus clouds in order to give an idea of the basic techniques that do not involve microwave radiometry. Few of the above studies attempted to retrieve ice water path (IWP), and those that did had to make gross assumptions of particle sphericity and cloud homogeneity. Most of the methods to measure effective particle size also assumed spherical particles. The active sensing methods are not currently viable for space-based platforms, but will be so in the future as instrumentation evolves.

Because of the lack of high frequency microwave radiometers, there has been little work directed specifically at passive microwave remote sensing of cirrus. Wu (1987) used the Advanced Microwave Moisture Sounder (AMMS) with channels at 92,183$\pm$2,5,9 GHz

combined with the infrared radiometry data to infer the IWC and geometrical thickness of clouds. The algorithm was based on a forward microwave radiative transfer model, though the details are not given. The situation was mainly deep convection, with correspondingly high IWC, so the clouds were probably not cirrus. Gasiewski (1992) performed a theoretical study of the use of microwave frequencies from 90 to 410 GHz. Through radiative transfer simulations he examined the sensitivity of the brightness temperatures to water vapor, precipitation, and water clouds as well as ice clouds. He discussed the concept of additional degrees of freedom using multiple frequencies in connection with typical particle sizes. Only one-parameter size distributions (Marshall-Palmer and Sekhon-Srivastava), however, were considered so the characteristic particle size was directly related to the IWC. Water and ice spheres were used for modeling scattering so the effect of particle shape was not dealt with. Overall the paper was a general sensitivity study, and was not geared toward the remote sensing of cirrus properties.

The work on microwave remote sensing of cirrus described in this dissertation was presented in a somewhat different form in a conference proceedings (Evans and Stephens, 1992). That work used power law particle size distributions with three different slopes, rather than the more realistic and diverse gamma distributions used here. In addition, the current work includes an extra shape (equivalent volume spheres) to simulate spatial (non-planar) rosette particles.

### 3.2 Microwave Modeling of Cirrus

The goal of passive microwave remote sensing of cirrus clouds should be to detect cirrus and measure the ice water path (IWP) and the effective size of the ice particles. The potential observables to measure these quantities are the upwelling brightness temperatures (radiances) at different frequencies, polarizations, and angles. Because there is such a small amount of water vapor at the levels of cold ($T < -40°C$) cirrus and above, the microwave window channel absorption is small both in and above cirrus clouds. This means that cirrus can be thought of as simply modulating the upwelling microwave radiation incident upon it from below. Since cirrus ice particles for the most part have a high single scattering albedo at microwave frequencies they mainly scatter rather than absorb radiation. Thus the primary effect of cirrus is to reduce the radiation reaching a satellite sensor, thus creating a brightness temperature depression as compared to the clear sky value. Cirrus clouds are expected to be optically thin at microwave frequencies, so everything else fixed, the brightness temperature depression would be directly proportional to the integrated ice mass (IWP). The major problem in microwave remote sensing of cirrus is that other factors that influence the size of the temperature depression are not fixed. As shown below the most important factors are the size distribution of ice particles and their shapes.

The work described in this chapter investigates these factors by computing the scattering properties of five shapes for 13 discrete sizes at four frequencies using the DDA method. The scattering properties for the discrete sizes are combined for 18 gamma size distributions. The polarized radiative transfer model is used to compute the upwelling brightness temperatures from a number of atmospheric configurations. These simulated brightness temperatures are examined to find ways of sensing IWP, characteristic size, and particle shape.

### 3.2.1 DDA modeling

The scattering and radiative transfer computations are made at four frequencies (85.5, 157, 220, and 340 GHz). The choice of these frequencies was guided by the channels on current and future instruments. The 85.5 GHz channel is on SSM/I, and 157 GHz was a planned channel for AMSU/B. NASA is developing the Millimeter-Wave Imaging Radiometer (MIR) which has channels near all four of these frequencies (89, 150, 183$\pm$1,3,7, 220, and 325$\pm$1,3,9 GHz). Because the microwave scattering properties change slowly with frequency, only a small number of frequencies are required to determine the spectral characteristics.

At the cold temperatures characteristic of most cirrus clouds (about $< -30°$C) vapor depositional growth of ice crystals occurs along the $c$ axis resulting in hexagonal columnar shapes (Pruppacher and Klett, 1980). This includes solid and hollow columns and also columns grown around frozen water drops, i.e. bullets and rosettes. Growth along the $a$ axis occurs above $-22°$C, resulting in hexagonal plate shapes. For this work five ice crystal shapes are chosen: solid columns, hollow columns, hexagonal plates, planar rosettes, and spheres. Bullets are not modeled separately, as their shape and aspect ratios are similar to columns. The long axis of the particles are assumed to be randomly oriented in the horizontal plane as a result of aerodynamic forces. Ono (1969) observed that columns and plates fall in this orientation, and lidar studies (e.g., Platt et al., 1978) indicate that plates fall oriented horizontally to within a few degrees. Since columns are expected to rotate about their long axis, solid columns are modeled by cylinders while hollow columns are modeled by cylinders with cones removed from each end. This simplification is justified at the wavelengths used here, which do not resolve the corners precisely. In nature, rosette shaped crystals have bullets attached to a central drop at seemingly random angles, but for this modeling the rosette shape has been simplified to four coplanar cylinders meeting at right angles. Equivalent volume spheres are used to model spatial rosettes with columns meeting at arbitrary angles. The volume of the spheres goes as $V = \frac{\pi}{6} D^3 (D/10\mu\text{m})^{-1/2}$, to simulate the decreasing density of larger spatial rosettes ($D$ is diameter). These specific shapes are modeled, instead of something generic like different aspect ratio oblate and prolate spheroids, because ice crystals do grow in particular habits and do not have a continuum of shapes.

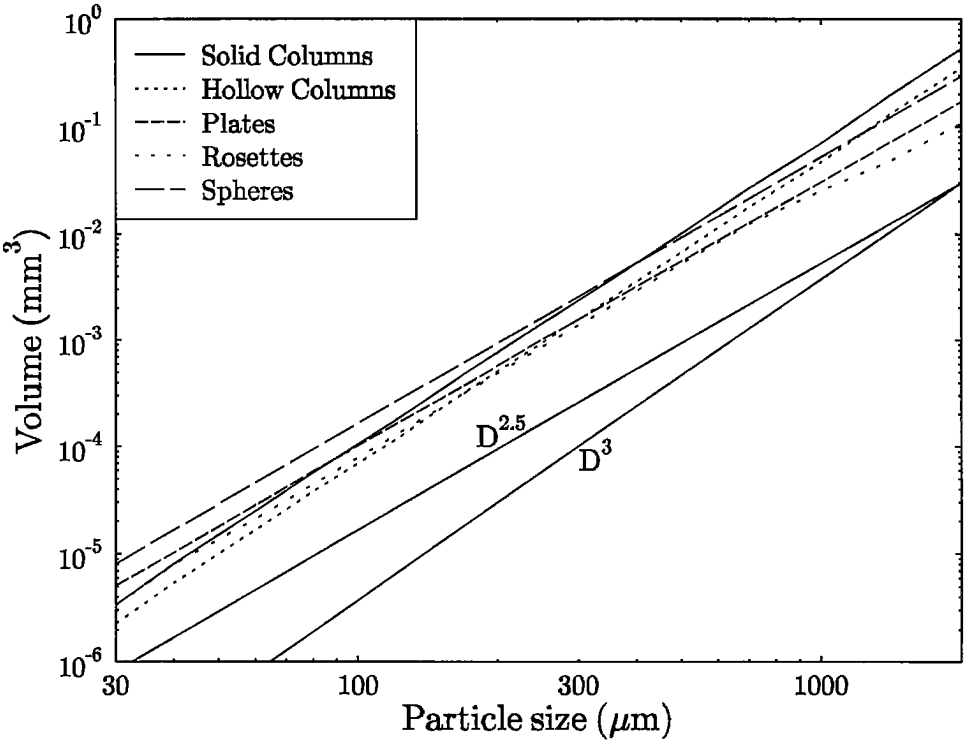


Figure 3.1: The particle volume vs. size for the five particle shapes. Also plotted for comparison are $D^{2.5}$ and $D^3$ sloped lines.

In order to simulate a size distribution of ice crystals the scattering is computed from 13 discrete maximum particle diameters from 30 $\mu$m to 2000 $\mu$m (intervals of about 1.4). The aspect ratio of the crystals is taken from empirical formulae developed by Heymsfield (1972) (also in Pruppacher and Klett (1980), namely $h = .260D^{.927}$ for columns, $h = 0.0141D^{.474}$ for plates, and $h = .1526D^{.7856}$ $D < 300\mu$m, and $h = .0630D^{.532}$ $D > 300\mu$m, for bullets in rosettes, where $h$ is the thickness (cm) and $D$ is the maximum particle dimension (cm). The maximum particle diameter $D$ is used to characterize the particle size, rather than the equivalent volume sphere diameter $D_{eq}$, because the maximum particle extent is usually what is reported in cirrus microphysical measurements. Figure 3.1 shows the volume vs. particle size for the five shapes. The ordering of volume with shape varies with the particle size because of the different aspect ratio functions.

The scattering properties for the spheres are computed with Mie theory (Bohren and Huffman, 1983), while those for the other four shapes are computed with the DDA method. The major and minor dimension, dipole size, number of dipoles, and DDA solution method are listed in Table 3.1. The dipole size relative to the wavelength ($|m|kd$) go as high as 0.92 for the 2.0 mm column at 340 GHz. A test comparing this case to one with half the dipole size (11880 dipoles) gives an rms fractional difference of 0.0015 for the scattering matrix

Table 3.1: Particle sizes and DDA dipole layouts

| DDA Setup for Columns | | | | | |
|---|---|---|---|---|---|
| Major Dim ($\mu$m) | Minor Dim ($\mu$m) | Dipole Size ($\mu$m) | Total Dipoles Solid Columns | Hollow Columns | Method |
| 2000 | 580 | 72.5 | 1680 | 1416 | fft |
| 1400 | 420 | 52.5 | 1620 | 1356 | fft |
| 1000 | 300 | 37.5 | 1620 | 1356 | fft |
| 700 | 220 | 44 | 400 | 356 | inv |
| 500 | 160 | 32 | 400 | 356 | inv |
| 350 | 115 | 23 | 400 | 356 | inv |
| 250 | 85 | 22 | 192 | 176 | inv |
| 170 | 60 | 15 | 192 | 176 | inv |
| 120 | 43 | 11 | 176 | 168 | inv |
| 80 | 30 | 8 | 160 | 152 | inv |
| 60 | 23 | 6 | 160 | 152 | inv |
| 40 | 16 | 4 | 160 | 152 | inv |
| 30 | 12 | 3 | 160 | 152 | inv |

| | Setup for Plates | | | | Setup for Rosettes | | | |
|---|---|---|---|---|---|---|---|---|
| Major Dim ($\mu$m) | Minor Dim ($\mu$m) | Dipole Size ($\mu$m) | Total Dipoles | Method | Minor Dim ($\mu$m) | Dipole Size ($\mu$m) | Total Dipoles | Method |
| 2000 | 66 | 66 | 645 | inv | 190 | 64 | 720 | fft |
| 1400 | 56 | 56 | 442 | inv | 150 | 50 | 624 | inv |
| 1000 | 47 | 47 | 326 | inv | 130 | 44 | 387 | inv |
| 700 | 40 | 40 | 228 | inv | 110 | 37 | 315 | inv |
| 500 | 34 | 34 | 159 | inv | 85 | 30 | 279 | inv |
| 350 | 29 | 29 | 115 | inv | 64 | 22 | 336 | inv |
| 250 | 25 | 25 | 78 | inv | 49 | 17 | 243 | inv |
| 170 | 20 | 20 | 60 | inv | 36 | 12 | 243 | inv |
| 120 | 17 | 17 | 48 | inv | 27 | 9 | 288 | inv |
| 80 | 14 | 14 | 26 | inv | 20 | 7 | 240 | inv |
| 60 | 12 | 12 | 25 | inv | 16 | 6 | 192 | inv |
| 40 | 10 | 10 | 16 | inv | 12 | 4 | 192 | inv |
| 30 | 9 | 9 | 12 | inv | 9 | 3 | 192 | inv |

and 0.013 for the extinction matrix over 16 zenith angles. The index of refraction for ice at $-60°$C (Warren, 1984) at the four frequencies (85.5, 157, 220, and 340 GHz) is given in Table 3.2. The Lorentz-Lorenz mixing rule is used for edge dipoles, and other dipoles are assumed to be solid ice. The scattering properties are computed for eight Lobatto quadrature zenith angles per hemisphere (incident and outgoing). The scattering matrix is averaged over 16 outgoing azimuth angles, and the horizontal orientation averaging is done with 8 incident azimuths over a 180° range. The matrix inverse solution method is used when allowed by available memory, as it is substantially faster because of the many incident directions used. The conjugate gradient iterations for the FFT solution method are done until a solution accuracy of $10^{-4}$ is reached (the average number of iterations ranges from 14 to 101 per DDA run).

Table 3.2: Index of refraction of ice for the four frequencies.

| Frequency (GHz) | Wavelength (cm) | Index of Refraction (−60°C) |
|---|---|---|
| 85.5 | .351 | (1.778,–0.0012) |
| 157 | .191 | (1.779,–0.0019) |
| 220 | .136 | (1.780,–0.0024) |
| 340 | .088 | (1.781,–0.0033) |

### 3.2.2 Discrete size distributions

The scattering properties (extinction, scattering, and emission) are averaged over the 13 discrete ice particles sizes distributed in a gamma size distribution, defined here by

$$N = aD^{\alpha}e^{-bD} \qquad b = \frac{\alpha + 3.67}{D_m}, \tag{3.1}$$

where $N$ is the number concentration per size interval and the distribution is defined by $D_m$ and $\alpha$. $D_m$ is the diameter of the median of the third moment of the distribution, which is not the median of the volume because the particle volumes increase more slowly than the third power. The parameter $\alpha$ is related to the width of the distribution by

$$\frac{1}{1+\alpha} = \frac{\langle D^2 \rangle}{\langle D \rangle^2}\,, \tag{3.2}$$

where $\langle \ldots \rangle$ implies averaging over the size distribution, so a larger $\alpha$ means a narrower distribution. The gamma distribution has been used by Matrosov et al. (1992) and Matrosov et al. (1993) for radar remote sensing of cirrus. Kosarev and Mazin (1989) analyzed many cirrus size distributions and found that gamma distributions were an adequate representation with the width parameter $\alpha$ usually ranging from 0 to 2. Heymsfield and Platt (1984) fit two-slope piecewise power laws to observed cirrus size distributions. This takes into account the lowering of the slope (log-log) at smaller particle sizes, but the number concentration diverges at the lower boundary, so a minimum particle size is needed. The gamma distribution concentration goes to zero for small sizes if $\alpha > 0$. The gamma distribution is chosen because this two parameter distribution can simply represent a variety of size distributions.

Because there are only 13 particle sizes care must be taken when converting the size distribution integral to a weighted sum. In the procedure used here each discrete size $D_i$ represents a range of sizes from $D_i^l$ to $D_i^u$. The integral is approximated by

$$\int_0^{\infty} N(D)\mathbf{k}(D)dD \approx \sum_{i=1}^{n} \mathbf{k}(D_i) \int_{D_i^l}^{D_i^u} N(D) \left(\frac{D}{D_i}\right)^p dD = \sum\sum_{i=1}^{n} N_i \mathbf{k}(D_i)\,, \tag{3.3}$$

where $\mathbf{k}$ represents all the scattering quantities being summed together. The $(D/D_i)^p$ factor takes into account that the scattering properties are not constant but generally

Table 3.3: Nadir effective size for five shapes and six distributions.

| $D_m$ | $\langle V\rangle/\langle A\rangle$ ($\mu$m) | | | | |
|---|---|---|---|---|---|
| ($\mu$m) | Column | Hollow | Plate | Rosette | Sphere |
| 70 | 18.3 | 12.2 | 12.1 | 12.6 | 16.2 |
| 100 | 24.6 | 16.4 | 14.1 | 16.1 | 19.0 |
| 150 | 35.4 | 23.5 | 17.1 | 21.9 | 23.1 |
| 250 | 56.3 | 37.5 | 22.0 | 32.6 | 29.8 |
| 400 | 86.5 | 57.7 | 27.6 | 46.8 | 37.7 |
| 700 | 144.4 | 96.4 | 35.9 | 69.2 | 49.8 |

increase over the size interval. The power $p$ should be the average power law increase of the scattering properties. For this work $p = 3$ (for solid columns at 340 GHz there is only about 1% difference in the resulting scattering properties between $p = 3$ and $p = 4$). For gamma distributions the weights for the sum are

$$N_i = aD_i^{-p}b^{-(\alpha+p+1)}\left[\Gamma(\alpha+p+1, bD_i^u) - \Gamma(\alpha+p+1, bD_i^l)\right] , \tag{3.4}$$

where $\Gamma$ is the incomplete gamma function $\Gamma(a,x) = \int_0^x t^{a-1}e^{-t}dt$. Since the $D_i$ have logarithmic spacing the size ranges are set to the geometric mean of the particle sizes: $D_i^l = \sqrt{D_{i-1}D_i}$ and $D_i^u = \sqrt{D_iD_{i+1}}$. At the endpoints, we choose $D_1^l = 10\mu$m and $D_n^u = 2000\mu$m.

Using the above procedure 18 gamma size distributions for each of the five shapes are computed. Six $D_m$'s (70,100,150,250,400,700$\mu$m) that cover the observed ranges of sizes (Heymsfield et al. 1990) are used. For each $D_m$ there are three $\alpha$'s (0,1,2). Figure 3.2 shows the 18 discrete size distributions for solid columns. For spherical particles the effective radius is often used when relating the microphysical and radiative aspects of clouds. The effective radius, $r_{eff}$, is the ratio of the third moment of the size distribution to the second moment. An equivalent quantity for nonspherical particles is $\langle V\rangle/\langle A\rangle$, which is the ratio of the particle volume averaged over the size distribution to the average projected particle area. This quantity depends on the particle shape and orientation as well as the size distribution (for spheres $\langle V\rangle/\langle A\rangle = 4r_{eff}/3$). For solid columns with $\alpha = 1$ and a nadir view $\langle V\rangle/\langle A\rangle = 0.17D_m^{0.92}$ for units in cm. Table 3.3 lists effective size for a nadir view for the five shapes and gamma size distributions with $\alpha = 1$

There are two areas one could question the accuracy of the discrete distribution in approximating a continuous gamma distribution: whether the smallest size is small enough and whether 13 sizes is enough. If the volume of the particles goes as $D^{2.5}$ then the size distribution with the most small particles ($D_m = 70\mu$m, $\alpha = 0$) has 13% of its mass below the smallest discrete size (30$\mu$m), though only 0.6% below 10$\mu$m. Since the smallest particles are nearly purely absorbing, the extinction goes as the volume, and the discrete size summing procedure should adequately take into account the mass below the smallest discrete size. Most of the size distributions have negligible mass below 30$\mu$m, anyway.

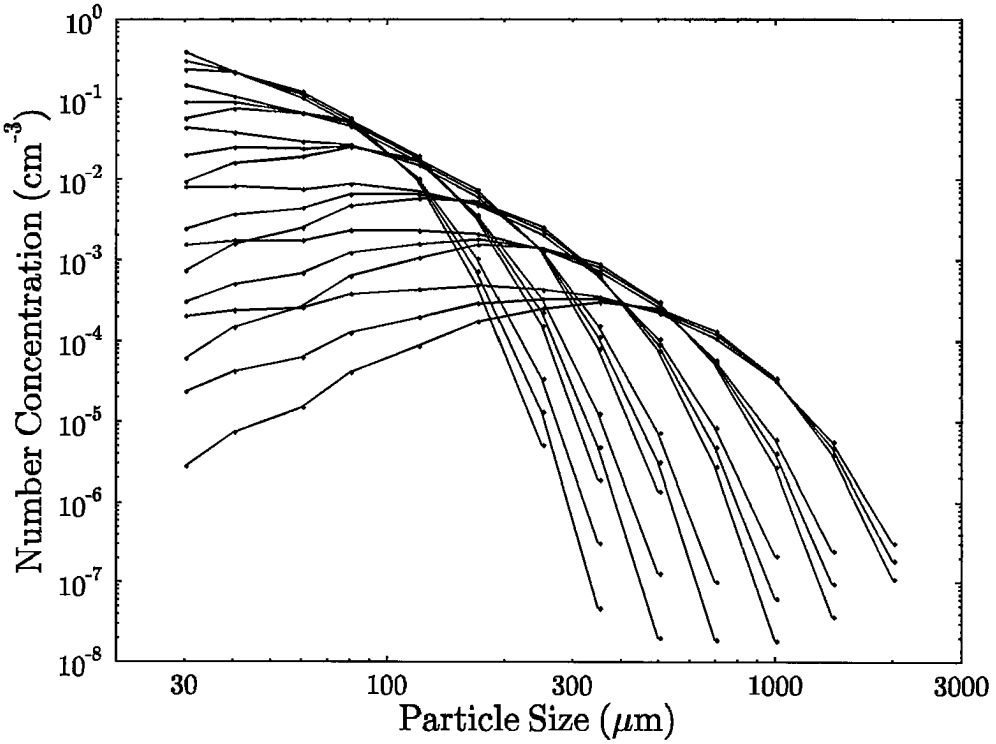


Figure 3.2: The 18 gamma size distribution for solid columns.

One way to test the accuracy of the discrete size distribution is to compare the 13 size distribution with one having many more sizes. This can be done for spherical particles because the scattering properties of spheres can be computed rapidly. An approximately continuous size distribution is made using the same gamma distribution procedure above, but using 399 sizes (interval of 5 microns) from 10 to 2000 microns. Comparisons are made at 85.5 and 340 GHz for all 18 gamma size distributions. The fractional difference in extinction is always less than 2.4% and the difference in single scattering albedo is always less than 0.01.

## 3.3 DDA Scattering Results

The results of the DDA and Mie scattering computations are presented two ways. The first way is is to plot single scattering quantities that are chosen for their relevance to the radiative transfer process. The second way is to present the results of fits to functions that can be used in a simple first order radiative transfer model to compute upwelling brightness temperatures.

### 3.3.1 Plots of scattering results

The microwave single scattering results computed by the DDA and by Mie theory are plotted both for discrete sizes and for size distributions. The results are shown for two angles, nadir and about 49°, which is near the SSM/I observation angle and is typical for the maximum angle of scanning instruments. For horizontally oriented particles a non-nadir angle must be used to observe polarization signatures. The size distribution scattering results are presented as a function of the $D_m$ parameter which characterizes the particle size of the distribution.

The extinction provides an indication of how much the cirrus particles will depress the brightness temperature. Figures 3.3 and 3.4 show the nadir extinction as a function of particle size for the five shapes at 85 and 340 GHz, respectively. The normalization is such that are 10 particles per $m^3$ if the extinction has units of $km^{-1}$. The extinction increases dramatically with size and is, of course, larger at the higher frequency. Three regimes can be identified for the rate of increase with particle size. For small particles ($< 300\mu$m at 85 GHz, or $< 100\mu$m at 340 GHz), absorption dominates, and the extinction goes as the volume, which is less than the third power of size because of the changing aspect ratio. For larger particles, scattering dominates, and the extinction goes as the square of the volume as long as the sizes are in the Rayleigh regime ($< 500\mu$m at 340 GHz). Beyond the Rayleigh regime the extinction curve goes up more slowly again. The difference in extinction between the shapes is primarily due to the different volumes (see fig. 3.1).

The next series of four plots shows extinction as a function of size distribution $D_m$, for distributions with an ice water content of 0.01 $g/m^3$. Figure 3.5 shows the effect of

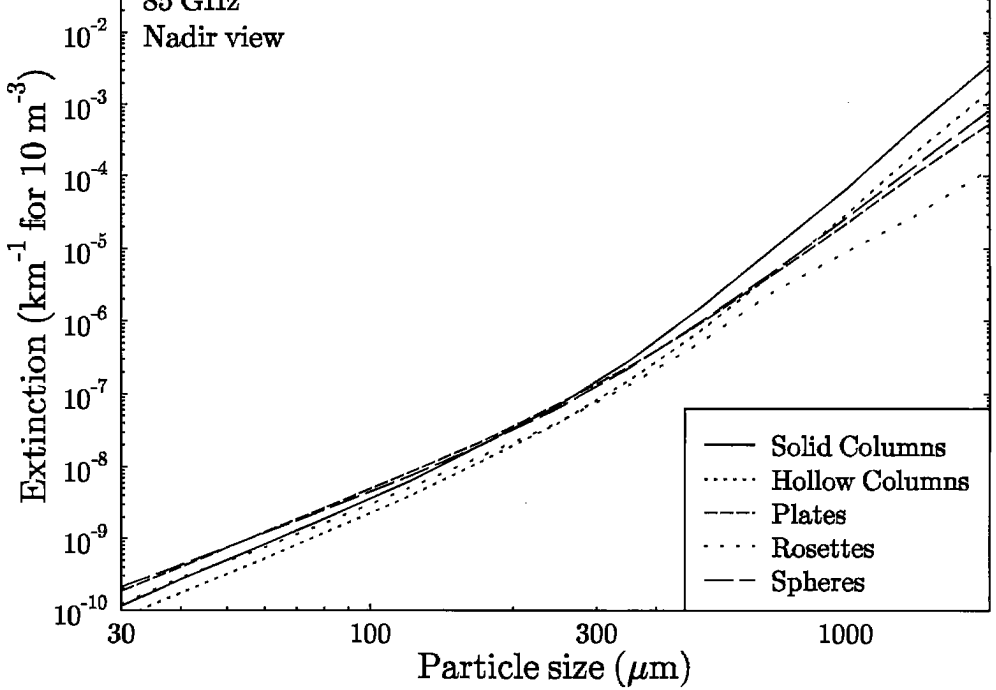


Figure 3.3: Extinction vs. particle size at 85 GHz.

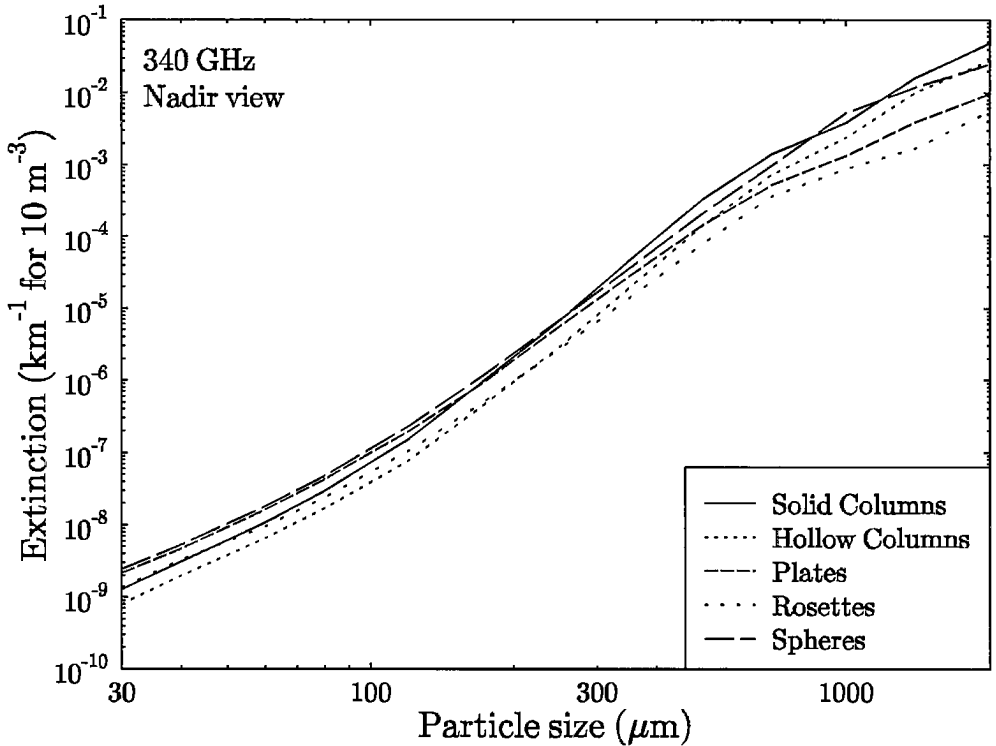

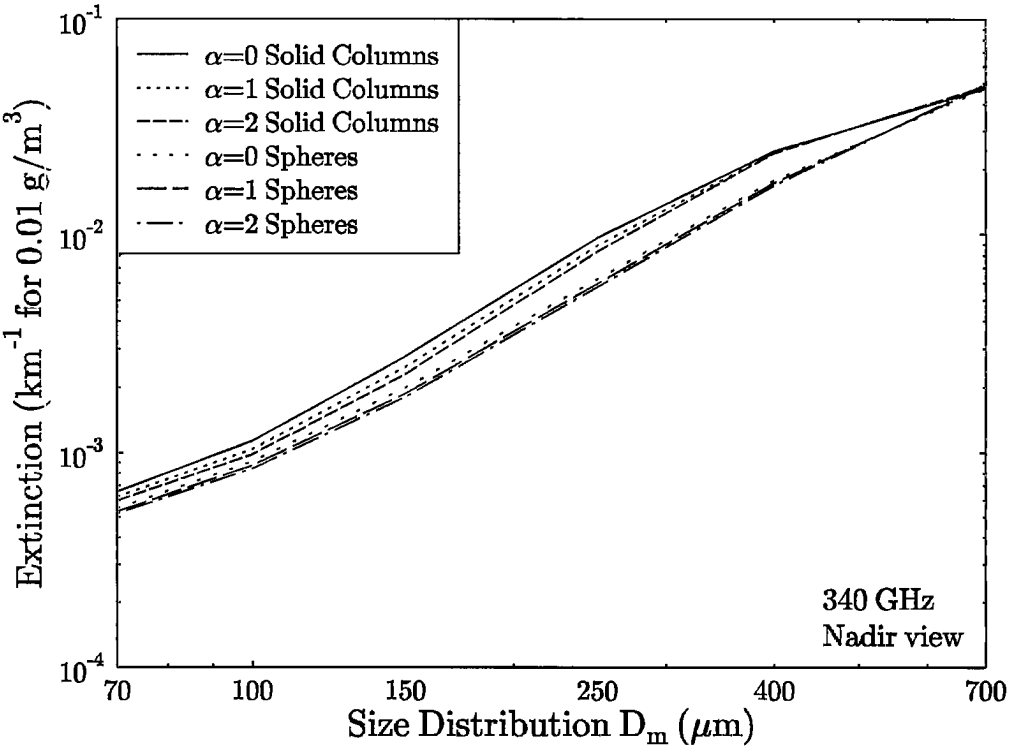


Figure 3.5: Extinction vs. size distribution for columns and spheres at 340 GHz.

the gamma size distribution width parameter $\alpha$ for columns and spheres at 340 GHz. The width of the distribution is relatively less important than the mean size in determining the scattering properties. The widest distribution generally has the highest extinction due to its greater number of larger particles. There is a similar behavior in other scattering properties (not shown), so that the wider distribution behaves as if it had a slightly larger mean particle size. Because the effect of the distribution width is small, and to simplify the plots, only the $\alpha = 1$ distributions are shown from now on.

Figure 3.6 shows the extinction for size distributions of all five shapes at 220 GHz. Even though the all the distributions have the same IWC there is a range up to a factor of three in the extinction between the various shapes. Rosettes generally have the smallest extinction and, for the larger size distributions, solid columns have the largest extinction. The extinction for distributions of solid columns at all four frequencies is shown in Fig. 3.7. The extinction increases dramatically with frequency. In addition, how the extinction increases with the distribution $D_m$ varies with frequency. Figure 3.8 illustrates how the extinction is different at the two observation angles considered here (0° and 49°). In general, the nadir angle has higher extinction because this angle presents the greatest area to the oncoming microwave radiation. This effect is especially large for the plates, which are very thin.

The next series of plots shows the ratio of extinction for vertical polarization to that for horizontal polarization at 49°. This is one way to characterize how much the ice particles

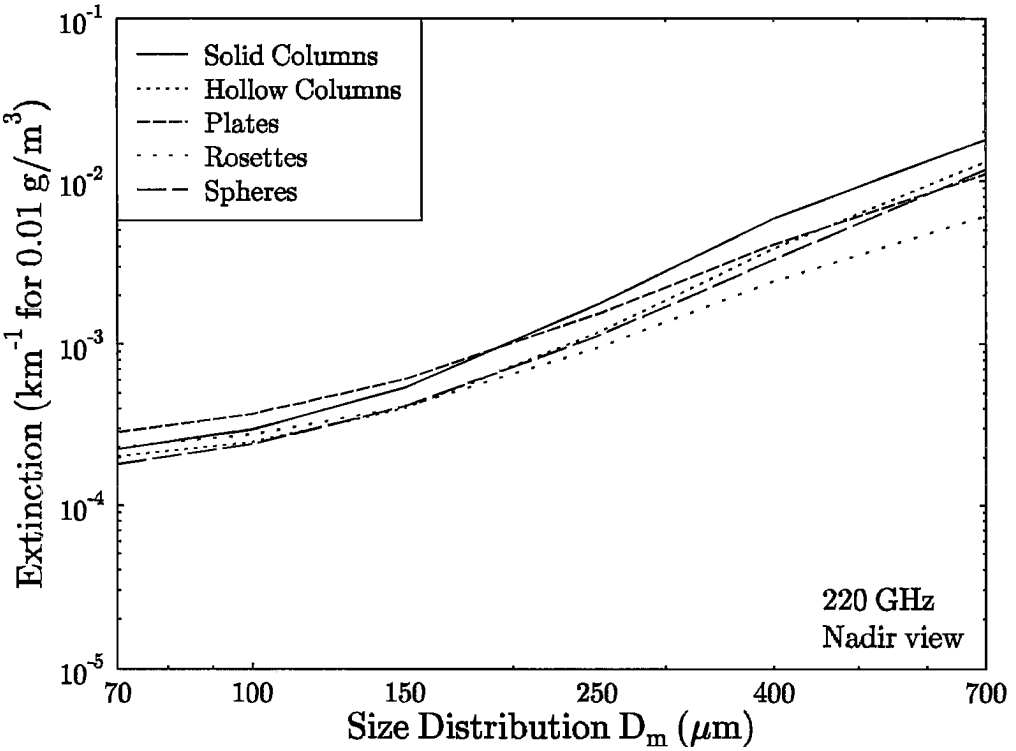


Figure 3.6: Extinction vs. size distribution for five shapes at 220 GHz.

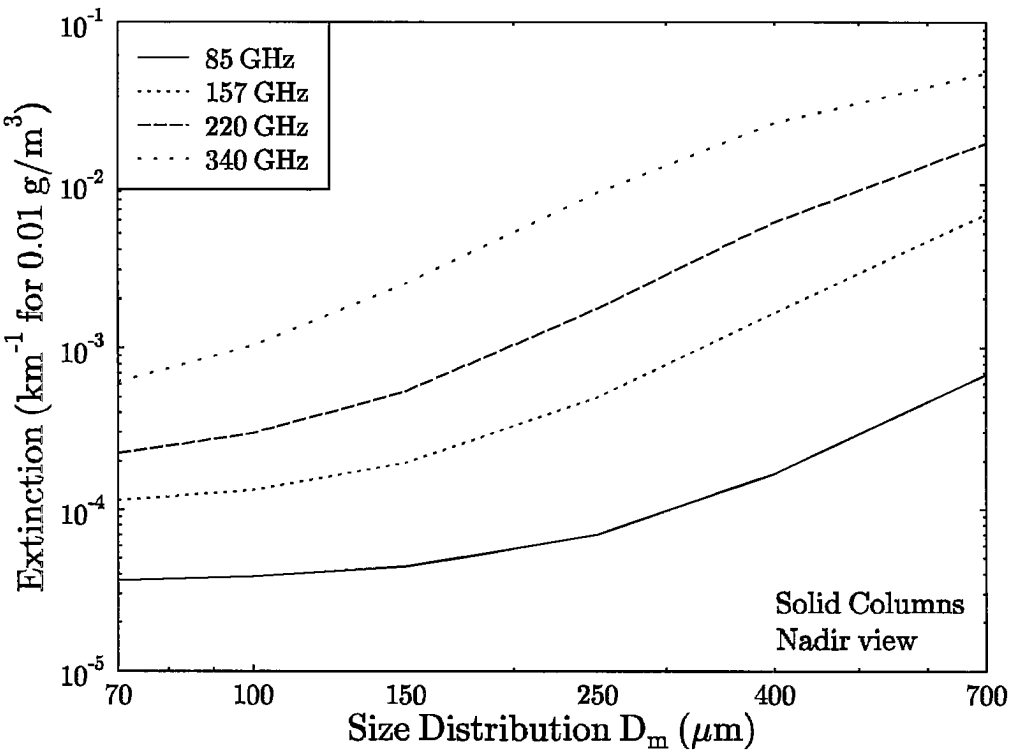


Figure 3.7: Extinction vs. size distribution for solid columns at four frequencies.

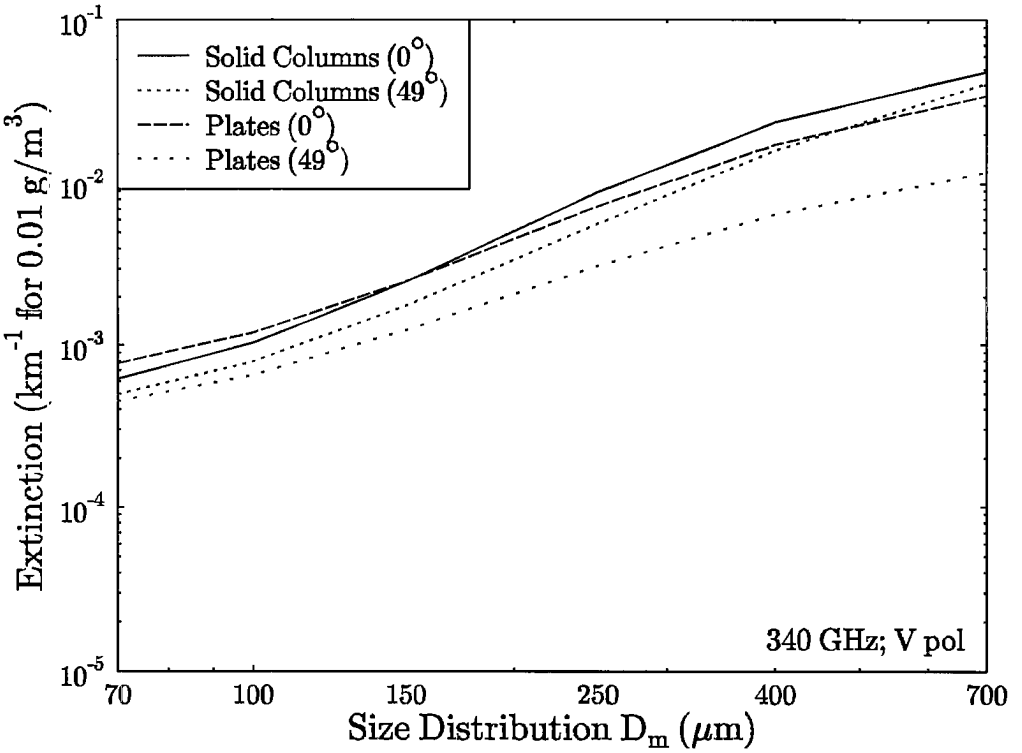


Figure 3.8: Extinction vs. size distribution for columns and plates at 0° and 49°.

will polarize microwave radiation upwelling through cirrus clouds. Since the horizontal polarization extinction is larger than the vertical polarization extinction for horizontally oriented particles, the polarization ratio is less than one. Spheres are not shown because their polarization ratio is always one. Figures 3.9 and 3.10 plot the extinction polarization of four shapes as a function of particle size for 85 and 340 GHz, respectively. Plates are the most polarizing, having a ratio of around 0.5 owing to their thinness, followed by rosettes and then columns. Solid columns are slightly more polarizing than hollow columns. There is a tendency for the polarization ratio to decrease with particle size as the aspect ratio decreases (see 85 GHz plot). At 340 GHz there are large oscillations in the polarization ratio with particle size. This is a manifestation of the non-Rayleigh scattering regime, for which the polarization ratio seems especially sensitive. This non-Rayleigh behavior starts at particle sizes of 300 to 500$\mu$m at 340 GHz, and is apparent at 1000$\mu$m at 157 GHz. One way of explaining the oscillations in the polarization ratio is that the two polarizations see different effective particle sizes due to the nonsphericity of the particles. This means that where the extinction size dependence begins to oscillate, beyond the Rayleigh regime, the two polarizations will be out of phase, so the polarization ratio will oscillate. Figure 3.11 shows that averaging over a size distribution reduces, but does not eliminate, the oscillations in the polarization ratio. Thus, the polarization ratio depends on both the particle shape, and to a lesser extent, the size distribution.

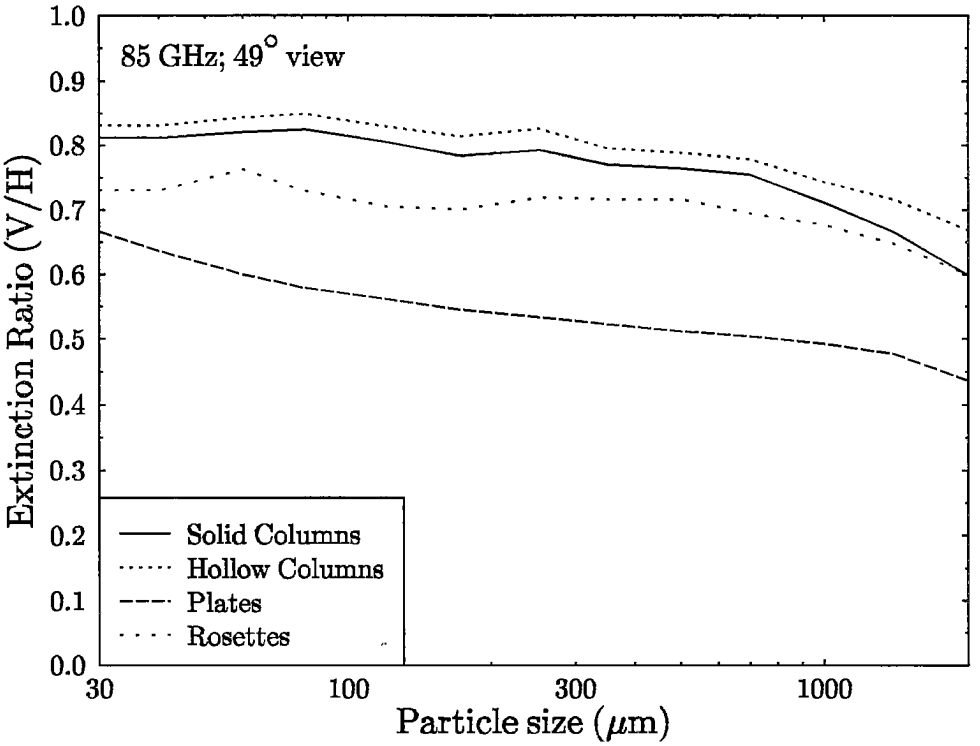


Figure 3.9: Extinction polarization ratio vs. particle size for four shapes at 85 GHz.

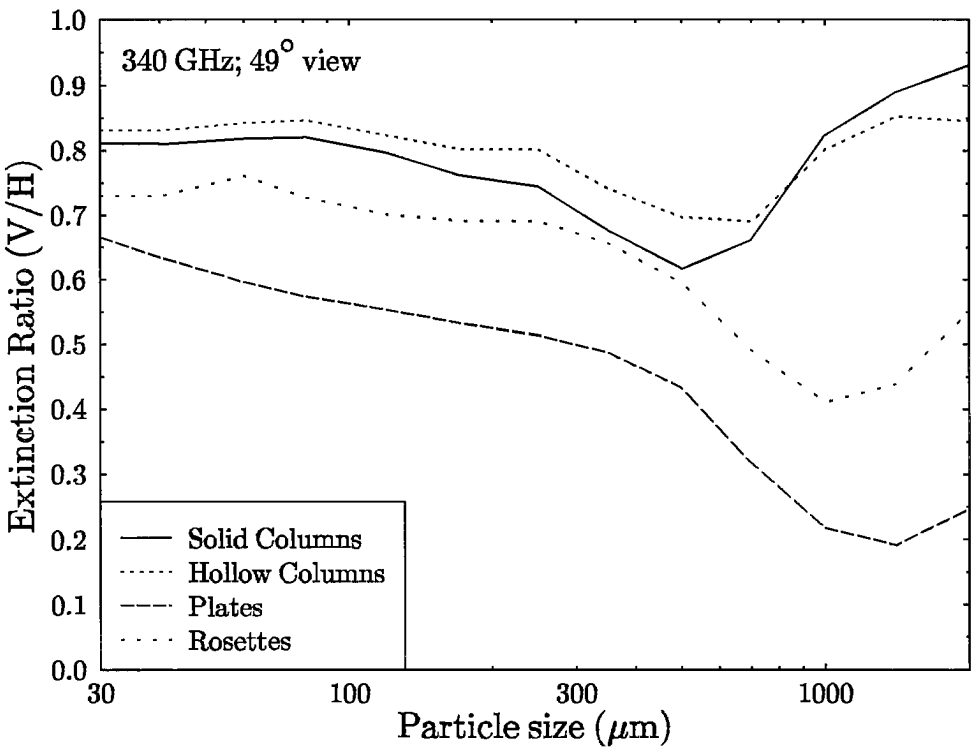


Figure 3.10: Extinction polarization ratio vs. particle size for four shapes at 340 GHz.

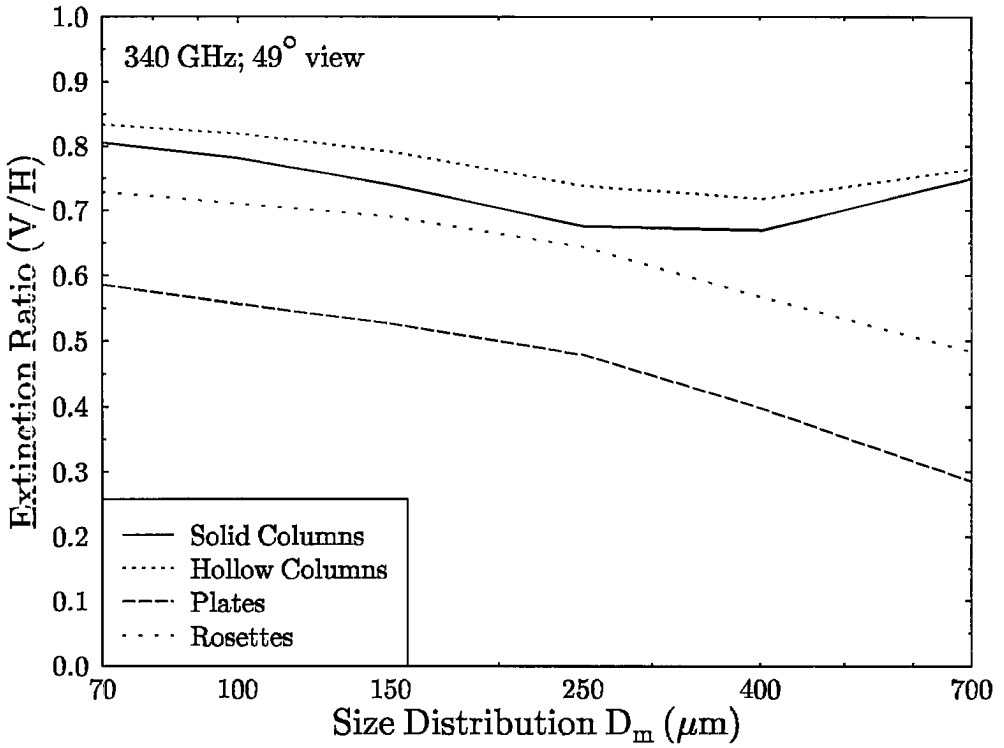


Figure 3.11: Extinction polarization ratio vs. size distribution for four shapes at 340 GHz.

The single scattering albedo is crucial for understanding the radiative transfer process of microwave radiation in cirrus. Low albedo means that radiation interacts with the cirrus particles by absorption and emission, whereas high albedo means that radiation interacts primarily through scattering. The single scattering albedo as a function of particle size is shown in fig. 3.12 for solid columns at the four frequencies. For all frequencies the smallest particles (30$\mu$m) have an albedo near zero, while the largest particles ($> 1000\mu$m) have an albedo near one. The transition from absorbing to scattering behavior varies considerably with frequency: an albedo of 0.5 occurs at 330$\mu$m at 85 GHz but down to 110$\mu$m at 340 GHz. A similar type of transition occurs with the size parameter $D_m$ for distributions (Fig.3.13). At 85 GHz only the two largest size distributions (with $D_m \geq 400$) have a single scattering albedo above 0.75, while for 340 GHz four size distributions (with $D_m \geq 150$) have albedos above 0.75. Figure 3.14 shows the single scattering albedo for size distributions for the five particle shapes at 220 GHz. While the variation in albedo with particle shape is not as large as with frequency, there is significant variation, with larger volume shapes (columns) scattering more than smaller volume shapes (rosettes). There is very little change in albedo with polarization or angle.

The last single scattering quantity to look at is a measure of the degree of forward scattering. This is important for radiative transfer because more forward scattering to the radiometer will decrease the brightness temperature depression. The usual measure of the

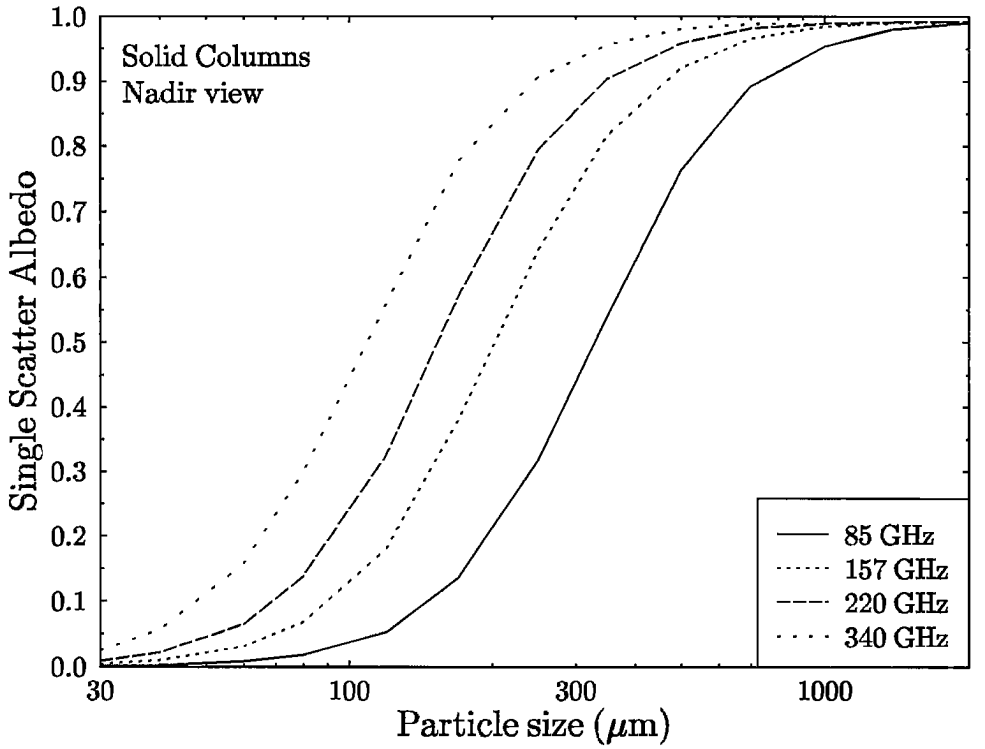


Figure 3.12: Single scattering albedo vs. particle size for solid columns at four frequencies.

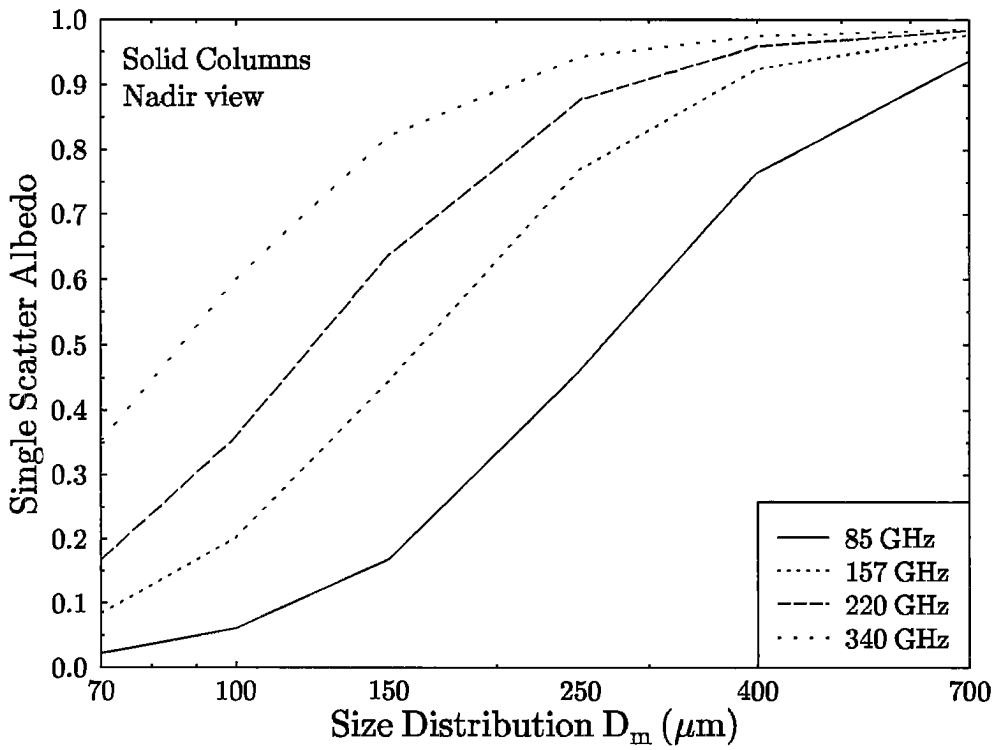


Figure 3.13: Single scattering albedo vs. size distribution for columns at four frequencies.

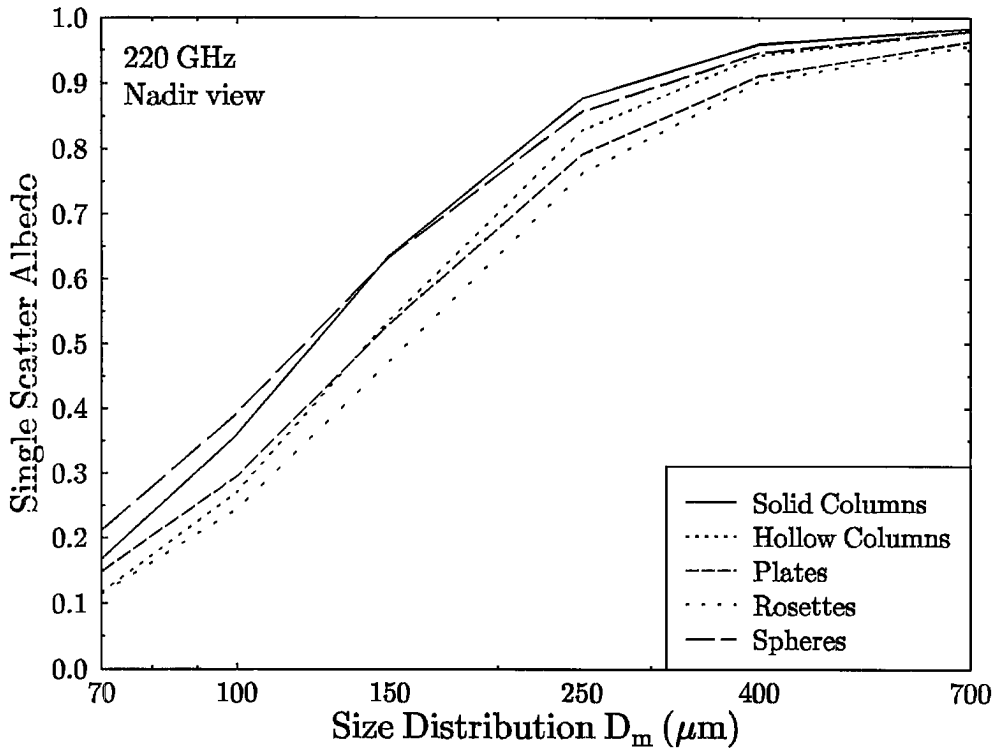


Figure 3.14: Single scattering albedo vs. size distribution for five shapes at 220 GHz.

amount of forward scattering is the asymmetry parameter, which is the cosine weighted average of the phase function. That cannot be computed from the azimuthally averaged scattering matrix calculated here, except for nadir incidence. Instead we use a scattering ratio, defined for each upwelling outgoing angle as the ratio of integral of the scattering matrix over upwelling incident angles divided by the total scattering (incident over all incident angles). It is the fraction of scattered radiation that would come from upwelling incident angles if the sample was isotropically illuminated by unpolarized radiation. Figure 3.15 shows the scattering ratio as a function of particle size for the five shapes at 340 GHz. Small particles are in the Rayleigh regime, scattering forward as much as back, so the scattering ratio is 0.5. For spheres and columns the largest particle sizes have some 80% of the radiation scattered into the zenith coming from the upwelling incident angles. The thinner shapes have lower scattering ratios at all sizes. For nadir view the scattering ratio for plates stays at 0.5, because they are modeled as one dipole thick. A similar behavior is seen in the scattering ratio for distributions (Fig. 3.16), with the ratio increasing with distribution $D_m$ for the thicker particle shapes. Figure 3.17 shows the scattering ratio as a function of size distribution for hollow columns at the four frequencies. The scattering ratio is significantly larger than 0.5 only for the higher frequencies and for distributions with larger particles. The scattering ratio is lower for off-nadir angles (not shown). It is also larger for vertical than horizontal polarization for off nadir angles, even for plates.

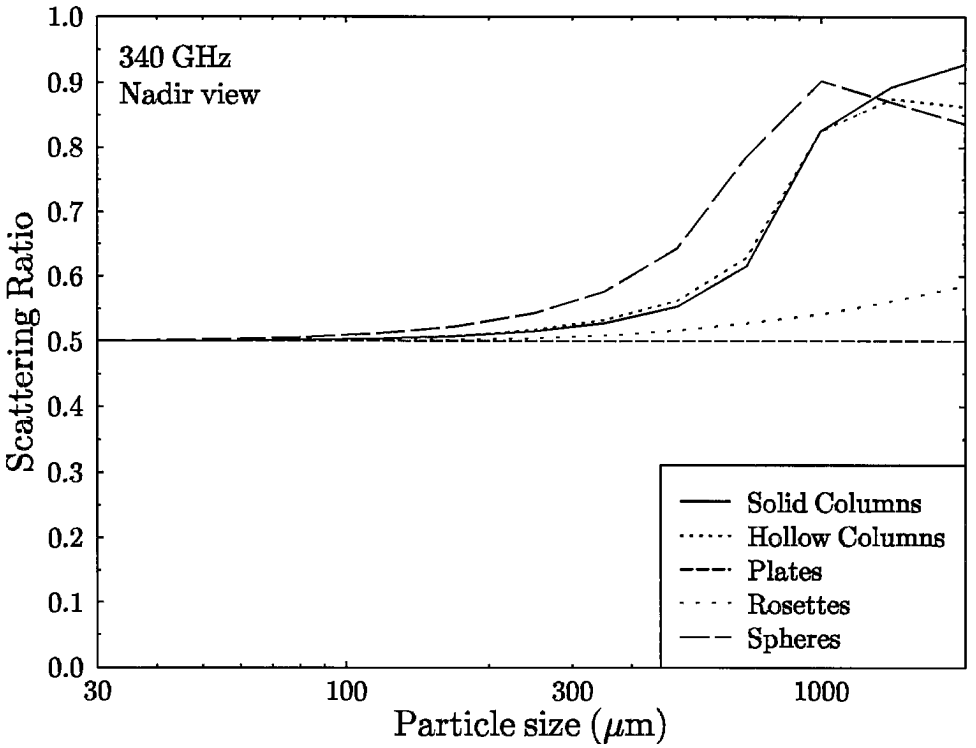


Figure 3.15: Scattering ratio vs. particle size for five shapes at 340 GHz.

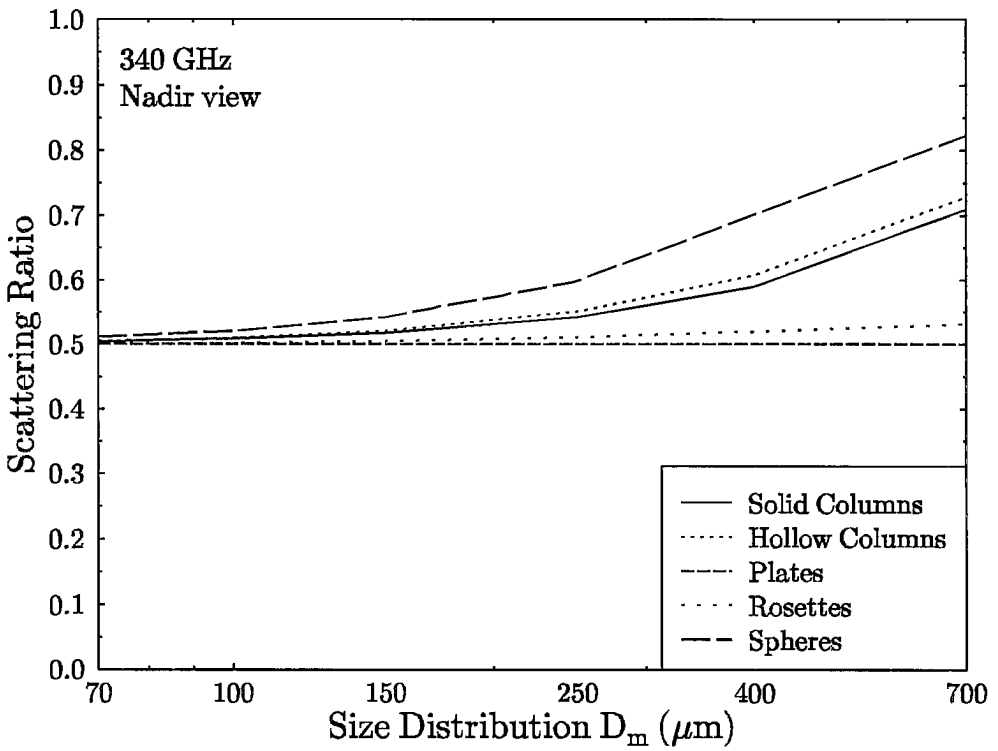


Figure 3.16: Scattering ratio vs. size distribution for five shapes at 340 GHz.

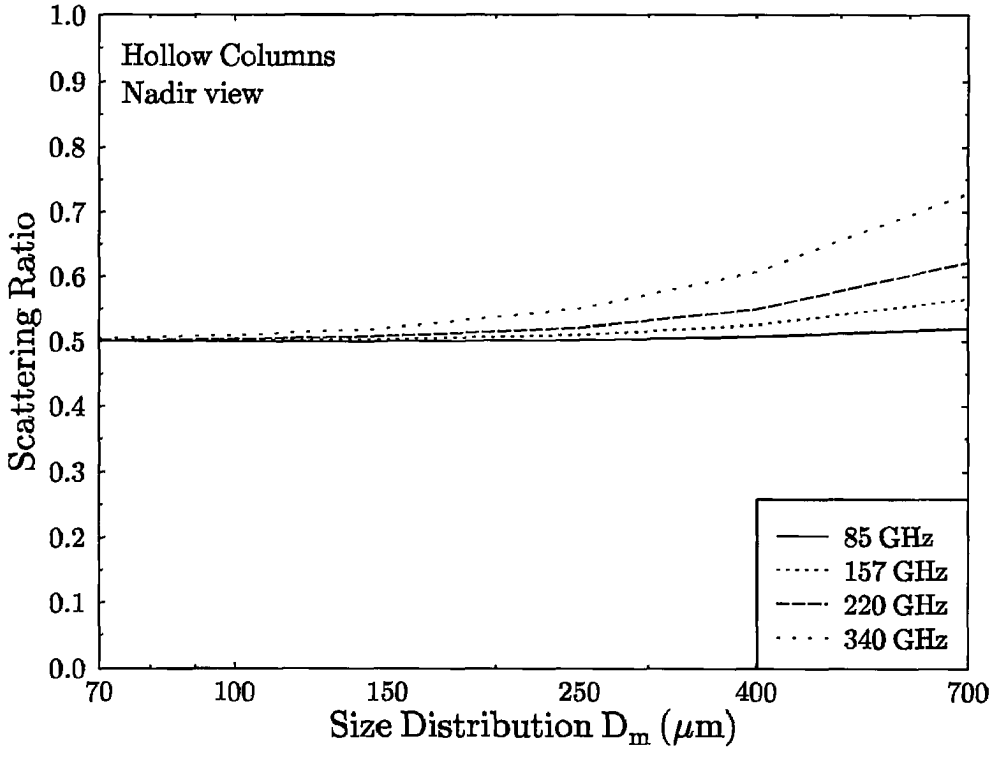


Figure 3.17: Scattering ratio vs. size distribution hollow columns at four frequencies.

### 3.3.2 Fits of scattering results

The scattering results are also presented by tabulating coefficients of fits as a function of particle size. This provides a way for others to use the DDA results for research in microwave remote sensing algorithms without having to go to the complication and expense of generating them. Because the single scattering properties are fit to functions of size from 30$\mu$m to 2000$\mu$m, great flexibility will be allowed in the future choice of size distributions. The fits of scattering properties are presented for the four non-spherical particle shapes at 85.5, 157, 220, and 340 GHz for upwelling angles of 0° and 49°. While it is somewhat restrictive to fit the results only for these two angles, it is considerably more accurate to tabulate for particular angles then to also fit to functions of zenith angle. The form of the scattering properties presented here is specifically for the use in a simple first order radiative transfer model.

The scattering properties that are needed for remote sensing at a particular observation angle $\mu$ are the polarized extinction $K_p(\mu)$, emission $\sigma_p(\mu)$, and scattering $M_{pp'}(\mu,\mu')$ where $p$ and $p'$ refer to polarization (V or H), and $\mu'$ is an incident direction (in this notation these quantities have units of inverse distance). It is assumed that the upwelling radiation incident on a cirrus layer is unpolarized. This is partly done to reduce the number of scattering function quantities tabulated, but is also justified in terms of actual atmospheres. Land surfaces are expected to be virtually unpolarized, and a moist atmosphere is optically thick enough at the higher frequencies to totally depolarize the upwelling microwave radiation. Since the upwelling radiation from a clear sky incident on a cirrus layer is usually a smooth function of zenith angle, its angular structure is approximated by a quadratic, hence

$$I(\mu) = I_0 + I_1\mu + I_2\mu^2 \ . \tag{3.5}$$

Then we only need to consider the first three moments of the scattering function over the upward incident angles:

$$M_p^{(\ell)} = \int_0^1 \left(M_{pV}(\mu,\mu') + M_{pH}(\mu,\mu')\right) \mu'^{\ell} d\mu' \tag{3.6}$$

This reduces the problem to fitting five quantities over particle size $(K, \sigma, M^{(0)}, M^{(1)}, M^{(2)})$ for each observation angle/polarization and particle shape.

The optically thin nature of cirrus clouds at microwave frequencies allows the use of a particularly simple formula for the solution to the radiative transfer problem. If the order of scattering solution to the polarized radiative transfer equation is expanded to first order in the layer thickness the change in upwelling unpolarized radiance as it interacts with the cirrus layer is

$$\Delta I_p(\mu) = \left[-K_p(\mu)I(\mu) + \sigma_p(\mu)B(T) + M_p^{(0)}(\mu)I_0 + M_p^{(1)}(\mu)I_1 + M_p^{(2)}(\mu)I_2\right] \frac{\Delta z}{\mu} \ , \tag{3.7}$$

where $p$ is the polarization (V or H), and $B(T)$ is the Planck function at the average cloud temperature $T$.

The assumptions of this first order radiative transfer model are

1. The cloud is optically thin enough that the order of scattering solution may be expanded to first order in optical depth.

2. The incident upwelling radiation can be approximated by a quadratic function.

3. The cloud is above significant gaseous absorption, so that the incident radiation is the same as the clear sky top of the atmosphere radiance, there is no incident radiation from above the cloud, and extinction and emission properties are due entirely to the cirrus particles.

4. There is no reflection from the surface or scattering outside the cloud so the incident radiation is independent of the cloud.

The least squares fits of the scattering properties as functions of particle size are made to the quantities plotted in the previous section: log of extinction, single scattering albedo, and three scattering ratios. This was found to be more accurate than fitting directly to the scattering quantities used in eq. (3.7). The resulting formulae for the fits as function of maximum particle size $D$ are

$$\ln(K) = \sum_{i=0}^{5} K_i (\ln D)^i \tag{3.8}$$

$$\omega = 1 - \frac{\sigma}{K} = \frac{1}{1 + (D/\omega_0)^{-\omega_1}} - \omega_2 \tag{3.9}$$

$$\frac{M^{(0)}}{K - \sigma} = 0.5 + \exp\left[M_0^{(0)} + M_1^{(0)} \ln D + M_2^{(0)} (\ln D)^2\right] \tag{3.10}$$

$$\frac{M^{(1)}}{M^{(0)}} = M_0^{(1)} + M_1^{(1)} D \tag{3.11}$$

$$\frac{M^{(2)}}{M^{(0)}} = M_0^{(2)} + M_1^{(2)} D \quad . \tag{3.12}$$

The constant coefficients in the first and second moment scattering ratios ($M_0^{(1)}$ and $M_0^{(2)}$) are not fit, because the small size limit can be used. For nadir angle and horizontal polarization at any angle the $M^{(1)}/M^{(0)}$ ratio is 0.563, while $M^{(2)}/M^{(0)}$ ratio is 0.400. These ratios (9/16 and 2/5) can be computed theoretically from the Rayleigh phase function, $M(\mu') \propto 1 + \mu'^2$. The two scattering ratios for vertical polarization depend on angle and the Rayleigh limit shape, and so are listed in Table 3.4.

The fit coefficients are tabulated for nadir (no polarization) and for $\mu = 0.65239$ (49° V and H polarizations) for the four shapes and four frequencies. The coefficients are for extinction $K$ in $\mathrm{km}^{-1}$ for 10 particles per $\mathrm{m}^3$ (same as plots in section 3.3.1) and for

Table 3.4: Small size limit of scattering ratios

| Angle /Pol | Shape | $M_0^{(1)}$ | $M_0^{(2)}$ |
|---|---|---|---|
| 0 | All | .563 | .400 |
| H | All | .563 | .400 |
| 49V | Column | .475 | .305 |
| 49V | Hollow | .473 | .302 |
| 49V | Plate | .496 | .328 |
| 49V | Rosette | .485 | .316 |

the particle size $D$ in mm. The coefficients for extinction and the resulting rms error in the logarithm over the 13 particles sizes are listed in Table 3.5. The fit to extinction is, of course, smoother than that computed by DDA, but given the error in the individual DDA calculations, may be of equivalent or better accuracy. Table 3.6 contains the fit coefficients for the single scattering albedo and the three scattering ratios. By using the coefficients in these two tables with the formulae in eqs. 3.8-3.12 the scattering properties at the available angles for any particle size may be calculated. The scattering quantities, after integration over appropriate size distributions, may be used in eq. 3.7 to compute easily the brightness temperature depression from various cirrus crystals at the tabulated microwave frequencies. The accuracy of the scattering fits and the first order radiative transfer model are tested in section 3.4.2.

Table 3.5: Fit coefficients for extinction

| Freq. (GHz) | Angle /Pol | Shape | Extinction Coefficients | | | | | | |
|---|---|---|---|---|---|---|---|---|---|
| | | | Error | $K_0$ | $K_1$ | $K_2$ | $K_3$ | $K_4$ | $K_5$ |
| 85 | 0 | Column | 0.029 | -9.5846 | 5.8211 | 0.2752 | -0.4562 | -0.1586 | -0.0151 |
| 85 | 0 | Hollow | 0.026 | -10.4004 | 5.7334 | 0.3732 | -0.4478 | -0.1758 | -0.0186 |
| 85 | 0 | Plate | 0.008 | -10.7182 | 4.7919 | 0.1523 | -0.4418 | -0.1700 | -0.0187 |
| 85 | 0 | Rosette | 0.072 | -11.6516 | 3.9966 | -0.1152 | -0.2157 | -0.0212 | 0.0035 |
| 85 | 49H | Column | 0.029 | -9.6280 | 5.7582 | 0.2596 | -0.4426 | -0.1511 | -0.0141 |
| 85 | 49H | Hollow | 0.026 | -10.4254 | 5.6903 | 0.3503 | -0.4500 | -0.1745 | -0.0184 |
| 85 | 49H | Plate | 0.009 | -10.7955 | 4.6520 | 0.0751 | -0.4496 | -0.1655 | -0.0178 |
| 85 | 49H | Rosette | 0.072 | -11.7066 | 3.8930 | -0.1837 | -0.2336 | -0.0223 | 0.0036 |
| 85 | 49V | Column | 0.030 | -9.9649 | 5.6017 | 0.1463 | -0.4872 | -0.1575 | -0.0142 |
| 85 | 49V | Hollow | 0.024 | -10.7165 | 5.5820 | 0.2905 | -0.4740 | -0.1790 | -0.0185 |
| 85 | 49V | Plate | 0.007 | -11.5026 | 4.5670 | -0.0017 | -0.5118 | -0.1854 | -0.0202 |
| 85 | 49V | Rosette | 0.064 | -12.0966 | 3.7607 | -0.2670 | -0.2177 | 0.0017 | 0.0080 |
| 157 | 0 | Column | 0.025 | -7.1243 | 5.3688 | -1.1105 | -1.0723 | -0.2594 | -0.0203 |
| 157 | 0 | Hollow | 0.028 | -7.9582 | 5.5609 | -0.7301 | -0.9240 | -0.2362 | -0.0190 |
| 157 | 0 | Plate | 0.017 | -8.4649 | 4.4849 | -0.7229 | -0.6683 | -0.1473 | -0.0098 |
| 157 | 0 | Rosette | 0.077 | -9.3733 | 3.8942 | -0.7408 | -0.2790 | 0.0546 | 0.0187 |
| 157 | 49H | Column | 0.020 | -7.2179 | 5.4420 | -0.6889 | -0.6993 | -0.1357 | -0.0062 |
| 157 | 49H | Hollow | 0.025 | -8.0258 | 5.5532 | -0.5458 | -0.7396 | -0.1722 | -0.0115 |
| 157 | 49H | Plate | 0.029 | -8.6615 | 4.4567 | -0.2408 | -0.1943 | 0.0147 | 0.0088 |
| 157 | 49H | Rosette | 0.085 | -9.5277 | 3.7842 | -0.5606 | -0.0582 | 0.1344 | 0.0281 |
| 157 | 49V | Column | 0.028 | -7.6967 | 5.2974 | -0.3756 | -0.3378 | -0.0042 | 0.0096 |
| 157 | 49V | Hollow | 0.025 | -8.4085 | 5.4180 | -0.3800 | -0.5262 | -0.0926 | -0.0018 |
| 157 | 49V | Plate | 0.026 | -9.4727 | 4.0665 | -0.6838 | -0.4612 | -0.0581 | 0.0013 |
| 157 | 49V | Rosette | 0.080 | -10.0323 | 3.4588 | -0.7520 | -0.0608 | 0.1603 | 0.0331 |
| 220 | 0 | Column | 0.083 | -6.2016 | 4.4136 | -1.0397 | -0.1403 | 0.1749 | 0.0364 |
| 220 | 0 | Hollow | 0.046 | -6.8759 | 4.8350 | -1.0165 | -0.4820 | 0.0144 | 0.0157 |
| 220 | 0 | Plate | 0.034 | -7.4351 | 3.8101 | -1.0122 | -0.3548 | 0.0322 | 0.0145 |
| 220 | 0 | Rosette | 0.078 | -8.1965 | 3.4764 | -1.0841 | -0.1499 | 0.1575 | 0.0335 |
| 220 | 49H | Column | 0.027 | -6.1145 | 4.7184 | -1.1170 | -0.4864 | 0.0113 | 0.0142 |
| 220 | 49H | Hollow | 0.031 | -6.8929 | 4.9730 | -0.8374 | -0.4184 | 0.0187 | 0.0150 |
| 220 | 49H | Plate | 0.028 | -7.5005 | 4.2293 | -0.3876 | -0.0708 | 0.0795 | 0.0165 |
| 220 | 49H | Rosette | 0.076 | -8.3447 | 3.5913 | -0.6193 | 0.1943 | 0.2575 | 0.0438 |
| 220 | 49V | Column | 0.033 | -6.5432 | 4.8466 | -0.7449 | -0.2974 | 0.0465 | 0.0162 |
| 220 | 49V | Hollow | 0.026 | -7.2658 | 4.9917 | -0.5624 | -0.2243 | 0.0715 | 0.0201 |
| 220 | 49V | Plate | 0.036 | -8.5668 | 3.4933 | -0.6732 | 0.0288 | 0.1614 | 0.0288 |
| 220 | 49V | Rosette | 0.081 | -9.0070 | 3.1330 | -0.6530 | 0.4069 | 0.3638 | 0.0584 |
| 340 | 0 | Column | 0.090 | -5.3261 | 3.3519 | -0.7091 | 0.7085 | 0.4753 | 0.0679 |
| 340 | 0 | Hollow | 0.071 | -5.8476 | 3.7585 | -0.9631 | 0.2599 | 0.3201 | 0.0514 |
| 340 | 0 | Plate | 0.053 | -6.4898 | 2.8519 | -0.7235 | 0.4645 | 0.3391 | 0.0487 |
| 340 | 0 | Rosette | 0.094 | -7.0441 | 2.6804 | -0.8509 | 0.6552 | 0.4812 | 0.0717 |
| 340 | 49H | Column | 0.031 | -5.1398 | 3.5197 | -1.1359 | 0.1975 | 0.2924 | 0.0466 |
| 340 | 49H | Hollow | 0.043 | -5.7338 | 3.9660 | -1.1468 | -0.0759 | 0.1828 | 0.0341 |
| 340 | 49H | Plate | 0.032 | -6.1160 | 3.6841 | -0.9238 | -0.3070 | -0.0041 | 0.0041 |
| 340 | 49H | Rosette | 0.050 | -6.8820 | 3.2137 | -0.9528 | 0.1306 | 0.2373 | 0.0392 |
| 340 | 49V | Column | 0.018 | -5.3859 | 3.9246 | -1.0654 | -0.0894 | 0.1427 | 0.0261 |
| 340 | 49V | Hollow | 0.038 | -5.9848 | 4.1881 | -1.0964 | -0.2565 | 0.0849 | 0.0204 |
| 340 | 49V | Plate | 0.032 | -7.6040 | 2.8999 | -0.3737 | 0.5438 | 0.3165 | 0.0423 |
| 340 | 49V | Rosette | 0.038 | -7.7266 | 2.9199 | -0.4675 | 0.6787 | 0.4291 | 0.0616 |

Table 3.6: Fit coefficients for single scattering albedo and scattering ratios

| Freq. (GHz) | Angle /Pol | Shape | Coefficients | | | | | | | |
|---|---|---|---|---|---|---|---|---|---|---|
| | | | $\omega_0$ | $\omega_1$ | $\omega_2$ | $M_0^{(0)}$ | $M_1^{(0)}$ | $M_2^{(0)}$ | $M_1^{(1)}$ | $M_1^{(2)}$ |
| 85 | 0 | Column | 0.3290 | 3.1206 | 0.0010 | -4.3375 | 1.8093 | -0.0730 | 0.0154 | 0.0166 |
| 85 | 0 | Hollow | 0.3797 | 3.1777 | 0.0010 | -4.2077 | 1.8359 | -0.0602 | 0.0121 | 0.0127 |
| 85 | 0 | Plate | 0.3923 | 2.8139 | 0.0029 | -100 | 0.0000 | 0.0000 | 0.0234 | 0.0257 |
| 85 | 0 | Rosette | 0.4116 | 2.8489 | 0.0093 | -6.0093 | 1.2076 | -0.2182 | 0.0167 | 0.0183 |
| 85 | 49H | Column | 0.3296 | 3.1056 | 0.0015 | -4.7667 | 1.7842 | -0.1084 | 0.0090 | 0.0095 |
| 85 | 49H | Hollow | 0.3803 | 3.1665 | 0.0013 | -4.6385 | 1.8290 | -0.0926 | 0.0081 | 0.0083 |
| 85 | 49H | Plate | 0.3939 | 2.7667 | 0.0052 | -100 | 0.0000 | 0.0000 | 0.0140 | 0.0152 |
| 85 | 49H | Rosette | 0.4127 | 2.8057 | 0.0114 | -33.268 | 31.890 | 11.366 | 0.0115 | 0.0124 |
| 85 | 49V | Column | 0.3297 | 3.0921 | 0.0021 | -3.4951 | 1.8776 | -0.1043 | 0.0232 | 0.0227 |
| 85 | 49V | Hollow | 0.3807 | 3.1549 | 0.0017 | -3.7947 | 1.8987 | -0.0835 | 0.0185 | 0.0188 |
| 85 | 49V | Plate | 0.3935 | 2.7693 | 0.0053 | -4.1973 | 1.7878 | 0.3905 | 0.0525 | 0.0549 |
| 85 | 49V | Rosette | 0.4097 | 2.7876 | 0.0126 | -3.7783 | 1.8853 | 0.0147 | 0.0209 | 0.0200 |
| 157 | 0 | Column | 0.2023 | 2.9868 | 0.0027 | -3.2535 | 2.2748 | 0.3749 | 0.0484 | 0.0552 |
| 157 | 0 | Hollow | 0.2339 | 3.0142 | 0.0025 | -3.0738 | 2.1102 | 0.2857 | 0.0376 | 0.0415 |
| 157 | 0 | Plate | 0.2250 | 2.6560 | 0.0054 | -100 | 0.0000 | 0.0000 | 0.0824 | 0.0954 |
| 157 | 0 | Rosette | 0.2428 | 2.7585 | 0.0073 | -4.8255 | 1.2362 | -0.0186 | 0.0505 | 0.0581 |
| 157 | 49H | Column | 0.2028 | 2.9678 | 0.0033 | -3.6658 | 1.9196 | 0.2184 | 0.0029 | 0.0019 |
| 157 | 49H | Hollow | 0.2343 | 2.9999 | 0.0029 | -3.5028 | 1.9740 | 0.1917 | 0.0105 | 0.0106 |
| 157 | 49H | Plate | 0.2258 | 2.6021 | 0.0083 | -100 | 0.0000 | 0.0000 | -0.0002 | -0.0010 |
| 157 | 49H | Rosette | 0.2433 | 2.7140 | 0.0098 | -5.2800 | 1.0247 | -0.1497 | 0.0093 | 0.0104 |
| 157 | 49V | Column | 0.2027 | 2.9494 | 0.0043 | -2.3426 | 1.6206 | -0.3916 | 0.0290 | 0.0262 |
| 157 | 49V | Hollow | 0.2344 | 2.9852 | 0.0036 | -2.6243 | 1.8034 | -0.1367 | 0.0299 | 0.0288 |
| 157 | 49V | Plate | 0.2246 | 2.6020 | 0.0100 | -2.8977 | 1.7969 | -0.3306 | 0.0725 | 0.0742 |
| 157 | 49V | Rosette | 0.2407 | 2.6887 | 0.0129 | -2.5532 | 1.6654 | -0.4291 | 0.0362 | 0.0340 |
| 220 | 0 | Column | 0.1531 | 2.9416 | 0.0038 | -2.2802 | 2.6703 | -0.8889 | 0.0829 | 0.0970 |
| 220 | 0 | Hollow | 0.1769 | 2.9569 | 0.0037 | -2.1774 | 2.2600 | -0.5102 | 0.0730 | 0.0832 |
| 220 | 0 | Plate | 0.1635 | 2.5939 | 0.0069 | -100 | 0.0000 | 0.0000 | 0.1388 | 0.1699 |
| 220 | 0 | Rosette | 0.1794 | 2.7000 | 0.0073 | -4.1269 | 1.2862 | 0.0066 | 0.0812 | 0.0975 |
| 220 | 49H | Column | 0.1535 | 2.9199 | 0.0044 | -2.9142 | 2.0554 | 0.1267 | 0.0031 | 0.0015 |
| 220 | 49H | Hollow | 0.1773 | 2.9409 | 0.0041 | -2.7082 | 2.0354 | -0.0860 | 0.0072 | 0.0059 |
| 220 | 49H | Plate | 0.1645 | 2.5393 | 0.0092 | -100 | 0.0000 | 0.0000 | -0.0213 | -0.0264 |
| 220 | 49H | Rosette | 0.1802 | 2.6557 | 0.0091 | -4.6635 | 0.9596 | -0.1577 | -0.0008 | -0.0020 |
| 220 | 49V | Column | 0.1535 | 2.8991 | 0.0055 | -1.7852 | 1.2741 | -0.6830 | 0.0376 | 0.0342 |
| 220 | 49V | Hollow | 0.1774 | 2.9262 | 0.0049 | -1.9326 | 1.6027 | -0.7670 | 0.0369 | 0.0346 |
| 220 | 49V | Plate | 0.1630 | 2.5395 | 0.0123 | -2.2822 | 1.5045 | -0.6042 | 0.0760 | 0.0744 |
| 220 | 49V | Rosette | 0.1780 | 2.6321 | 0.0130 | -1.9668 | 1.2509 | -0.8404 | 0.0366 | 0.0320 |
| 340 | 0 | Column | 0.1078 | 2.8760 | 0.0058 | -1.2290 | 1.4847 | -1.3773 | 0.1406 | 0.1707 |
| 340 | 0 | Hollow | 0.1247 | 2.8819 | 0.0055 | -1.2102 | 1.2847 | -1.4779 | 0.1342 | 0.1615 |
| 340 | 0 | Plate | 0.1094 | 2.5369 | 0.0093 | -100 | 0.0000 | 0.0000 | 0.1948 | 0.2492 |
| 340 | 0 | Rosette | 0.1226 | 2.6283 | 0.0075 | -3.1509 | 1.1632 | -0.2190 | 0.0895 | 0.1148 |
| 340 | 49H | Column | 0.1081 | 2.8524 | 0.0069 | -1.8631 | 1.9070 | -1.0067 | 0.0067 | 0.0000 |
| 340 | 49H | Hollow | 0.1249 | 2.8641 | 0.0063 | -1.6979 | 1.5986 | -1.4333 | 0.0041 | -0.0022 |
| 340 | 49H | Plate | 0.1104 | 2.4788 | 0.0107 | -100 | 0.0000 | 0.0000 | -0.0519 | -0.0620 |
| 340 | 49H | Rosette | 0.1234 | 2.5819 | 0.0090 | -3.9251 | 1.0819 | -0.0267 | -0.0142 | -0.0189 |
| 340 | 49V | Column | 0.1081 | 2.8293 | 0.0081 | -1.3835 | 0.8047 | -0.4362 | 0.0562 | 0.0494 |
| 340 | 49V | Hollow | 0.1250 | 2.8488 | 0.0070 | -1.3908 | 0.8007 | -0.8232 | 0.0577 | 0.0525 |
| 340 | 49V | Plate | 0.1090 | 2.4830 | 0.0154 | -1.7342 | 1.0314 | -0.5159 | 0.0739 | 0.0655 |
| 340 | 49V | Rosette | 0.1218 | 2.5613 | 0.0136 | -1.5634 | 0.6545 | -0.6238 | 0.0310 | 0.0219 |

Table 3.7: Water surface index of refraction and emissivity.

| | $T_{sfc} = 272°K$ | | | | $T_{sfc} = 300°K$ | | | |
|---|---|---|---|---|---|---|---|---|
| Freq. (GHz) | Index | Emissivity 0° | 49°V | 49°H | Index | Emissivity 0° | 49°V | 49°H |
| 85.5 | $2.85 - 1.44i$ | 0.675 | 0.822 | 0.520 | $3.72 - 2.21i$ | 0.548 | 0.703 | 0.404 |
| 157 | $2.51 - 0.90i$ | 0.765 | 0.894 | 0.613 | $2.95 - 1.58i$ | 0.652 | 0.802 | 0.498 |
| 220 | $2.41 - 0.68i$ | 0.797 | 0.917 | 0.651 | $2.68 - 1.27i$ | 0.707 | 0.849 | 0.552 |
| 340 | $2.42 - 0.82i$ | 0.783 | 0.907 | 0.633 | $2.42 - 0.82i$ | 0.783 | 0.907 | 0.633 |

## 3.4 Radiative Transfer Modeling

### 3.4.1 Modeling setup

Upwelling polarized microwave radiation is computed for cirrus clouds containing various particle shapes and size distributions. To simulate a range of conditions the cirrus clouds are placed in tropical and midlatitude winter standard model atmospheres. The tropical atmosphere has 80% relative humidity, and the midlatitude atmosphere has 60% humidity. The microwave absorption is computed using the MPM92 model of Liebe (see section 2.2.1). Figure 3.18 shows the profiles of temperature with height for the two model atmospheres. In addition the transmission to space as a function of height is plotted for the four frequencies considered. In the tropical atmosphere only 85 GHz has significant contribution from the surface, while even in the very dry midlatitude winter atmosphere 340 GHz is substantially opaque. The transmission goes to one quickly with height in the lower atmosphere, following the moisture profile. At 340 GHz the transmission to space is greater than 0.99 at 10 km in the tropical atmosphere and at 8 km in the midlatitude winter atmosphere (roughly around $-40°$). So at typical heights of cirrus clouds there is little absorption in and above the clouds at these microwave frequencies.

The polarized plane-parallel multi-stream model described in section 2.2.2 is used to simulate the upwelling radiance from cloudy and clear atmospheres. The atmosphere is divided up into 20 1.0 km thick layers which are homogeneous in scattering and absorption properties. The cirrus cloud layer is 3 km thick and placed at an appropriate height in the atmosphere: from 9 to 12 km in the midlatitude atmosphere ($226 - 219°K$) and from 14 to 17 km in the tropical atmosphere ($210 - 195°K$). The particle concentration of the clouds and hence the ice water content is adjusted for each case so that the nadir brightness temperature depression is 2.0°K for the tropical profile over land. This is done so the change in radiance is small enough to keep the radiative transfer in the linear regime, yet large enough so the change in brightness temperature can be accurately computed (brightness temperatures are output to 0.01°K). At an angle of 49° the brightness temperature depression ranges from 0.77°K to 4.33°K over the four frequencies, five shapes, and 18 size distributions for the tropical/land profile.

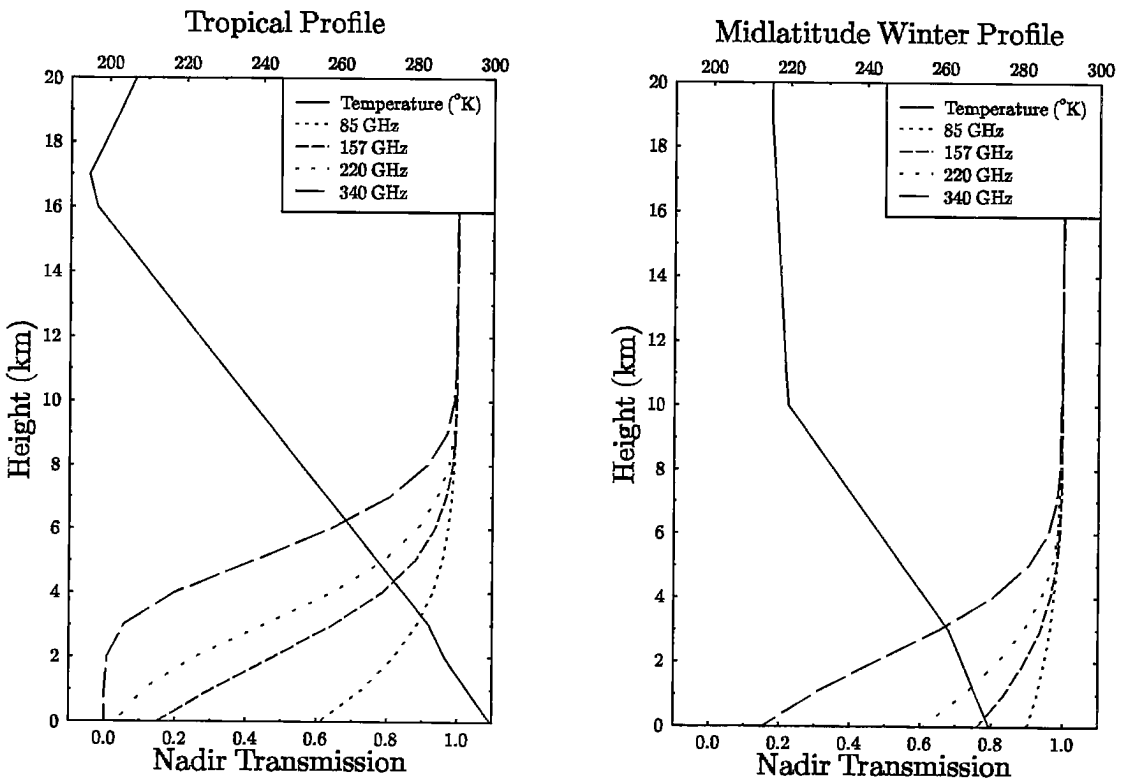


Figure 3.18: Temperature and transmission profiles for the two model atmospheres.

Table 3.8: True size of cosmic background radiation

| Frequency (GHz) | $B(2.7)/B(270)$ |
|---|---|
| Rayleigh-Jeans | 0.01000 |
| 85.5 | 0.00429 |
| 157 | 0.00185 |
| 220 | 0.00081 |
| 340 | 0.00015 |

The radiative transfer simulations are done for both land and water surfaces because of their marked contrast in microwave radiometric properties. The land is modeled as a Lambertian surface with a constant emissivity of 0.95. The water is modeled as a flat dielectric Fresnel reflecting surface with the index of refraction of water varying with frequency and temperature (see table 3.7). The skin temperature of the surface is the same as the bottom of the atmosphere (300°K for tropical and 272°K for midlatitude winter). The cosmic background radiation from above is ignored because at the high microwave frequencies considered here it is insignificant. Table 3.8 shows the ratio of the Planck function at 2.7°K to that at 270°K. This shows that at these frequencies the 2.7 K blackbody curve is departing from the Rayleigh-Jeans limit in such a way as to make it much smaller than indicated by the brightness temperature.

The radiative transfer calculation is carried out with radiances having units of W $m^{-2}$ $ster^{-1}$ $\mu^{-1}$ and the Rayleigh-Jeans approximation is not used. The $I$ and $Q$ Stokes radiances computed by the multi-stream model are converted to V and H polarizations and these are then translated to equivalent blackbody brightness temperatures. The doubling-adding technique is carried out with 8 Lobatto quadrature angles per hemisphere, though results are presented only for the nadir angle ($\mu = 1$) and around 49° ($\mu = 0.65239$).

The radiative transfer procedure described above is carried out for four frequencies (85.5, 157, 220, and 340 GHz), five particle shapes (solid columns, hollow columns, hexagonal plates, planar rosettes, and equivalent volume spheres), and 18 gamma size distributions ($D_m = 70, 100, 150, 250, 400, 700$ $\mu m$ and $\alpha = 0, 1, 2$). The 90 different cirrus cloud cases are done for the tropical and midlatitude standard atmospheres over land and water surfaces.

### 3.4.2 Testing the first order radiative transfer model

The accuracy of the scattering fits and the first order radiative transfer model (eq. 3.7) for remote sensing are tested by comparing the brightness temperature depressions computed using the fits and the first order (FORT) model with the complete DDA scattering information and the polarized multi-stream radiative transfer model. The 18 discrete gamma size distributions are simulated by evaluating the fit equations above and summing over the 13 particle sizes with the appropriate concentrations. There are two sources

of error in the fitting/FORT approximation: 1) the error inherent in the first order radiative transfer model, and 2) the error in the fits to the scattering properties. By using the first order radiative transfer model on the actual scattering properties (i.e. with no particle size fitting) the first source of error alone is evaluated, and thus we can find the radiative error from the fitting procedure. The first order model is run for the same atmospheric situations as the multi-stream model was in the previous section. The upwelling clear sky radiances for standard tropical and midlatitude winter atmospheres are computed with the multi-stream radiative transfer model and fit to a quadratic to input to the FORT model. The average cloud temperatures (201 K for tropics and 220 K for midlatitude) are also input to the FORT model. As before, the cirrus layers are 3 km thick and the ice water contents have been adjusted to give a brightness temperature depression at nadir of 2.0 K.

The errors in the first order radiative transfer and scattering fits are expressed in terms of the fractional difference in brightness temperature *depression* as compared to the polarized multi-stream results. The brightness temperature depressions are compared for the three angles/polarizations (0°, 49° V, and 49° H), the 18 size distributions, the four particle shapes, and the four frequencies. Table 3.9 lists the rms and maximum fractional difference for the four frequencies for different combinations of atmospheres and surfaces. At 85 GHz for the tropical atmosphere and frequencies below 340 GHz for the midlatitude winter atmosphere there are significant to very large errors in the first order model. These errors in the brightness temperature depression are caused by the assumption of no reflection below the cloud. Small amounts of surface reflection (even the 5% for the land case) can cause large errors in the brightness temperature depression computed by the first order model. This occurs because there is considerable cancellation between the negative extinction term and the positive emission or scattering terms, i.e. the emission or scattering from the cloud is large compared to the brightness temperature depression, so small amounts of reflected radiance cause large fractional errors. There is more cancellation when emission dominates for small particle sizes at the lower frequencies and so the errors from ignoring reflection are larger in those cases. Reflection could be included in the first order radiative transfer model but this requires accurate knowledge of the surface reflection and atmospheric transmission. The effect of surface reflection does not matter when the atmosphere is opaque as it is in the tropics above 150 GHz.

The error in brightness temperature depression due to both the scattering fits and the first order model, but without the surface reflection problem, can be seen by considering the tropical atmosphere at the three higher frequencies, for which the typical error is 2% and maximum error is 8%. The error due solely to the scattering fits is shown in table 3.10, which lists the rms and maximum fractional differences in $\Delta T_B$ from the first order model with and without the fitting. As expected there is little difference between the various atmospheres and surfaces. The typical error goes from about 1% at 85 GHz to 2%

Table 3.9: Fractional difference in $\Delta T_B$ between FORT and multi-angle results

| | | | 85 GHz | | 157 GHz | | 220 GHz | | 340 GHz | |
|---|---|---|---|---|---|---|---|---|---|---|
| Atmos | Surface | Fit | RMS | MAX | RMS | MAX | RMS | MAX | RMS | MAX |
| trop | land | no | 0.041 | 0.056 | 0.016 | 0.025 | 0.015 | 0.024 | 0.017 | 0.028 |
| trop | land | yes | 0.040 | 0.075 | 0.020 | 0.069 | 0.024 | 0.070 | 0.027 | 0.080 |
| trop | water | no | 1.227 | 3.545 | 0.018 | 0.031 | 0.015 | 0.024 | 0.017 | 0.028 |
| trop | water | yes | 1.218 | 3.545 | 0.022 | 0.066 | 0.024 | 0.070 | 0.027 | 0.080 |
| midw | land | no | 0.236 | 0.456 | 0.098 | 0.202 | 0.053 | 0.110 | 0.030 | 0.045 |
| midw | land | yes | 0.233 | 0.456 | 0.097 | 0.202 | 0.056 | 0.103 | 0.038 | 0.084 |

Table 3.10: Fractional difference in FORT $\Delta T_B$ due to size fitting

| | | 85 GHz | | 157 GHz | | 220 GHz | | 340 GHz | |
|---|---|---|---|---|---|---|---|---|---|
| Atmos | Surface | RMS | MAX | RMS | MAX | RMS | MAX | RMS | MAX |
| trop | land | 0.010 | 0.035 | 0.014 | 0.052 | 0.020 | 0.069 | 0.020 | 0.069 |
| trop | water | 0.012 | 0.042 | 0.014 | 0.052 | 0.020 | 0.069 | 0.020 | 0.069 |
| midw | land | 0.011 | 0.039 | 0.015 | 0.058 | 0.021 | 0.070 | 0.021 | 0.066 |

at 340 GHz with the maximum error of 7%. At 85 and 157 GHz the differences are mainly due to the rosette particle shape. The results show that the first order radiative transfer model is accurate in most of the situations relevant to the microwave remote sensing of cirrus. The fitting procedure for the scattering properties does not add much additional error to the brightness temperature depressions, partly because a size distribution tends to wash out the errors at particular particle sizes.

### 3.4.3 Tests of remote sensing concepts

One advantage of remotely sensing cirrus clouds with microwave radiometry is that the radiative transfer will usually be in the linear regime. The means that the signal (brightness temperature depression) is proportional to the integrated ice mass. Linearity also means that the signal is affected by the integrated or average properties of the cirrus cloud, so that the one does not need to know the vertical or horizontal distribution of cirrus properties. Thus the complicating effects of cloud heterogeneity are not felt.

When considering the linear radiative transfer regime a natural quantity to use is the ratio of the brightness temperature depression to the ice water path ($\Delta T_b/IWP$), which here is called the sensitivity. To demonstrate the range of linearity the sensitivity is plotted as a function of IWP for a particular simulated cirrus cloud in Fig. 3.19. Two angles (nadir and 49°) are shown, and the IWP includes the secant angle effect. The sensitivity is constant over a wide range of IWP before it begins to fall as the radiative transfer saturates. The useful range of linearity is about a factor of ten in integrated ice mass from the detectability limit (say $\Delta T_b \approx 3$°K) to where the sensitivity drops by about 10%. Obviously, the signal still contains useful information beyond the linear regime, but is somewhat more difficult to interpret.

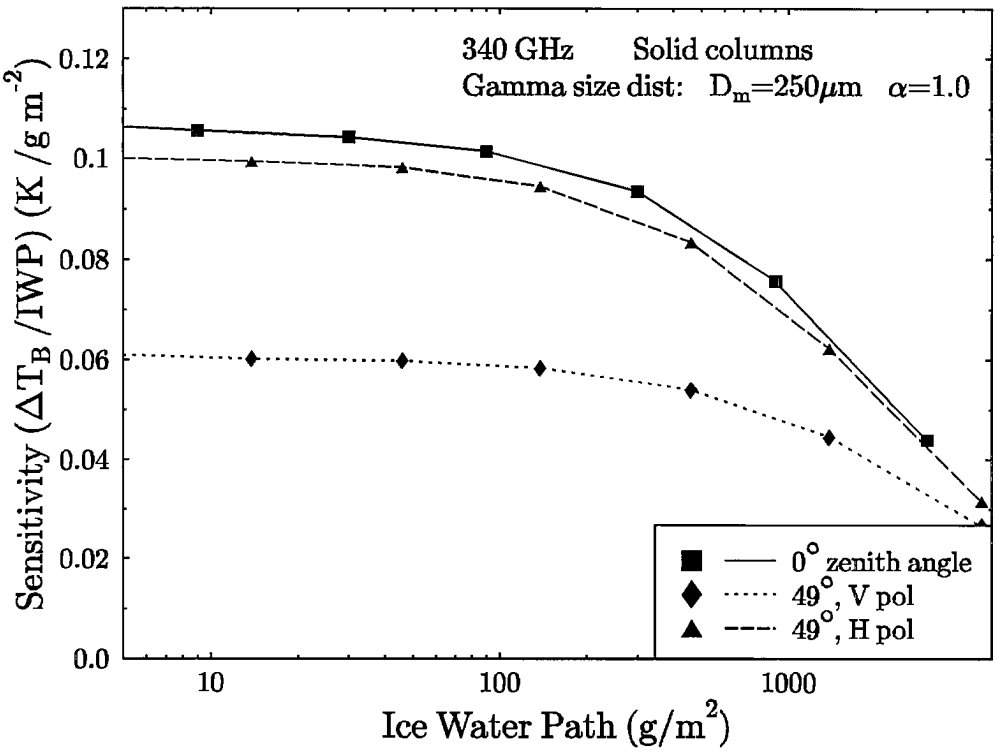


Figure 3.19: Sensitivity vs. ice water path showing the range of radiative transfer linearity.

Another advantage of passive microwave sensing of cirrus is that since it is a scattering based technique knowledge of the temperature, and hence height, of the cloud is not required. To test this assertion the sensitivities from a tropical atmosphere over land were compared between cirrus clouds at two difference heights. The standard level of 14 to 17 km has an average temperature of 201°K, while the other level of 11 to 14 km has an average temperature of 220°K. The fractional difference in sensitivity between the two cloud temperature cases is averaged over the three angles/polarizations (0, 49V, 49H) for the six size distributions with $\alpha = 1$ and the four frequencies and plotted in Fig. 3.20. The error bars show the range in the fractional difference in sensitivity over the five shapes. At the higher frequencies only the size distributions dominated by small particles have significant differences in sensitivity. The smaller particle distributions and the lower frequencies have significant emission and so a larger dependence of the sensitivity on temperature. In an actual retrieval the cloud temperature could be estimated more accurately than the 19°K difference used here, and so the errors would be correspondingly less.

Because at microwave frequencies cirrus clouds are above the radiatively active part of the atmosphere and primarily scatter radiation, the modulation of upwelling radiation by cirrus is relatively independent of the atmospheric profile. To test this idea of a decoupling between the cirrus layer and the underlying atmosphere, a comparison is made

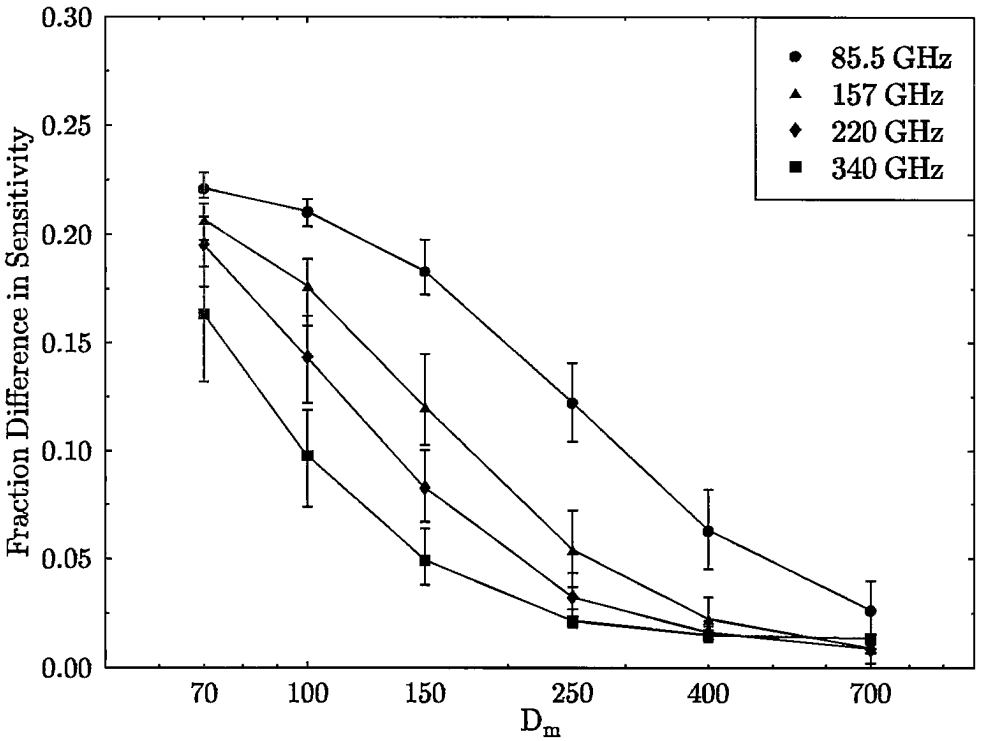


Figure 3.20: Fractional difference in sensitivity between clouds with average temperatures of 201°K and 220°K in a tropical atmosphere. The error bars show the range over the five particle shapes.

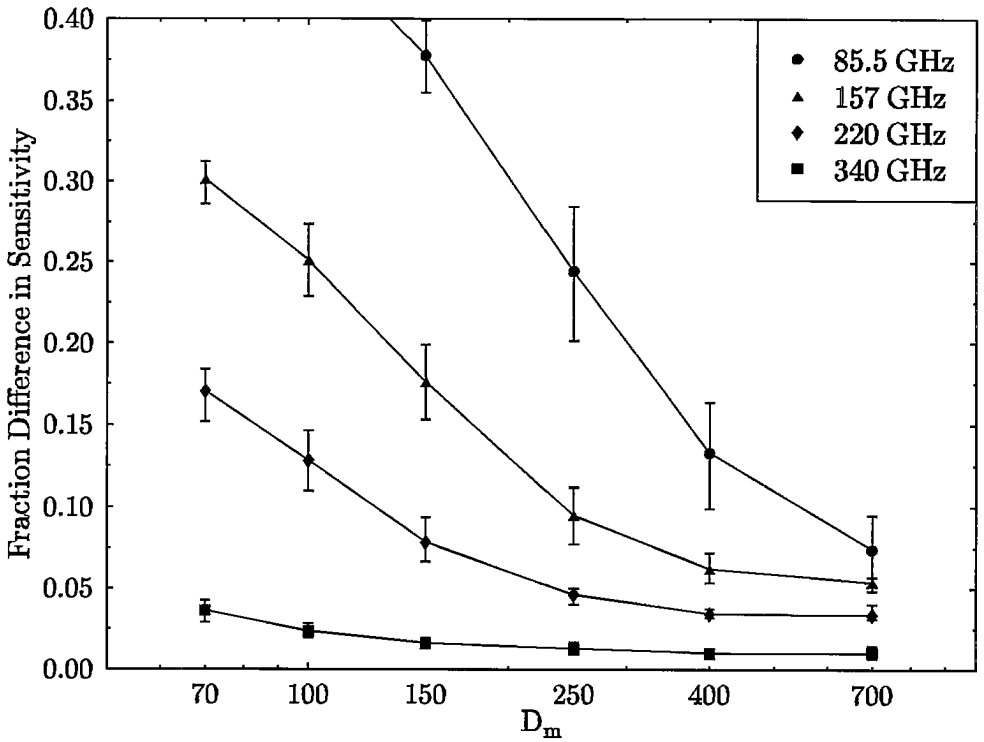


Figure 3.21: Fractional difference in normalized sensitivity between clouds with same average temperature of 220°K but different patterns of incident radiation from tropical and midlatitude winter atmospheres. The error bars show the range over the five particle shapes.

between sensitivities from the tropical and midlatitude winter atmospheres over a land surface. The average temperature of the cirrus layers in both cases is 220°K, so the only difference is the temperature and absorption of the underlying atmosphere. This time the sensitivities normalized by the upwelling brightness temperature ($\Delta T_b/(IWP\ T_b)$) are compared (see Fig. 3.21). The normalized sensitivities for the two atmospheres are within 10% for 340 GHz and all but the two smallest size distributions at 220 GHz. The brightness temperature depressions from the smaller size distributions and lower frequencies, because of the high amount of emission, are not simply proportional to the upwelling brightness temperature and so have considerable differences in sensitivity. In fact, for the midlatitude winter atmosphere over a water surface the sensitivities of some of the smaller size distributions at 85 and 157 GHz are actually negative (the cirrus cloud causes a rise in brightness temperature) because the cloud is warmer than the brightness temperature of the radiation emitted from the surface. Again, in actual practice the structure of the underlying atmosphere would be much better known than in this comparison.

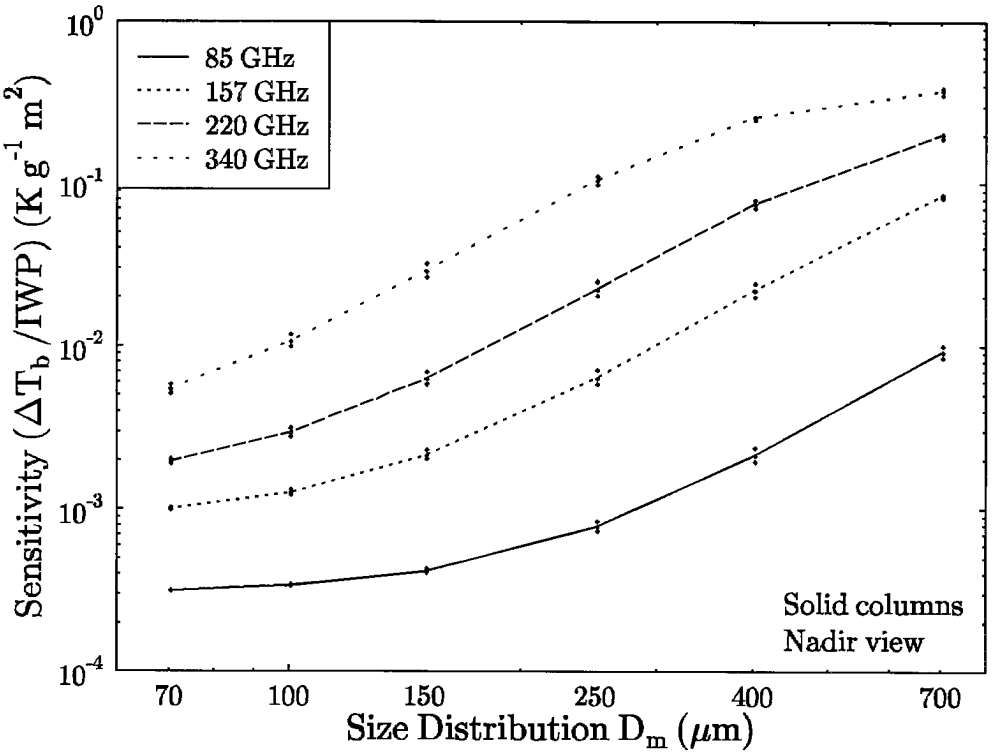


Figure 3.22: Nadir view sensitivity as a function of size distribution for solid columns.

### 3.4.4 Radiative transfer results

The sensitivity ($\Delta T_b/IWP$) of a cirrus cloud depends most strongly on the frequency and the gamma size distribution parameter $D_m$ (the median size of the third moment). Figure 3.22 shows the sensitivity for solid columns for the 18 size distributions and four frequencies. The size distributions with large particles ($D_m \geq 400\mu$m) have much higher sensitivity (roughly a factor of thirty) compared to the ones with small particles ($D_m \leq 100\mu$m). The effect of the gamma size distribution parameter $\alpha$ (related to the width of the distribution) is much less pronounced as indicated by the range of the three vertical dots at each $D_m$. For the tropical atmosphere above a land surface the sensitivity varies on average 7% and at most 20% over $\alpha = 0, 1, 2$ for all angles, particle shapes, and size distributions. This implies that the gamma distribution parameter $D_m$ characterizes the "average" size of the distribution rather well. The range in sensitivity over the various particles shapes is fairly large. As an example, Fig. 3.23 shows the sensitivity at 340 GHz for the 18 size distributions and five particle shapes. For the tropical atmosphere the range in sensitivity over the five shapes is a factor of 1.9 on average and a maximum of 4 over all angles and size distributions. For 340 GHz and nadir view angle (as in the figure) the maximum range is, however, only a factor of 2.0.

One problem with passive microwave remote sensing of cirrus is that, depending on the maximum frequency of observation, much of the cirrus cloudiness may be too thin to

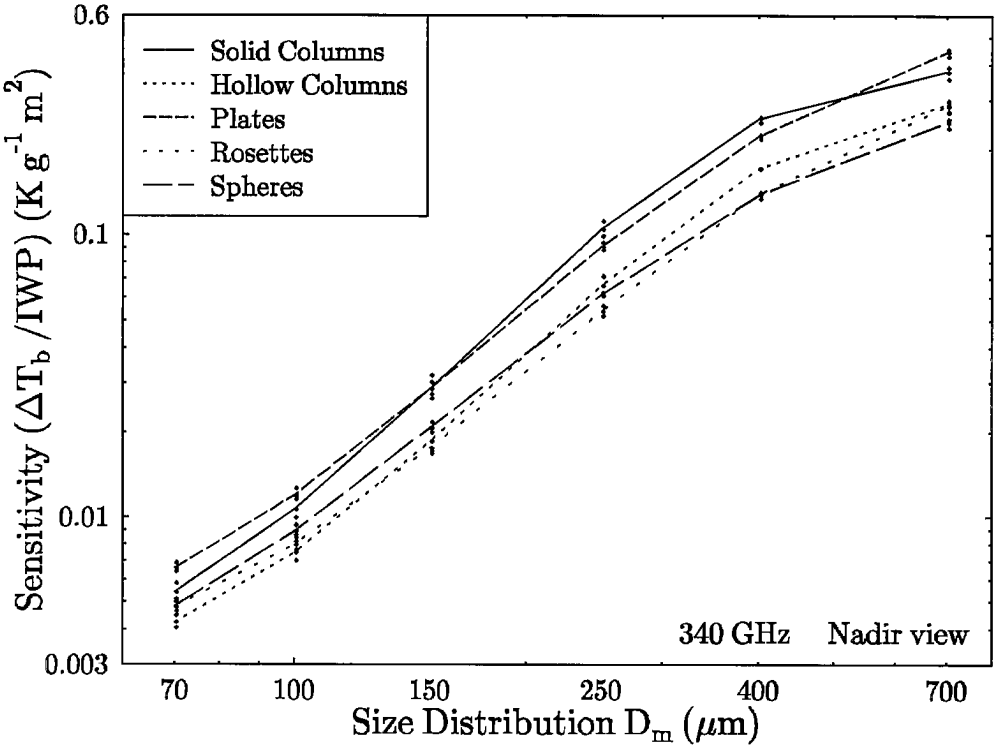


Figure 3.23: Nadir view sensitivity as a function of size distribution for 340 GHz.

detect. If the geometric limit for extinction in the visible is used then the optical depth can be related to the integrated ice water path by

$$\tau = 2\frac{\langle A \rangle}{\langle V \rangle}\frac{IWP}{\rho_i} , \tag{3.13}$$

where $\langle A \rangle$ is the projected particle area averaged over the size distribution, $\langle V \rangle$ is the average volume, and $\rho_i$ is the density of ice. For solid columns with the aspect ratios used here and a gamma distribution with $\alpha = 1$ the visible optical depth is approximately related to the $D_m$ parameter by

$$\tau \approx 10\frac{IWP}{D_m} , \tag{3.14}$$

where the $IWP$ is in g/m$^2$ and $D_m$ is in $\mu$m. Cirrus as thin as $\tau = 0.03$ is detectable visually from the ground (Sassen and Cho, 1992). For a given IWP, larger particle sizes cause a reduction in the visible signal but a dramatic increase in the microwave signal. A minimum detectable cirrus IWP can be defined by the IWP required to give a brightness temperature depression of 3°K. Figure 3.24 shows the minimum detectable IWP for nadir viewing angle with a tropical atmosphere over a land surface for the gamma size distributions with $\alpha = 1$. The five shapes and six distributions are shown for each frequency. For example, at 340 GHz solid columns with $D_m = 250$ $\mu$m an IWP of 30 g/m$^2$ gives a $\Delta T_b = 3$°K, so a 3 km thick cirrus layer with an IWC of 0.01 g/m$^3$ would be detectable.

At the maximum frequency considered here (340 GHz) the thicker cirrus clouds, especially with larger particles, would be detectable but much visible cirrus would not.

Given the wide range in sensitivities for different particle shapes and size distributions it is important to have some method to infer these cirrus properties so that the integrated ice mass can be uniquely retrieved. For passive microwave radiometry the potential observables are brightness temperatures at different frequencies, for V and H polarizations, and perhaps at different angles. One way to use the additional information from multiple channels is to take ratios of brightness temperature depressions, which is equivalent to ratios of sensitivities if the observations are in the linear radiative transfer regime so that the IWP drops out. In the following discussion the sensitivities for the tropical atmosphere over a land surface are used.

Ratios of brightness temperature depressions at different frequencies provide information about the characteristic particle sizes in cirrus. Figure 3.25 has plots of sensitivity as a function of frequency ratio for three frequencies. The six different size distribution parameters $D_m$ are plotted with different symbols, so the progression of characteristic size along the curves can be seen clearly. Unfortunately, for the frequencies with useful sensitivities (220 and 340 GHz) the relationship between sensitivity and frequency ratio is multivalued. If one does not have some additional information about the particle sizes in the cirrus then one cannot make even an approximate determination of the characteristic particle sizes. If it is known that the particle sizes are in the upper part of the range considered here than one may be able to use just the upper part of sensitivity vs. frequency ratio curve.

One might think that it would help to use two or more frequency ratios instead of one, but there is a limit to how much information can be extracted from multiple frequencies. Because the scattering properties of ice vary smoothly in the microwave (no absorption bands), frequencies must be well separated to give distinct information. On the other hand, frequencies that are very widely separated (more than a factor of two) will have such divergent sensitivities that the cirrus will not be detectable with the lower frequency (this is certainly true if the higher frequency is still in the linear regime, $\Delta T_b < 30°\mathrm{K}$). For this reason it is probable that only one frequency ratio will be useful.

We might expect that if even higher frequencies were used then most of the size distributions would end up on the upper part of the curve, thus lessening the multivalued problem. To test this idea, scattering and radiative transfer calculations were carried out at 460 GHz only for the spherical particles (which could be done easily). The same particle densities, size distributions, and radiative transfer procedures described above were used. Figure 3.26 shows sensitivity vs. frequency ratios for 220, 340, and 460 GHz for all the size distributions of spheres. The curve for the 460 to 340 GHz ratio has the distributions with $D_m \geq 150$ $\mu$m on the upper part of the curve, so perhaps most cirrus distributions would not have a multivalued frequency ratio/size distribution relation. Another advantage

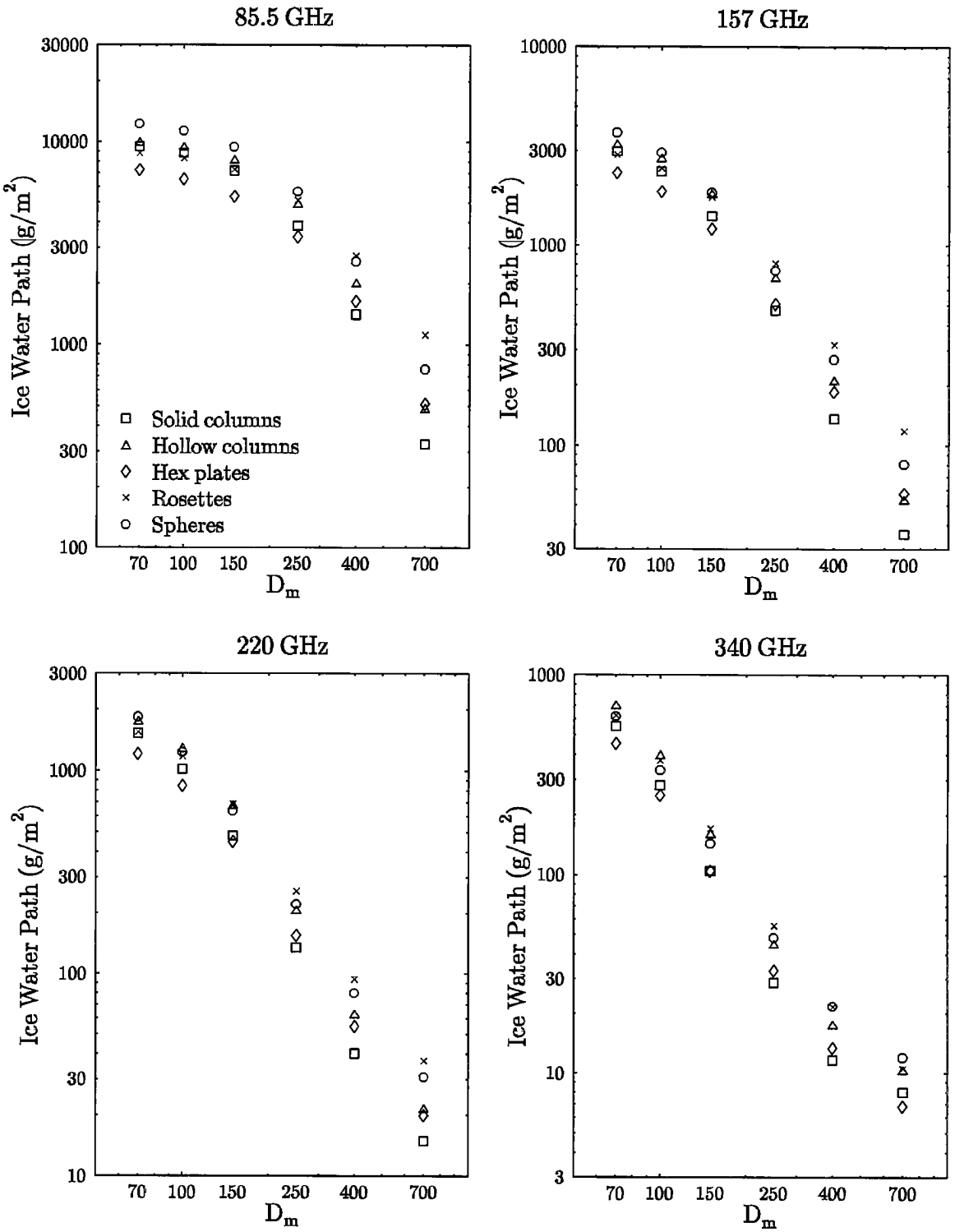


Figure 3.24: Minimum detectable cirrus ice water path (IWP) for $\Delta\ T_b = 3°$K for nadir view. Only the $\alpha = 1$ distributions are plotted.

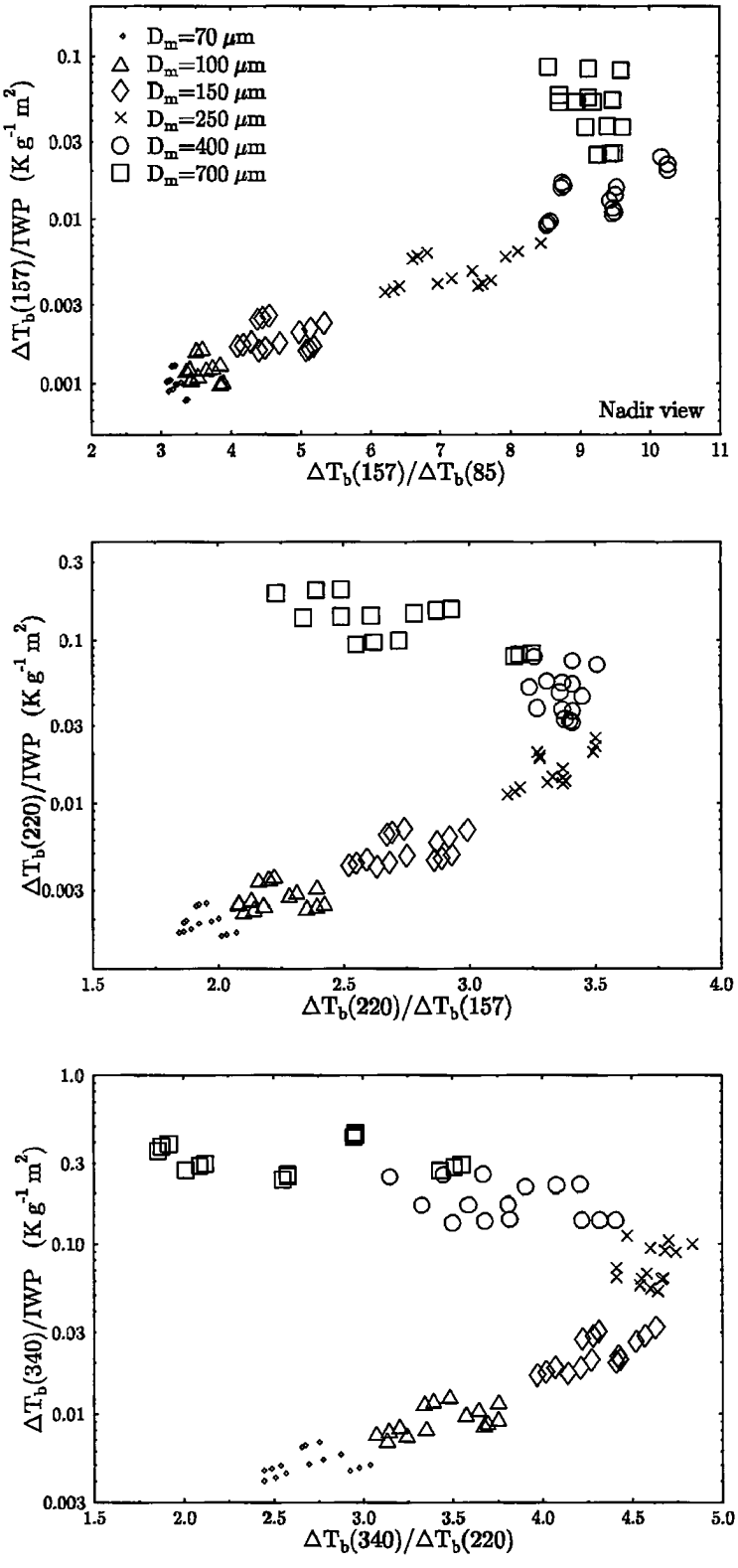


Figure 3.25: Sensitivity vs. ratio of $\Delta T_b$ at different frequencies. The sensitivity is shown for three frequencies at a nadir view angle. Plotted on each graph are the 5 shapes and 18 size distributions, with the 6 different size distribution parameters $D_m$ shown by symbols.

of higher frequencies is that the sensitivities, besides increasing and lowering the IWP detectability limit, increase more slowly with particle size. This means that less accuracy is needed in knowing the characteristic size of the particles in order to have acceptable accuracy in the retrieved ice mass.

Besides the limitations of instrumentation there is a limit to how far up in frequency one can go and still have the same microwave behavior. The imaginary part of the index of refraction of ice, which governs absorption, goes up rapidly in the THz ($10^{12}$ Hz) region, so that cirrus clouds would leave the scattering regime and enter the absorption regime as in the infrared. For the spherical particles at $-60°$C with a gamma distribution $D_m = 400$ $\mu$m, the single scattering albedo goes down to 0.90 at 1260 GHz. Another problem is that the water vapor absorption increases with frequency so that there will be significant emission from the atmosphere in and above the cirrus clouds. Finally, there is the technical problem that CPU time and memory for the DDA solution go as the third power of the frequency.

The ratio of brightness temperature depressions for the two polarizations (H over V) contains information about cirrus particle shapes. Figure 3.27 has plots of sensitivity as a function of polarization ratio for 220 and 340 GHz, with the shapes plotted as different symbols. The major contributing factor for the sensitivity is the size distribution parameter $D_m$, rather than the shape, so the six size distributions for each shape tend to be aligned along the sensitivity axis. The polarization ratio separates the particles shapes according to the aspect ratio, from the spheres with a ratio of 1.0 to the plates with a ratio from 1.7 to as much as 4. There is a tendency for the polarization ratio to increase with characteristic particle size, mainly because of the decreasing aspect ratio. For columns the polarization ratio decreases for distributions with the largest particles, because of the scattering process. With information about the characteristic size of the distributions it looks possible to use the polarization ratio to determine a distribution of particle shapes. Actual bullet-rosettes complicate the picture greatly. Because of the presumably random attachment of bullets, they are likely to be closer to the spheres than the planar rosettes in their polarization ratios. Assuming rosettes fall through the air with their largest "side" horizontal, they should still have a polarization ratio greater than one. Better microphysical information combined with more DDA modeling could address this issue with a distribution of rosette shapes. Distributions containing more than one particle shape will have intermediate polarization ratios. In the linear radiative transfer regime the brightness temperature depressions of such a mixture will be a linear combination of the single shape $\Delta T_b$'s.

The ratio of brightness temperature depressions at two angles (0° to 49°) has information much like that from the polarization ratio. Figure 3.28 shows the angular $\Delta T_b$ ratio vs. the polarization ratio for 220 and 340 GHz. The plot is basically a straight line (except for the large particle distributions at 340 GHz), indicating that the information

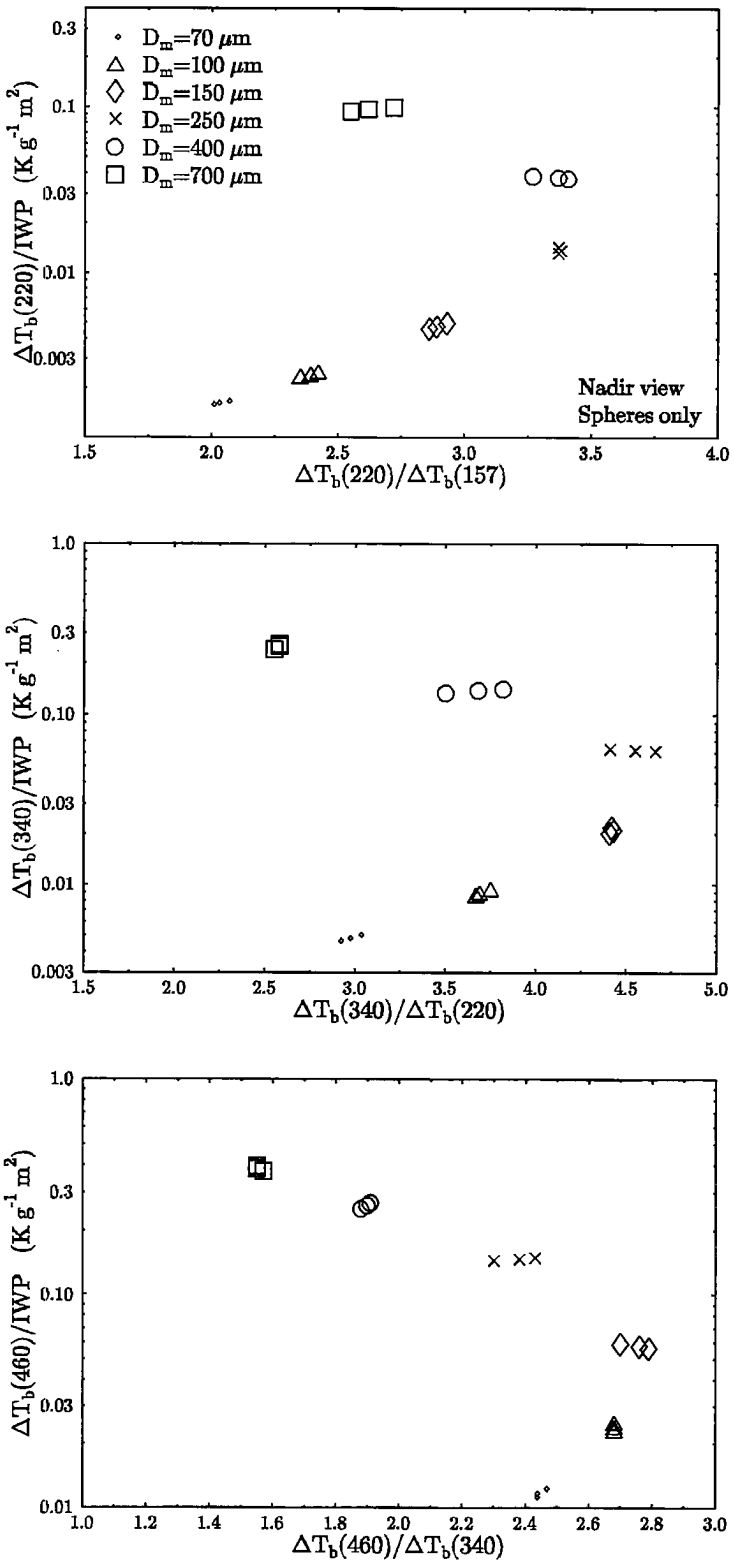


Figure 3.26: Sensitivity vs. ratio of $\Delta T_b$ at different frequencies. The sensitivity is shown only for spheres for 220, 340, and 460 GHz at a nadir view angle. Plotted on each graph are the 18 size distributions, with the 6 different size distribution parameters $D_m$ shown by symbols.

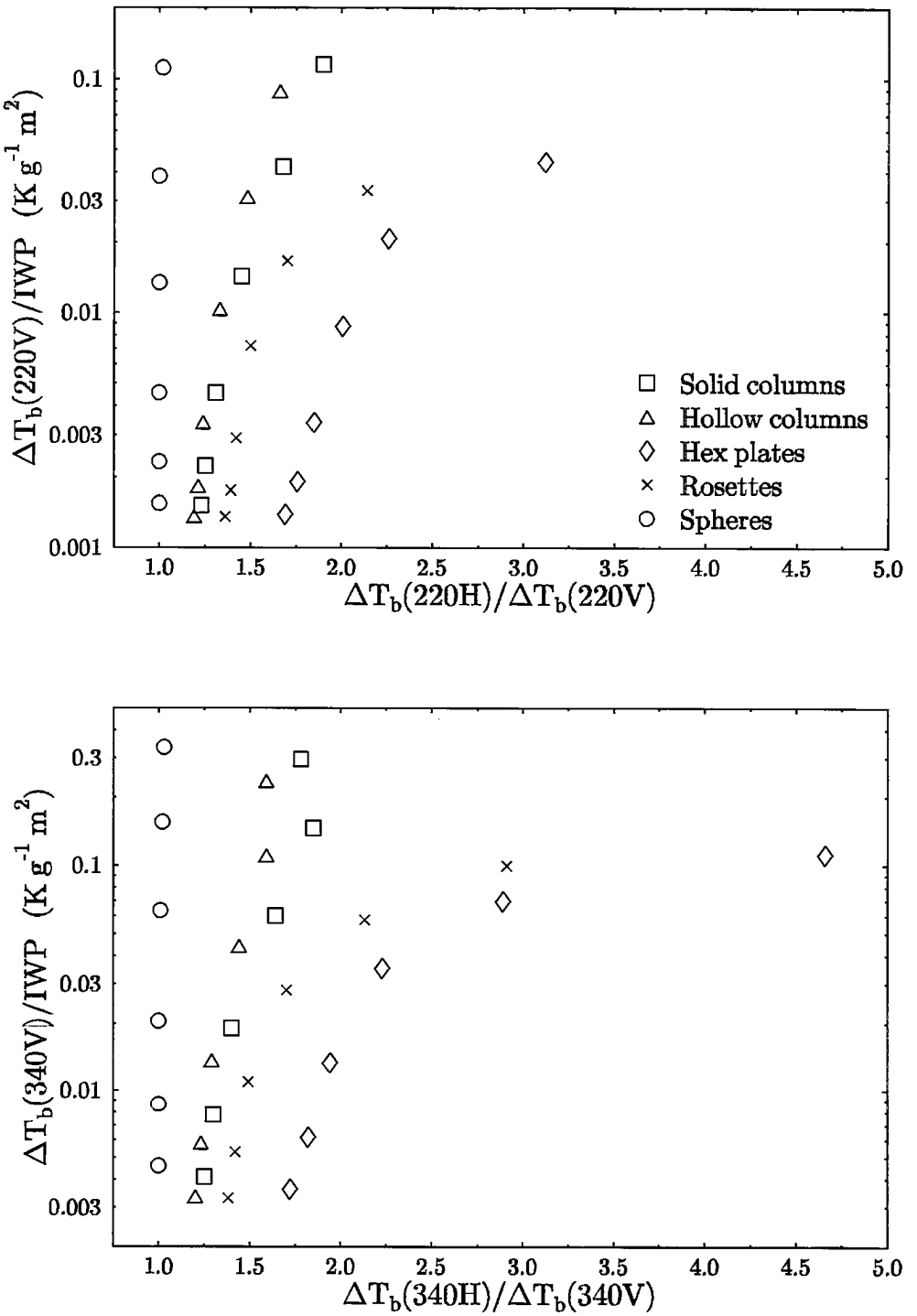


Figure 3.27: Sensitivity vs. ratio of $\Delta T_b$ for H polarization to that for V polarization at 49°. The sensitivity is shown for 220 and 340 GHz. Plotted on each graph are the 6 size distributions with $\alpha = 1$ and the 5 particle shapes, with the different shapes shown by symbols.

from the angular pattern of the brightness temperature depression is almost equivalent to the polarization information. It is generally much easier to measure the two polarizations at a fixed angle than to measure the same cloud volume at two angles, so there is probably little point in trying to use the angular pattern of radiation for microwave remote sensing of cirrus.

Part of the effect of shape on sensitivity is due to the aspect ratio, but part is also due to the particle volume. The planar rosettes, for example, have less volume than the columns for the same maximum particle extent $D$. Even though the concentration is normalized to get the same ice water content, this means that the rosettes have a smaller "effective" size. To examine this particle volume effect Fig. 3.29 plots the 340 GHz sensitivity at nadir viewing angle against a characteristic size based on the maximum diameter and one based on a equivalent volume sphere diameter. This characteristic size is $\langle D^6 \rangle^{1/6}$, which for the equivalent volume diameter is proportional to the Rayleigh scattering cross section. The characteristic sizes based on volume are quite a bit smaller than those based on the maximum particle diameter. Using the volume characteristic size spreads out the shapes but does not really tighten up the relationship. The columns and rosettes fall on a smooth curve, but the plates and spheres are above and below. At nadir the plates have relatively more scattering for their volume while the spheres have relatively less. Figure 3.30 shows that, for vertical polarization at 49°, there is a much tighter relationship between sensitivity and characteristic size if one bases the size on the particle volume. To quantify this, the sensitivity for the four middle size distributions is fit (linearly in the logs) against the characteristic size. For nadir angle and H-pol at 49° the rms error is about 0.24 for both types of characteristic sizes, while for V-pol at 49° the rms error decreases from .30 to .13 from using the volume characteristic size. So there appear to be certain angles and polarizations that minimize the confounding effects of particle shape if the particle volume is taken into account when assigning a "characteristic size" to the size distribution.

Particle shape is really only important as it affects the sensitivity and hence the retrieval of IWP. If $\Delta T_b$ polarization and frequency ratios can uniquely determine the sensitivity then the effect of shape can be dealt with through the polarization information without specifically finding the shape. To look at the feasibility of this, Fig. 3.31 depicts 340 GHz V-pol sensitivity as a function of frequency and polarization ratios. The sensitivity is mainly a function of frequency ratio and secondarily of polarization ratio. For the larger particle distributions there is still ambiguity in the sensitivity because of shape that the polarization ratio cannot resolve.

### 3.4.5 Ideas for cirrus retrieval methods

The details of a cirrus microwave remote sensing algorithm will, of course, depend on the particular instrument (frequencies, polarizations, etc.) and experimental setup. Since

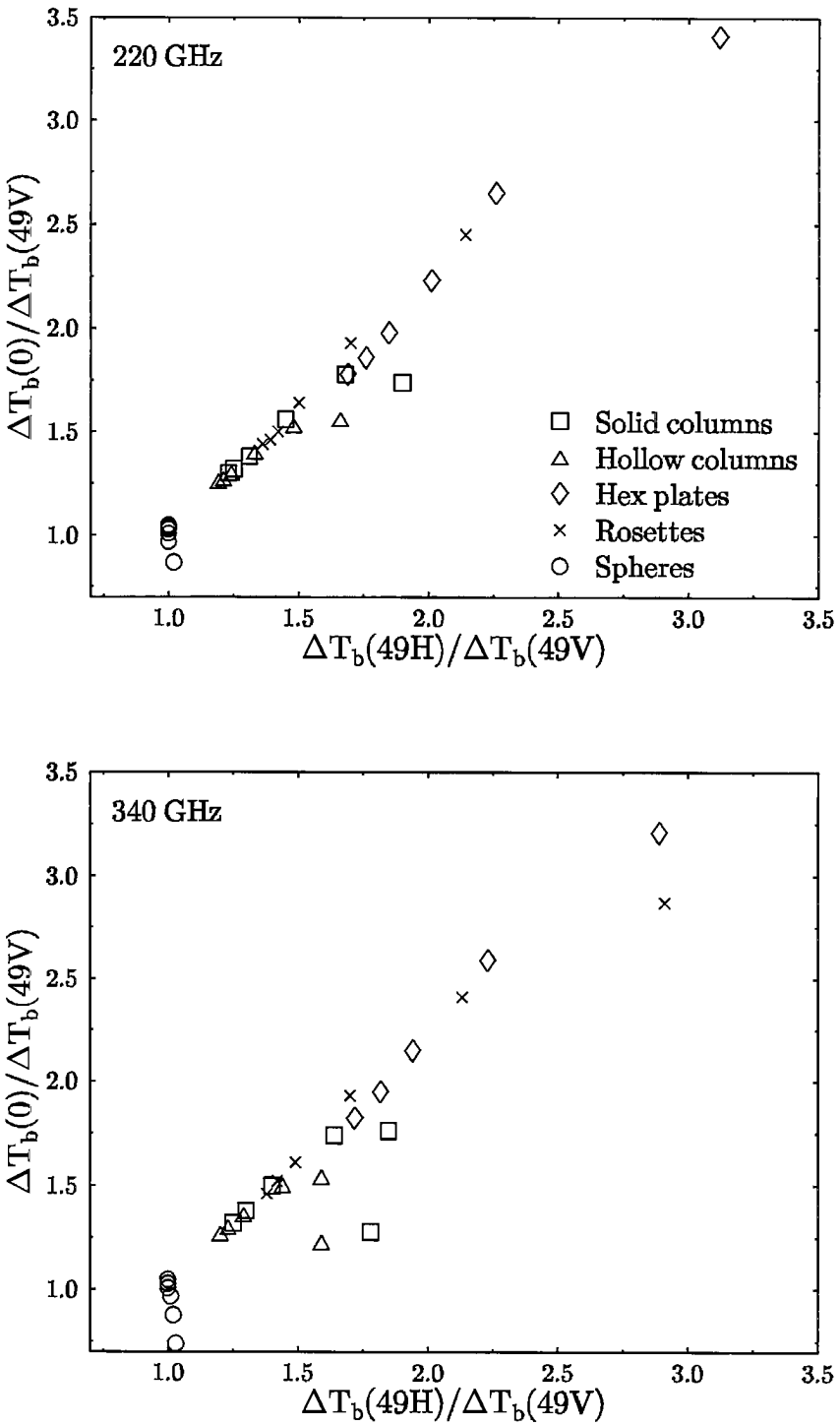


Figure 3.28: Ratio of $\Delta T_b$ for 0° to that for 49° vs. ratio of $\Delta T_b$ for H polarization to that for V polarization at 49°.

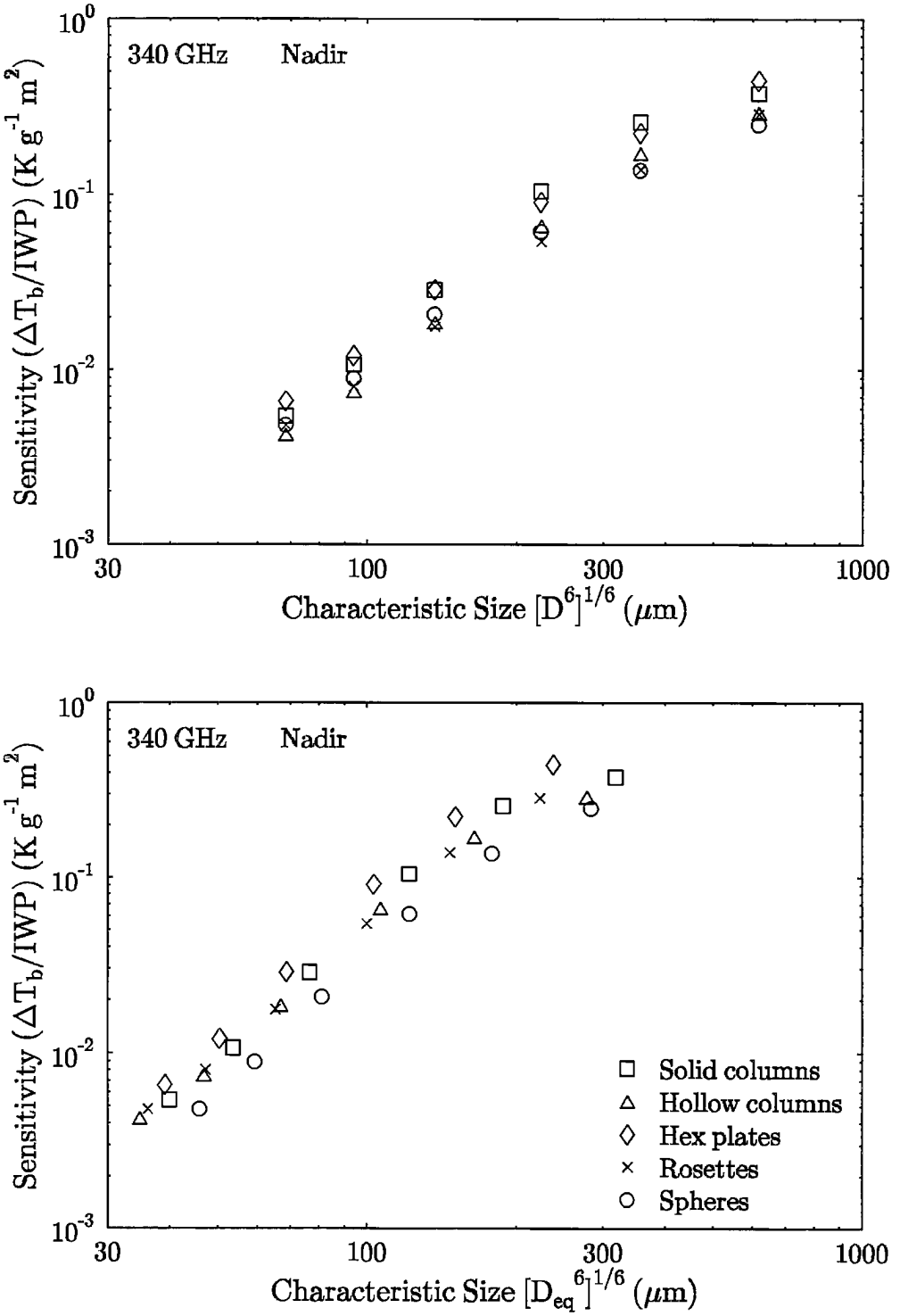


Figure 3.29: Nadir view sensitivity at 340 GHz vs. a characteristic particle size of the distributions. This characteristic size is the sixth root of the sixth moment of the distribution. In the top panel the characteristic size uses the maximum particle extent, while in the bottom panel it uses the equivalent volume sphere diameter. The $\alpha = 1$ distributions are plotted for the five shapes.

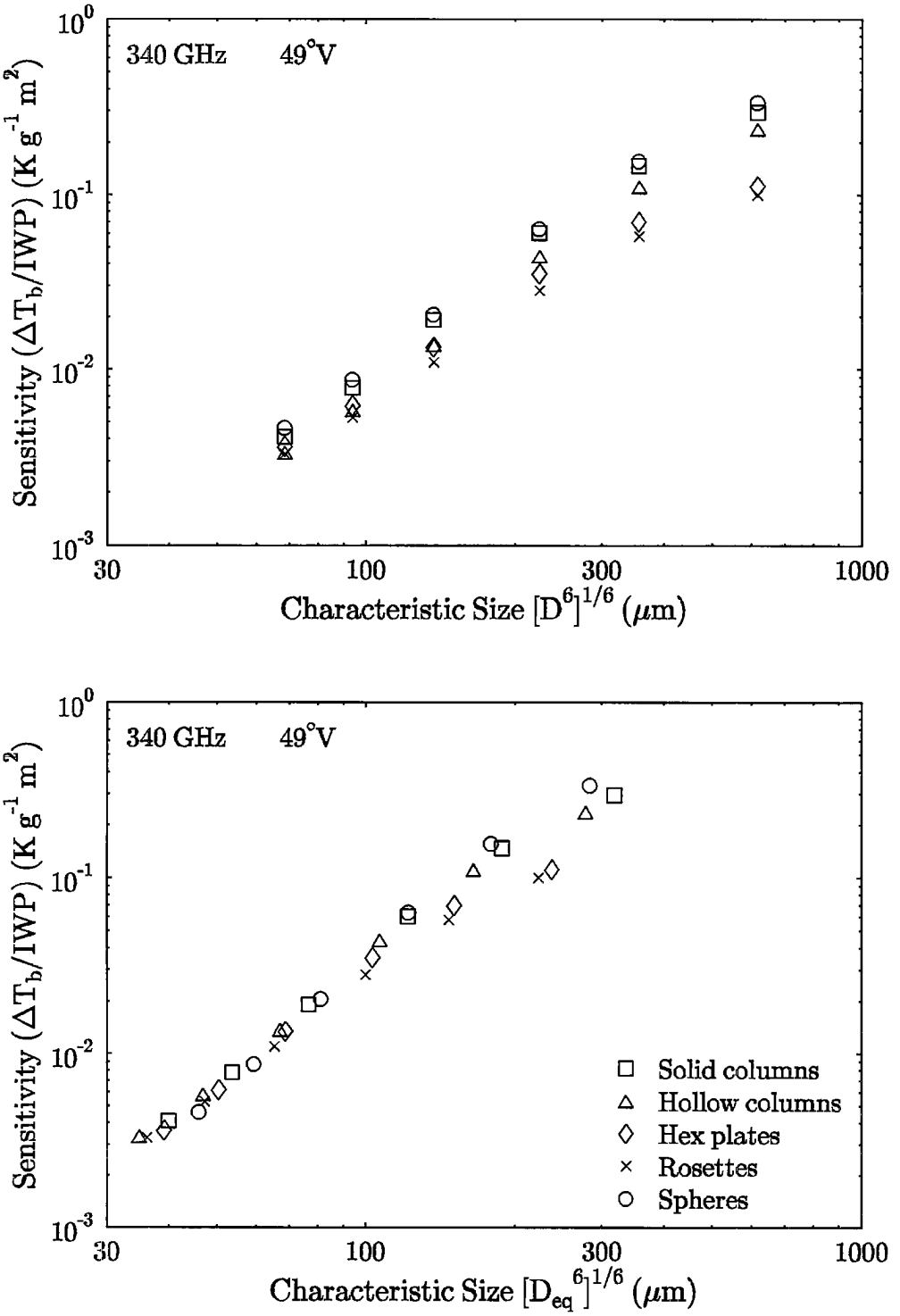


Figure 3.30: 49° V-pol sensitivity at 340 GHz vs. the characteristic particle size of the distributions. Other quantities as in previous figure.

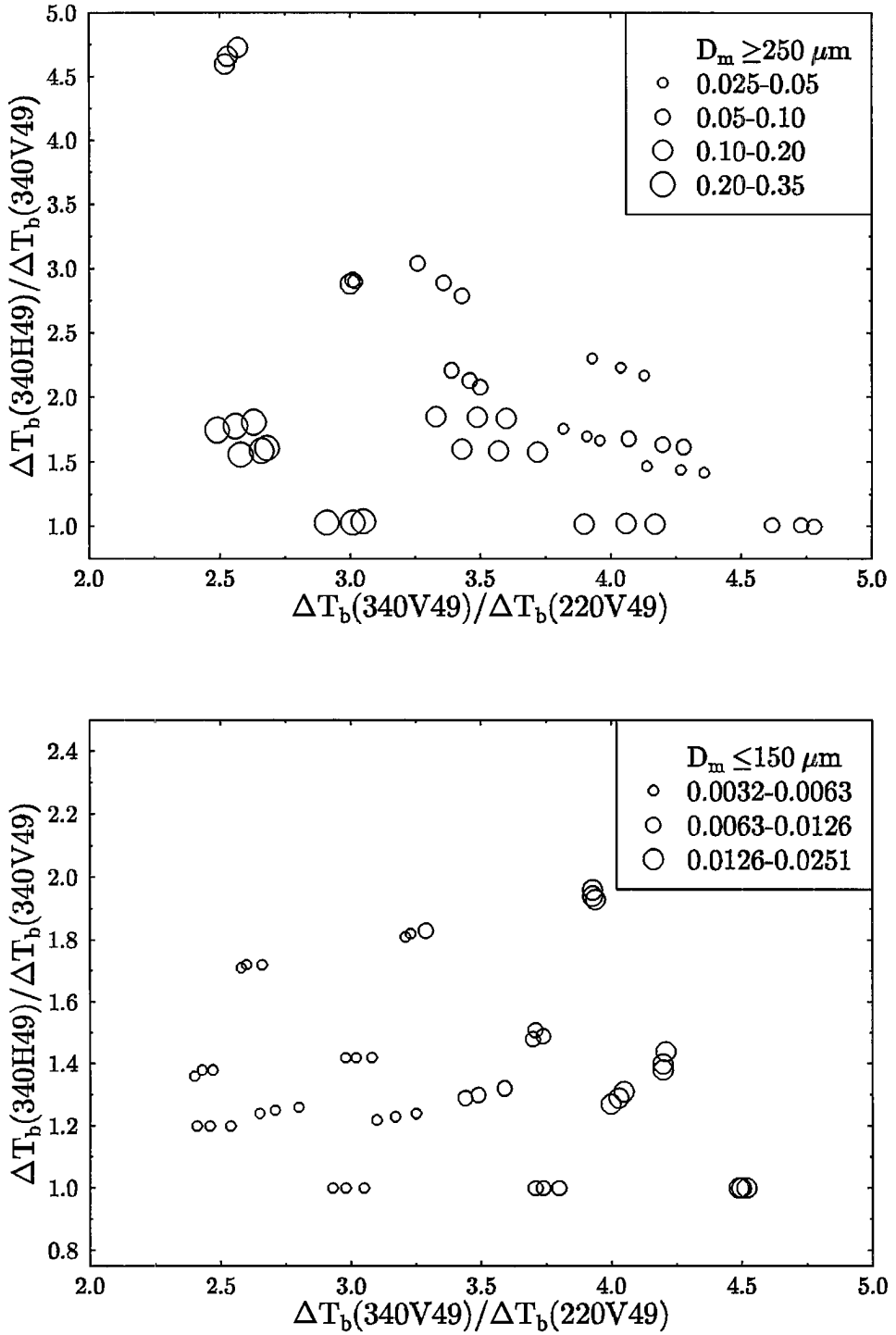


Figure 3.31: 49° V-pol sensitivity at 340 GHz represented by symbol size as a function of $\Delta T_b$ frequency (340 to 220 GHz) and polarization (H to V) ratios. The top panel is for the three larger size distributions, and the bottom panel is for the three smaller distributions (the two different branches of Fig. 3.25).

high frequency microwave observations of cirrus are not available for this dissertation, a specific algorithm is not proposed. Instead general concepts will be discussed that should aid in applying the numerical results above to develop a future retrieval algorithm.

Since the basic signal relating to the mass of cirrus is the brightness temperature depression, as with many cloud detection and measurement methods, knowledge of the clear sky brightness temperature is required. Perhaps the simplest method of obtaining the clear sky brightness temperature is to use nearby pixels having very thin cirrus or no cirrus at all. This requires the assumption that the atmosphere beneath the cirrus layer is homogeneous. In atmospheres having at least a modest amount of water vapor, the higher microwave frequencies (say > 200 GHz) are effectively opaque to the surface. Thus possible subcirrus inhomogeneities would be caused by water vapor irregularities and lower, water clouds. In an absolute sense the amount of water vapor is likely to be fairly stable over a typical field of view (10-100 km), but since high precision (of order $\Delta T_b \approx 1°\mathrm{K}$) is desired, this is a significant concern. The lower microwave frequencies that are insensitive to cirrus could be used to correct for water vapor, and potentially even lower cloud, irregularities. Water vapor profiling channels such as ones at 183 GHz may help in correcting for humidity irregularities, though these channels would also be modified by scattering in cirrus clouds. In general, a cirrus remote sensing algorithm should make sure that the changes in brightness temperature are consistent across the wide range of frequencies available before making an interpretation.

Once the brightness temperature depressions ($\Delta T_b$) have been computed, the procedure for determining the ice water path (IWP) is to find the correct sensitivity ($\Delta T_b / IWP$) and divide. This assumes that radiative transfer is in the linear regime. This will usually be the case, because depending on the frequency, larger brightness temperature depressions are likely to be caused by precipitating systems such as deep convection or mesoscale stratiform areas rather than cirrus clouds. Of course, if the cirrus is thick enough to be beyond the linear regime, then a radiative transfer model can be used. To determine the correct sensitivity to use, one must know, firstly the characteristic particle size, and secondly the particle shape. In many situations there will be a mixture of particle shapes, and some idea of the shape mixing fractions is needed. The characteristic particle size can be estimated from $\Delta T_b$ ratios at different frequencies (see Fig. 3.25). If there is uncertainty about which branch of the curve to use, or if the $\Delta T_b$ at the highest frequency is too small for a frequency ratio to be measurable, then a characteristic size would have to be assumed. This could come from successfully found sizes in adjacent pixels, crude sizes based on parameterizations using cloud temperature, or effective radius retrievals using infrared channels (see below). If polarization information (H and V channels) is available then that can be used to help determine particle shape using the ratio of $\Delta T_b$ at the two polarizations (see Fig. 3.27). There is some ambiguity in the relationship between particle shape and polarization ratio, so extra information would be useful. If no polarization

information is available then it may be best to assume a crystal habit based on environmental conditions (columns in coldest clouds, bullet-rosettes in more convective regimes, plates in warmer clouds, etc.).

A more numerical method would use a radiative transfer model, perhaps the first order model described above, that operates on tabulated scattering properties. A particle size distribution with one characteristic size parameter, e.g. the gamma distribution with $\alpha = 1$, would be assumed. If polarization information was available then a single parameter could be used that determined the mixing between two expected shapes (say column and plate). If polarization was not available then the particle shape would be assumed. The radiative transfer model would then be iterated to find brightness temperatures that match the observations by adjusting the ice water path and particle size parameter, and maybe shape and underlying water vapor parameters.

A rough estimate of the likely uncertainties in ice water path retrievals can be made. Since all the basic quantities are in terms of brightness temperature depression, it should be pointed out that having a $\Delta T_b$ that is detectable is not the same as accurately measurable. For example, if $\Delta T_b = 6°\text{K}$ and the uncertainty is 2°K then the error is over 30% error to start with. The errors due to the DDA scattering calculations and finite size distributions are negligible compared with other sources. A potentially significant, but difficult to quantify error is that from deviations in the aspect ratio from the empirical fits used. Of the error sources specifically considered in the previous section the one due to size distribution width ($\alpha$) is the smallest being less than 10% if the $\alpha = 1$ distribution is used. If no shape information is available, then the error in sensitivity due to shape varies with frequency and angle, but is near a factor of 1.5 for nadir view at 340 GHz. The biggest source of uncertainty in sensitivity comes from the "average" particle size. Over the range in size distributions considered here ($70 \leq D_m \leq 700$ $\mu$m), the sensitivity varies by a factor of around 70 at 340 GHz, so clearly some particle size information is crucial. In the middle range of size distributions for solid columns with a nadir view at 340 GHz the sensitivity goes as a 2.54 power of $D_m$, so knowing $D_m$ to as well as 20% translates to about a factor 1.6 error in sensitivity. As an illustrative example, say $\Delta T_b(340) = 18°\text{K}$ and $\Delta T_b(220) = 5 \pm 1°\text{K}$; then the frequency ratio has a range $3.0 \leq \Delta T_b(340)/\Delta T_b(220) \leq 4.5$; using Fig. 3.25 and assuming no information about particle shape, the sensitivity ranges from 0.06 to 0.3 °K $\text{g}^{-1}$ $\text{m}^2$. Although this is an oversimplified example, it indicates some of the difficulties involved.

It would be best to use collocated visible and infrared channels in conjunction with the microwave frequencies to measure cirrus properties. The visible and thermal IR channels could first of all be used to detect the presence of cirrus. Since the microwave channels are only able to detect moderate to large optical depths, the cirrus emissivities will be fairly large and a good estimate of cloud top temperature could be made. The cloud temperature can be used to aid in the selection of ice crystal habit and perhaps particle size.

Several near infrared channels can be combined to estimate effective radius, although these techniques have problems with determining the scattering from nonspherical particles. Combining data from a spaceborne millimeter wave radar with those from microwave radiometers would be very useful because of the independent information provided about particle size and shape.

A new instrument under development that will be used for remote sensing of cirrus is NASA's Millimeter-Wave Imaging Radiometer (MIR) (Gasiewski, 1992). The MIR is a cross-track scanning ($\pm 50°$) instrument that can be mounted on the ER-2 and flown at an altitude of around 20 km. It has total power channels at 89, 150, 183$\pm$1,3,7, 220, and 325$\pm$1,3,9 GHz, so no polarization information is available. The 183 and 325 GHz frequencies are primarily for water vapor profiling but can also be used for cirrus observations, especially using the wing channels. The channels have identical 3.5° beamwidths, which greatly simplifies the use of multiple frequency algorithms. Since this instrument currently lacks polarization capability, particle shape will have to be based on indirect inference. The large selection of frequencies will aid in computing $\Delta T_b$ by removing lower atmosphere irregularities and in using frequency ratios for particle size determination. The scanning geometry will require the tabulation and interpolation of scattering properties at a number of zenith angles. The advantages of polarization and even higher frequencies will have to wait for upgrades to the current instrument configuration or altogether new instruments. The ideas expressed in this section will undoubtedly need to be revised when we gain experience with high frequency microwave data from the MIR and try to measure cirrus cloud properties.

# Chapter 4

# BAYESIAN PRECIPITATION RETRIEVAL ALGORITHM

## 4.1 Overview of Passive Microwave Remote Sensing of Precipitation

It is usual to divide the interaction of microwave radiation with precipitation into the emission regime and the scattering regime depending on frequency. For frequencies below about 25 GHz precipitation sized ice particles do not attenuate the radiation strongly and the primary interaction is absorption and emission by water drops. Above around 60 GHz both ice and water precipitation size particles attenuate strongly and the dominant effect for remote sensing is the scattering of radiation by ice particles. In between these two regimes both physical processes are important and must be considered. The basis for passive microwave remote sensing of rain in the emission regime is that the brightness temperature increases with the amount of rain when viewed against a water surface, which has low emissivity and so is radiometrically cold. Since the emission from raindrops is relatively unpolarized there is also a decrease in polarization with rain rate over the highly polarized water surface. The amount of brightness temperature increase depends on the rain rate and rain layer thickness and eventually saturates as the rain layer becomes opaque, which happens at lower rain rates with higher frequencies. Emission techniques generally cannot be used over land because there is neither significant brightness temperature nor polarization contrast between the rain and the high emissivity surface. The basis for remote sensing of rain in the scattering regime is more indirect. The strong scattering of upwelling microwave radiation by ice particles causes a decrease in the brightness temperature that is related to the amount of frozen hydrometeors. The amount of scattering depends on the size and particle density of ice particles and also on the amount of collocated liquid cloud water. Scattering techniques can be used over land or water because the rain underlying the frozen hydrometeors generally obscures the surface. Along with the effects mentioned above, the rain or ice particle size distributions, particle shapes, cloud droplet mass, water vapor, temperature, surface emissivity, and vertical and horizontal inhomogeneities all affect the upwelling microwave radiation from a precipitating atmosphere.

The methods of passive microwave remote sensing of precipitation can be divided crudely into statistical and physical approaches. The work of Spencer et al. (1983) is an example of a purely statistical method. They used multiple regression to relate the

brightness temperatures of seven channels (10 to 37 GHZ) from the Scanning Multichannel Microwave Radiometer (SMMR) to weather radar derived rain rates. Petty and Katsaros (1990) related 37 GHz polarization difference to radar observations and found that there was considerably better correlation with rain coverage than rain intensity. Prabhakara et al. (1992) empirically related the 37 GHz brightness temperature warming above a minimum value to the rain rate in a field of view with a nonlinear relationship that was tuned with GATE radar data. Statistical techniques can also be combined with physical radiative transfer modeling. Wilheit and Chang (1991) developed a probability distribution matching algorithm to estimate area averaged rainfall for 5° boxes over the ocean from brightness temperature histograms using a $T_b$-rainrate relation obtained from radiative transfer modeling. Another combined physical/statistical method is to simulate microwave brightness temperatures from hydrometeor profiles produced by numerical cloud models and use multiple regression to find a multichannel rain rate-$T_b$ relation (e.g., Adler et al., 1989).

The precipitation retrieval methods that are based on radiative transfer modeling can be divided into those that assume a simple precipitation structure and those that retrieve hydrometeor profiles. The prototypical simple physical algorithm is the 19 GHz emission method of Wilheit et al. (1977). This method, which has been used in several forms over the years, assumes a uniform rain layer below the freezing level with no ice particles and a prescribed liquid water cloud. The height of the freezing level can be obtained from climatology or from a 22 GHz channel. These assumptions allow a simple relationship between the 19 GHz brightness temperature and the rain rate to be derived from a radiative transfer model. Weinman and Guetter (1977) considered a single rain layer at 37 GHz and used a combination of the two polarizations to remove the double-valued dependence of the brightness temperature on the rain rate over water. Spencer et al. (1989) used a similar quantity at 85 GHz, called the polarization corrected temperature, as a precipitation indicator. Huang and Liou (1983) simulated upwelling radiation at 19, 37, and 85 GHz with a multi-stream radiative transfer model from a precipitating atmosphere with variable thickness rain and ice layers, but did not specifically define a retrieval algorithm. Olson (1989) used a finite cloud radiative transfer model with a two layer precipitation structure and a complex inverse algorithm to retrieve rain rate and the rain area filling fraction in a tropical cyclone from multi-channel SMMR data. Weng (1992) developed a probability matching method to retrieve monthly mean precipitation. The method used a polarized radiative transfer model with a two layer precipitation structure to relate surface rain rate to polarized corrected brightness temperatures at 19 and 85 GHz. Recently, Liu and Curry (1992) developed a method that relates a linear combination of 19 and 85 GHz brightness temperatures to rain rate. Radiative transfer modeling was done for three simple hydrometeor structures, and a power law was fit to the rain rate vs. brightness temperature change relation. A common characteristic of most of these simple physical

models is the use of one quantity, perhaps a combination of several channels, that is related to surface rain rate by assuming some type of hypothetical hydrometeor profile. Typically there are a few homogeneous layers and the mass contents of the hydrometeors are slaved to the surface rain rate.

Along with work on retrieval algorithms there have been other studies that have led to a deeper understanding of how microwave radiation interacts with realistic profiles of hydrometeors. Fulton and Heymsfield (1991) qualitatively compared hydrometeor information inferred from multi-parameter radar data of intense convection with brightness temperatures at 18, 37, 92, and 183 GHz. Their results suggest that even the lowest frequency (18 GHz) is significantly obscured by the large ice mass in the deep convection. Yeh et al. (1990) and Vivekanandan et al. (1990) used radiative transfer models to simulate microwave brightness temperatures of radar derived hydrometeor profiles, and compared the results with brightness temperatures observed from aircraft. Yeh et al. (1990) conclude that the different types of size distributions of ice particles and significant supercooled liquid water are needed to explain the microwave radiometer observations. The issue of the nonuniqueness of multichannel brightness temperatures in determining hydrometeor structure was investigated by (Evans, 1990), who showed that many channels are required to determine the parameters uniquely in even a very simple precipitation structure. The use of microwave radiative transfer simulations of hydrometeor profiles derived from cloud models has led to a number of useful insights. A warm cloud model that predicts droplet spectra was used for simulations of seven frequencies from 19 to 230 GHz by Mugnai and Smith (1988) and Smith and Mugnai (1988). They found that the vertical distribution of cloud water has important effects on the upwelling radiation which would confound simple precipitation retrieval schemes. Adler et al. (1991) used a three-dimensional simulation of a tropical oceanic squall line to investigate brightness temperature-rain rate relations at frequencies from 10 to 85 GHz. They showed a large scatter in the relations for 19 GHz and above due to variations in ice content and cloud liquid water, which vary systematically with the nature (convective or stratiform) of the precipitation. Mugnai et al. (1990), and more recently Smith et al. (1992) and Mugnai et al. (1993), used a bulk microphysics cloud model and radiative transfer model to simulate frequencies from 6 to 128 GHz. Their use of weighting functions allowed a detailed examination of the effects of the vertical distribution of various types of hydrometeors on the upwelling microwave radiation. They found that 19 GHz is a better estimator of integrated ice content than rain content and that most frequencies respond primarily to fluctuations in graupel mass.

These modeling studies have shown that passive microwave measurements of precipitating clouds are sensitive to the vertical distribution of various hydrometeor species and not to the surface rain rate. Since the microwave radiation is sensing the profile of hydrometeors and a number of frequencies are potentially available it would appear

to be profitable to retrieve hydrometeor profiles rather than only the surface rain rate. Profile retrieving algorithms are designed to use all the available channels rather than just the one or two that the simple models use. The vertical distribution of hydrometeors is important in its own right because it can be related to the vertical profile of latent heat release which governs the coupling to dynamical forcing (Tao et al., 1990). Profiling algorithms will work over land as well as water, although with reduced accuracy. Of course, simple physical models have their uses when speed or simplicity are the driving concern, but profiling algorithms make the best use of all the available data. The first profile retrieving method was that of Kummerow (Kummerow et al., 1989; Kummerow et al., 1991). This method used an iterative scheme that matched the observed brightness temperatures with those simulated from a relatively small number of somewhat adhoc specified profiles. This method is the furthest advanced of the profiling algorithms and has been successfully used in a variety of situations. Obviously one cannot expect to retrieve highly accurate detailed profiles from a handful of microwave channels. In fact, since there are typically multiple distinct profiles that can satisfy a small set of observations, other information about the vertical distribution of hydrometeors is needed to constrain the retrieval. Mugnai et al. (1993) have developed a profile retrieval method that uses a database of cloud model derived profiles and their corresponding simulated brightness temperatures. Profiles with brightness temperatures close to the observed ones are selected and combined using a weighted average with the weights adjusted so as to match the observations. A closely related algorithm that uses the same cloud-radiation database (Marzano et al., 1993) has been tested with the same land dataset as in the validation experiment in section 5.2. The hydrometeor profile retrieving algorithm developed here also uses cloud model information, though in a significantly different way.

## 4.2 The Bayesian Framework

The precipitation retrieval method described here uses Bayes theorem to combine forward radiative transfer modeling with statistical information from numerical cloud model output. For use here Bayes theorem may be stated as

$$f_{\Theta|X}(\vec{\theta}|\mathbf{x}) \propto f_{X|\Theta}(\mathbf{x}|\vec{\theta})\ f_{\Theta}(\vec{\theta})\ , \tag{4.1}$$

where $\vec{\theta}$ represents the atmospheric state vector (i.e. hydrometeor profile) and $\mathbf{x}$ represents the vector of observations (e.g. microwave $T_b$). $f_{\Theta}(\vec{\theta})$ is the prior probability distribution of atmospheric parameters, $f_{X|\Theta}(\mathbf{x}|\vec{\theta})$ is the conditional probability distribution of an observation given an atmospheric state, and $f_{\Theta|X}(\vec{\theta}|\mathbf{x})$ is the posterior probability distribution function of an atmospheric state given the observation. The normalization of the posterior distribution has been left out, hence the proportionality rather than equality.

The conditional distribution, which is the probability of an observation given an atmospheric state, is closely related to the forward problem, i.e. computing observables from a given atmosphere using radiative transfer. The prior distribution is the vehicle for extra information about the atmospheric state that will reduce the ill-conditioned nature of the inversion. Since a single vector (i.e. atmospheric profile) is usually desired for a retrieval the maximum or the expected value of the posterior probability distribution can be used.

There are several advantages to using Bayes theorem in a retrieval method:

1. Bayes theorem provides an elegant mathematical framework for adding prior information about precipitating systems to improve the accuracy of retrieval.

2. Different types of observational data (e.g. microwave, radar, infrared) can be incorporated easily because only the relatively well understood forward problem needs to be reformulated for each type of data.

3. Estimates of the uncertainties of the parameters, as well as the values, can potentially be computed, because the complete posterior probability density function is available.

4. If the probability distributions are formed correctly then using Bayes theorem is optimal in the sense that the most likely atmospheric state can be found.

### 4.2.1 Bayesian probability distributions

While Bayes theorem provides an overall framework there is still much to specify in the forms of the prior and conditional probability density functions (pdf's). To some extent the functional form of the pdf's must be chosen arbitrarily because of their ill-defined nature. In the Bayesian framework probability distributions do not represent the frequency of occurrence, but rather our degree of belief or understanding of a system. For example, if a weather forecaster analyzes numerical prediction output and states that the probability of rain at a particular location tomorrow is 30%, the forecaster is expressing a degree of belief about tomorrow given his or her knowledge and the current information available. One would hope that aggregated over enough similar circumstances it would rain about 30% of the time. However, the forecaster is predicting in a particular situation that will not repeat exactly, and is not talking about some experiment that can be repeated identically time after time.

Obviously, there is a tradeoff between simplicity and realism in the functional forms of the Bayesian pdf's, with the goal to capture the necessary behavior with as few parameters as possible. The conditional probability distribution is simply constructed by assuming that the observation vector ($\mathbf{x}$) is normally distributed around the simulated observation vector calculated from the forward model, $\mathbf{g}(\vec{\theta})$ (discussed in section 4.3):

$$f_{X|\Theta}(\mathbf{x}|\vec{\theta}) = N\left(\mathbf{x} - \mathbf{g}(\vec{\theta}), \vec{\sigma}\right) \ . \tag{4.2}$$

Table 4.1: Kolmogorov-Smirnov tests of lognormality on distributions of hydrometeors.

| Level (km) | Hydrometeor Parameter | Number of Points | K-S statistic | Significance |
|---|---|---|---|---|
| 0–2 | Rain Content | 2538 | 0.074 | 0.0 |
| 4–6 | Graupel Content | 3844 | 0.087 | 0.0 |

The observation uncertainties ($\sigma_m$ for each element $m$ of the observation vector) can be thought of a combination of the actual observation errors and the errors in the forward model. Independence is probably a good assumption for the observation errors but may not be so good for the forward modeling errors. The maximization of the posterior probability, by also tending to maximize the conditional probability, assures that the simulated observations are close to the actual observations. It does not, however, fit the retrieval to the noise in the observations or to the modeling error if the $\sigma$'s are chosen appropriately. The $\sigma$'s can be thought of as controlling the tradeoff between fitting more to the data vs. being closer to the prior distribution.

Use of a prior probability distribution of atmospheric parameters is the key improvement of the Bayesian retrieval algorithm over previous precipitation profile retrieval methods. The prior information about the atmosphere helps the retrieval choose the best precipitation structure of the many that satisfy the observations. For this work the prior probability distribution is assumed to be a multivariate lognormal distribution. The hydrometeor species important for microwave observations (rain, graupel, etc.) are known to have approximately lognormal distributions, as studies of radar data from GATE have shown (Kedem et al., 1990). The lognormal distribution is explicitly positive and becomes approximately normal when the mean is large compared to its standard deviation (as for temperature). Kolmogorov-Smirnov (K-S) testing was carried out to illustrate how well the lognormal distribution fits the hydrometeor parameters derived from the cloud model output used in section 5.1. The K-S test determines whether two distributions are significantly different. The K-S statistic is the maximum of the difference in cumulative probability between the two distributions. The results of the tests are presented in Table 4.1. The significance level is zero because the large number of data points makes the K-S test very precise. Thus the cloud model derived parameters don't have exactly a lognormal distribution, but the underlying distribution is fairly close to lognormal.

The multivariate aspect of the prior probability distribution is crucial because this is how information about the correlations between hydrometeors at various levels is introduced. The form of the prior distribution is

$$f_\Theta(\vec{\theta}) = \frac{1}{\sqrt{(2\pi)^n \det C}} \frac{1}{\prod_{i=1}^n \theta_i} \exp\left[-\frac{1}{2}(\mathbf{u}-\bar{\mathbf{u}})^{\mathbf{T}} \cdot C^{-1} \cdot (\mathbf{u}-\bar{\mathbf{u}})\right], \qquad (4.3)$$

where $\mathbf{u} = \ln\theta$ is the log of the precipitation parameter vector, $\bar{\mathbf{u}}$ is the first log moment of the atmospheric vector, and $C$ is the central second log moment of the atmospheric vector. The constants $\bar{\mathbf{u}}$ and $C$ are measured statistically from the numerical cloud model output (see section 4.2.3). The lognormal distribution is the maximum entropy distribution, i.e. it assumes the least amount of information, given the constraints of the first and second moments of the logarithm. This functional form is the simplest way to introduce correlations between variables. However, it cannot represent nonlinear relations between variables, bimodalities, etc. One reason to use a simple function like this, rather than a higher order function, is that a more general function having more parameters requires substantially more data for a reliable fit.

### 4.2.2 Precipitation structure

Since the Bayesian precipitation retrieval method uses a radiative transfer model to simulate observations, it is necessary to incorporate an underlying model of a precipitating atmosphere. The structure of the precipitating atmosphere may be chosen with a high degree of flexibility as to the number and heights of the layers and what parameters are variable in the layers. There is an important distinction between the total set of atmospheric parameters that are used in the forward radiative transfer calculation and the subset of those parameters that are free to be adjusted in the retrieval process.

Table 4.2 lists the atmospheric and surface parameters of the forward radiative transfer model. A layer is specified by its thickness, interface temperature, water vapor mass, and by the properties of the various hydrometeor species that may exist in the layer. The model ignores small pristine "cloud ice" particles because of their lack of effect on the lower frequency microwave radiation used here. Four hydrometeor species are available in the model: rain, a mixed-phase melting particle, and two types of ice particles. All particles are assumed to be spherical and have an exponential size distribution. Modeling the particles by spheres is justified because many precipitation size hydrometeors are roughly spherical or randomly oriented, and the errors introduced by this assumption are small compared to other sources. The two parameters specifying the exponential distribution are the mass content and the average particle diameter. The purpose of having two ice particle species is to simulate different types of particles, e.g. graupel and snow, by using two different bulk densities. For this work the coated particle type is not used, because the cloud model data available does not have a melting particle species in it. Due also to the limitations of the cloud models, the mass content is the only hydrometeor parameter that is variable in the retrieval (though the average particle size may vary with the mass content by fixing the intercept of the distribution). The priors calculation from the cloud model requires that the thickness of the layers be fixed in order to be able to compute statistics. The surface parameters are temperature and parameters for the very simple emissivity model.

Table 4.2: Total set of atmospheric and surface parameters which may be chosen to model a precipitating atmosphere.

| Atmospheric Parameters for each Layer | |
|---|---|
| Name | Description |
| HEIGHT | thickness of layer (km) |
| TEMP | temperature of top of layer (°K) |
| WATVAPOR | water vapor density ($g/m^3$) |
| CLOUDLWC | cloud liquid water content ($g/m^3$) |
| RAINCONT | rain water content ($g/m^3$) |
| RAINSIZE | average size (diameter) of rain drops (mm) |
| COATCONT | coated (melting) particle mass content ($g/m^3$) |
| COATSIZE | coated particle average size (mm) |
| COATDENS | coated particle ice core density ($g/cm^3$) |
| COATMELT | coated particle melt index |
| ICE1CONT | first ice particle mass content ($g/m^3$) |
| ICE1SIZE | first ice particle average size (mm) |
| ICE1DENS | first ice particle density ($g/cm^3$) |
| ICE2CONT | second ice particle mass content ($g/m^3$) |
| ICE2SIZE | second ice particle average size (mm) |
| ICE2DENS | second ice particle density ($g/cm^3$) |

| Surface Parameters | |
|---|---|
| Name | Description |
| HEIGHT | height (MSL) of surface (km) |
| TEMP | surface temperature |
| EMIS0 | emissivity parameter |
| EMIS1 | emissivity frequency slope parameter |

A precipitation structure is set up for a retrieval by fixing the number of layers and choosing the atmospheric and surface parameters that will be allowed to vary (the free parameters). This defines the parameters making up the atmospheric state vector. Varying all the parameters in a precipitation structure with many layers would lead to an impossibly large number of free parameters (150 for ten layers), so a judicious choice has to be made. Section 5.1 tests a number of precipitation structures to determine the best tradeoff between the convenience of a few parameters versus the more accurate representation of many parameters.

### 4.2.3 Computing prior probability distributions

Numerical cloud models are the only feasible source of the detailed information on the vertical distribution of hydrometeors that is needed to make a suitable prior distribution. Radar data, especially multiparameter data, is also a source of detailed information, but it cannot provide cloud liquid water amounts, size distribution information for ice particles, or distinguish very well between types of ice particles. Output from two different cloud models is used in this work. The theoretical testing described in section 5.1 uses fields from the Goddard Cumulus Ensemble Model, circa. 1987 (Tao and Simpson, 1989). The retrieval validation with AMPR microwave data and CP-2 radar data discussed in section 5.2 uses output from the Regional Atmospheric Model System (RAMS) (Nicholls et al., 1991). Both of these models have one parameter distributions for the precipitation species, i.e. only mixing ratio is predicted. The temperature and mass contents ($g/m^3$) for water vapor, cloud liquid water, rain, pristine cloud ice, snow or aggregate, and graupel are stored in a compressed logarithmic format for all the cloud model points for a number of simulation times. The basic state height, pressure, temperature, air density, and water vapor density profiles are also stored.

To compute statistics of the retrieval model parameters from the cloud model variables a transformation is necessary. The many vertical levels of the cloud model are mapped into the few thicker layers of the precipitation structure. For each column the mass content of the water species is averaged vertically for each retrieval model layer. The snow or aggregate category is associated with the ICE1 parameter, and the graupel with the ICE2 parameter, or the two categories may be combined into one. The bulk densities of the two ice parameters are fixed at whatever the cloud model parameterization or user specifies. The moments that determine the multivariate lognormal prior probability distribution are calculated from the cloud model derived parameter vectors by

$$\bar{u}_i = \frac{1}{N}\sum_{k=1}^{N} \ln \theta_{i,k} \tag{4.4}$$

$$C_{ij} = \left(\frac{1}{N}\sum_{k=1}^{N} \ln \theta_{i,k}\ \ln \theta_{j,k}\right) - \bar{u}_i \bar{u}_j \tag{4.5}$$

where $\theta_{i,k}$ is the $i$'th element of the parameter vector of the $k$'th cloud model point. All hydrometeor mass contents are clipped at $10^{-4}$ g/m$^3$ to prevent the zero mass points from contaminating the lognormal distribution parameter estimation too much. A vertically integrated rain mass cutoff is used to avoid non-raining pixels that do not belong to the underlying lognormal distribution. Any range of cloud model times may be selected in order to make prior distributions from different phases in the evolution of the system.

### 4.2.4 Overview of BPR system

The Bayesian precipitation retrieval method is logically divided into two parts: first, finding the prior probability distribution, and second, performing the retrieval for a set of observations. These two parts are implemented as the programs `PRIORS` and `BPR`. Figure 4.1 shows the data flow in files between the two programs and a top level view of the retrieval program `BPR`. The retrieval system is very flexible with regards to the form of the precipitation structure and in terms of the number and characteristics of the passive microwave channels. The precipitation structure file, which is used by both `PRIORS` and `BPR`, specifies the number of layers and the parameters that are variable in each layer. The values of the constant parameters and the mean and standard deviation of variable parameters may be specified, in which case these values override those derived from cloud model output. The format of the precipitation structure file is shown in Fig. 4.2. The `PRIORS` program reads in hydrometeor profiles from the cloud model database file, selects the desired times, and converts the atmospheric parameters from the cloud model form to that of the precipitation structure. First and second moments of the logarithm are calculated for the variable parameters, and means are computed for the constant parameters. These data, along with any overriding initialization and standard deviation information from the precipitation structure file, is output to the priors file.

Along with the precipitation structure and the prior probability information the retrieval program (`BPR`) needs to know the number and types of observations. This information is supplied by the observation format file (see Fig. 4.3 for an example). The basic data flow for a retrieval in `BPR` is:

1. The forward radiative transfer model computes the simulated observations from the atmospheric parameter vector.

2. The posterior probability function is calculated from a) the simulated and actual observations (the conditional probability) and b) the prior information and the state vector (the prior probability).

3. Using the posterior function the optimization routine chooses a new atmospheric parameter vector so as to maximize the posterior probability density function.

The `BPR` program can also do the forward problem of simulating observations, with added noise, from precipitation profiles derived from the cloud model output.

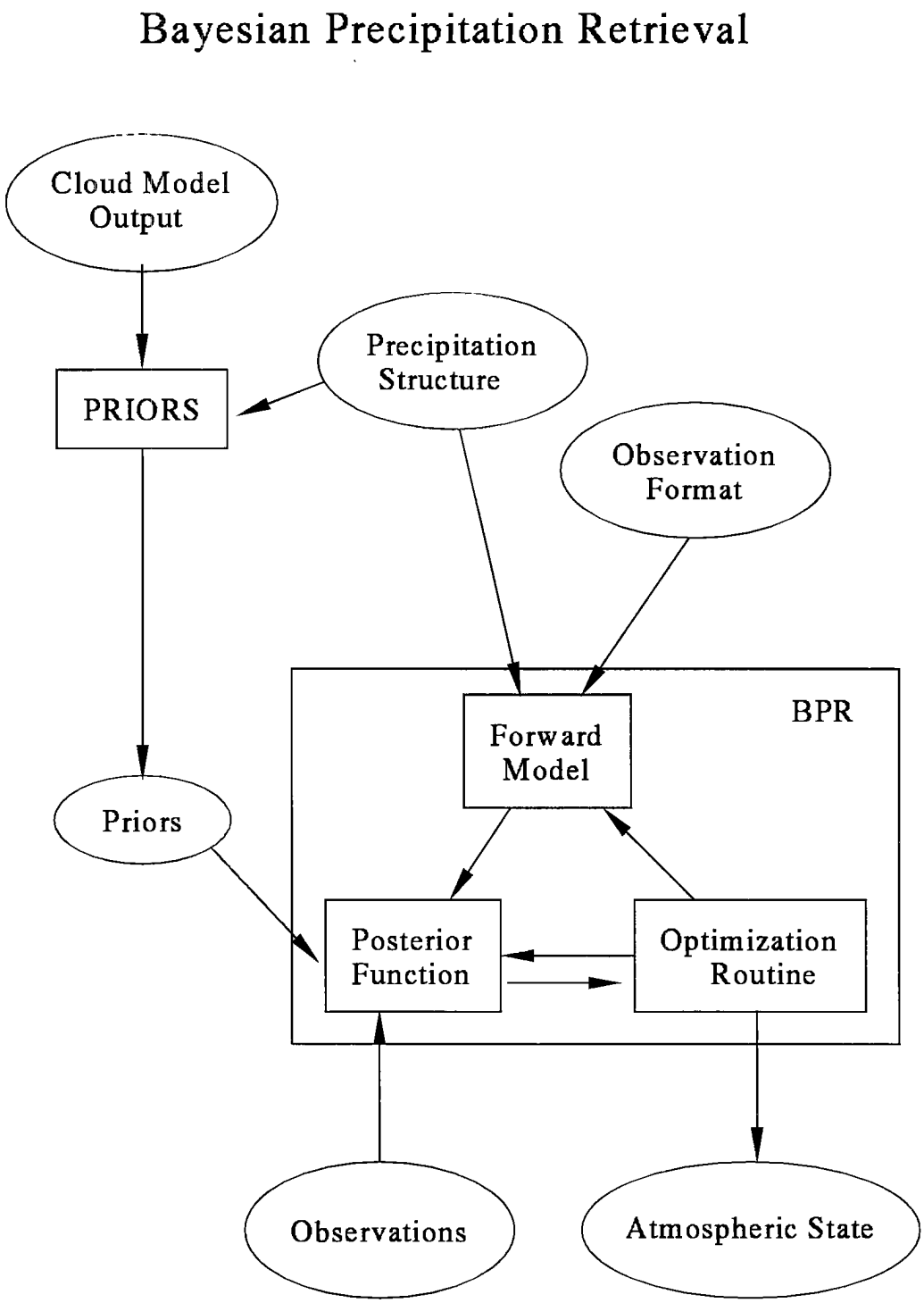


Figure 4.1: Flowchart of the Bayesian precipitation retrieval system. The ellipses represent data stored in files, while the boxes represent procedures that operate on the data.

Figure 4.2: An example precipitation structure file. There are two precipitating layers and five variable parameters. The heights of the layers and the surface temperature are specified. The mean and standard deviation of the surface emissivity are also specified. The rest of the prior information comes from the cloud model.

```
VARIABLES
  SURFACE
    EMIS0
  LAYER=1
    RAINCONT CLOUDLWC
  LAYER=2
    ICE2CONT CLOUDLWC
INITIALIZE
  SURFACE
    HEIGHT=0.0  TEMP=300  EMIS0=0.90
  LAYER=1
    HEIGHT=4.0
  LAYER=2
    HEIGHT=4.0
STDERRORS
  SURFACE
    EMIS0=0.05
```

Figure 4.3: An example observation format file. Three passive microwave channels are specified along with their corresponding properties.

```
OBS=1  TYPE=MICROWAVE  FREQ=19.35  ANGLE=53  POL=V  NOISE=2.0
OBS=2  TYPE=MICROWAVE  FREQ=37.1   ANGLE=53  POL=V  NOISE=2.0
OBS=3  TYPE=MICROWAVE  FREQ=85.5   ANGLE=53  POL=V  NOISE=2.0
```

## 4.3 The Forward Radiative Transfer Model

The forward radiative transfer model is the core of the conditional probability distribution part of the precipitation retrieval method. The forward model consists of two parts: 1) gaseous absorption and Mie scattering calculations, and 2) radiative transfer calculations to simulate the passive microwave observations.

### 4.3.1 Absorption and scattering calculations

The microwave absorption due to oxygen, water vapor, and cloud water are computed using Liebe's MPM92 model (described in section 2.2.1) and stored as coefficients before proceeding with the retrieval. For each observation frequency the gaseous absorption averaged over each layer in the precipitation structure is computed for 0% and 100% relative humidity. The saturated (RH=100%) water vapor content averaged over each layer (taking into account the lapse rate of temperature) is also stored. Later the forward model interpolates between the two extremes, computing the relative humidity as the ratio of the given layer water vapor content to the saturated content. Similarly, the cloud water absorption coefficient is computed for each frequency and layer, since it depends on the average temperature of the layer.

The computations to determine the microwave scattering properties of the exponential distributions of precipitation-sized hydrometeors are done by interpolating from tables of pre-computed Mie scattering results. An interpolation approach is necessary in view of the many forward model computations that must carried out for each retrieval. There are Mie tables for each observation frequency and particle type. For passive microwave observations the tabulated quantities are extinction, single scattering albedo, and asymmetry factor. All of the tables are two dimensional, and the scattering quantities are bilinearly interpolated. For rain the two dimensions are average size and temperature; for ice they are average size and particle density; and for coated particles they are average size and melt index. The mass content of the distribution does not appear in the tables because, for all other parameters fixed, the scattering properties simply scale with the mass content.

The Mie tables are computed using an adaptive scheme that insures that the interpolation from the tables will be within a desired tolerance. The grid for the average size parameter is chosen adaptively, while the grid for the other dimension is held fixed. For rain there are six grids for temperature (evenly spaced from -20 to 30°C), and for ice there are 15 grids for bulk density (stretched from 0.02 to .90 g/cm$^3$) and the temperature is fixed at -20°C. The grid spacing in the average size dimension is chosen with a binary search so that the maximum tolerance criterion is within the desired range (1.0 to 2.0% is used for this work). The tolerance criterion is the maximum of the percent difference in extinction and absolute difference in albedo and asymmetry between the bilinearly interpolated value at the center of each grid cell and the correct Mie calculated value. The average size table

ranges from 0.05 mm to 5.00 mm, and the number of grid cells required is typically less than 25. The index of refraction of water is computed following Ray (1972) and for ice is interpolated from the tables in Warren (1984). For ice particles with a density lower than solid ice the index of refraction is reduced according to the ice volume fraction using the Lorentz-Lorenz mixing rule. The equivalent volume sphere method of modeling low density ice particles can be accomplished simply by using a smaller average diameter with solid ice. The Mie calculations are performed by integrating over 100 evenly spaced sphere diameters up to a maximum diameter of 10 times the average size, which is far enough to assure that there is no significant contribution left out. The extinction, single scattering albedo, and asymmetry parameter are computed using well known formula (e.g., Bohren and Huffman, 1983).

If the mass content of a hydrometeor species is a variable in the precipitation structure, but the average size parameter is not, then either the average size of the exponential distribution is fixed at the value given in the priors file, or it may be related to the mass content using the Rutledge and Hobbs (1984) parameterization. This scheme fixes the intercept ($N_0$) of the exponential distribution (like Marshall-Palmer) and computes the average size parameter ($\overline{D}$) from the mass content ($M$) and the particle density ($\rho$) using

$$\overline{D} = \left( \frac{M}{\pi \rho N_0} \right)^{0.25} . \tag{4.6}$$

$N_0$ is chosen according to the hydrometeor species: 8000 $\mathrm{mm^{-1}\ m^{-3}}$ for rain and 4000 $\mathrm{mm^{-1}\ m^{-3}}$ for snow or graupel.

### 4.3.2 Eddington radiative transfer

The radiative transfer model used for simulating passive microwave measurements is an Eddington type plane-parallel two-stream model (e.g., Weinman and Davies, 1978). The two-stream model, while less accurate than a multi-stream model or a model that takes into account the true three dimensional structure, is necessary in view of the computational burden of the many forward calculations the retrieval method requires. Kummerow (1993) has carried out a comparison between the Eddington approximation and a plane-parallel multi-stream (discrete ordinate) model, showing that the differences in microwave brightness temperatures are always less than 3°K for realistic precipitating cloud profiles. The plane-parallel assumption is likely to be a more significant problem, but we leave for the future the development of parameterizations for dealing with this complicated issue. The Eddington model operates on the basic radiative properties of the layers: optical depth, single scattering albedo, asymmetry parameter, and the temperature of the interfaces. The model works by calculating the reflection, transmission, and thermal source terms for each layer from the input properties. A tri-diagonal matrix solver is then used to compute the internal diffuse radiation at each layer from the applied boundary

conditions. The diffuse Eddington fluxes incident on each layer are then used to find the scattering integral source term in the radiative transfer equation. With the known scattering and thermal source terms the radiative transfer equation can be analytically integrated. The radiation exiting at the observation angle is summed over the layers, first from the top down to the surface, then reflected, and summed from the bottom to the top of the atmosphere. The calculations are done in double precision to avoid numerical instabilities in the solution method. The Rayleigh-Jeans approximation is assumed so the transfer calculations are done in terms of brightness temperatures. See Appendix B for the mathematical development of the radiative transfer model.

When modeling low density (snow or aggregate) ice particles at 85 GHz, large errors were found in the Eddington approximation. The reason for these errors is the large degree of forward scattering (or high asymmetry parameter) as computed by Mie theory with the Lorentz-Lorenz mixing rule for the index of refraction. Fig. 4.4 shows the asymmetry parameter at 85.5 GHz for a range of ice sphere densities and exponential distribution mean diameters. The asymmetry parameter is greater than 0.85 for low densities ($\rho \leq 0.1$ g/cm$^3$) for mean diameters greater than 1.00 mm. For near nadir angles the Eddington approximation gives poor results for asymmetry parameter greater than around 0.6. The Eddington comparison in Kummerow (1993) only considered Marshall-Palmer distributions of solid ice, and thus did not have this problem. The standard method for dealing with high asymmetry parameters is to use the delta-Eddington method (Joseph et al., 1976). This modification represents the highly peaked phase function by a delta function of height $f$ and the normal Eddington phase function with a lower asymmetry parameter. The result is the same as the Eddington method but with rescaled extinction $k$, single scattering albedo $\omega$, and asymmetry parameter $g$:

$$k' = (1 - \omega f)k \quad \omega' = \frac{1-f}{1-\omega f}\omega \quad g' = \frac{g-f}{1-f} \quad f = \chi_2/5 \; . \tag{4.7}$$

The scaling factor $f$ is obtained from the second Legendre coefficient of the phase function ($\chi_2$) ($g = \chi_1/3$). This scaling can be done when making the Mie scattering tables thereby allowing the use of the Eddington model in unmodified form (the scaling is equivalent before or after the scattering properties for different particle species are combined). To illustrate the original problem and the improvement of using delta-Eddington a calculation of the difference between the Eddington and the spherical harmonic spatial grid method (see section 5.1.2) for an ice layer with an optical depth of 2 is shown in Fig. 4.5. For the plain Eddington approximation the nadir brightness temperature differences are as large as 40°K for the largest, low density distributions. With the delta-Eddington method the differences are in the range of 0 to −3°K.

The boundary conditions for the radiative transfer model are the 2.7°K blackbody cosmic background radiation from above and surface emission and reflection from below.

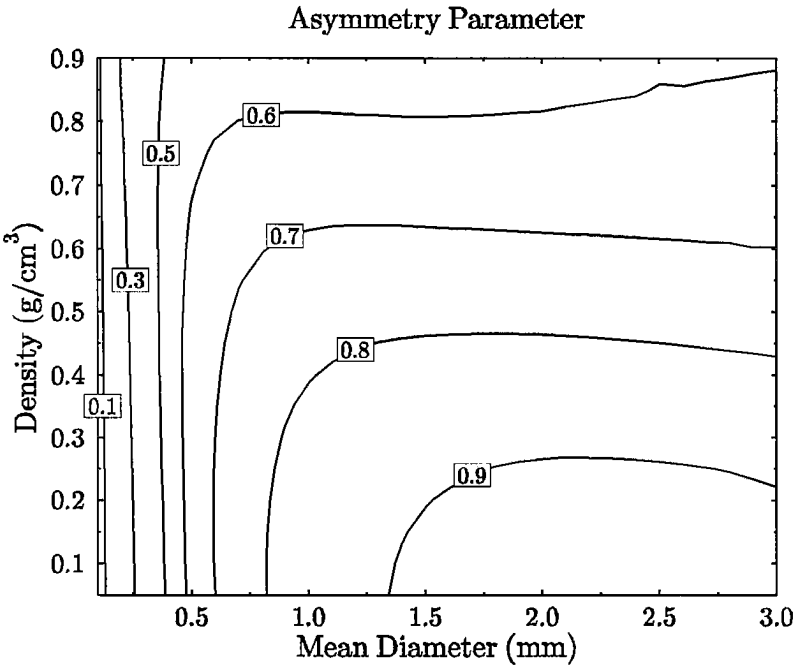


Figure 4.4: Asymmetry parameter computed from Mie theory for 85.5 GHz as a function of ice particle density and mean diameter of an exponential distribution. The maximum diameter in the distribution is 10 times the mean.

The surface type is assumed to be known as either land or water. The land surface is modeled as a Lambertian reflector with emissivity a linear function of frequency. The water surface is modeled as a flat Fresnel reflector whose index of refraction depends on frequency and the climatological temperature. The first emissivity parameter in this case then acts as a multiplier on the emissivity. The Eddington model needs a diffuse emissivity for the flux calculation and an emissivity for the particular observation angle. The only source of polarization in this radiative transfer model is from a water surface, in which case the surface emissivity depends on the polarization. For simulating observations from the AMPR instrument, which mixes the polarizations as it scans, the final brightness temperature is a linear combination of V and H polarizations according to the observation angle: $T_{AMPR} = T_V \sin^2(\theta - 45°) + T_H \cos^2(\theta - 45°)$ .

## 4.4 Retrieval of Hydrometeor Profiles

From the prior probability distribution and the forward model it is simple to compute the posterior distribution from eq. 4.1 for any given atmospheric state vector. The difficulty is finding the atmospheric state that represents the best retrieved profile from the high-dimensional posterior function. For retrieving a profile from a single multichannel pixel, finding the maximum of the posterior probability density function seems desirable because that would in some sense be the most likely profile. There can be problems with the actual task of finding the maximum (the optimization procedure) because there may

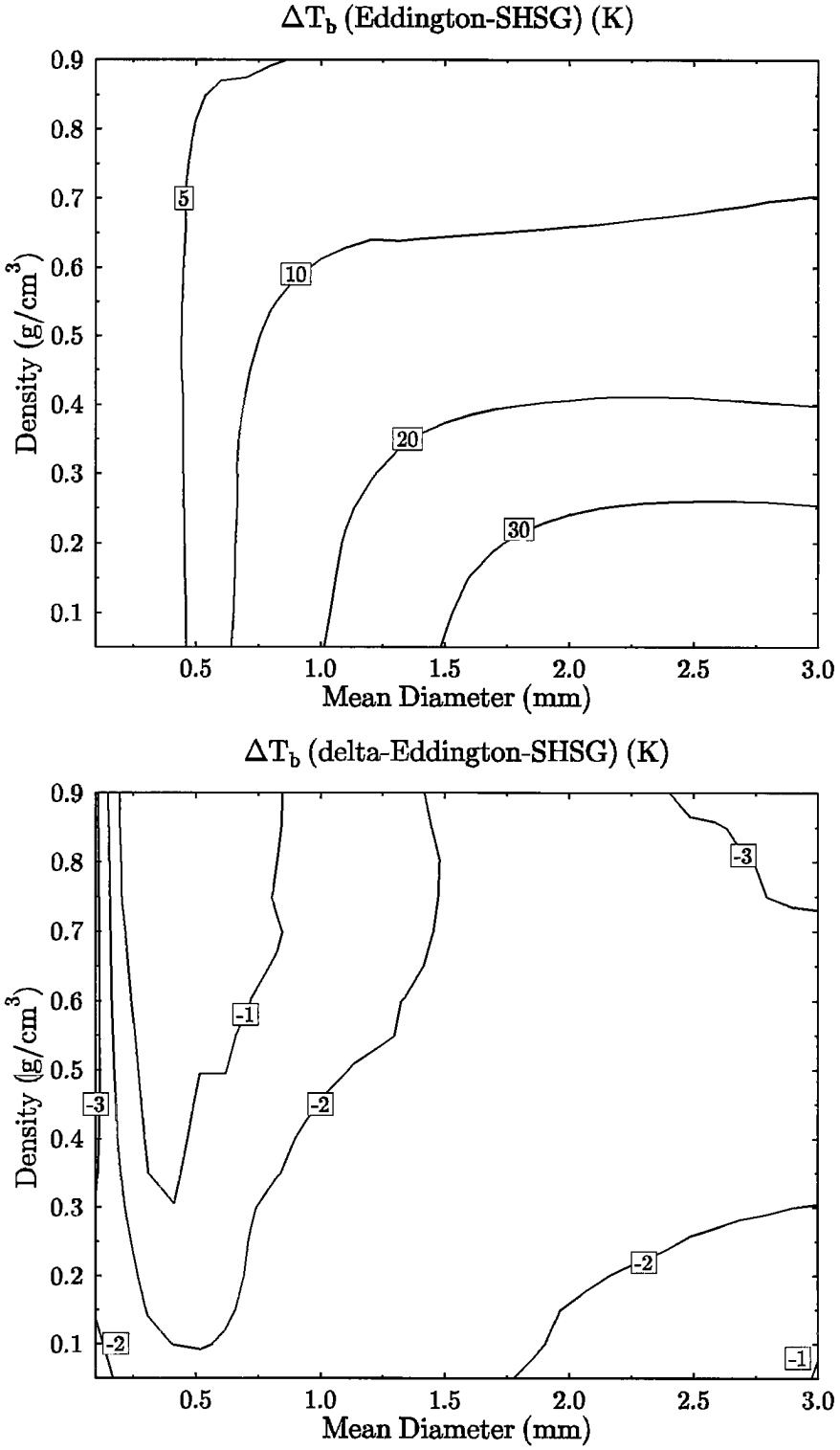


Figure 4.5: Difference in nadir brightness temperature between the Eddington approximation and spherical harmonic ($L = 11$) radiative transfer methods. There is a single homogeneous ice layer of optical depth 2 at 85.5 GHz with temperature from 270 to 245°K above a blackbody at 270°K. The top panel is for the unscaled Eddington, and the bottom panel is for the scaled delta-Eddington.

be many local maxima that trap the optimization algorithm. Another approach is to use Monte Carlo integration over the posterior distribution to find some sort of average profile. This is the correct method for finding the mean or distribution of precipitation over a region.

### 4.4.1 Monte Carlo integration method

One way of picking a representative point out of the posterior distribution is by integration to find averages or other types of moments. The only way to perform numerical integrations over such a high dimensional space (up to 30 variable parameters in the precipitation structure) is by Monte Carlo integration. This method approximates the integral by summing over the function evaluated at random points. The integration method is not used in this work because single pixel retrievals are desired and the simulated observations from retrievals using the Monte Carlo method can be quite far from the actual observations. The Monte Carlo integration method is presented to show how the Bayesian retrieval should be done for computing area averages.

The $l$'th ($l = 1, 2$) arithmetic moment of the posterior distribution is

$$\overline{(\vec{\theta})^l} = \frac{\int f_{X|\Theta}(\mathbf{x}|\vec{\theta})\ f_{\Theta}(\vec{\theta})\ (\vec{\theta})^l\ d\vec{\theta}}{\int f_{X|\Theta}(\mathbf{x}|\vec{\theta})\ f_{\Theta}(\vec{\theta})\ d\vec{\theta}} \quad , \tag{4.8}$$

where the integral is carried out separately for each component of the atmospheric state vector $\vec{\theta}$. The logarithmic moments $\overline{(\ln\vec{\theta})^l}$ are defined similarly with $(\ln\vec{\theta})^l$ replacing $(\vec{\theta})^l$. The integrals are done by sampling the atmospheric parameter space with a large number of random points. Because the prior probability distribution does not change over a set of retrievals and is a simple function it can be absorbed into the sampling of the points, i.e. the random points are chosen according to the multivariate lognormal prior distribution. This involves making an independent multivariate normal distribution of appropriate size, rotating it to produce the correct correlations between parameters, and then exponentiating to make a lognormal distribution. The procedure for a $n$ dimensional $\vec{\theta}$ is as follows:

1. Make the random vector $\vec{\phi}$, where $0 < \phi_i < 1$.

2. Transform to a normal distribution: $\psi_i = \sqrt{2/\lambda_i}\mathrm{erfc}^{-1}(2 - 2\phi_i)$ ,
   where $\lambda_i$ are the eigenvalues of the inverse of the log covariance matrix $C$. The inverse of the complementary error function is done with a cubic spline look up table.

3. Rotate and translate: $\mathbf{u} = A\vec{\psi} + \bar{u}$ ,
   where $A$ is the eigenvector matrix of $C^{-1}$ and $\bar{u}$ is the log mean.

4. Exponentiate: $\theta_j = \exp(u_j)$

The "random" points are chosen from the quasi-random Halton sequence that covers space more uniformly (see O'Brien, 1992) and is more accurate than pseudorandom points for Monte Carlo integrations.

With the transformed random points ($\theta_j$) the integrals are approximated by

$$\overline{(\ln\vec{\theta})^l} = \frac{\sum_{j=1}^{N} f_{X|\Theta}(\mathbf{x}|\vec{\theta})\ (\ln\vec{\theta})^l}{\sum_{j=1}^{N} f_{X|\Theta}(\mathbf{x}|\vec{\theta})}\ , \tag{4.9}$$

where $N$ points are used to sample the integral. The normalization on the conditional probability distribution divides out so that the conditional function is

$$f_{X|\Theta}(\mathbf{x}|\vec{\theta}) = \exp\left[\sum_{m=1}^{N_{obs}} \frac{\left(x_m - g_m(\vec{\theta})\right)^2}{2\sigma_m^2}\right]\ , \tag{4.10}$$

where $\mathbf{x}$ is the vector of $N_{obs}$ observations, $\sigma$ is the assumed uncertainties, and $\mathbf{g}(\vec{\theta})$ is the forward radiative transfer model. The number of integration nodes $N$ needed depends on how smooth the conditional density function is, which is governed by the $\sigma_m$'s. Thus the Monte Carlo approximation to the integral is more accurate when there are fewer channels or more uncertainty in the forward modeling. Much computer time is saved by processing the set of observation pixels in parallel. For each of the random points in the integration the forward radiative transfer model is evaluated once for each observation channel, and then used in eq. 4.9 for all the observation pixels. Since the computation of the forward model takes most of the time, the computer time for retrieval is then independent of the number of observation vectors.

If one is trying to estimate the parameters of an assumed lognormal distribution of precipitation over an area from a set of observations, then the Monte Carlo integration should use the log moments, because the log mean and log variance are the maximum likelihood estimators for a lognormal distribution. The arithmetic precipitation average is then the expectation of the lognormal distribution, or

$$\overline{\theta} = \exp\left[\overline{\ln\theta} + \overline{(\ln\theta)^2}/2\right]\ . \tag{4.11}$$

One advantage of using this procedure, rather than simple averaging of pixel-by-pixel retrievals, is that the average is not biased by missing the rare large rain events. The arithmetic moments can be used for single pixel retrievals. The mean of the posterior distribution is the Bayesian estimate for a squared error loss function; the Bayesian estimate being the value that minimizes the expectation value of the loss function (Larson, 1982). The arithmetic variance can then be used to provide an uncertainty estimate. In tests done with simulated data (similar to those in sec. 5.1) the domain average precipitation was much more accurately retrieved using the log moments as compared to the arithmetic moments. The precipitation retrievals in this work use the maximum probability density method, rather than the Monte Carlo method, because single pixel retrievals are done.

### 4.4.2 Maximum probability density method

There is an appeal in finding the maximum of the posterior probability distribution because then the retrieval is the "most likely" atmospheric state. There is, however, some arbitrariness in "maximizing probability". The probability of any continuous distribution at a single point is, of course, zero; only ranges have nonzero probabilities. Furthermore, the maximum of a probability density function depends upon what space the density function is expressed in. This can be seen by dividing the density function up into discrete bins; which bin has the maximum probability then depends on how the bins are spaced. For example, consider a one-dimensional lognormal distribution

$$f(\theta) = \frac{1}{\sqrt{(2\pi)\sigma^2}} \frac{1}{\theta} \exp\left[\frac{-(\ln\theta - \bar{u})}{2\sigma^2}\right] , \tag{4.12}$$

with $\bar{u}$ the first log moment and $\sigma^2$ the central second log moment. The maximum of the density function in regular space is at $\exp(\bar{u} - \sigma^2)$ while in log space the distribution is normal and the maximum is at $\bar{u}$. So the question is what type of ranges are appropriate? Is a range of 1 mm/hr appropriate for values of rain rate from 0.1 to 100 mm/hr? Here we use logarithmically spaced ranges, which seems natural when using lognormal distributions.

Since the posterior probability function varies over large range it is convenient to define an objective function $J$ to be minimized, which (to within a constant) is the negative of the log of the posterior function. The objection function is then

$$J = (\mathbf{u} - \bar{\mathbf{u}})^{\mathrm{T}} \cdot C^{-1} \cdot (\mathbf{u} - \bar{\mathbf{u}}) \quad + \sum_{m=1}^{N_{obs}} \frac{\left(x_m - g_m(\vec{\theta})\right)^2}{\sigma_m^2} . \tag{4.13}$$

A large penalty function is added for negative parameter values to keep things positive.

A somewhat complex algorithm is used to minimize the objective function in an attempt to deal with the problem of multiple local minima. The prior distribution is a completely smooth and relatively broad function. In the usual case of many more variable parameters than observations the forward distribution function has a sharp valley that is presumably zero in a large subspace, i.e. there are many precipitation profiles that exactly satisfy the observations. The purpose of the prior distribution is to lift this degeneracy so there will be one lowest point. There can be (and are) local minima that trap traditional optimization techniques. A newer optimization method that can deal with local minima, called simulated annealing, was tried and found to be too slow. Since the objective function is basically smooth, a modification of traditional optimization algorithms was found to be effective.

The idea behind the algorithm is to start off a standard optimization routine from a number of places that are likely to be close to the desired global minimum. This is done by

precomputing the forward radiative transfer model for a large set of precipitation profiles. For each observation vector those profiles that match the observations to within a certain distance are selected. These are sorted by the value of the prior probability function and several of the highest prior profiles are used to initialize Powell's method of optimization. By selecting those profiles that are close to matching the observations and have a high prior probability, the optimization routine is able to get quite close to the global minimum.

The initial $n$-dimensional random points, representing the trial profiles, are chosen according to the lognormal prior distribution in a manner similar to that used in sec. 4.4.1. A higher log mean ($\bar{u}' = \bar{u} + \sigma^2/2$) is used because there is no point in simulating many low precipitation cases that end up having equivalent brightness temperatures. By using a pseudo-random sequence that generates a random vector from an index, only the simulated observations need to be stored; the precipitation parameters for those points that match the observations are recreated later from the index. Typically, the number of initial points and simulated observations made is $10^6$. For each actual observation those points with simulated observations within a specified normalized distance,

$$S = \left( \sum_{m=1}^{N_{obs}} \frac{\left(x_m - g_m(\vec{\theta})\right)^2}{\sigma_m^2} \right)^{1/2} , \tag{4.14}$$

are selected. A sequential search is currently used to find the matches, although a more intelligent look up table method could be developed. If less than the desired number of observation matching points is found then the acceptable distance is increased until some are found. A maximum of 10000 matching points is found and then sorted to find the highest prior probability function.

Of the atmospheric state vectors that are close to the observation a specified number (the number of tries) of the ones with the highest prior probability densities are used to initialize Powell's direction set optimization method. This method (see Acton, 1990) performs a minimization using only the objective function values, i.e. it does not need derivative information. Starting with an orthogonal set of $n$ directions it finds the minimum along successive directions and constructs a new direction to replace one in the set. Iterating this procedure produces a set of directions that are mutually conjugate. For a quadratic objective function $n(n+1)$ line minimizations are required to exactly minimize the function. Each line minimization using Brent's method takes around 10 function calls. Because the set of directions can become linearly dependent, the Powell method is restarted a number of times if this significantly lowers the objective function. The purpose of doing a number of tries of the minimization is to attempt to make sure that the resulting lowest function value is close to the true global minimum. Some of the optimizations may get trapped in higher local minima, but hopefully several will get to the global minimum. If a specified number of minimizations get the same function value

then the tries can be discontinued to save time. A test to see whether the results of the number of optimizations are significantly different is described in sec. 5.1. This testing indicates that this method overcomes the problem of multiple local minima. All this multiple optimization does mean that the retrieval algorithm takes an excessive amount of computer time. The tests of different precipitation structure, for example, took between $10^4$ and $10^5$ objective function evaluations. Little attempt has been made to speed up the optimization, and it is possible that better optimization methods could be developed in the future.

Besides retrieving the atmospheric profile, the posterior distribution may also be used to compute uncertainties in the retrieved parameters. There are a number of methods that could be used to obtain the uncertainties, depending on the definition of the error bars. Probably the most correct definition of the uncertainty comes from the marginal posterior distribution, i.e. the one dimensional function that remains after integrating over all the other parameters. The simplest method for computing this type of marginal error bar is to use the Monte Carlo integration method to find the second moment for each variable. If the maximum probability density function method is used, one may define a parameter uncertainty in which the other variables are held fixed at their retrieved values. This is like looking at the posterior density function along a line rather than integrating over the other dimensions. By sampling the density function on this line an appropriate error bar could be derived (e.g., 90% certainty that the parameter is in a particular range given that the other parameters are fixed). If there is significant correlation between the parameters making up the precipitation structure profile, then this method would give smaller uncertainties than the more correct profile. Because of the difficulties in interpreting the uncertainties with this method, error bars are not computed for the single pixel retrievals done in this work.

# Chapter 5

# TESTING OF BAYESIAN PRECIPITATION RETRIEVAL

## 5.1 Theoretical Simulation Tests

The Bayesian precipitation retrieval method is a very flexible and complex system with choices to be made on the precipitation structure, the width of the forward probability distribution, and how the prior probability distribution is made. To determine the effect of these various choices a number of theoretical tests are performed that investigate the response to a number of different configurations. Upwelling brightness temperatures are simulated from cloud model derived hydrometeor fields using a radiative transfer model more accurate than the one built into the retrieval method. The advantage of theoretical tests is that one may control the simulation and retrieval processes to look into particular issues and that the "true" hydrometeor profiles are known. The following tests are done:

1. Precipitation structure test
   Use of different number of layers and variable parameters.

2. Observation width test
   Use of various widths of forward probability distributions.

3. Microphysical assumption test
   Use of different microphysical assumptions in retrieval.

4. Priors content test
   Use of various prior information, e.g. from different stages of storm development.

5. Frequency combination test
   Investigate different combinations of frequencies.

### 5.1.1 Cloud modeling

The cloud model output used for the theoretical tests is from a simulation by Tao and Simpson (1989) using the Goddard Cumulus Ensemble (GCE) model. The output is from a two dimensional simulation of a tropical squall line. The atmospheric environment used to initialize the cloud model was a composite of three squall-type storms observed during the GATE experiment over the tropical Atlantic in 1974. The 2D model domain is perpendicular to the convective line, which travels through the domain. The model

has 34 levels in the vertical (Z) in a stretched coordinate system that has approximately 200 m spacing at the ground and 1000 m spacing at the highest level, which is near 20 km. There are 512 grid cells in the horizontal coordinate (X) with 1000 m spacing, and a periodic boundary condition is used. The cloud simulation was run for 15 hours, and the temperature, water vapor, and hydrometeor fields were provided for each grid cell at one hour intervals.

The microphysical parameterization scheme of the model is of great importance for computing microwave brightness temperatures from cloud model hydrometeor fields. In this simulation the GCE model used the microphysical scheme described in Rutledge and Hobbs (1984). There are two categories of liquid water (cloud water and rain) and three categories of ice phase (cloud ice, snow, and graupel). The cloud water and cloud ice are modeled as monodisperse distributions of small particles (less than 20 micron diameter). For simulating the microwave observation only the mass content of the cloud droplets particles is relevant. The pristine ice crystals are not used for these simulations because of their small extinction at the relatively large wavelengths considered here. The precipitation sized hydrometeors are modeled in the parameterization by exponential distributions of spheres:

$$N(D) = N_0 \exp\left(-D/\overline{D}\right) \tag{5.1}$$

where $N(D)$ is the number concentration per size interval and $D$ is the particle diameter. The cloud model fixes the intercept parameter ($N_0$) and allows the average size parameter ($\overline{D}$) to vary. Thus each microphysical species is specified by a single parameter, the mixing ratio $q$. In this study the mass content of the particles is used in place of the mixing ratio: $M = \rho q$, where $\rho$ is the density of air. The relationship between the mass content and the average size of the distribution is

$$\overline{D_p} = \left(\frac{M_p}{\pi \rho_p N_{0p}}\right)^{0.25} , \tag{5.2}$$

where the subscript $p$ indicates the particle species, and $\rho_p$ is the particle bulk density. Table 5.1 lists the values of $N_0$ and $\rho$ for rain, snow, and graupel.

Table 5.1: Constant parameters for precipitating particles in the GCE model.

| Particle | $N_0$ ($\mathrm{mm^{-1}/m^3}$) | $\rho$ ($\mathrm{g/cm^3}$) |
|---|---|---|
| rain | 8000 | 1.00 |
| snow | 4000 | 0.10 |
| graupel | 4000 | 0.40 |

The evolution of the simulated squall line is shown in Fig. 5.1. Each plot shows the total precipitating hydrometeors (rain, snow, and graupel) for the full 2D model domain. The precipitating mass content is displayed at two hour intervals from two to twelve hours

simulation time. The convection is initiated by a 12 km warm bubble at the center of the model space, which becomes the main convective line propagating leftward. A time dependent large-scale vertical ascent is also imposed on the model. Four hours into the simulation the system is still mainly convective and has a large core of high precipitating mass content. By six hours a large stratiform region has developed and another convective line has been established. As the storm evolves further, first the convective region and then the stratiform region begin to dissipate. Three regions from two different model times are used in the theoretical tests. Area "A" from 201 to 250 km at 120 minutes is chosen as an example of the intensification stage with predominantly warm rain processes occurring. Area "B" (51 to 200 km) and area "C" (331 to 430 km) are from the mature stage at 480 minutes. The latter two areas have strong convective cores and extensive stratiform regions, although area "B" is more evolved. Figure 5.2 shows the cloud water, rain, snow, and graupel fields for the three areas combined together. It is the combination of these different microphysical fields that determines the particular signature of the synthetic upwelling brightness temperatures.

### 5.1.2 Forward radiative transfer modeling

The microwave radiative transfer simulations are carried out for 10.7, 19.4, 37.0, and 85.5 GHz at an observation angle of 53°. First the absorption and hydrometeor scattering calculations are carried out for each cloud model grid point. The microwave absorption from oxygen, water vapor, and cloud water is computed using Liebe's MPM92 model (see section 2.2.1). The absorption coefficients are precomputed for each vertical level and scaled appropriately. The rain, snow, and graupel particles are modeled as spheres with the size distributions computed from the mass contents using eq. 5.2. Mie calculations are integrated over 100 sizes of the exponential distribution up to 10 times the average diameter $\bar{D}$. A fine-grained two-dimensional look up table in $\bar{D}$ and temperature speeds up the computation. The extinction, single scattering albedo, and the full phase function information in the form of a Legendre series are output.

Upwelling brightness temperatures are computed from the scattering properties using the spherical harmonic spatial grid (SHSG) model (Evans, 1993). This model computes two-dimensional radiative transfer, although here it is used in the "independent pixel" mode, which means separate plane-parallel calculations on the cloud model columns. Thus the issues of multidimensional radiative transfer and beam filling are not addressed in these theoretical tests. The SHSG method expresses the angular distribution of radiation as a spherical harmonic series. For these forward simulations an $L = 7, M = 0$ truncation is used, meaning there are 8 zenith angle modes and azimuthal symmetry is assumed. The spatial aspect of the radiation field is represented with a uniform grid with resolution varying from 0.5 to 0.1 km from 10.7 to 85.5 GHz. The Rayleigh-Jeans approximation is assumed so the calculations are carried out in terms of brightness temperatures. The

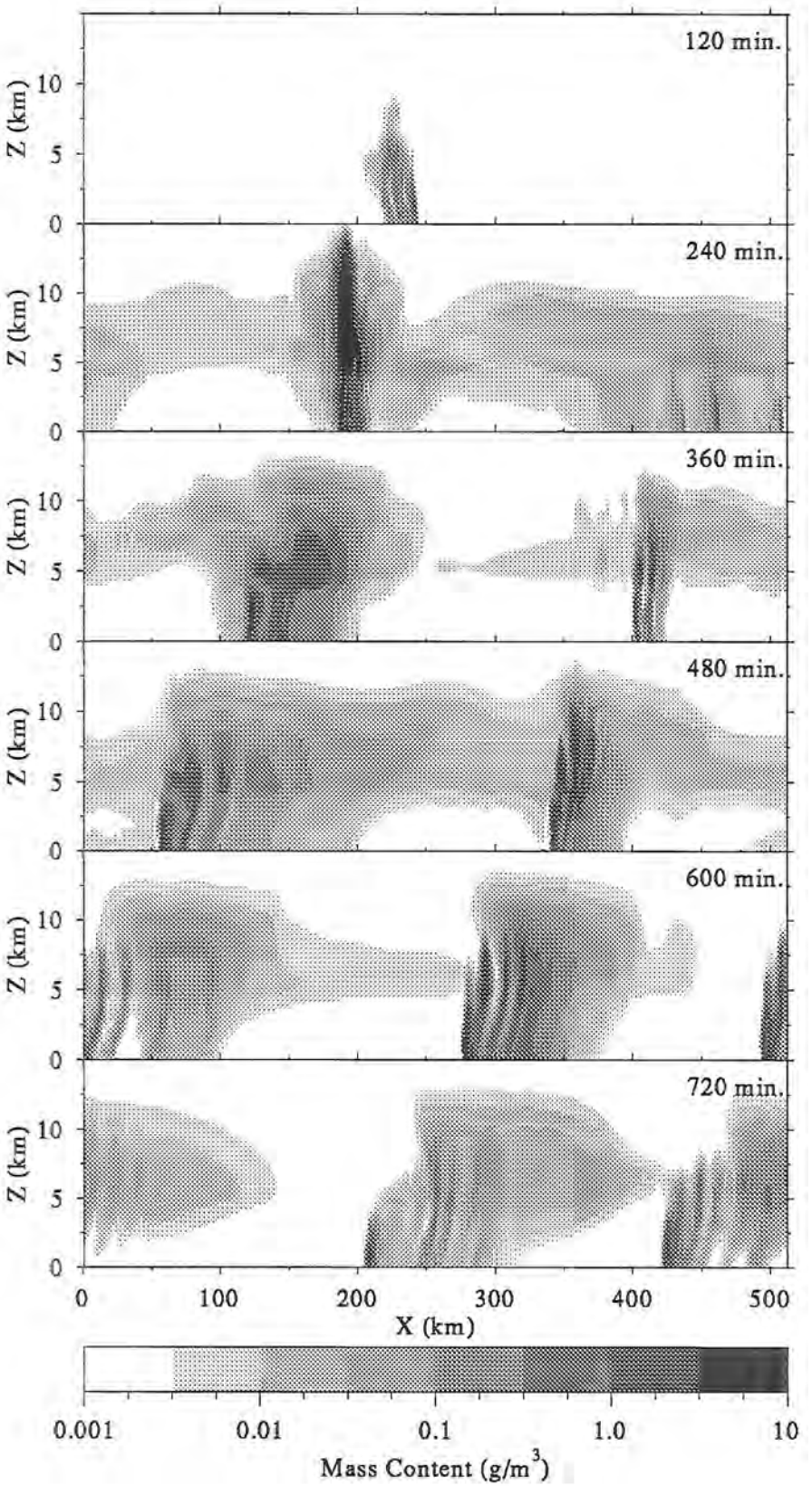


Figure 5.1: Total precipitating hydrometeor (snow, graupel, rain) mass content for six model times from the tropical squall line simulation (Tao and Simpson, 1989). The mass content is displayed logarithmically from $10^{-3}$ to 10 g/m$^3$.

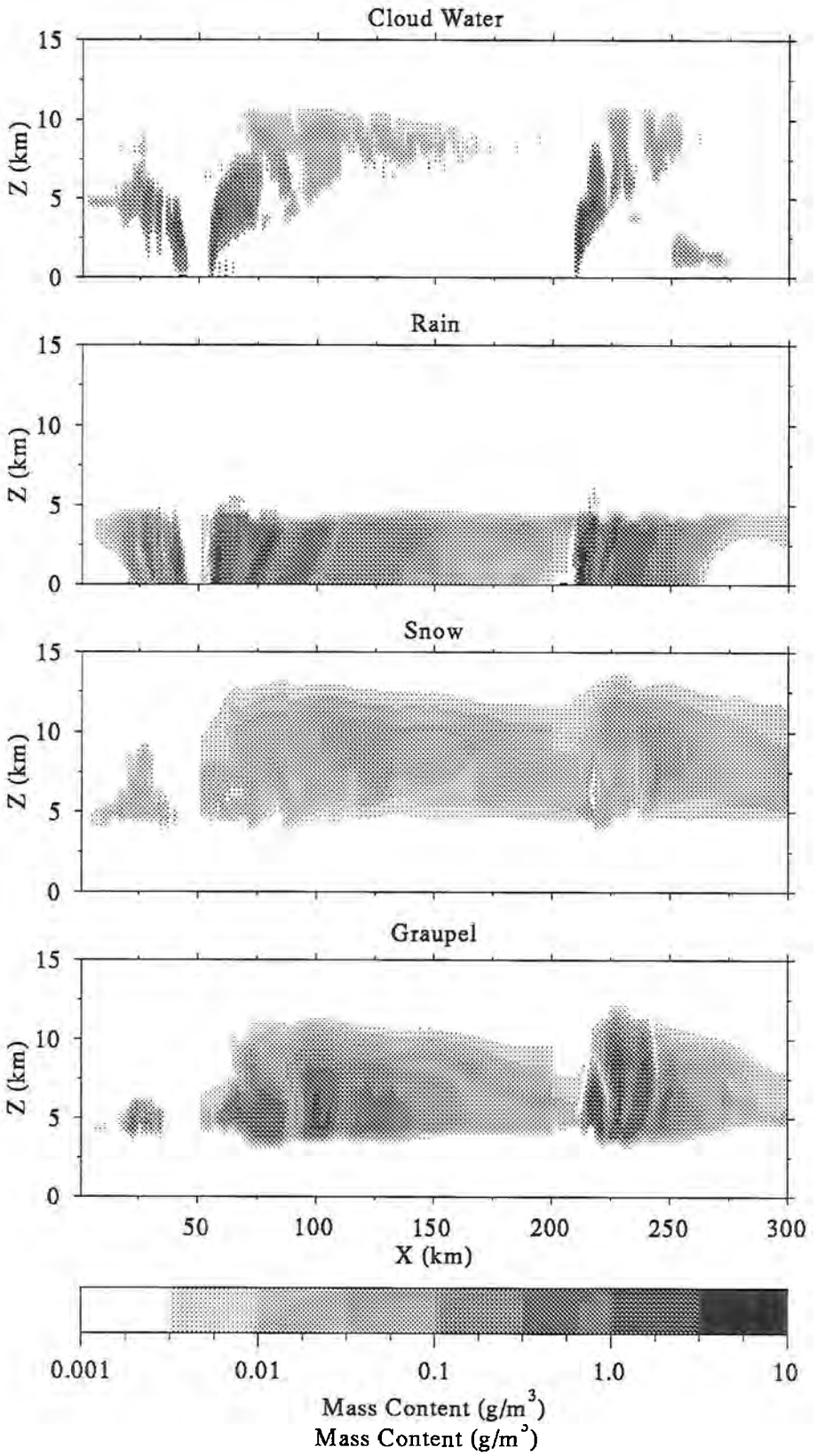


Figure 5.2: Mass contents for cloud, rain, snow, and graupel fields for the three test areas combined horizontally. The mass content is displayed logarithmically from $10^{-3}$ to 10 g/m$^3$.

boundary conditions are the 2.7°K cosmic background radiation and either a land surface (Lambertian) with an emissivity of 0.9 or a flat water surface (Fresnel) at a temperature of 299°K. The SHSG system is solved iteratively to find the spherical harmonic terms at each grid point. The upwelling radiance is then computed by integrating the source function in a method similar to the Eddington model used for the precipitation retrieval method (the two radiative transfer models are basically equivalent for a $L = 1, M = 0$ truncation). For a water surface the radiances are integrated separately for vertical and horizontal polarization, the surface being the only source of polarization. The microwave brightness temperatures at the four frequencies are assembled and 1°K rms gaussian noise is added to make the synthetic observations.

Figure 5.3 shows the computed upwelling brightness temperatures at 10.7, 19.4, 37.0, and 85.5 GHz for land and water surfaces. The correlation between the mass content of graupel in Fig. 5.2 and the brightness temperature depressions at 37.0 and 85.5 GHz can be seen clearly. In area A (the first 50 pixels) the 85 GHz brightness temperature does not fall below 250°K because of the low concentration of ice. Over water the brightness temperature at 10 GHz follows the rain mass closely. The validity of the synthetic brightness temperatures are limited by the plane-parallel and microphysical assumptions, but nonetheless they offer a realistic dataset to use for the tests described in the following sections.

### 5.1.3 Setup for theoretical tests

The theoretical tests are performed by having a base retrieval situation and changing one particular aspect of the retrieval input parameters for each type of test. The basic precipitation structure is the structure 5 in the precipitation structure test described below, which is the simplest one that gives good retrieval results. It has 5 layers (not equally spaced) up to 10 km. The 11 variable parameters represent the rain mass content below 5 km, graupel content above 4 km, and cloud water content at all levels. The temperature and water vapor content are fixed at their climatological values from the cloud model, and no snow is allowed. In all of the tests the emissivity and surface temperature are fixed at the correct values. All four frequencies (10.7, 19.4, 37.0, and 85.5 GHz, H-polarization) are used and the forward probability distribution width ($\sigma_m$) is set to 3°K for each channel. The prior probability distribution parameters are computed from all 15 cloud model times, using a integrated rain cutoff of 0.04 kg/m$^2$ (about 1 mm/hr) giving 2410 sample cloud model profiles. The optimization process is run with $10^6$ initial points, selecting those within a normalized distance of 2.0; a maximum of 15 (and minimum of 8) of those points with the highest prior probability density are used to start off the Powell optimization routine.

The basic results of these tests are rms differences in hydrometeor mass contents between the retrieved profiles and the original cloud model. The comparison is done in terms

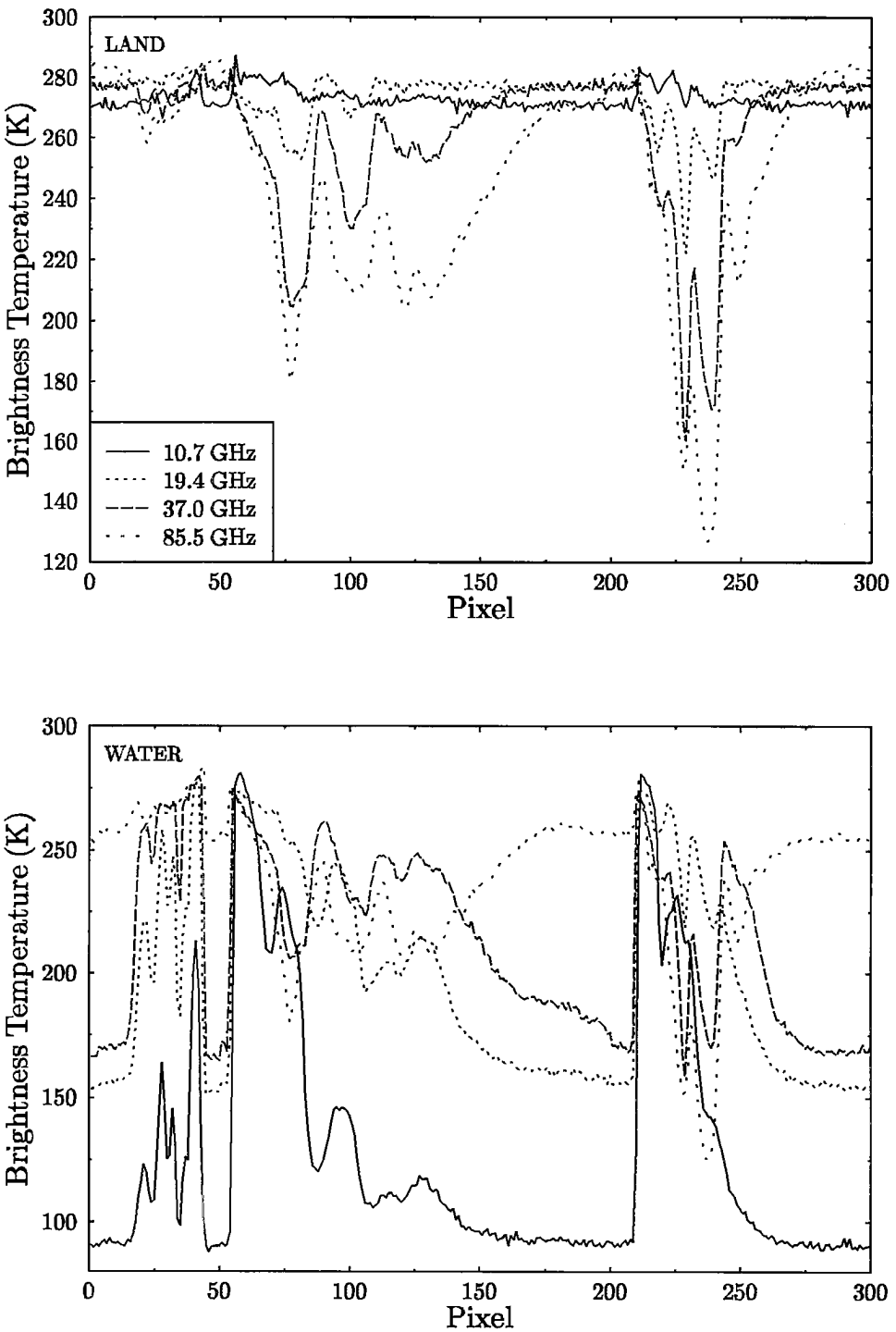


Figure 5.3: Synthetic brightness temperatures for the theoretical tests. The top panel is for a land surface (emissivity of 0.9), while the bottom panel is for horizontal polarization from a flat water surface.

of the retrieval precipitation structure (i.e. truth is the average cloud model mass content for a retrieval layer), so the true value of surface rain mass or integrated hydrometeor depends on the structure. The rms differences are broken down by area (A,B,C), and are computed both in an absolute sense (arithmetic) and fractionally (logarithmic). Because of the wide range in rain rates the logarithmic comparison is useful, though obviously one does not care about the difference between mass contents of $10^{-3}$ g/m$^3$ and $10^{-4}$ g/m$^4$. The true values are also compared to fixed climatological (prior) values which are the mean of the cloud model samples. The hydrometeor quantities used for the comparison are surface rain mass content and integrated rain, ice, and cloud content.

Before discussing the series of tests the issue of optimization with multiple local minima is considered. For this the base situation is used with differing number of optimization tries. The successive optimizations often do not get to exactly the same point, but do arrive quite close. To quantify this the hydrometeor quantities for each retrieval are compared to the one with 32 tries. Table 5.2 shows the absolute rms difference for 1, 2, 4, 8, and 16 numbers of tries. The large difference in rain retrieval for the 1 try case for water is caused by a bad retrieval for the heaviest raining pixel in the C area. The rms differences become very small with just a few tries, typically being 0.01 kg/m$^2$ while the domain average of the integrated hydrometeors is of the order of 1 kg/m$^2$. There continue to be small differences for different number of optimization tries because the prior distribution is fairly broad so that small variations in profiles can have the same posterior probability density. This test does not prove that the global minimum is being reached consistently, but it does give some evidence that multiple local minima are not causing undue problems for the retrieval method.

Table 5.2: Absolute rms differences between different number of optimization tries.

| Number of tries | Surface Rain (g/m$^3$) | | Integrated Rain (kg/m$^2$) | | Integrated Ice (kg/m$^2$) | | Integrated Cloud (kg/m$^2$) | |
|---|---|---|---|---|---|---|---|---|
| | Water | Land | Water | Land | Water | Land | Water | Land |
| 1 | 0.2163 | 0.0125 | 0.7535 | 0.0312 | 0.0491 | 0.0306 | 0.0550 | 0.0592 |
| 2 | 0.0045 | 0.0036 | 0.0035 | 0.0136 | 0.0352 | 0.0404 | 0.0146 | 0.0075 |
| 4 | 0.0038 | 0.0035 | 0.0030 | 0.0120 | 0.0342 | 0.0292 | 0.0125 | 0.0056 |
| 8 | 0.0032 | 0.0019 | 0.0019 | 0.0070 | 0.0189 | 0.0226 | 0.0102 | 0.0049 |
| 16 | 0.0025 | 0.0016 | 0.0017 | 0.0053 | 0.0110 | 0.0130 | 0.0106 | 0.0029 |

### 5.1.4 Precipitation structure testing

The purpose of the precipitation structure test is to determine how the accuracy of the retrieval depends on the number of layers and complexity of the hydrometeor representation. Tables 5.3 and 5.4 give the layer and variable setup for the 10 structures. The simplest is a two layer ice-above-rain structure, while the most complex structure has

variable rain, snow, graupel, cloud water, water vapor, and temperature. The retrieval of lowest layer rain mass content and integrated ice for structure 5 over a water surface is shown in Fig. 5.4. The retrieval for rain is quite good because this is for a water surface. The ice is measured well because the size distribution and particle density of graupel are known, though there are the complicating effects of cloud water and snow. The retrieved surface rain (actually a 2 km thick layer) has a horizontal offset in the stratiform region (75 to 125 km) probably due to the slanted cells, which does not appear in the integrated rain mass. The retrieved integrated rain for the heaviest pixels is low by roughly 30% because of saturation at 10 GHz and the prior distribution pulling the value toward the average.

Table 5.3: Layer locations in precipitation structure tests.

| Precip. Structure | Number of Layers | Layer Height Ranges (km) |
|---|---|---|
| 1 | 2 | 0-4, 4-8 |
| 2 | 2 | 0-4, 4-8 |
| 3 | 3 | 0-4, 4-5, 5-8 |
| 4 | 5 | 0-2, 2-4, 4-5, 5-7, 7-10 |
| 5 | 5 | 0-2, 2-4, 4-5, 5-7, 7-10 |
| 6 | 5 | 0-2, 2-4, 4-5, 5-7, 7-10 |
| 7 | 7 | 0-2, 2-4, 4-5, 5-6, 6-8, 8-10, 10-12 |
| 8 | 7 | 0-2, 2-4, 4-5, 5-6, 6-8, 8-10, 10-12 |
| 9 | 11 | 0-1, 1-2, 2-3, 3-4, 4-5, 5-6, 6-7, 7-8, 8-9, 9-10, 10-12 |
| 10 | 6 | 0-2, 2-4, 4-5, 5-7, 7-9, 9-11 |

Table 5.4: Variable parameters in precipitation structure tests. The number of layers and variables is listed for each structure. The range in km that each hydrometeor is variable is given (N means none, C means climatological value).

| Precip. | | | Height Range that Parameter is Variable | | | | | |
|---|---|---|---|---|---|---|---|---|
| Structure | $N_{lay}$ | $N_{var}$ | Rain | Snow | Graupel | Cloud | Vapor | Temp |
| 1 | 2 | 2 | 0-4 | N | 4-8 | N | C | C |
| 2 | 2 | 4 | 0-4 | N | 4-8 | 0-8 | C | C |
| 3 | 3 | 7 | 0-5 | N | 4-8 | 0-8 | C | C |
| 4 | 5 | 6 | 0-5 | N | 4-10 | N | C | C |
| 5 | 5 | 11 | 0-5 | N | 4-10 | 0-10 | C | C |
| 6 | 5 | 14 | 0-5 | 4-10 | 4-10 | 0-10 | C | C |
| 7 | 7 | 14 | 0-5 | N | 4-12 | 0-10 | C | C |
| 8 | 7 | 18 | 0-5 | 4-12 | 4-12 | 0-10 | C | C |
| 9 | 11 | 22 | 0-5 | N | 4-12 | 0-10 | C | C |
| 10 | 6 | 27 | 0-5 | 4-11 | 4-11 | 0-11 | 0-7 | 0-11 |

The accuracy of the retrieval for different precipitation structures is shown for the various hydrometeor species in Figs. 5.5 through 5.9. Fig. 5.5 shows the error in surface rain mass for land and water retrievals as compared to the error of assuming climatology from the prior. As expected the error in rain retrieval is much worse over land than water,

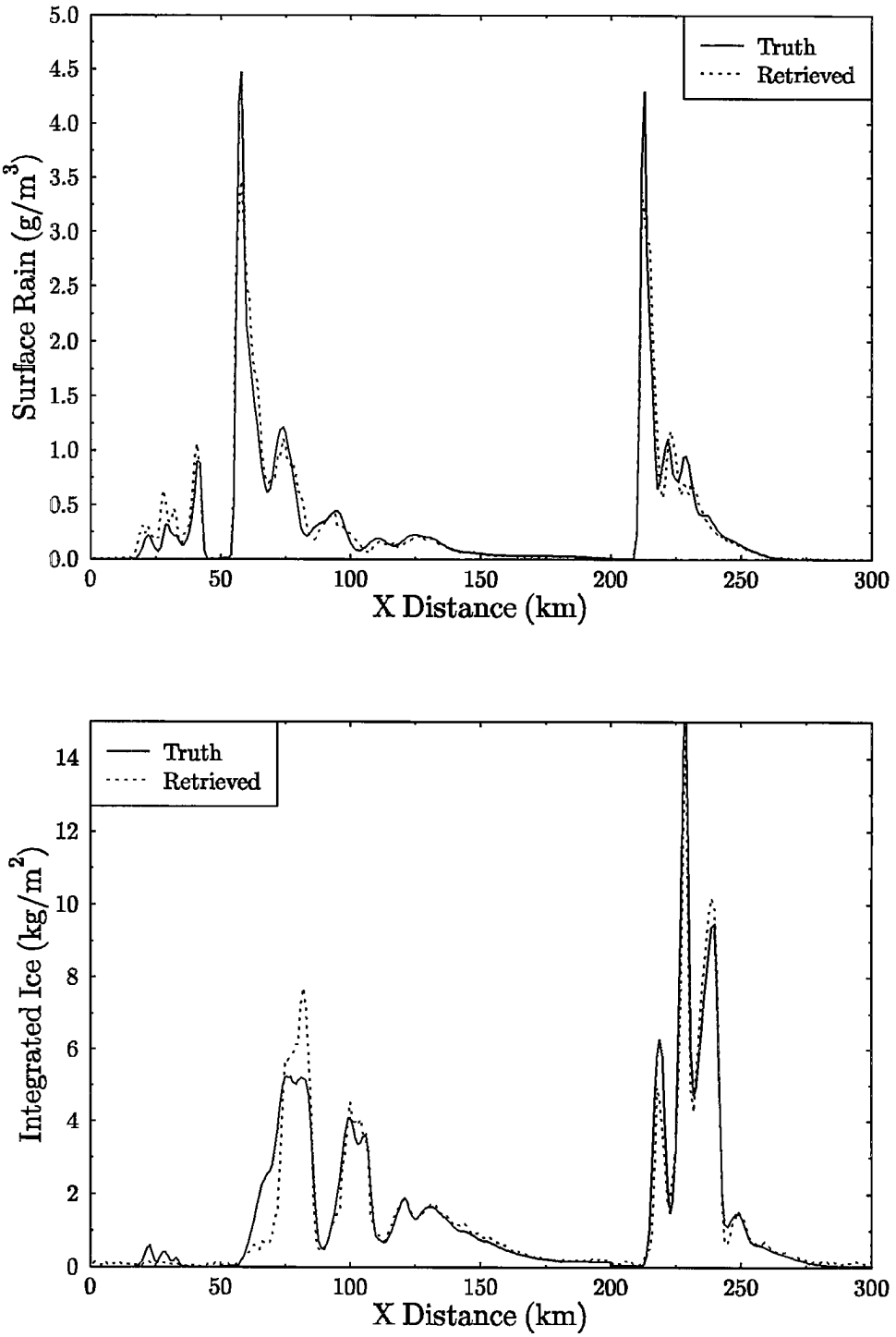


Figure 5.4: Retrieved and true surface rain mass content (top) and integrated ice content (bottom) for precipitation structure 5 over a water surface.

except for area A which has small amounts of ice. The error over land is much worse for those structures that have no cloud water (1 and 4). The surface rain retrieval is poorer for structure 9 because it has a 1 km thick lowest layer which has more variability than the 4 km layers for structures 1–3 or the 2 km layers for the other structures. The integrated rain results are shown in Figs. 5.6 and 5.7 for arithmetic and logarithmic comparisons respectively. The error is basically the same for structures 5 and above for both land and water. The retrieved rms error is a smaller fraction of the climatology error when measured logarithmically. This measure of retrieval skill is appropriate for the lognormal prior distribution. Area A has a higher log rms error because the retrieved integrated rain does not go to zero for non-raining pixels.

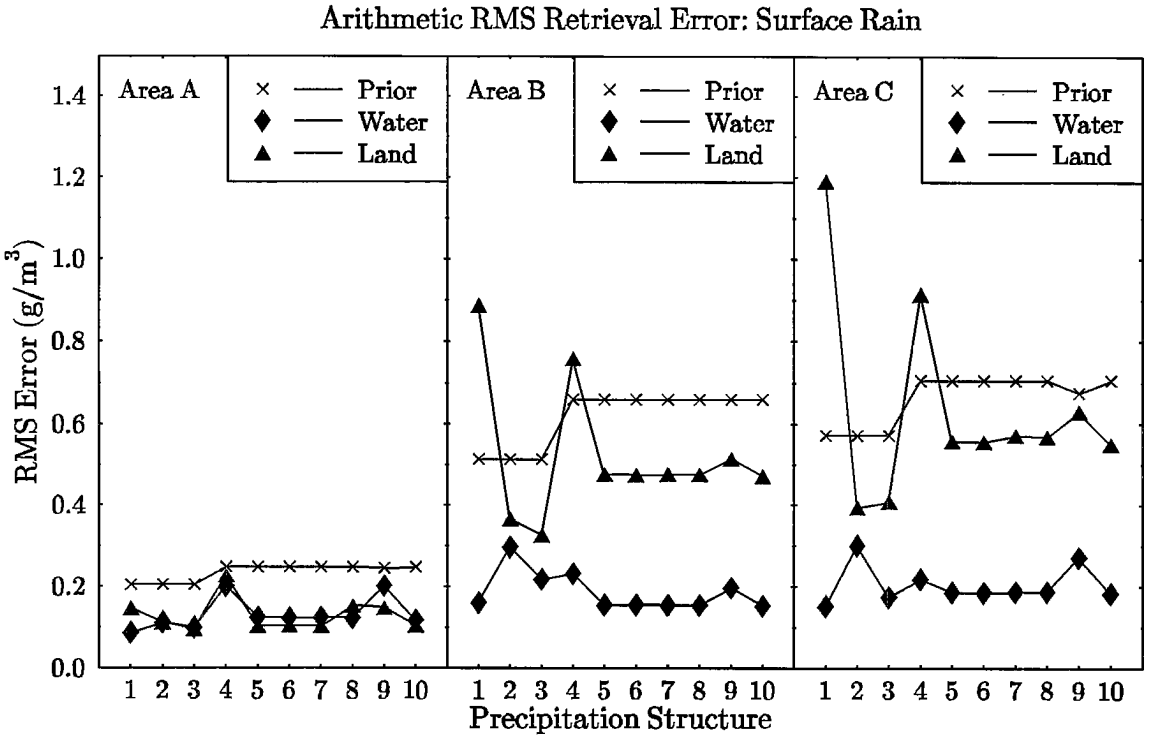


Figure 5.5: Arithmetic RMS retrieval error of surface rain mass content for the 10 precipitation structures for each of the three test areas. The retrieval error over water and land is compared with the error of assuming a fixed climatological value from the prior information.

The retrieval of integrated ice (see Fig. 5.8) is significantly more accurate for structures that include cloud water. Again, structures 5 and above are similar in the error for integrated ice. The error is very low for area A because there is very little ice there. The prior error varies because the maximum height varies with structure and snow is included only for some structures. The logarithmic retrieval error for integrated cloud water is shown in Fig. 5.9. The fractional error for cloud water is much larger than for rain or ice, though the retrieval is considerably better than using fixed (from prior) cloud

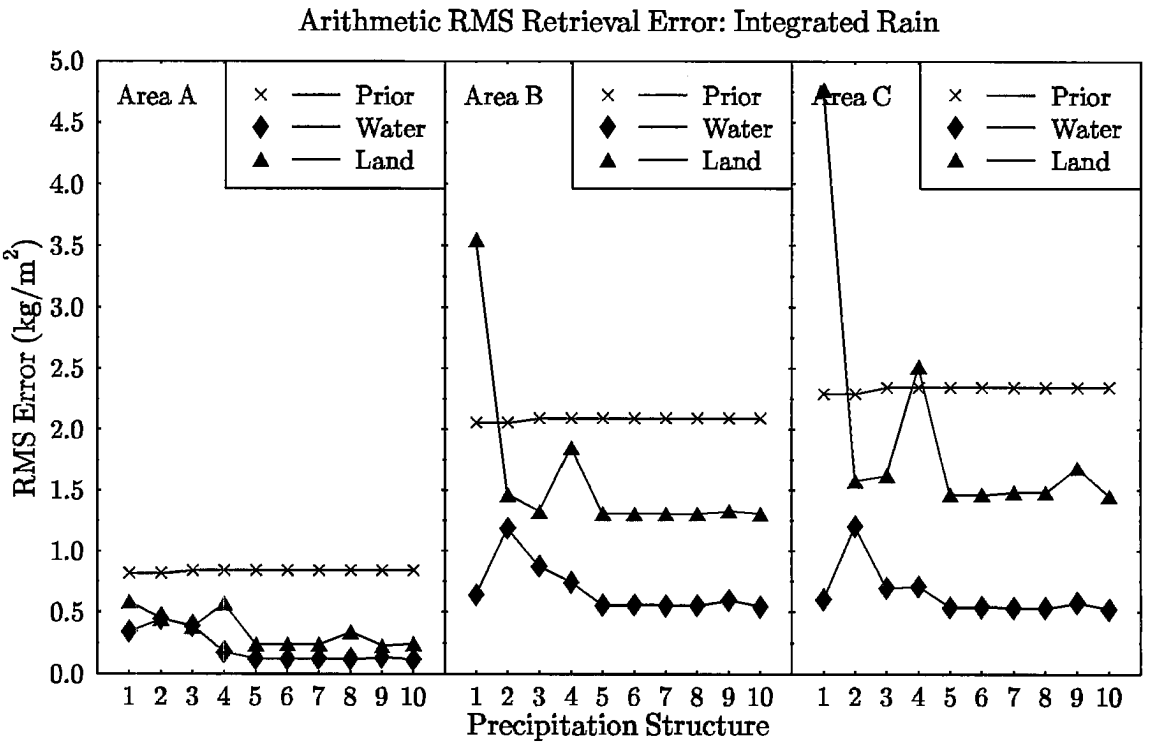


Figure 5.6: Arithmetic RMS retrieval error of integrated rain mass content for the 10 precipitation structures for each of the three test areas.

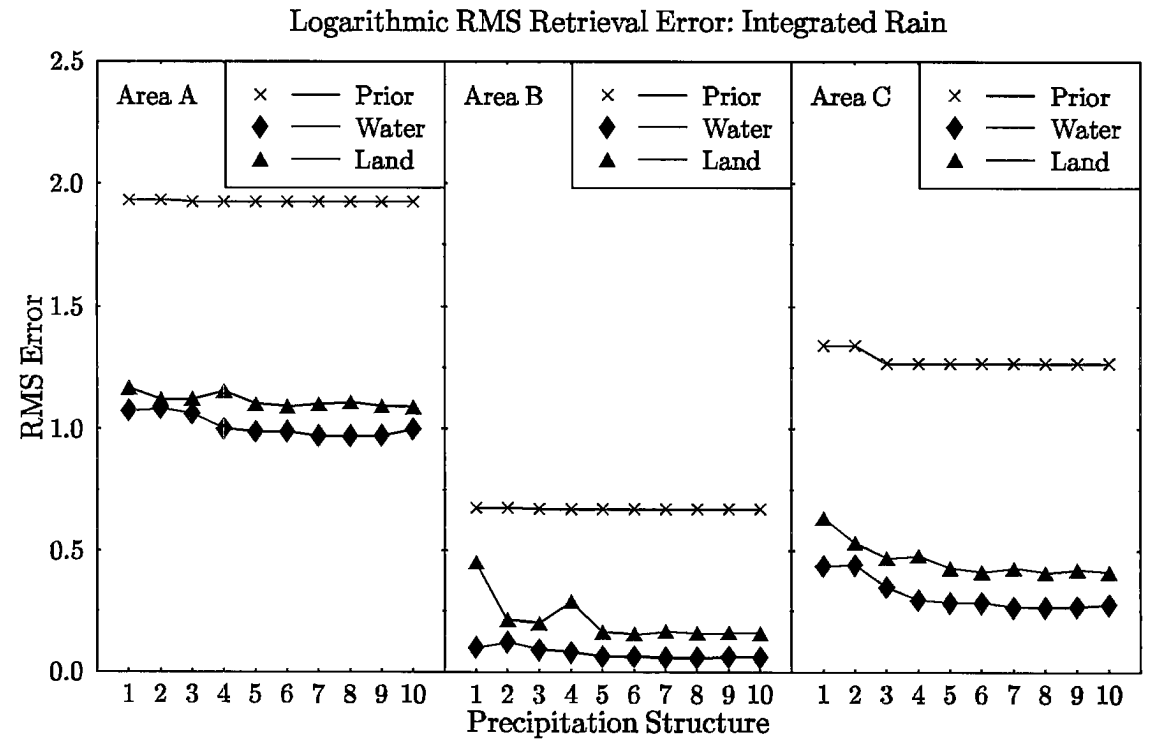


Figure 5.7: Logarithmic (base 10) RMS retrieval error of integrated rain mass content for the 10 precipitation structures for each of the three test areas.

water amount. When significant amounts of ice are present (areas B and C) the retrieval error over land and water is equivalent. There is little improvement with more complex structures. In the presence of precipitation it is very difficult to accurately retrieve cloud water with microwave radiometry.

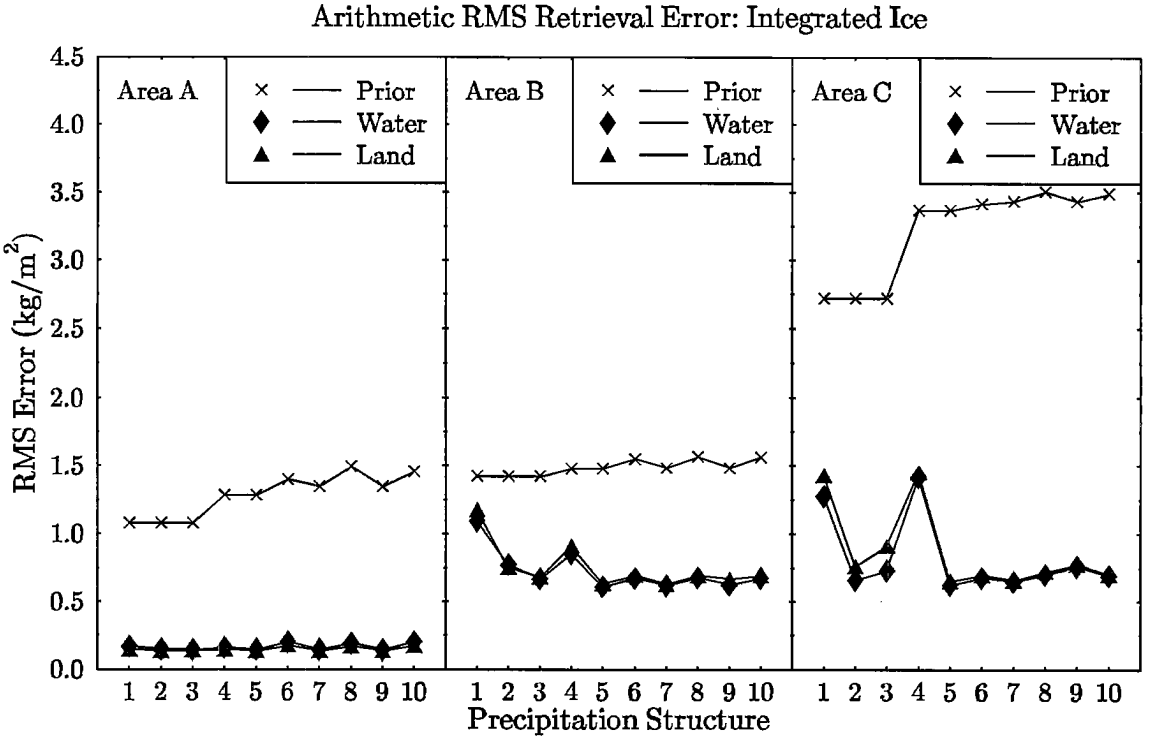


Figure 5.8: Arithmetic RMS retrieval error of integrated ice mass content for the 10 precipitation structures for each of the three test areas.

The domain averaged integrated rain mass is shown for the different precipitation structures in Fig. 5.10. Most structures retrieve the average integrated rain accurately over a water surface. The average rain is somewhat too high in area A over water because the retrieved average cloud water is too low. Over land the retrieved average rain is generally closer to the climatology. The structures 5 and above are equivalent in the retrieved average rain. Structure 9 is somewhat closer to truth for average integrated rain over land, although worse in terms of rms error.

Since the Bayesian precipitation retrieval method does not require the modeled observations to be the same as the actual observations, it is useful to compare the two. Table 5.5 shows the rms and maximum difference over the four channels for the 10 precipitation structures. Structure 1 with only two variables cannot match the observations very well, and structure 4 without cloud water is relatively poor as well. The differences for structures 5 and above is constant at 1.2°K for the rms and around 8°K for the maximum. It should be noted that the rms difference is less than the 3°K standard deviation in the forward probability distribution.

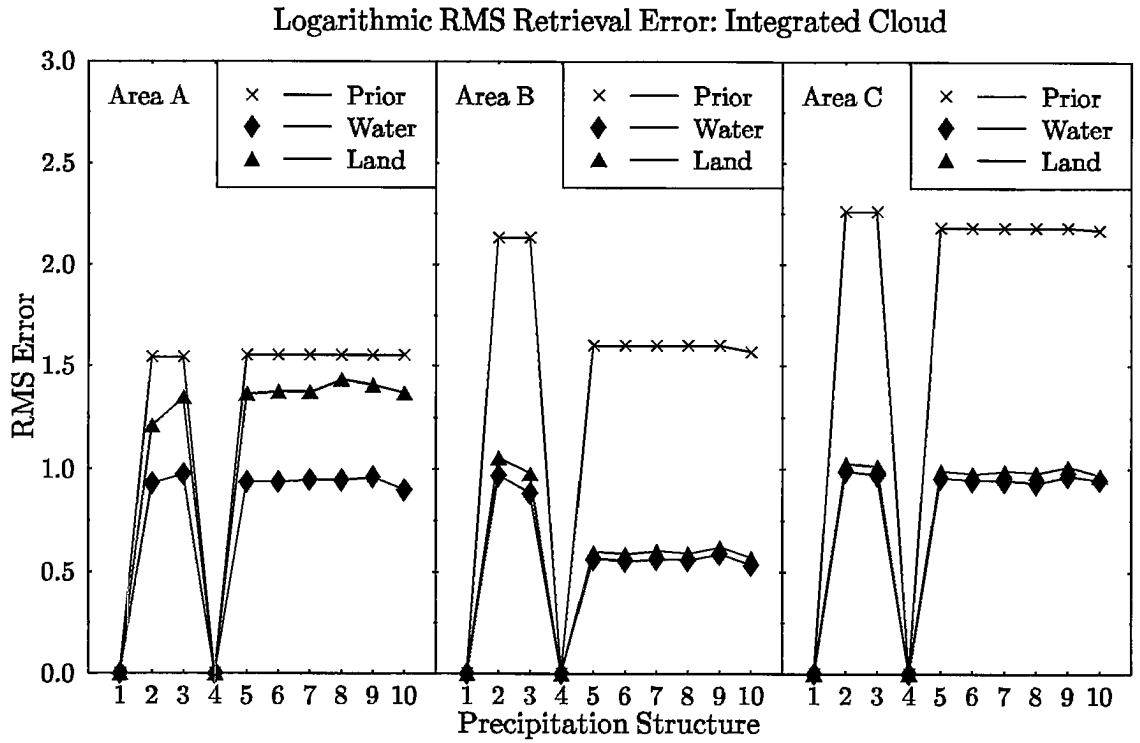


Figure 5.9: Arithmetic RMS retrieval error of integrated cloud mass content for the 10 precipitation structures for each of the three test areas.

An example of the vertical structure of the retrieval is shown in Fig. 5.11. The true and retrieved rain and graupel fields are shown for precipitation structure 9 over water. Along with retrieving the horizontal variations accurately the method also does fairly well at obtaining the vertical structure of the hydrometeors. Presumably much of the information on the vertical profile comes from the cloud model (prior) data, since just four channels cannot provide details about vertical variations. Obviously, a retrieval with real data would not perform this well.

The results of the precipitation structure testing show that there is little to be gained from using structures more complex than the five layer structure 5 with rain, ice, and cloud water. Simpler two or three layer structures do not appear to work as well. Comparison of structures 4 and 5 indicate that including cloud water is important. Including snow is not really necessary here, perhaps because of its small mass content and density compared with graupel. The finer resolution of structure 9 seems to be slightly detrimental to the Bayesian retrieval method. The extra variables (water vapor and temperature) of structure 10 neither help nor hurt, but it does take much longer to optimize with that many variables. These conclusions give some indication of what precipitation structures to use for Bayesian precipitation retrieval, but cannot be generalized automatically to all other situations.

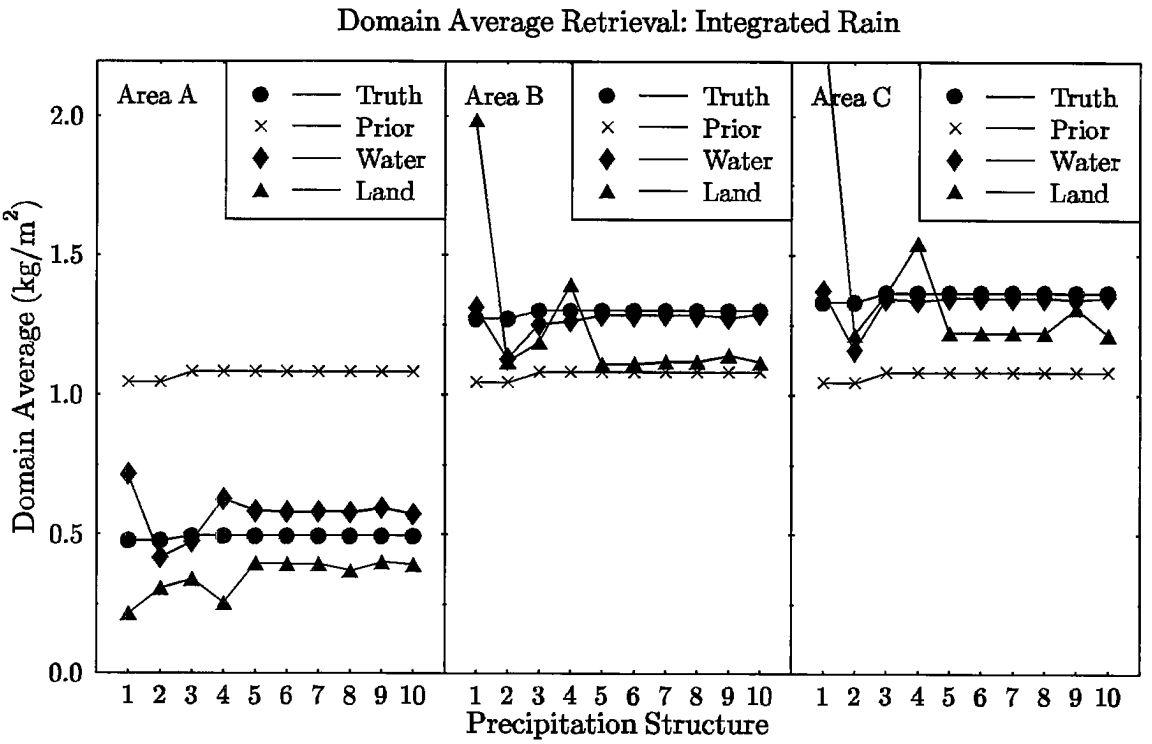


Figure 5.10: Domain average integrated rain for 10 precipitation structures. The average for the cloud model truth, the prior mean (climatology), and retrievals over water and land are shown.

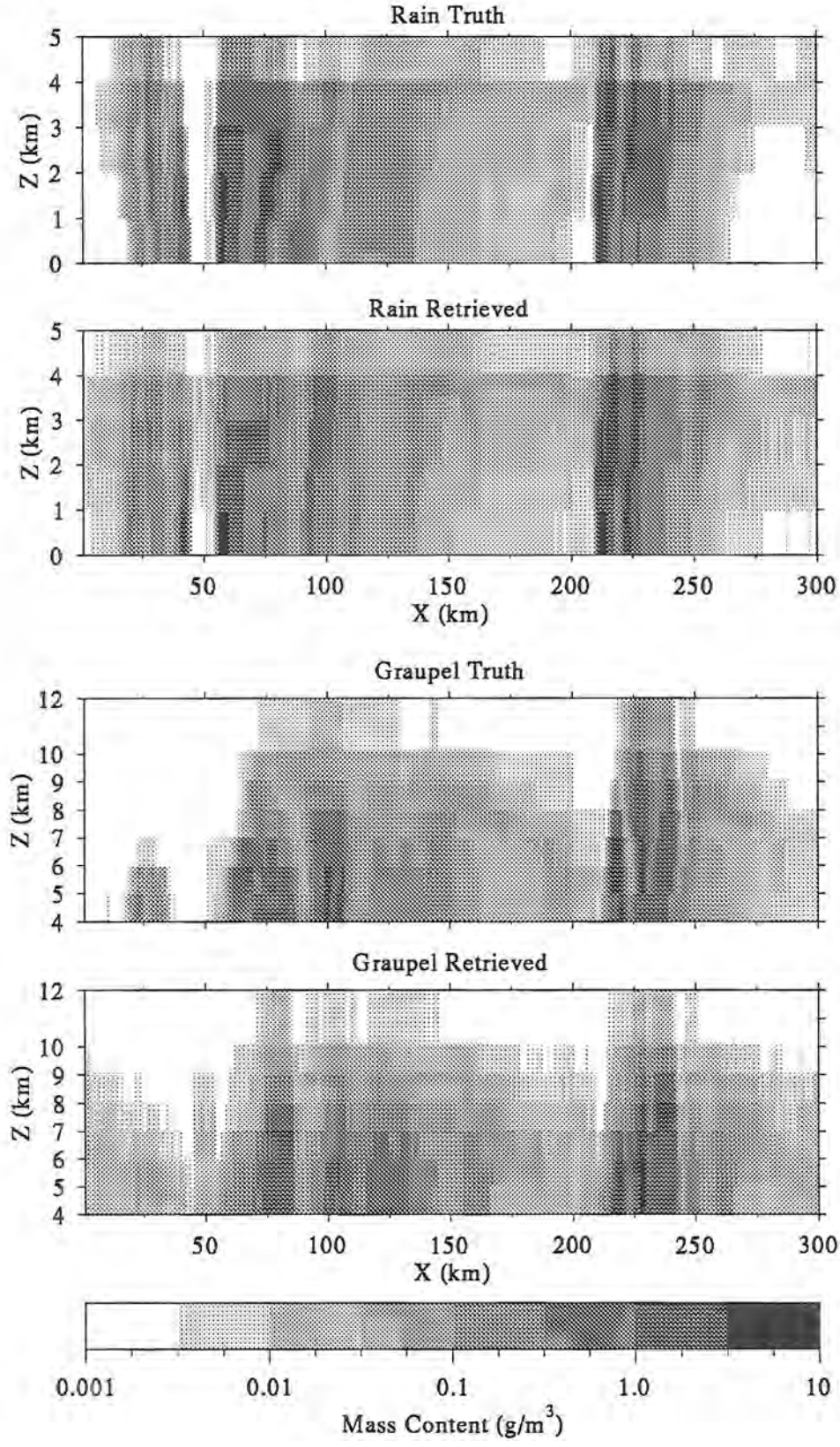


**Figure 5.11: Retrieved and true fields of rain and graupel for the three test areas combined horizontally. The retrieval is done with precipitation structure 9 over a water surface. The mass content is displayed logarithmically from $10^{-3}$ to 10 g/m$^3$.**

Table 5.5: RMS and maximum difference between "observed" brightness temperatures and those simulated from the retrieved profiles over all four channels for the 10 precipitation structures over water and land surfaces.

| Precip. Structure | Water Sfc. RMS | Water Sfc. MAX | Land Sfc. RMS | Land Sfc. MAX |
|---|---|---|---|---|
| 1 | 5.72 | 34.72 | 3.23 | 24.83 |
| 2 | 1.55 | 8.26 | 1.36 | 6.76 |
| 3 | 1.48 | 9.63 | 1.25 | 7.44 |
| 4 | 2.46 | 16.28 | 1.96 | 11.30 |
| 5 | 1.18 | 7.84 | 1.13 | 7.12 |
| 6 | 1.19 | 7.90 | 1.15 | 7.13 |
| 7 | 1.17 | 7.89 | 1.14 | 7.15 |
| 8 | 1.17 | 7.92 | 1.18 | 9.00 |
| 9 | 1.16 | 8.05 | 1.11 | 7.12 |
| 10 | 1.14 | 8.03 | 1.14 | 6.96 |

### 5.1.5 Observation width testing

One choice to be made with the Bayesian precipitation retrieval method is the width of the forward probability distribution. This parameter for each channel governs how closely the modeled observations must fit the actual observations. It should be set to a value that is typical of the modeling error, which in general will depend on the channel. The test here modifies the base situation by setting the forward distribution width, $\sigma_m$, for all channels, to 1, 2, 4, and 8°K (the normalized distance for selecting matching profiles is adjusted to keep the same number of matches). Table 5.6 lists the rms, minimum, and maximum differences between the synthetic observations and those made by using the retrieval radiative transfer model with the true cloud model values in the precipitation structure. Thus these rms values are a measure of the modeling errors. The rms differences are around 2°K except for the 85 GHz channel which is about 4°K, due to Eddington modeling error (see section 5.2.5).

Table 5.6: RMS, minimum, and maximum differences between synthetic brightness temperatures and those from the forward model of the retrieval method using precipitation structure 5.

| | | Synthetic $T_b$ - Forward modeled $T_b$ | | | |
|---|---|---|---|---|---|
| Surface | | 10 GHz | 19 GHz | 37 GHz | 85 GHz |
| water | rms | 2.65 | 2.55 | 2.59 | 4.25 |
| water | min | -1.71 | -4.13 | -6.41 | -8.85 |
| water | max | 9.05 | 8.13 | 9.85 | 16.09 |
| land | rms | 1.11 | 1.65 | 2.25 | 4.39 |
| land | min | -3.72 | -4.05 | -6.27 | -9.83 |
| land | max | 3.01 | 7.59 | 10.39 | 17.33 |

Fig. 5.12 shows the rms retrieval error for surface rain for the four different observation widths. If the width is substantially less than the true model errors (e.g. $\sigma = 1$°K for area C rain content over land) then the retrieval fits to modeling error, which causes occasional

bad retrievals and an increase in the rms error. The $\sigma = 1°$ retrievals are noisier pixel to pixel than the larger observation widths. On the other hand, if the observation width is too large (e.g. $\sigma = 8°$K here) then the retrievals relax toward climatology which also increases the rms error. The rms error for integrated ice (see Fig. 5.13) shows an increase in error only for the larger width. Even though the $\sigma = 1°$ width is below the rms modeling error as listed in Table 5.6, it usually performs better, although it is less stable. The domain average integrated rain and ice contents, for example, are closest to the truth for $\sigma = 1°$. The model errors in this test are fairly low because a plane-parallel model and the same microphysics were used to generate the synthetic observations.

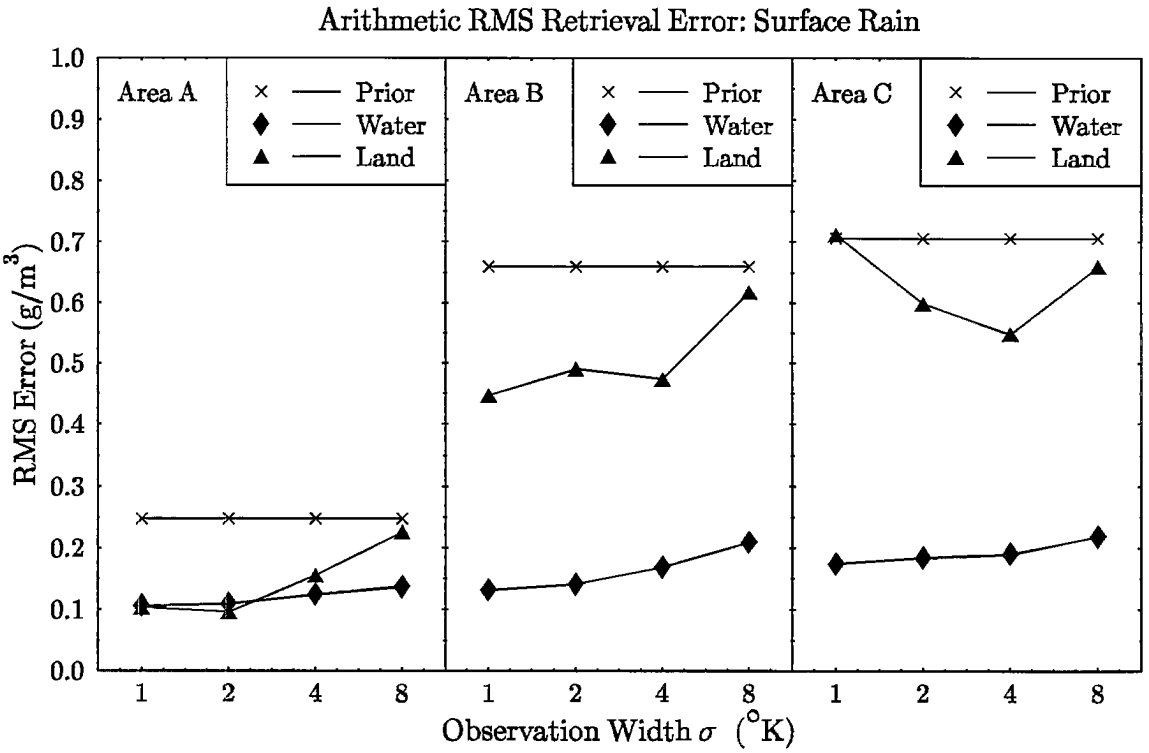


Figure 5.12: Arithmetic RMS retrieval error of surface rain content for the 4 forward distribution widths for each of the three test areas.

### 5.1.6 Microphysical assumption testing

Up to now the same microphysical assumptions concerning size distributions and ice particle density have been used in the retrieval as were made in making the synthetic brightness temperature observations. Unless the prior information from cloud modeling can provide at least distributions of average size of hydrometeors as well as the mass content, some rather bold assumptions must be made. The effect of differing microphysical assumptions is tested here by modifying the base situation so that the retrieval uses differing assumptions for determining the size distribution parameters and ice particle densities that go into the scattering calculation. The base microphysical assumption is the

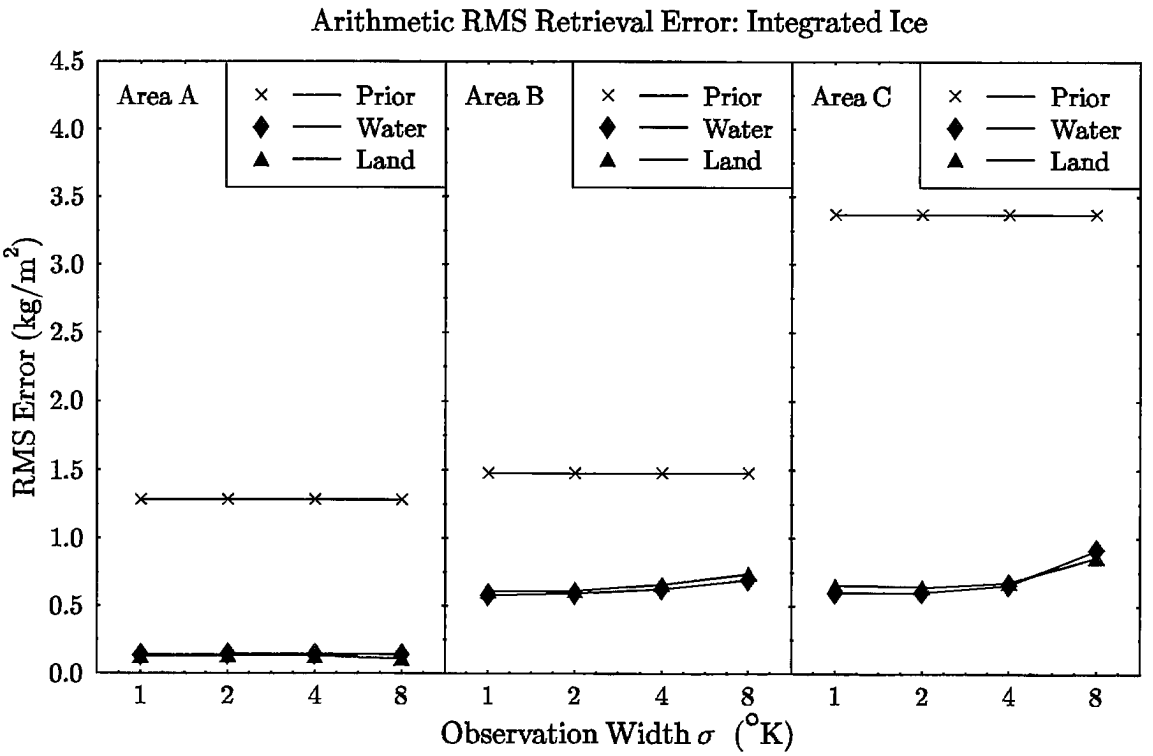


Figure 5.13: Arithmetic RMS retrieval error of integrated ice content for the 4 forward distribution widths for each of the three test areas.

Rutledge and Hobbs scheme described in section 5.1.1. The second and third microphysical schemes are variants of the one used in RAMS. These have a fixed average size (or slope) of the exponential size distribution of precipitating hydrometeors. For both scheme 2 and 3 the average diameter of the raindrops is 0.54 mm. The Rutledge and Hobbs formulation (eq. 5.2) has this average size for a mass content of 2.1 $g/m^3$, so scheme 1 usually has smaller raindrops. Scheme 2 has a graupel average size of 1.0 mm and density of 0.9 $g/cm^3$ (solid ice), while scheme 3 has a graupel average size of 0.8 mm and density of 0.4 $g/cm^3$. The parameters for snow are not relevant since snow is not in the base precipitation structure.

The resulting rms retrieval error of integrated rain mass for the three microphysical assumptions are shown in Fig. 5.14. Schemes 2 and 3 have significantly higher error than the correct scheme 1, especially for area A which does not contain much ice. The rain size distribution clearly affects the integrated rain retrieval, even over a water surface. Scheme 3 has sightly lower error than scheme 2 for areas B and C over water even though the rain assumptions are the same, indicating that the ice physics is playing a part in the retrieval. The retrieved domain average integrated rain, which over water is very close to the truth for the correct scheme, goes down to around half of the true value for the schemes with fixed average size. This occurs because the larger average size of schemes 2 and 3 cause higher extinction for the same mass content even at 10 GHz.

The rms retrieval error for integrated ice mass is given in Fig. 5.15. The scheme with larger solid ice graupel (2) has a much higher error than the one with lower density graupel (3) for areas with significant ice. This happens because there is much more scattering for the higher density ice, and hence a much lower mass content (about a factor of 4 below the actual value) is required to satisfy the observations. The Rutledge and Hobbs parameterization had the lowest retrieval error, of course, because that scheme was used to generate the synthetic observations, but this does not imply that it has the correct microphysical assumptions. This test shows the importance of using the right microphysical assumptions, although the correct average size-mass content relationship will not usually be known. It would be best to obtain the information about hydrometeor size distribution from cloud models with two parameter distributions that have been validated with independent measurements.

### 5.1.7 Priors content testing

The prior probability distribution can be made with different times from the cloud model simulation, with varying minimum rain cutoffs, or with the covariance information turned off. These options form the basis for the priors content testing. Doing a retrieval without any information about the correlations between hydrometeors tests whether the covariance information is as important as claimed. One would hope that the rain cutoff that distinguishes between raining and non-raining pixels would not affect the retrieval

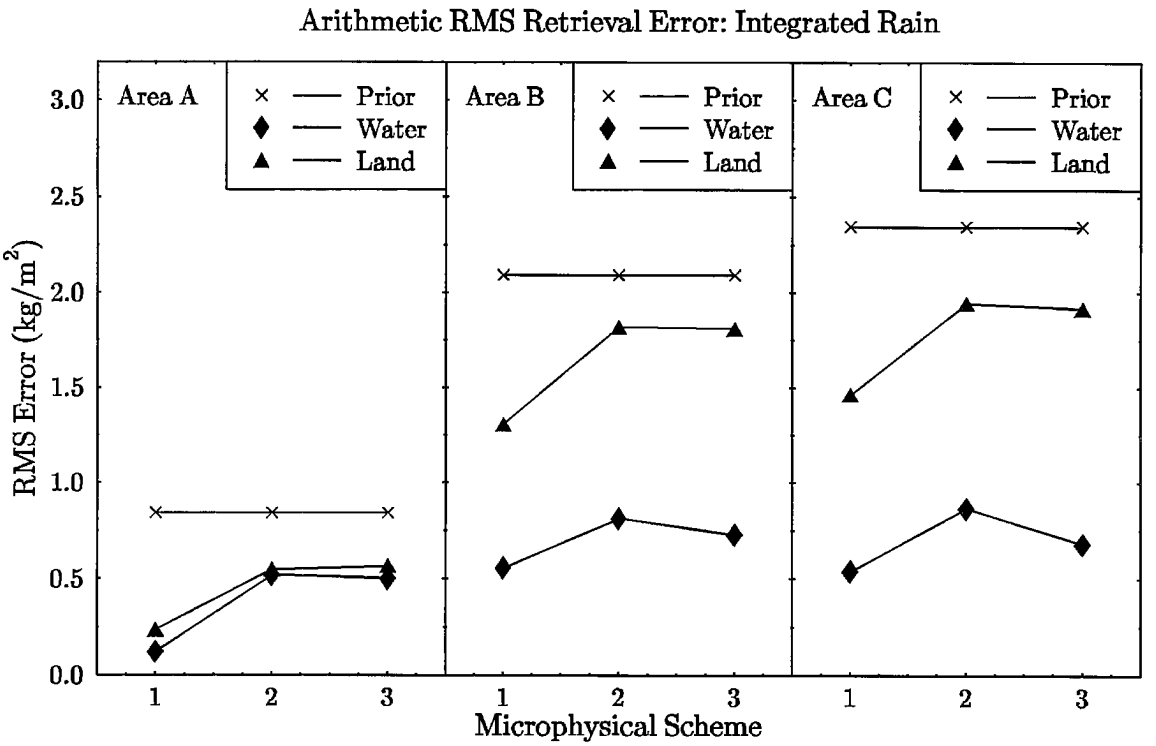


Figure 5.14: Arithmetic RMS retrieval error of integrated rain content for the 3 microphysical assumptions for each of the three test areas.

too much even though it does change the mean and variance of the lognormal prior distribution. Obtaining prior information from different stages of storm development should have a more subtle effect; presumably retrievals made with a prior more similar to the actual precipitation situation will be better. The base situation (structure 5, etc.) is run with the modifications listed in Table 5.7 (case 2 is the base case). The early cloud model times (1-3) include the time of for area A, while the middle times (6-9) include the time of areas B and C. Note the reduced number of samples for making the prior mean vector and covariance matrix, especially for the early cloud time.

Table 5.7: The setup for the five prior content tests.

| Priors Case | Cloud Times | Rain Cutoff (kg/m$^2$) | Covariance Information | Number of Samples |
|---|---|---|---|---|
| 1 | 1-15 | 0.04 | No | 2410 |
| 2 | 1-15 | 0.04 | Yes | 2410 |
| 3 | 1-3 | 0.04 | Yes | 78 |
| 4 | 6-9 | 0.04 | Yes | 964 |
| 5 | 1-15 | 0.01 | Yes | 3850 |

Figs. 5.16 and 5.17 show the rms retrieval error of the prior cases for surface rain mass content and integrated ice content, respectively. The accuracy of the surface and integrated rain content degrades significantly without the covariance information, even over

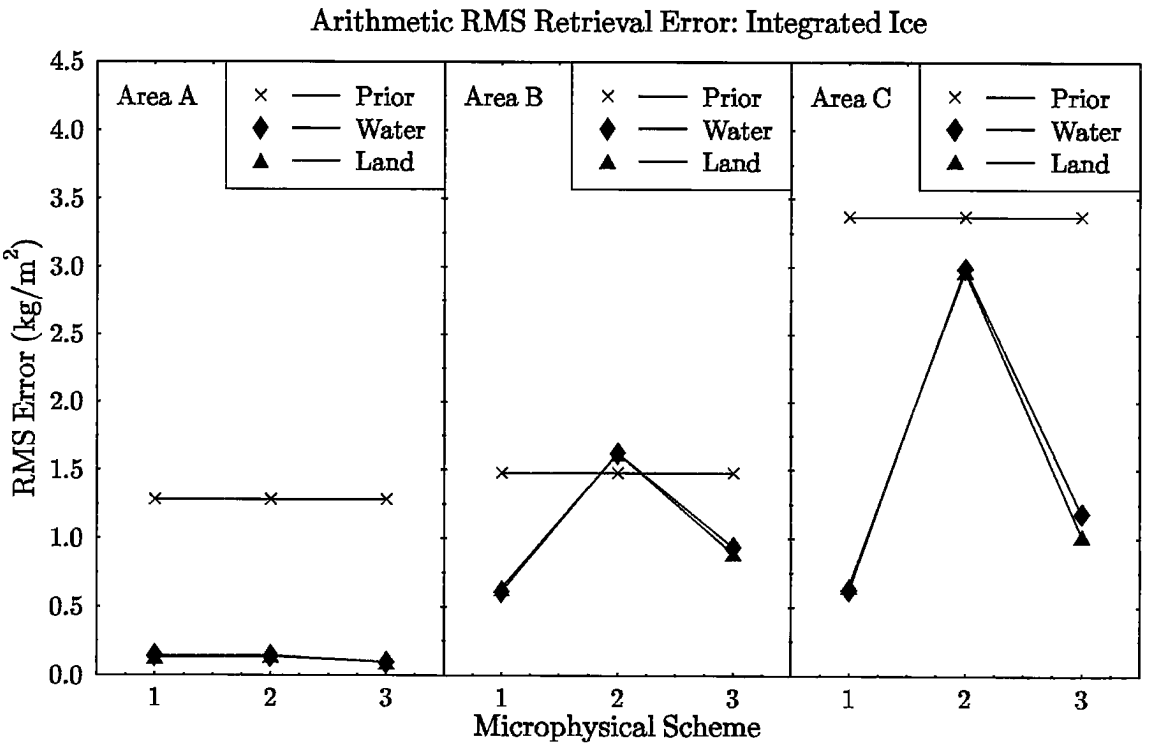


Figure 5.15: Arithmetic RMS retrieval error of integrated ice content for the 3 microphysical assumptions for each of the three test areas.

a water surface. The integrated ice content is not as sensitive to the lack of covariance information, probably because the ice is more directly related to the brightness temperature observations. The error in integrated cloud water mass is very much larger without the covariances, which indicates that much of the cloud water information is coming from its relationship to other hydrometeor species that have more effect on the microwave channels. The retrievals without covariances are noisier from pixel to pixel. Overall, the covariance information is not as crucial for the rain retrieval in this test with five layers as might be expected, though its importance would increase with the number of layers.

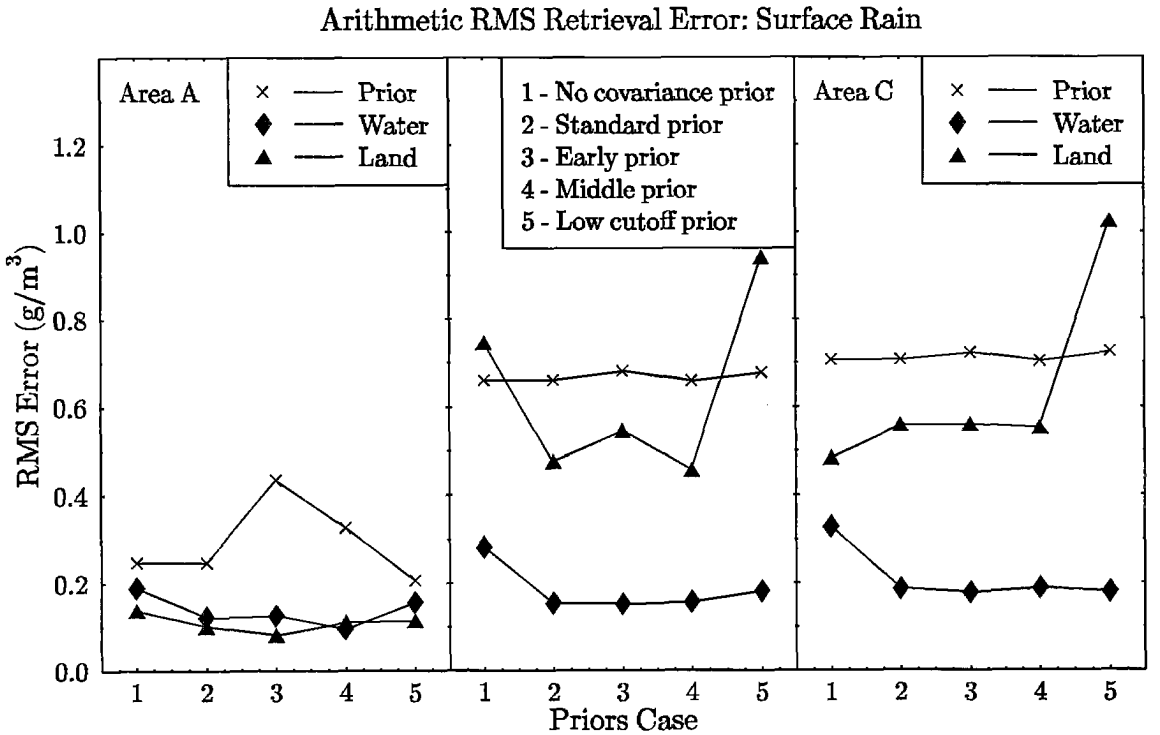


Figure 5.16: Arithmetic RMS retrieval error of surface rain content for the 5 prior cases for each of the three test areas.

The arithmetic rms error in surface rain mass increases dramatically for the over land cases for areas B and C for the lower rain cutoff. This is due to much too large rain retrievals in heavily raining areas. The lower rain cutoff increases the width of the lognormal prior distribution, and, being symmetric in log space, this allows much larger rain amounts in situations where the observations are not providing much information. The logarithmic rms error in surface rain is actually less for the lower rain cutoff.

There is some evidence in the rms error plots that the retrieval for area A is improved and the retrieval for areas B and C is degraded by using the early priors. The domain average integrated rain for area A over water, which has a low bias for the standard priors, is correct when using the early prior. The cloud model time of the priors does not have much effect on the integrated ice arithmetic retrieval error, although there is a significant

effect in the expected way for the logarithmic rms errors. The way the prior probability distribution is made has significant effects on those aspects of the hydrometeor profile for which the prior distribution is providing information beyond that available from the observations. One aspect of the prior distribution that could not be changed here was the assumed functional form; better retrievals would be expected if appropriate corrections to the lognormal and simple linear covariance form could be made.

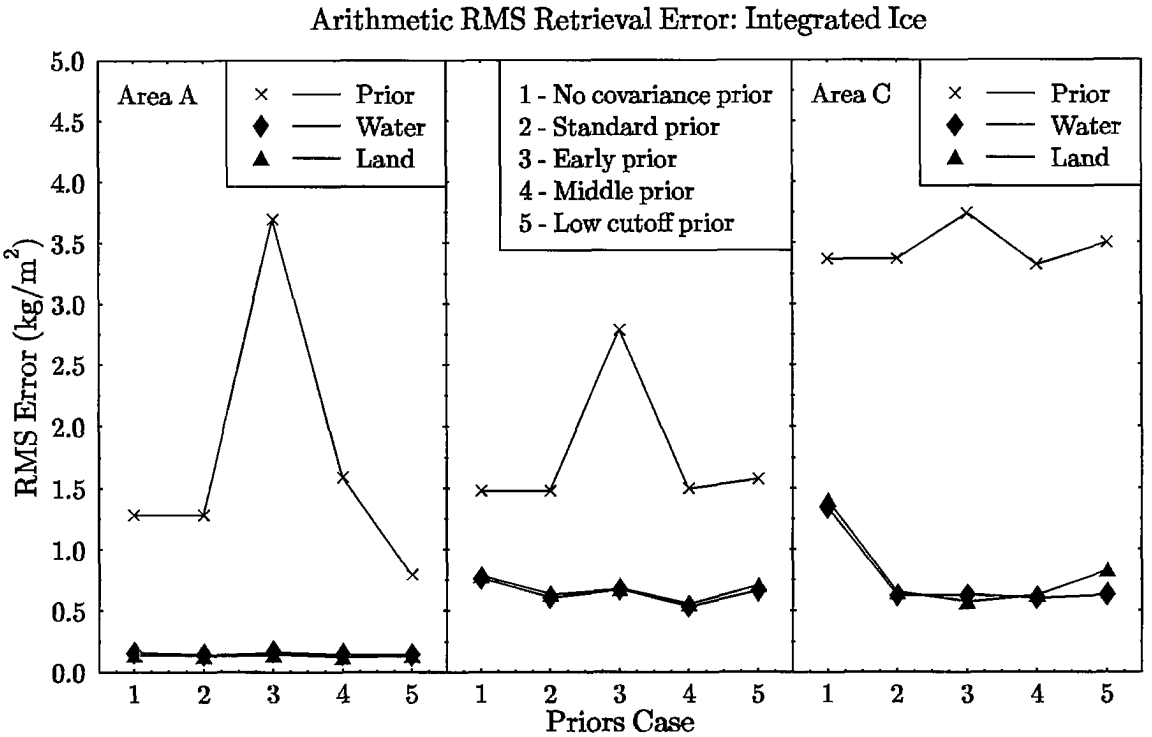


Figure 5.17: Arithmetic RMS retrieval error of integrated ice content for the 5 prior cases for each of the three test areas.

### 5.1.8 Frequency combination testing

The combination of frequencies used for a retrieval is not an input parameter in the normal sense because it is limited by the number of channels the instrument provides and one would want to use all the available channels. The Bayesian precipitation retrieval method can easily use any combination of frequencies available. This allows tests to be done to determine how the accuracy of precipitation retrieval falls as less channels are used. By examining the results of various combinations one can conclude which frequencies are making the most contribution to the retrieval of various hydrometeor species. For this test the base situation is used with the 8 combinations of frequencies listed in Table 5.8. This is not all possible combinations, but it does examine the effect of 10, 19, and 85 GHz in some detail in one, two, and three frequency combinations.

Table 5.8: The 8 frequency combinations tested.

| Case | Channels |
|---|---|
| 1 | 10H, 19H, 37H, 85H |
| 2 | 10H, 19H, 37H |
| 3 | 19H, 37H, 85H |
| 4 | 10H, 19H |
| 5 | 19H, 85H |
| 6 | 10H |
| 7 | 19H |
| 8 | 85H |

The results of the frequency combination testing on surface rain mass content are shown in Fig. 5.18 for arithmetic rms error and Fig. 5.19 for the domain average. For regions without much ice (area A) 19 GHz can substitute for 10 GHz over water, but 10 GHz is very useful over land for retrieving surface rain. For areas with significant amounts of ice 10 GHz is needed for accurate retrievals over water because scattering by ice effects the 19 GHz channel. Over land 85 GHz is not that useful for rainfall if 10 and 19 GHz are in the combination. The 85 GHz channel is useful over land for estimating very light rain, since without its extra sensitivity the rain mass is over estimated. The 85 GHz channel alone greatly underestimates the rainfall, whereas 10 GHz alone over a water surface is reasonably accurate.

The results for integrated ice mass are shown in Fig. 5.20 for arithmetic rms error and Fig. 5.21 for the domain average. The 85 GHz channel is very useful for determining ice content, but if used alone then it underestimates the ice amount and has high errors. Without the sensitivity of 85 GHz for land surfaces too much ice is retrieved for those pixels with very small ice mass. The combination of 10 and 19 GHz is a good combination for integrated ice mass if there is enough ice to register at 19 GHz. Single frequencies do not work well for ice mass, although 19 GHz is the best single channel over land.

The conclusions about the effectiveness of various frequency combinations will generalize somewhat to other methods, but will also depend on the particular algorithm used here. The issue of spatial resolution changing with frequency, which is a major disadvantage of 10 GHz, has not been dealt with here. The implications of the frequency combination testing for microwave remote sensing of precipitation agree with the ideas presented in Smith et al. (1992) and Mugnai et al. (1993).

These theoretical tests show that the precipitation structure needs to have some degree of complexity (e.g. five layers with variable rain, cloud, and ice), but that highly detailed vertical structure is not necessary. The retrievals are not highly sensitive to the width of the forward probability distribution, but the observation width should not be much below the typical size of the forward modeling errors. The microphysical assumptions that are used to derive hydrometeor size distributions from the mass content are

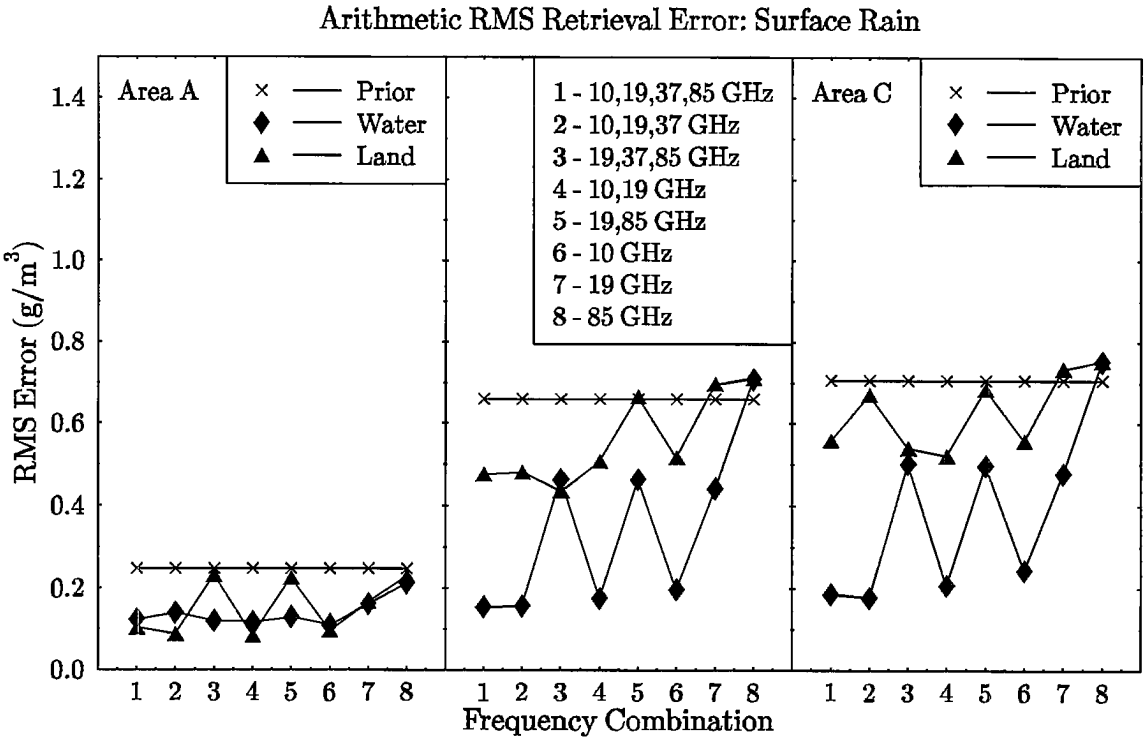


Figure 5.18: Arithmetic RMS retrieval error of surface rain content for the 8 frequency combinations for each of the three areas.

very important in determining the amounts of rain and ice retrieved. The covariance information in the prior probability distribution is indeed important, but the retrievals are not very sensitive to the stage of storm development in the cloud model. The tests performed here have illustrated how the Bayesian precipitation retrieval algorithm behaves, but they have a number of limitations. The limitations of the forward modeling that were not addressed include the simple fixed surface properties, especially for land, and the plane-parallel radiative transfer assumption. The tests of the prior distributions are limited by their use of the same cloud model output to make both the prior distribution and to synthesize the brightness temperatures. Real data usually will give worse retrieval results because of larger modeling errors and less applicable priors than was the case for these tests.

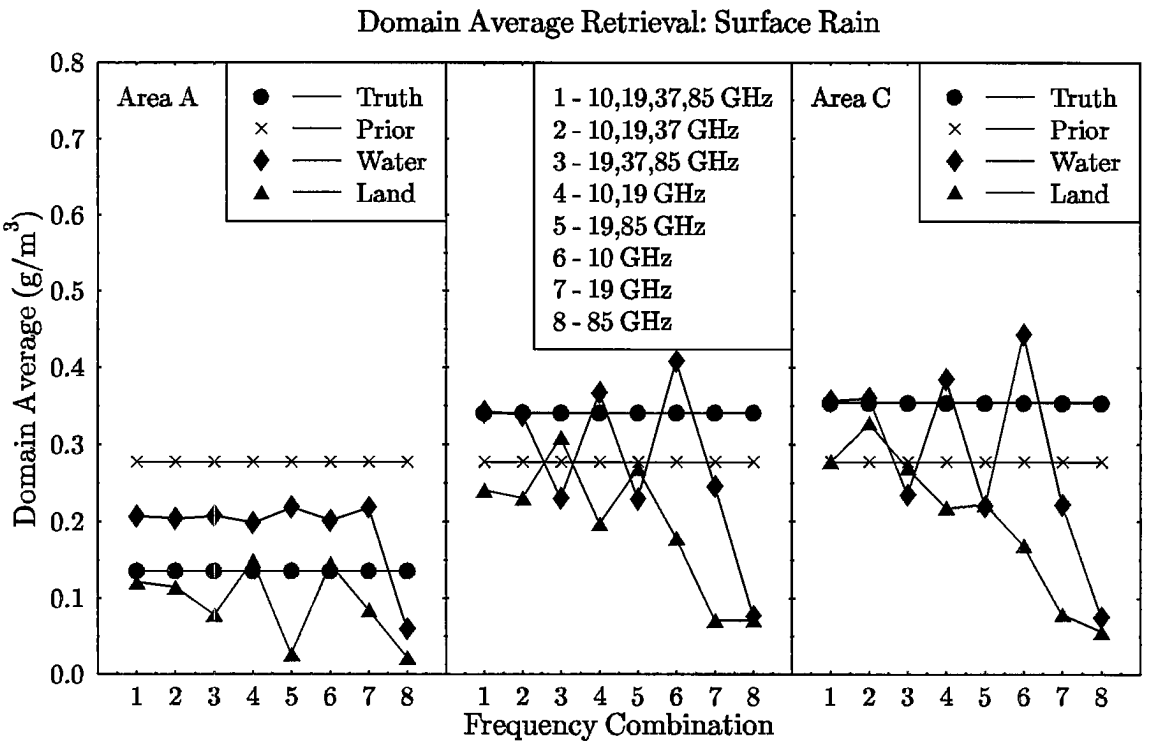


Figure 5.19: Domain average surface rain mass content for each of the three areas for the 8 frequency combinations. The average for the cloud model truth, the prior mean (climatology), and retrievals over water and land are shown.

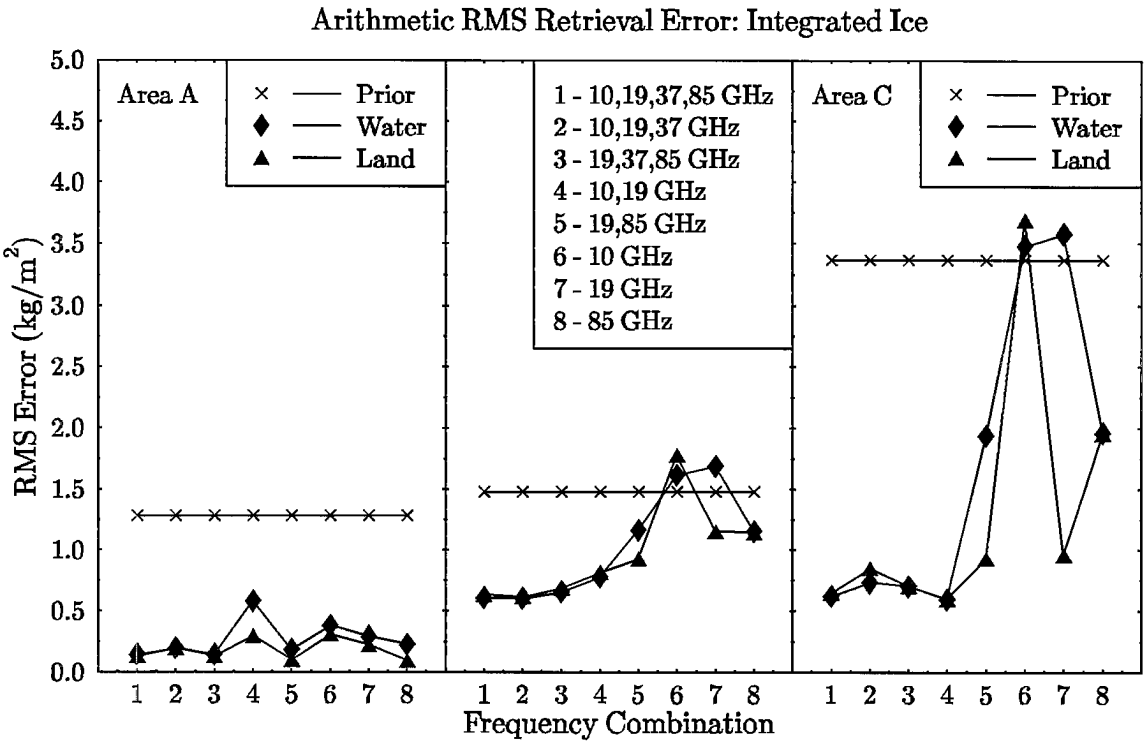


Figure 5.20: Arithmetic RMS retrieval error of integrated ice content for the 8 frequency combinations.

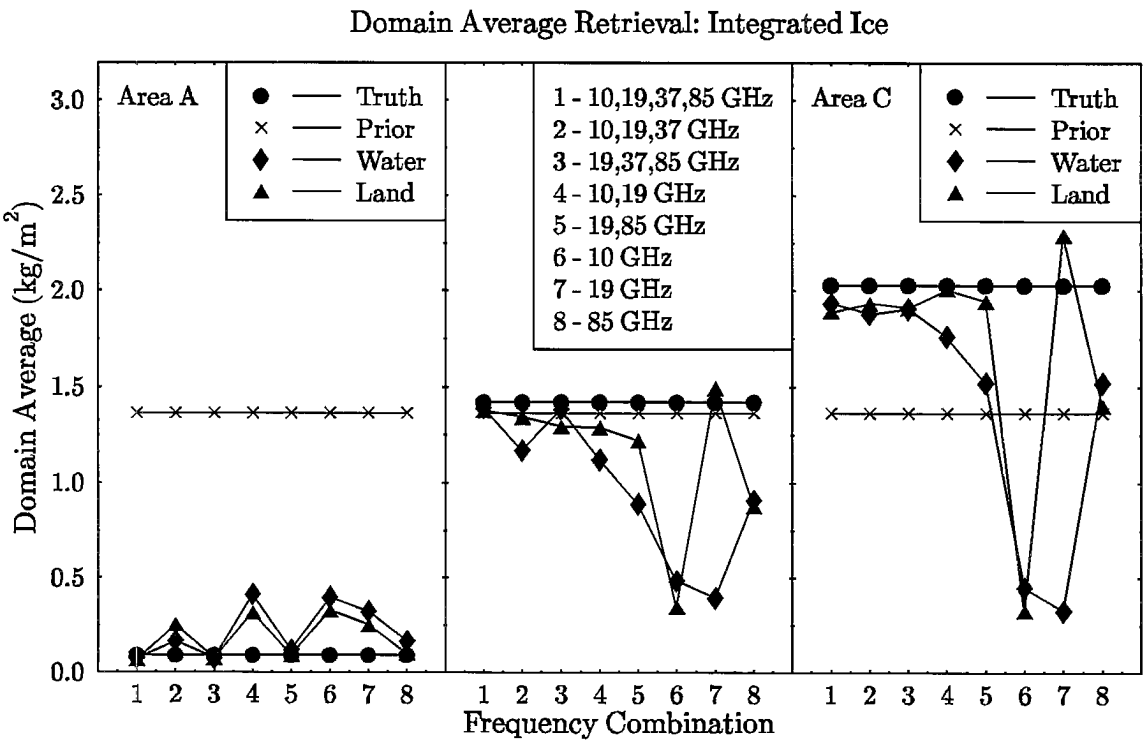


Figure 5.21: Domain average integrated ice mass content for the 8 frequency combinations.

## 5.2 CaPE Experiment Validation Tests

Any proposed remote sensing inversion technique must be validated by using the method on field observations and comparing the results with other accepted measurement techniques. Precipitation remote sensing validation is somewhat problematic because there are no highly accurate area-averaged measurement techniques. Literal ground truth in the form of raingauges offer only point measurements, and the very dense gauge networks needed for measurements in a collocated case study are impractical. Radar observations give the needed area/volume coverage but with uncertainties in rainfall estimation of perhaps a factor of two from uncertainties in drop size and precipitation inhomogeneities (Atlas and Ulbrich, 1990; Joss and Waldvogel, 1990). Polarimetric radars provide higher accuracy for rainfall estimation than radars that measure reflectivity only. Here the NCAR CP-2 multiparameter radar is used for validation.

A major component of a space-based precipitation retrieval method that is not yet implemented in the Bayesian precipitation retrieval system is a way of dealing with beam filling and the effects of multidimensional radiative transfer. Beam filling is the name for the problems caused by precipitation that is not uniform across the microwave radiometer field of view. Because the microwave signal is not linear in the precipitation amount, beam filling can cause large errors in rain estimation with coarse resolution satellite microwave data (e.g. the SSM/I with 15 to 60 km resolution). Fortunately, the beam filling problem can be reduced substantially by using data from high-resolution aircraft-based microwave radiometers. This allows for testing of the Bayesian retrieval method while minimizing the complicating effects of sub-field-of-view precipitation variability which the method is not equipped to handle. Another reason for using high resolution aircraft data is that the prior information for the retrieval is obtained from a cloud model with one kilometer resolution, and averaging the cloud model output over footprints tens of kilometer wide would greatly reduce the data available for estimating the prior distribution.

The passive microwave data used for this validation is from the Advanced Microwave Precipitation Radiometer (AMPR), which is the latest NASA aircraft-based microwave instrument appropriate for precipitation sensing. The AMPR has a wider range of frequencies (from 10 to 85 GHz) than previous instruments, such as the Microwave Precipitation Radiometer, and so is better for testing multichannel algorithms. The AMPR has very high resolution (from 0.6 to 2.8 km) which should resolve much of the spatial variability of convective precipitation.

The first organized field experiment that the AMPR flew in was the Convective and Precipitation/Electrification (CaPE) experiment in central Florida during the summer of 1991 (Williams et al., 1992). The AMPR and CP-2 data used for the validation test are from this experiment, during which collocated AMPR and CP-2 data of convective precipitation were acquired over the ocean and land. The small amount collocated data

available from CaPE makes this validation rather limited in nature. Thus, this test is meant to be preliminary, and future validation efforts will be needed for other types of precipitating systems in experiments at various locations.

### 5.2.1 The AMPR and CP-2 Instruments

The Advanced Microwave Precipitation Radiometer has been designed and built in the last five years under the direction of the NASA Marshall Space Flight Center (Spencer et al., 1993), (see also Vivekanandan et al., 1993). The AMPR mounts in the ER-2 aircraft which cruises at 20 km, allowing it overfly deep convection. The AMPR has the same multifrequency feedhorn as the SSM/I for its 19.35, 37.1, and 85.5 GHz channels and an additional specially designed feedhorn for 10.7 GHz. The 3 dB beamwidths are 8.0° for 10.7 and 19.35 GHz, 4.2° for 37.1 GHz, and 1.8° for 85.5 GHz, giving ground resolutions of 2.8, 1.5, and 0.6 km. The instrument scans across track through nadir from +45° (right side) to −45° (left side), in 50 beam spots every 1.8°. The three lower frequencies are thus oversampled in that they are sampled multiple times per beamwidth. A new scan is started every 3.0 seconds, which at the 200 m/s cruising speed of the ER-2 corresponds to 0.6 km (same as the 85.5 GHz beamwidth at the ground). Because the ER-2 flies relatively close to precipitating systems the perspective causes higher altitude features to appear broader than lower altitude ones of the same horizontal size.

Cross-track scanning with a 45° offset flat-plate reflector causes the instrument's polarization basis to rotate relative to the scene orientation. While the single polarization is always linear it rotates from horizontal at $\theta = +45°$ (start of scan) to vertical at $\theta = -45°$ (end of scan). The polarization measured by AMPR thus varies with angle, but is a linear combination of the vertical and horizontal polarization of the scene, given by

$$T_b^{AMPR} = T_b^H \cos^2(\theta - 45°) + T_b^V \sin^2(\theta - 45°) \; . \tag{5.3}$$

The 50 millisecond spot integration time results in a receiver noise figure ranging from 0.15 to 0.30°K. After every fourth scan the reflector rotates to view hot and cold calibration targets during one scan period. The hot target is heated to 320°K, while the cold target is cooled with ambient air to around 230°K. The absolute accuracy is estimated to be no better than several degrees, especially for the coldest brightness temperatures that must be extrapolated beyond the calibration temperature.

The CP-2 multiparameter radar is operated by the National Center for Atmospheric Research (NCAR). It provides dual frequency operation at S band (3 GHz) and X band (10 GHz) with matched 0.9° beamwidths (Bringi and Hendry, 1990). There are 512 range gates with a typical spacing of 300 m giving a maximum range of 150 km. The S band system has a coherent receiver so radial velocity is obtained. Pulse-to-pulse polarization switching at S band provides for the measurement of differential reflectivity

$Z_{DR} = 10\log(Z_{HH}/Z_{VV})$ in addition to the standard horizontal reflectivity $Z_{HH}$. There are two antennas at X band, one for horizontal polarization transmission and reception and one for vertical reception, so that the linear depolarization ratio $LDR$ and X band reflectivity can be measured. The X band specific attenuation can be derived by comparing S and X band reflectivity. Other propagation parameters can also be measured.

### 5.2.2 The AMPR datasets

Two AMPR dataset are used for the precipitation algorithm validation, one over land and one primarily over ocean. Uncooperative weather, the requirement that the precipitating systems be within CP-2 range, and several AMPR equipment failures severely limited the number of useful CaPE AMPR/CP-2 datasets available for algorithm validation. Fig. 5.22 shows a map of the experiment area with the location of the CP-2 radar, various upper air stations, and the two AMPR datasets. The datasets were both from 12 August 1991 and are identified here by their starting UTC times: 2059 for the one over land, and 2152 for the ocean one. The centers of the AMPR datasets are 108 and 99 km from CP-2. There is an additional dataset available 40 km northwest of CP-2 (2226Z), which is not used here. The ER-2 was flying north with the precipitation cell directly over the coast, so the lower frequency channels are contaminated by the combination of land and ocean background. These two datasets were provided by Joe Turk of Colorado State University in a very useful form combining the AMPR and CP-2 data (Vivekanandan et al., 1993). The CP-2 data is remapped into the AMPR scanning coordinate system by tracing AMPR beams through a three-dimensional grid of CP-2 data with 0.5 km spacing and extracting the closest grid point for each 0.5 km altitude. The natural coordinate system for AMPR is the pixel-scan system. The pixel number from 1 to 50 (right side to left side) is the cross-track coordinate, while the scan number (starting at 1 in the dataset) is the along-track coordinate (in the direction the aircraft flies).

Fig. 5.23 has images of the four AMPR channels for the 2059 time. This dataset is mainly over land with the lower left corner of the 10, 19, and 37 GHz images showing the low brightness temperatures characteristic of water surface emission. The strong precipitation core is clearly visible in the 19 GHz image with brightness temperatures below 190°K, and at 37 and 85 GHz with $T_b$'s dropping to around 105°K. The radar reflectivity exceeds 55 dBZ in the most intense area. The cold brightness temperature region at 85 GHz appears larger because of the perspective effect due to the channel sensing the upper portion of the precipitation. Along the center pixel there are two precipitation cells that are distinguished most easily at 37 and 85 GHz. The two spots of low brightness temperature at 10 and 19 GHz along pixel 40 are small lakes. To the left of the precipitation core there is a lower $T_b$ ($\approx$ 220°K) area that shows up only at 10 GHz and may be due to low emissivity from soil wetting. The very small (single pixel) low $T_b$ features at 10 and 19 GHz are clearly bad data (perhaps from interference), since they are

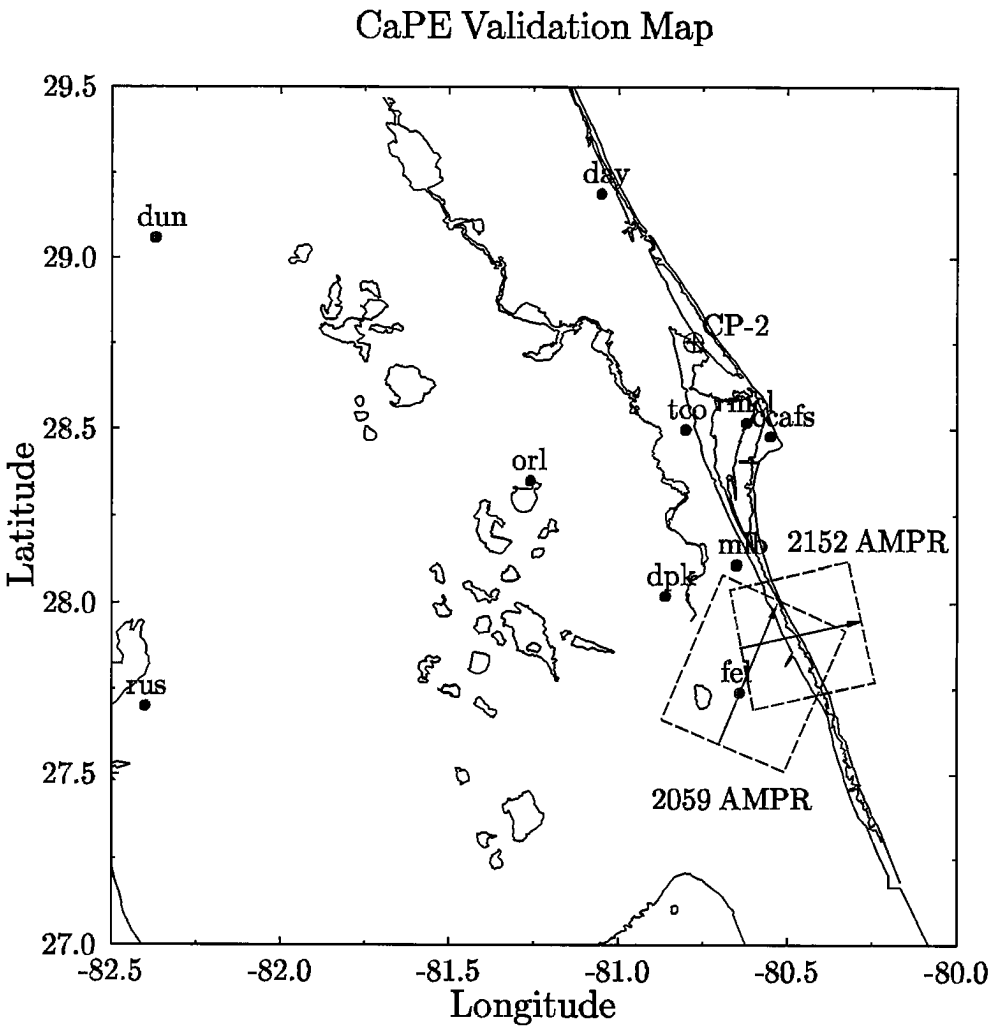


Figure 5.22: Map of the CaPE experiment area with locations of the two AMPR datasets. The arrows in the dataset boxes show the heading of the ER-2. The CP-2 radar position and the locations of the upper air stations are also shown.

below the resolution of these channels. Scans 1 to 60 of this AMPR dataset were chosen for the algorithm validation test in order to avoid the ocean scans at the end. Primarily the track along pixels 25 is considered, although tracks for pixels 20 and 30 are also used; there is little precipitation for pixels further from nadir.

The AMPR data for the 2152 dataset is shown in Fig. 5.24. The effect of the ocean emissivity changing with polarization and hence AMPR scan angle can be seen at the right sides of the 10 and 19 GHz images. The 10 GHz brightness temperatures change from about 90°K for H polarization (pixel 1) to about 150°K at V polarization (pixel 50). The 85 GHz channel is around 260°K in the nonprecipitating regions over the oceans because of screening due to water vapor and perhaps cloud water. For this dataset most of the precipitation is over the ocean. This means that the 10 and 19 GHz channels increase with the rainrate, as seen along pixel 25 in the center of the images. There is a moderately strong cell between scan 30 and 40 as indicated by the highest oceanic brightness temperatures at 10 GHz ($\approx$ 250°K). The 19 GHz channel clearly saturates near 250°K in the core region. The ice scattering lowers the 85 GHz brightness temperature to 160°K and the 37 GHz channel to 190°K. The region from scan 40 to 50 is less intense with 10 GHz brightness temperatures only up to around 160°K. The warm 85 GHz channel shows that there is only a small amount of ice, while 37 GHz has warmed up to 260°K because it can see through the thin ice to the rain below. Over the ocean the 37 GHz channel can be low due to scattering from large amounts of ice or from the low surface emissivity in regions of no precipitation. In order to restrict the data for validation to precipitation over the ocean, scans 30 to 60 are selected for pixels 20, 25, and 30. Further description of these two AMPR datasets and the collocated CP-2 radar data is available in Turk et al. (1993).

### 5.2.3 RAMS cloud model simulation

The prior probability information for the validation experiment is obtained from a simulation performed with the Colorado State University Regional Atmospheric Modeling System (RAMS) (Tripoli and Cotton, 1982; Cotton et al., 1982; Cotton et al., 1986). The simulation was a modification of a two-dimensional summertime Florida sea breeze simulation performed by Nicholls et al. (1991). The horizontal domain of 400 km has a land surface for the center 200 km. The land is modeled with an eight level soil model assuming unvegetated fairly dry sandy-clay soil. The horizontal resolution is 1 km, and Mesoscale Compensation Regions are used for the boundary conditions. The vertical atmospheric grid is a stretched coordinate of 32 levels ranging from 400 m to 1000 m spacing. The simulation was started at 0800 local standard time and run for 14 hours.

The simulation performed was like experiment 3 in Nicholls et al. (1991). The type 3 wind profile used for experiment 3 was the most similar to the winds obtained from the CaPE upper air stations on the morning of 12 August 1991. Fig. 5.25 compares the wind

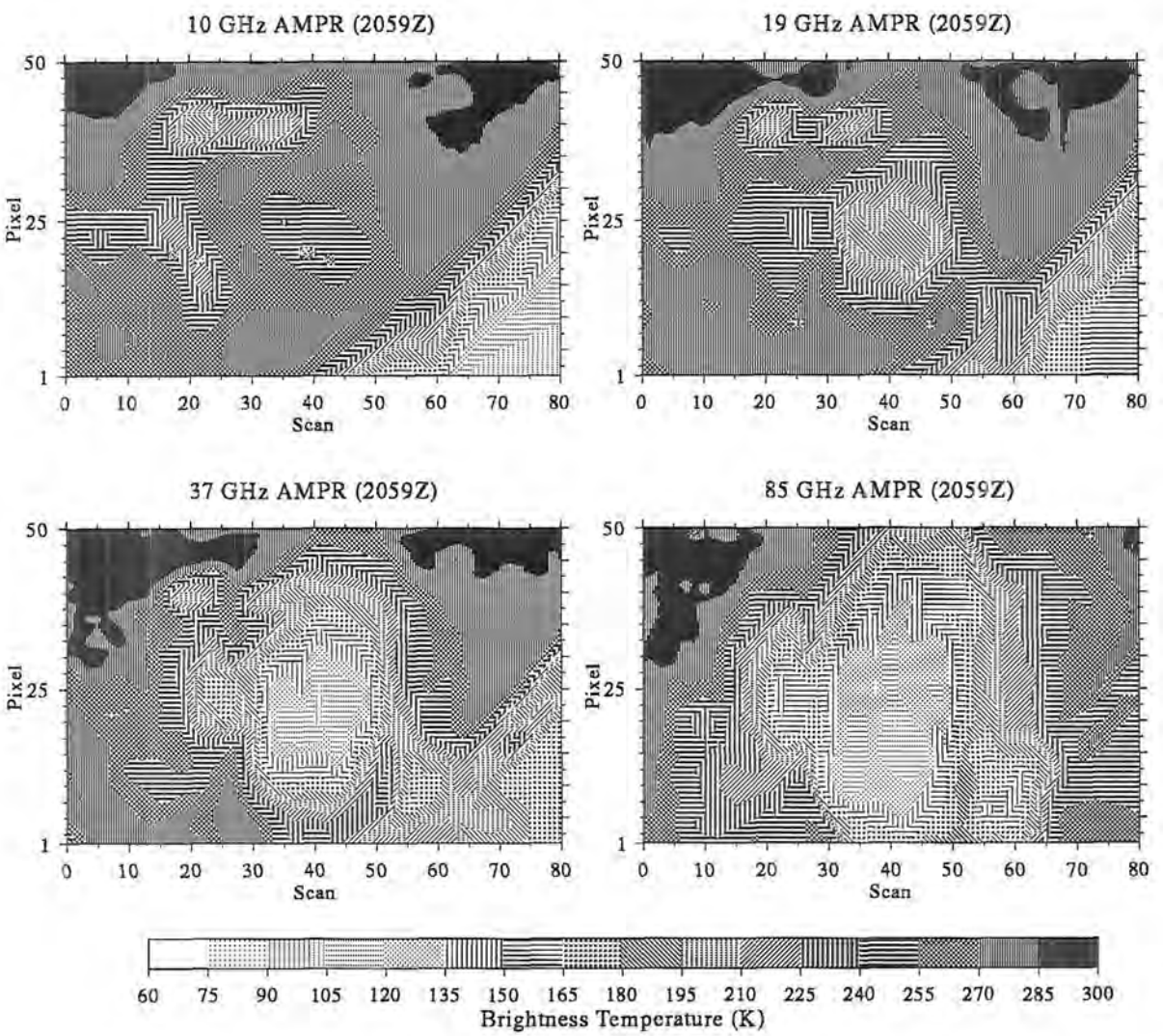


Figure 5.23: Brightness temperatures of the four AMPR channels for the 2059Z 12 August 1991 dataset. The pixel axis is across-track and the scan axis is along-track. The nadir resolution at the ground is 0.6 km per pixel in both directions.

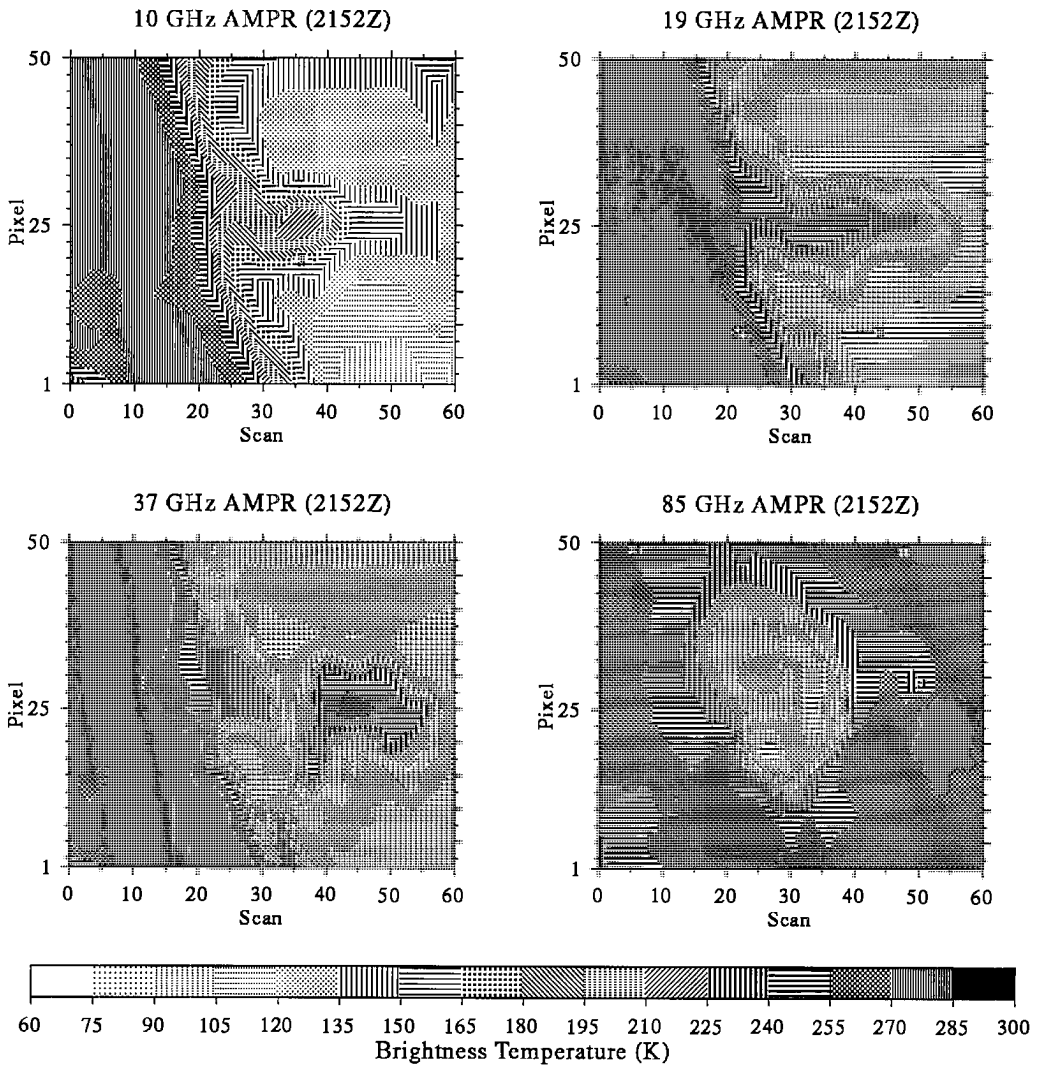


**Figure 5.24: Brightness temperatures of the four AMPR channels for the 2152Z dataset.**

profiles from the Dunnellon Airport and Ruskin stations at 0600 local standard time with the initial RAMS sounding. The wind fields are similar with weak westerlies below the easterlies. The temperature and water vapor are modified from the simulation of Nicholls et al. (1991), mainly by reducing the water vapor above 3 km to match the CaPE morning soundings. Fig. 5.26 compares the temperature and water vapor mixing ratio between the upper air soundings and the RAMS initialization.

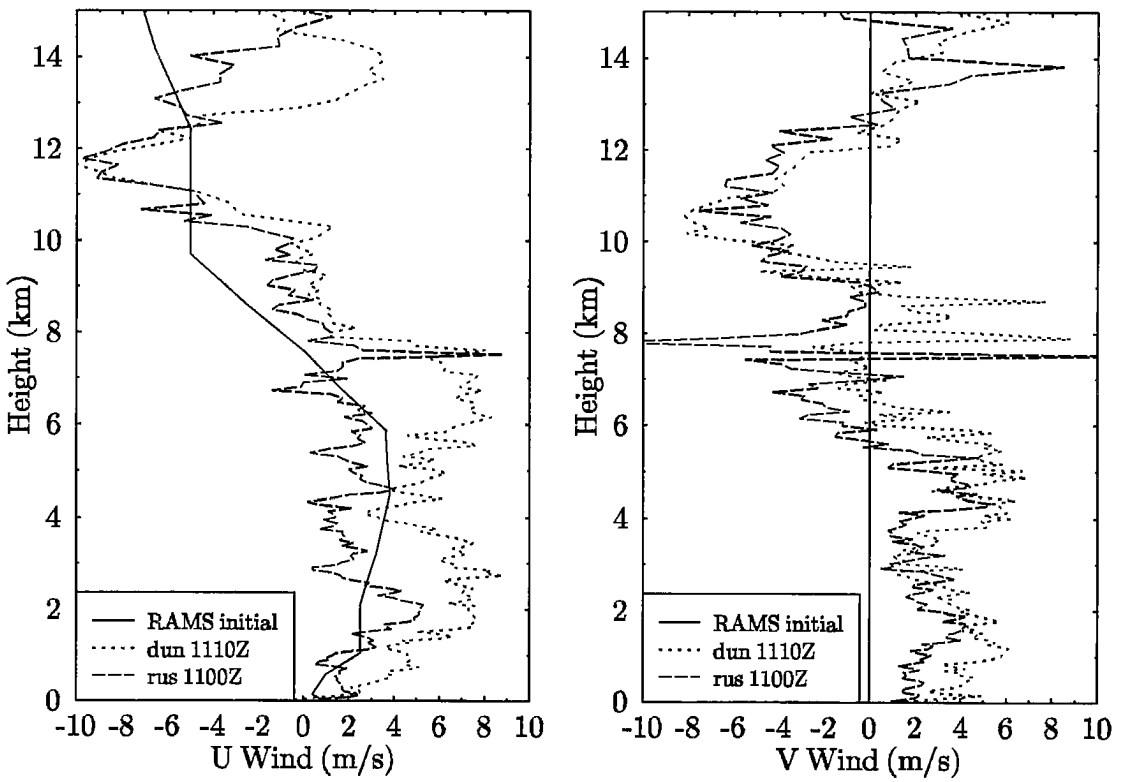


Figure 5.25: Wind velocity components from two CaPE upper air soundings and the RAMS initialization. The stations are Dunnellon Airport and Ruskin. The soundings were taken at approximately 0600 LST in the morning on 12 August 1991 (the day of the validation data).

The RAMS simulation used five categories of hydrometeors: liquid cloud droplets, rain, pristine ice crystals, aggregates, and graupel. The cloud droplets and pristine ice crystals have a monodisperse size distribution whose size varies. An exponential size distribution is assumed for the large hydrometeors, and only the mixing ratio is predicted. Another difference between the simulation described in Nicholls et al. (1991) and the one used here, besides the different version of RAMS (2c instead of 1a), are the microphysical assumptions. The previous simulation used an older, experimental scheme to predict the characteristic size of graupel and snow as well as the mixing ratio. In this simulation the average particle diameters were specified at 0.54 mm for rain, 3.30 mm for aggregate, and

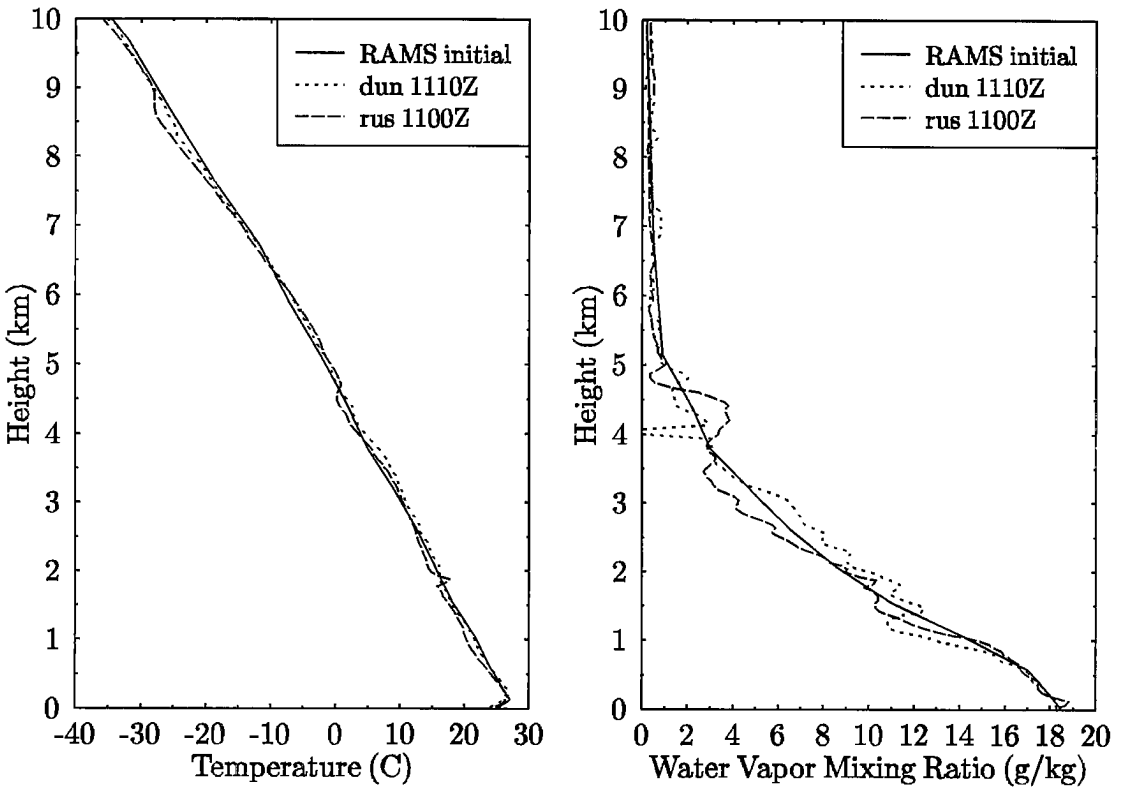


Figure 5.26: Temperature and water vapor mixing ratio from two CaPE upper air soundings and the RAMS initialization. The soundings were taken at approximately 0600 LST on 12 August 1991.

1.2 mm for graupel. The bulk densities of the ice particles are 0.9 g/cm$^3$ for graupel and 0.03 g/cm$^3$ for aggregate. These values are the default RAMS microphysics, except for the somewhat larger graupel (1.2 mm vs. 1.0 mm). The high density and large diameter of the "graupel" category is more like that of hail.

The sea breeze circulation develops a precipitating cloud about three hours into the simulation. The temperature, water vapor mass content, and hydrometeor mass contents from the simulation are stored every 15 minutes from 180 to 840 minutes simulated time. Fig. 5.27 shows the total precipitating hydrometeors for six cloud model times at two hour intervals. At first the west coast sea breeze front is stronger and produces a line of precipitation (240 minutes). By 360 minutes the west coast precipitation has died out and the east coast front convection is producing rain. The convection moves west and rapidly gathers strength, perhaps from the collision of the two sea breeze fronts (480 minutes). The storm then grows and develops a stratiform region, while the convective region is reduced in intensity (600 minutes). In the early evening the system dissipates, but still produces light rain.

### 5.2.4 Radar validation methods

There are two approaches to validating hydrometeor profiles retrieved from passive microwave measurements using radar observations. One is to retrieve profiles from the radar data and compare, for example, hydrometeor mass contents. The other is to simulate radar observables from the retrieved size distributions and compare these. The advantage of the latter approach is that the uncertainties of radar inversion are avoided. The disadvantage is that comparison is done in terms of radar parameters (e.g. reflectivity) instead of the desired end product of hydrometeor mass content or rainfall rate. Both approaches are used for this validation experiment.

The radar simulation computes reflectivity (dBZ) and attenuation (dB/km) at two different frequencies (e.g. S and X band). The same microphysical assumptions as for the Bayesian retrieval method are used to derive the hydrometeor size distribution and other properties. The same Mie calculation and integration procedure is done but now backscattering and extinction are computed for the exponential distributions. The attenuation due to cloud liquid water and water vapor is computed with the MPM92 model and added to the attenuation from particles. The effective reflectivity factor (in mm$^6$/m$^3$) is defined in terms of the backscattering by

$$Z_e = \frac{\lambda^4}{\pi^5 |K_w|^2} \sigma_b \ , \qquad |K_w|^2 = 0.93 \ , \tag{5.4}$$

and the equivalent reflectivity (in dBZ) is then $Z_E = 10 \log(Z_e)$. Differential reflectivity $Z_{DR}$ is not simulated because the calculations assume spherical particles. The simulated reflectivity is compared with the average of the horizontal and vertical reflectivity, which is fairly close to the equivalent volume sphere reflectivity for oblate raindrops.

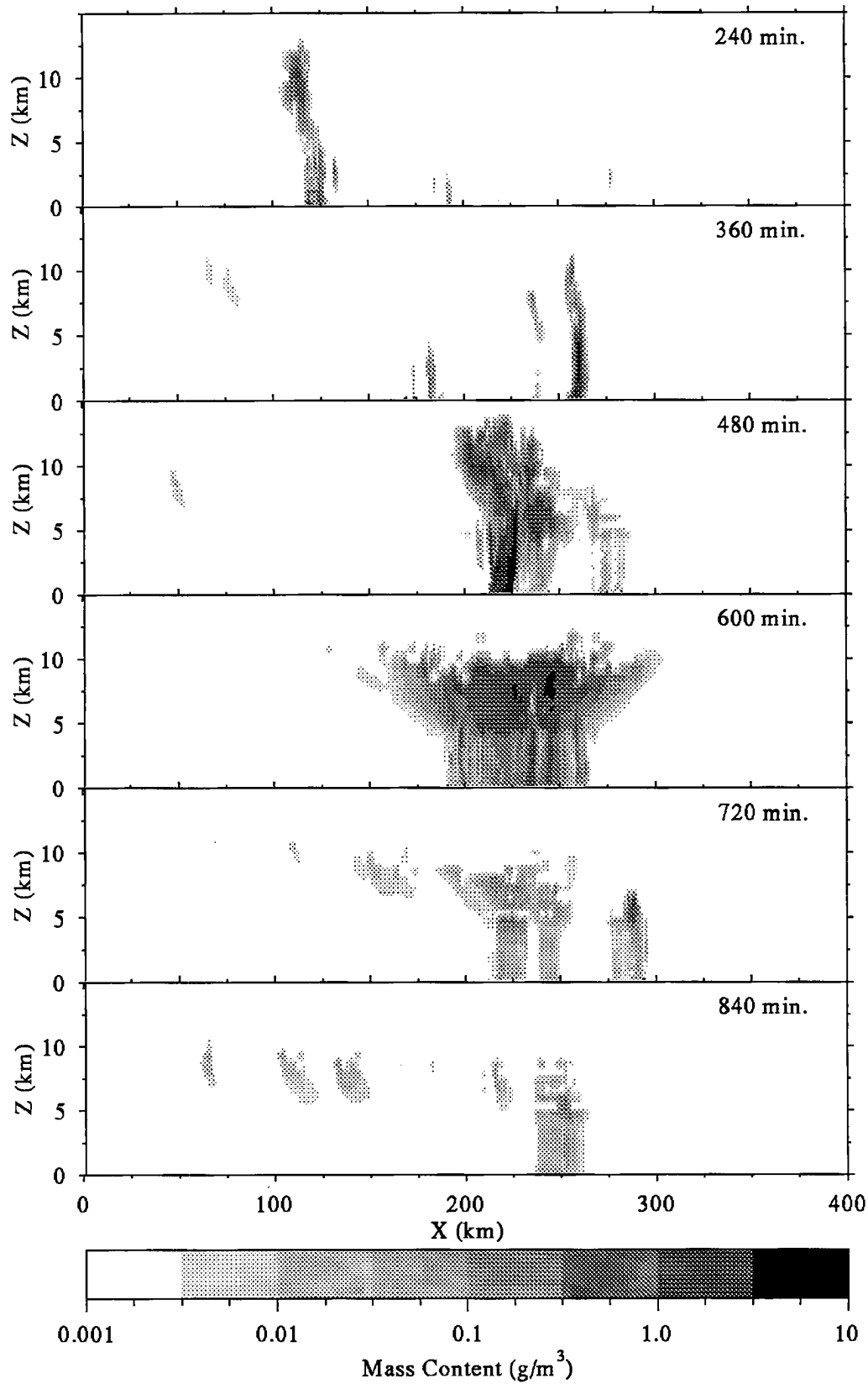


Figure 5.27: Total precipitating hydrometeor (aggregate, graupel, rain) mass content for six model times from the Florida sea breeze simulation after Nicholls et al. (1991). The mass content is displayed logarithmically from $10^{-3}$ to 10 g/m$^3$.

The process of inverting radar observables to find hydrometeor distributions is not unique and is an area of active research. Two radar inversion methods are used here. One method recently developed by Turk et al. (1993) retrieves gamma distributions of rain, ice, and melting particles mainly from reflectivity with a procedure that assures spatial continuity. The other method retrieves both parameters of the exponential distribution, only for rain, from reflectivity and differential reflectivity using formulae from Illingworth and Caylor (1989). Attenuation at X band is not available for the validation because the large radar range ($\approx$ 100 km) made the attenuation noisy and unreliable. The reflectivity and $Z_{DR}$ are averaged over a substantial volume because of the corresponding 1.6 km radar beamwidth. Obviously, S band reflectivity cannot measure cloud water, and the Illingworth and Caylor (1989) method can only be used for rain.

The radar inversion method described in Turk et al. (1993) retrieves the three parameters ($N_0$, $\Lambda$, and $m$) for a gamma size distribution $N(D) = N_0 D^m \exp(-\Lambda D)$ of equivalent volume spheres. The type of particle (water, ice, or melting) is assigned based on $Z_{DR}$, and a particle density of $\rho = 0.75$ g/cm$^3$ is assumed for ice. The melting particle composition is determined with a variable water fraction parameter. The procedure starts near the surface where an $N_0$ and $m$ are assumed and $\Lambda$ computed to agree with the reflectivity. For $Z_H < 35$ dBZ, $N_0 = 8000$ mm$^{-1}$ m$^{-3}$ and $m = 0$ for the initial point, but for higher reflectivity $N_0$ is decreased and $m$ increased (up to 5). The method then moves upward and adjusts the three parameters smoothly keeping agreement with the reflectivity. As the reflectivity decreases $\Lambda$ increases and $m$ decreases. The profiles are processed starting from the core region and moving radially outward, in such a way that there is continuity between profiles. The particle mass content is computed from the size distribution and compared with the passive microwave derived mass content at 0.5 km vertical intervals.

Retrieving the size distribution for rain is more straightforward than for ice because one does not need to make assumptions about composition or shape. Using the fact that the oblateness of raindrops is related to their volume, Seliga and Bringi (1976) showed how differential reflectivity could be used to infer the mean size of an exponential distribution of raindrops. With improved measurements of drop oblateness Illingworth and Caylor (1989) computed simple fits to the $D_0$-$Z_{DR}$ relation, which agreed closely with radar observations they presented. The median equivalent volume diameter $D_0$ is 3.67 times the mean diameter $\overline{D}$ used here. Table 5.9 lists the fit coefficients for $D_0$-$Z_{DR}$ and also for $Z_H$-$Z_{DR}$ with a fixed distribution intercept $N_0$. Here the fit for a maximum drop diameter of 10 mm is used. The fits give $Z_H$ correct to 0.2 dBZ. The retrieval procedure computes the mean drop diameter and distribution intercept from $Z_H$ and $Z_{DR}$ with the formulae in Table 5.9, and then calculates the corresponding mass content (5.2). The major problem with this inversion method appears to be contamination of the rain signal with ice below the freezing level. Large nearly spherical ice particles decrease $Z_{DR}$ while

increasing $Z_H$. The method interprets this situation as small average raindrop size with large reflectivity, which leads to extremely large computed mass contents. To deal partially with this problem the exponential distribution intercept $N_0$ is limited to a maximum value of 8000 $mm^{-1}$ $m^{-3}$, which was chosen to make the rain mass content fairly uniform vertically (and also because it is the Marshall-Palmer intercept). In addition the rain mass was retrieved only in areas below 4 km and with $Z_{DR} \geq 1.0$ dB.

Table 5.9: Fit coefficients for $D_0$-$Z_{DR}$ and $Z_H$-$Z_{DR}$ relations for raindrops from Illingworth and Caylor (1989) (Table 3). The first fit is used to find the exponential distribution slope or mean size $\overline{D}$ from $Z_{DR}$. The second is used to find the intercept $N_0$ by scaling $N_0$ to match $Z_H$. The fits assume a maximum drop diameter of 10 mm.

| $a_0$ | $a_1$ | $a_2$ | $a_3$ | $a_4$ | $Z_{DR}$ Range |
|---|---|---|---|---|---|
| $3.67\overline{D} = D_0 = \sum_i a_i Z_{DR}^i$ ($Z_{DR}$ in dB and $D_0$ in mm) | | | | | |
| 0.4453 | 1.311 | -0.9074 | 0.3863 | | 0.1 dB$\leq Z_{DR} \leq$1.0 dB |
| 0.5998 | 0.6762 | -0.04640 | 0.003804 | | 1.0 dB$\leq Z_{DR} \leq$4.5 dB |
| | | | | | |
| $Z_H = \sum_i a_i Z_{DR}^i$ for $N_0 = 8000 mm^{-1} m^{-3}$ ($Z_{DR}$ in dB and $Z_H$ in dBZ) | | | | | |
| 2.620 | 95.14 | -162.8 | 159.0 | -59.15 | 0.1 dB$\leq Z_{DR} \leq$1.0 dB |
| 16.58 | 22.64 | -5.020 | 0.6882 | -0.03818 | 1.0 dB$\leq Z_{DR} \leq$4.5 dB |

### 5.2.5 Bayesian precipitation retrieval setup

The procedures described in the previous chapter are used to perform the hydrometeor profile retrievals from the cloud model output and the AMPR brightness temperatures. A 7 layer precipitation structure with a maximum height of 13 km is chosen to facilitate comparisons with radar reflectivity. Table 5.10 lists the variable parameters in the precipitation structure. Only the hydrometeor mass contents are variable; the mean particle size is fixed. There is variable rain, ice, and cloud water. For the land case the surface emissivity is variable (i.e. retrieved) and a prior distribution with mean of 0.85 and standard deviation of 0.05 is assumed. For the ocean case the emissivity factor is fixed at unity, meaning pure Fresnel reflection is assumed. The ocean surface temperature is set to 301°K, while the land surface temperature is 305°K. The temperature and water vapor profiles are held fixed at their climatological values (from prior information).

It would seem to be desirable to have two categories of ice in the precipitation structure as the cloud model did. One category would be "graupel" or moderate size high density ice (say $\rho = 0.9$ g/cm$^3$), while the other would be "aggregate" with larger size low density ice (say $\rho \leq 0.1$ g/cm$^3$). Using the low density ice requires the delta-Eddington approach. Including the aggregate category (for example, with mean diameter 2.50 mm and density 0.1 g/cm$^3$) causes unstable retrievals because the observations can be matched only with difficulty. Forward radiative transfer modeling from the RAMS cloud model hydrometeor fields shows that the low brightness temperatures ($<$ 110°K for both 37 and

Table 5.10: The variable parameters in the precipitation structure used in the CaPE validation.

| Layer | Heights (km) | Variable Parameters |
|---|---|---|
| 1 | 0-2 | RAINCONT |
| 2 | 2-4 | RAINCONT ICE2CONT CLOUDLWC |
| 3 | 4-5 | RAINCONT ICE2CONT CLOUDLWC |
| 4 | 5-7 | ICE2CONT CLOUDLWC |
| 5 | 7-9 | ICE2CONT CLOUDLWC |
| 6 | 9-11 | ICE2CONT CLOUDLWC |
| 7 | 11-13 | ICE2CONT |

85 GHz) of the strong convection land case can be met only with aggregates having a high particle density. This is because low density particles do not scatter enough, and nearly all the ice mass in the fields is in the aggregate category rather than the graupel category. Since there is little point in having two ice particles with similar densities, a single ice category is used, and the mass of aggregate and graupel are combined for determining the prior distribution from the cloud model fields. This can be thought of as using the equivalent volume sphere method of approximating low density ice with smaller solid ice. The single category approach is simpler and reduces the number of free microphysical parameters from four (aggregate density and mean diameter of rain, graupel, and aggregate) to two (mean diameter of rain and ice). The microphysical consistency of the cloud model output may be violated by having a single ice category, but the brightness temperature observations are indicating that aspects of the microphysical output from the cloud model may not be correct.

Three sets of microphysical assumptions are made for the retrievals. The first is that of the RAMS simulation (rain mean diameter of 0.54 mm, graupel diameter of 1.20 mm), the second has larger raindrops and smaller ice (0.70 mm and 1.00 mm mean diameter, respectively), and the third uses the Rutledge and Hobbs fixed intercept ($N_0$) distributions. Since the ice particles are modeled as high density (0.9 g/cm$^2$), the unscaled Eddington approximation is used. The prior distribution is made from all 45 model output times of the simulation. The cutoff for raining pixels is 0.04 kg/m$^2$ of rain, which gives 1680 raining columns over the whole cloud simulation. The somewhat high rain cutoff is justified by this application to convective rainfall. The optimization parameters for the retrieval program were as in the theoretical tests except that at least 5 and at most 10 optimizations tries were made.

### 5.2.6 Precipitation retrieval results and comparisons

Hydrometeor retrievals are done for tracks along pixels 20, 25, and 30 in the two (water and land) AMPR datasets, however, special attention is paid to the nadir pixel (25). Figs. 5.28 and 5.29 show the AMPR brightness temperatures along these three

tracks for the ocean and land datasets, respectively. The large brightness temperature depressions for the 37 and 85 GHz channels for the 2059 dataset show that the convection over land is much stronger than the cell in the 2152 dataset over the ocean.

The comparison of the CP-2 radar reflectivity with the reflectivity simulated from the hydrometeor profiles is shown in Fig. 5.30 for the 2152 dataset and nadir track. This retrieval used the "standard" setup which has a mean diameter of 0.70 mm for rain and 1.00 mm for ice and a forward probability distribution width of $\sigma = 10°$K for all channels. The basic structure of the simulated reflectivity is roughly correct in terms of the location of the reflectivity maximum and the fall off with height. The reflectivity of the rain in the first cell is about right. The second rain cell, which is quite distinct in the CP-2 image, is not apparent in the AMPR derived radar image. This is to be expected, since the 10 GHz brightness temperature stays level between scans 45 and 50. The AMPR derived reflectivity is much too high in the non-raining area beyond scan 55. This is partly due the prior distribution, made only from raining pixels, which causes there to always be some rain. The 10 GHz channel is still decreasing for the last few scans, and has not reached its lowest value. This is probably due to slight brightness temperature warming from cloud water, which the radar does not see. The precipitation retrieval method is interpreting the brightness temperature warming as due to rain instead of cloud water. In addition the surface emissivity is probably underestimated, because a flat water surface is assumed, so light rain may be retrieved to compensate. Not surprisingly, microwave radiometry cannot detect the detailed vertical structure if it does not follow the expectations of the prior distribution; for example, the retrieval misses the reflectivity minimum around scan 45 at a height of 8 km.

A more quantitative comparison of the observed and simulated reflectivity images is shown in Fig. 5.31, which plots the rms reflectivity difference profile. For these plots the rms is done for a subset of the data that has reflectivity above about 24 dBZ. In addition to the standard retrieval discussed above (plotted as a dotted line), the retrievals for other microphysical assumptions are also plotted. The retrieval with the fixed intercept is clearly poorer than the others. The fixed intercept result in small mean diameters of ice in the top layers, which have low mass contents, giving reflectivities that are much too low. The reflectivity is also too low in the rain region for this method. Of the fixed mean size retrievals the one with smaller raindrops is slightly better in the rain layer, but significantly worse with the larger ice at higher altitudes. In this water surface situation the retrieval is relatively good, giving reflectivities in the rain layer to under 4 dB. Given the uncertainties in size distributions retrieving rain reflectivity to a factor of 2 (3 dB) may be considered a success. The rms difference in reflectivity in the midlevels is higher (8-10 dB), mainly because of the overestimate of ice above the second cell.

The rms reflectivity difference profiles shown in Fig. 5.32 compare the effect of using different observation widths ($\sigma$'s). Besides the standard $\sigma = 10°$K, fitting more closely

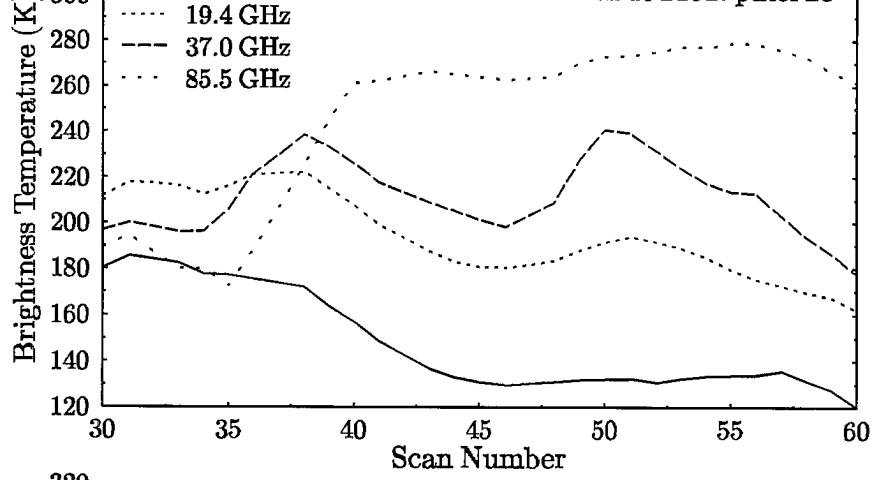
19.4 GHz
37.0 GHz
85.5 GHz
Brightness Temperature (K)
280
260
240
220
200
180
160
140
120
30
35
40
45
50
55
60
Scan Number

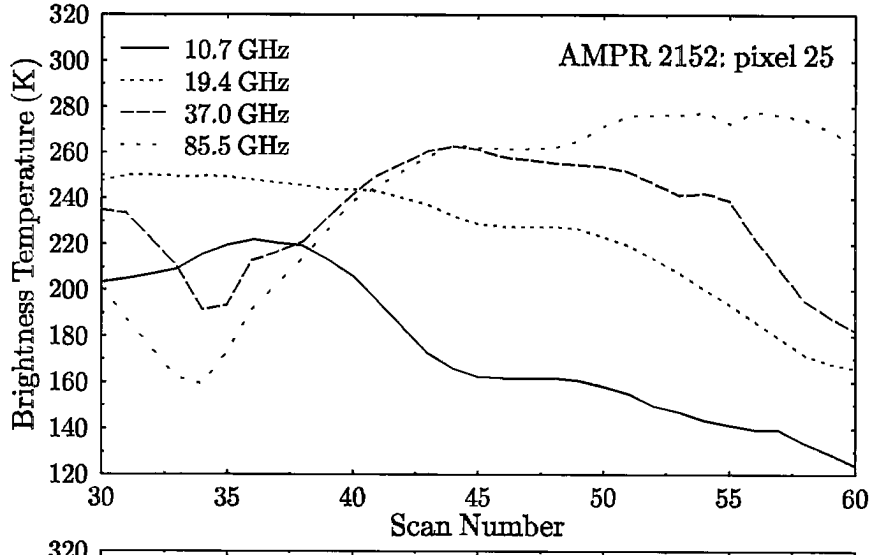
10.7 GHz
19.4 GHz
37.0 GHz
85.5 GHz
AMPR 2152: pixel 25
Brightness Temperature (K)
320
300
280
260
240
220
200
180
160
140
120
30
35
40
45
50
55
60
Scan Number

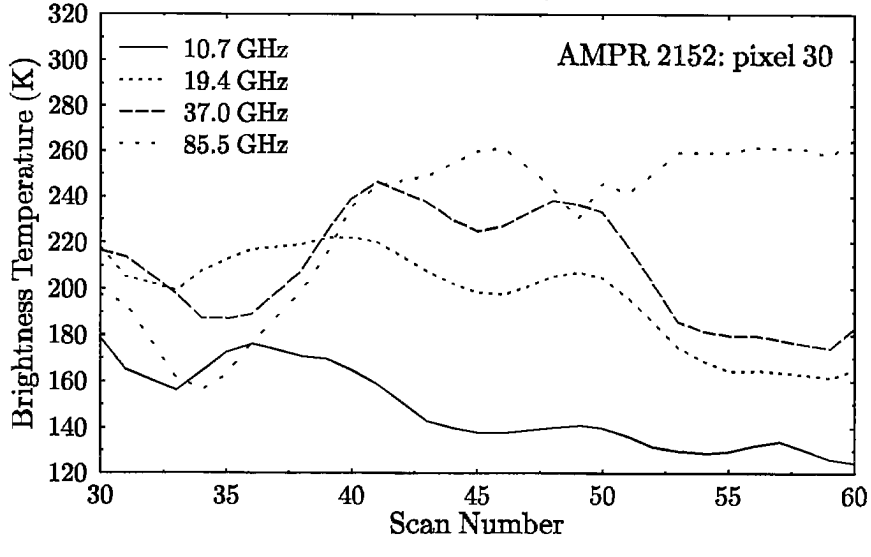
10.7 GHz
19.4 GHz
37.0 GHz
85.5 GHz
AMPR 2152: pixel 30
Brightness Temperature (K)
320
300
280
260
240
220
200
180
160
140
120
30
35
40
45
50
55
60
Scan Number

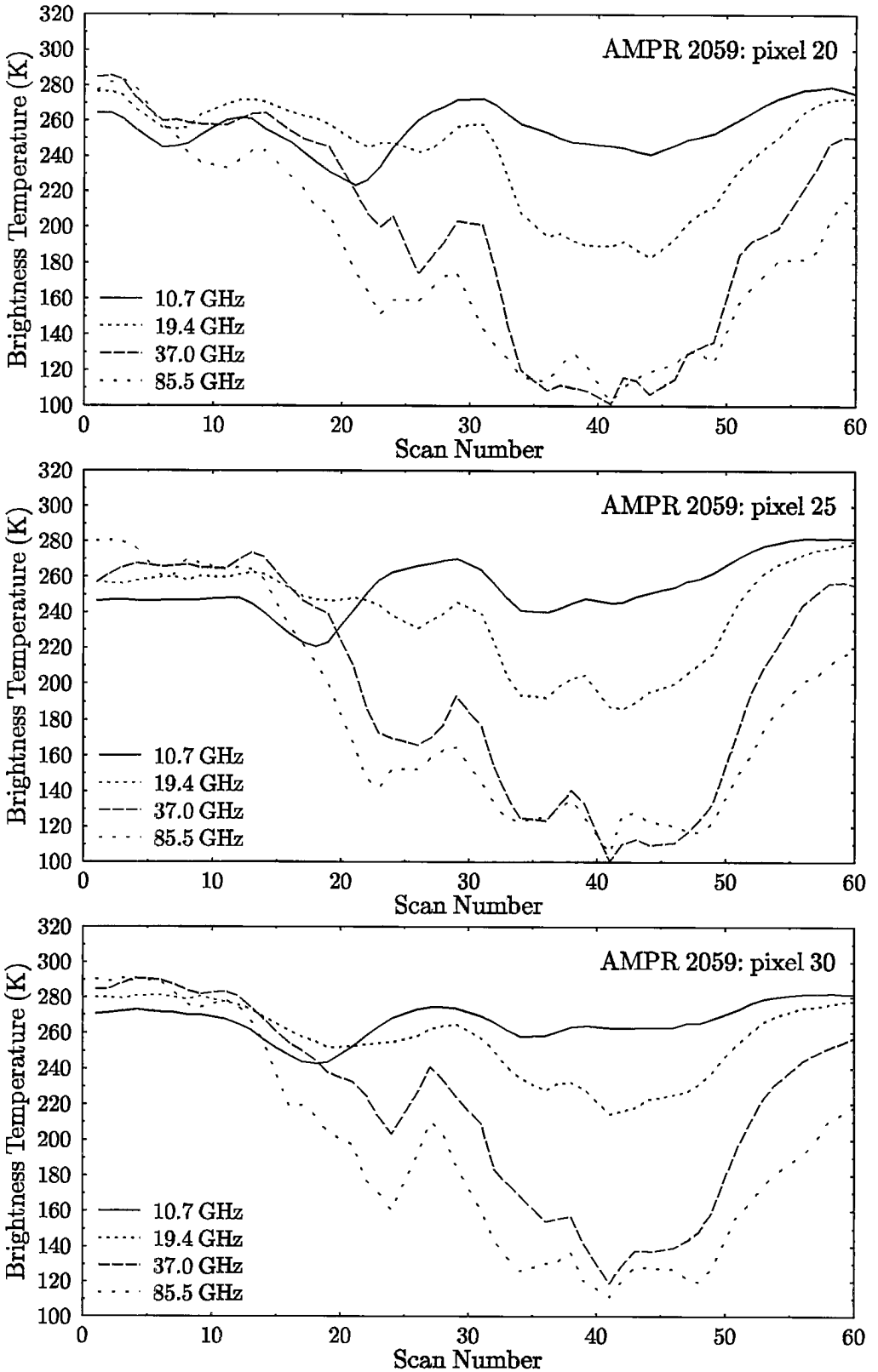


Figure 5.29: AMPR brightness temperature traces for pixels 20, 25, and 30 in the 2059Z (land) dataset. The scan direction is along the aircraft track.

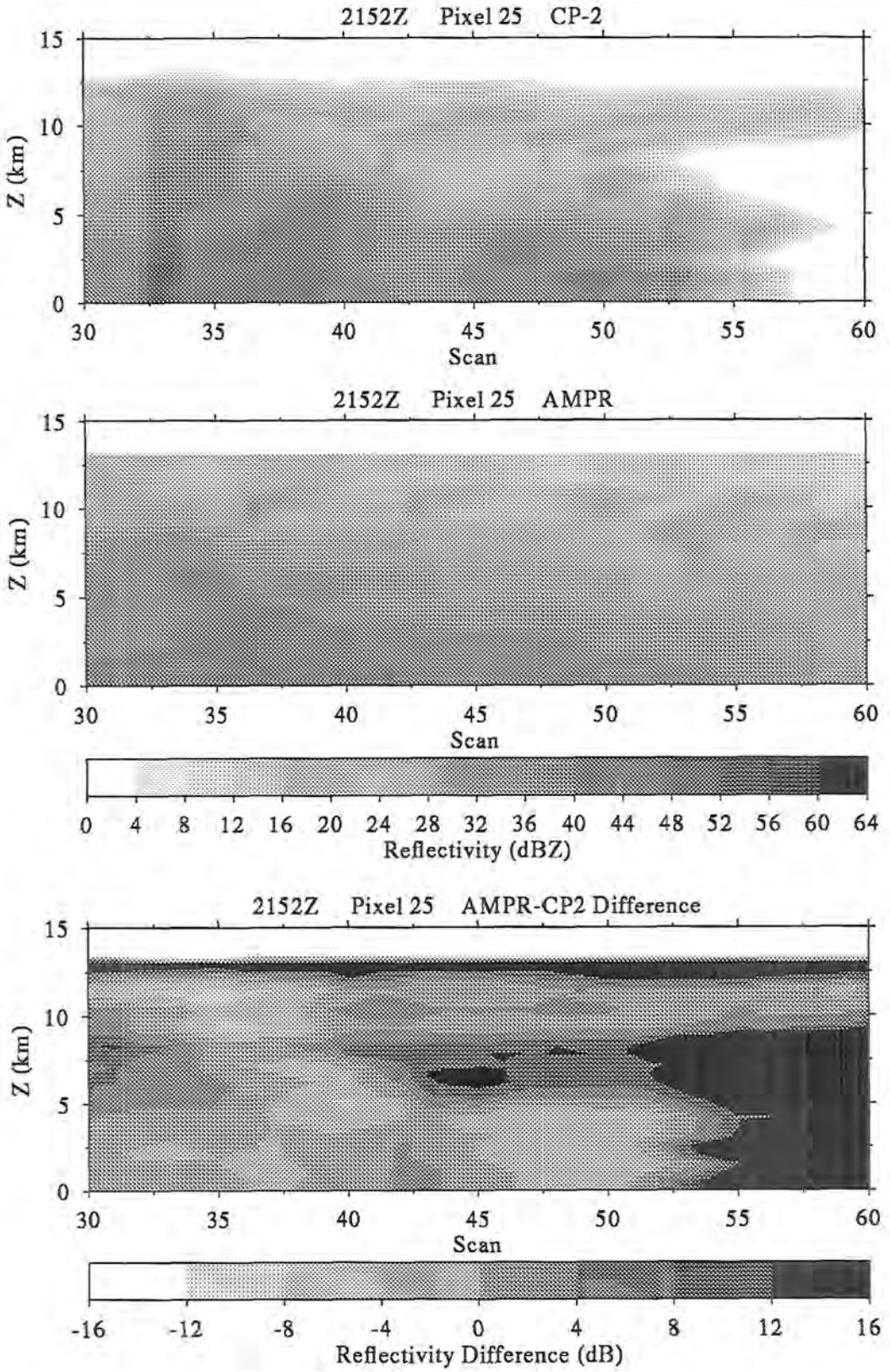


**Figure 5.30: Images of the reflectivity observed by CP-2 and reflectivity simulated from hydrometeor profiles retrieved from AMPR data for pixel 25 (nadir) in the 2152Z (ocean) dataset. The difference between the two reflectivity fields is also shown.**

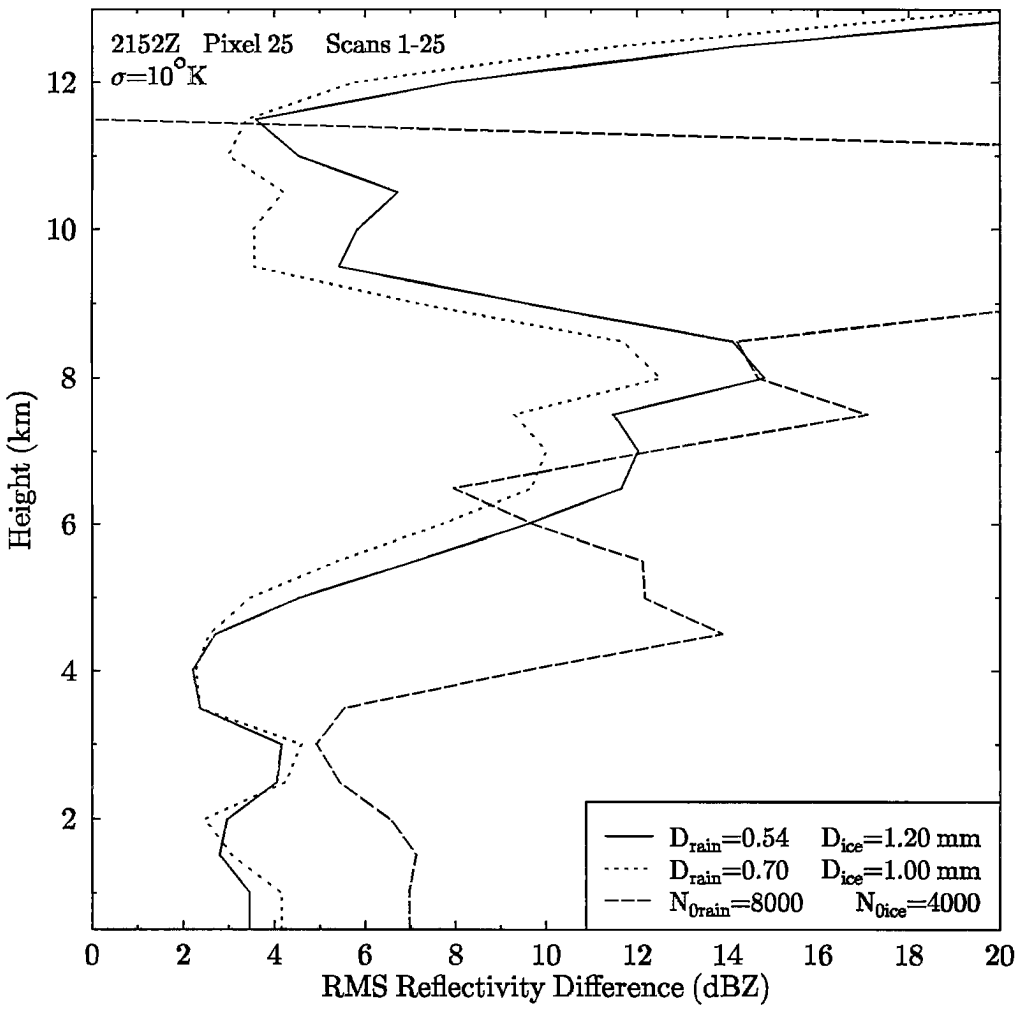


Figure 5.31: RMS difference between the observed CP-2 reflectivity and the AMPR derived reflectivity for the 2152Z dataset. Three different microphysical assumptions made for the microwave retrieval are shown.

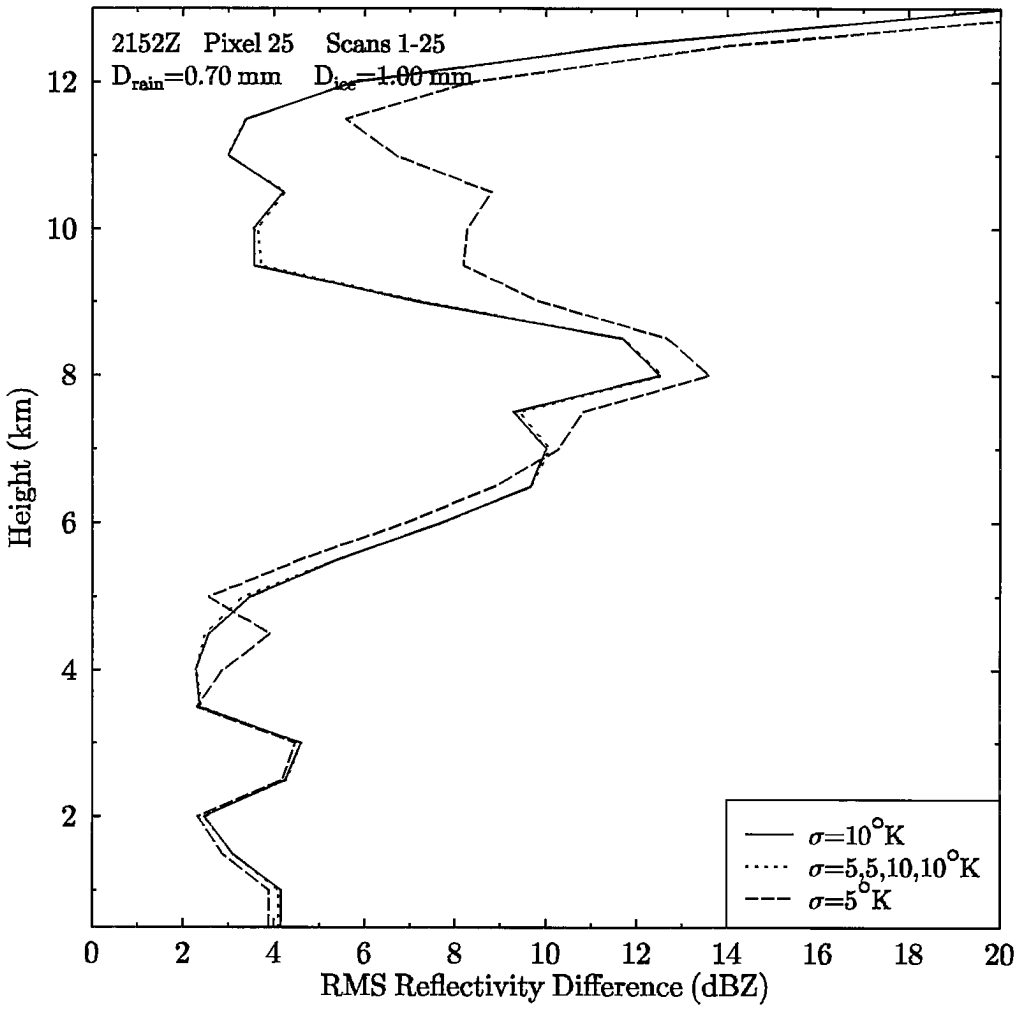


Figure 5.32: RMS difference between the observed CP-2 reflectivity and the AMPR derived reflectivity for the 2152Z dataset. Three different forward distribution widths used for the microwave retrieval are shown.

to all the channels ($\sigma$ = 5°K) and fitting more closely to just 10 and 19 GHz is tried ($\sigma = 5, 5, 10, 10$°K). There is not much difference in reflectivity error between the different observation widths, though $\sigma$ = 5°K is much worse at the higher ice levels. The wider forward distribution width ($\sigma$ = 10°K) is considered the standard here because overall (both datasets) it gave better agreement.

A comparison of radar derived and AMPR retrieved vertically integrated hydrometeor mass content for the ocean dataset is shown in Fig. 5.33. The difference in rain mass between the two radar inversions is perhaps indicative of the error in the radar mass retrieval. The method of Turk et al. (1993) gives roughly equal integrated rain mass for the two rain cells ($\approx$ 2 kg/m$^2$), while using the formula of Illingworth and Caylor (1989) gives much different rain mass for the two cells (4 vs. 2 kg/m$^2$). These two inversions

both match the reflectivity, but use different raindrop distributions. The $Z_{DR}$ is above 3 dB in the second cell and the Illingworth and Caylor (1989) method retrieves mean raindrop diameters of .60-.65 mm there, as compared to .50-.55 mm in the first cell. The smaller raindrops in the first cell lead to a higher mass content in order to give the same reflectivity. The mean diameters of the Turk et al. (1993) method are larger and more nearly equal for the two cells.

The integrated mass content traces are shown for AMPR retrievals with the three microphysical assumptions discussed above. The Rutledge and Hobbs assumption has the smallest mean diameter for raindrops and thus largest mass contents, followed by the 0.54 mm and then 0.70 mm mean drop diameters. The AMPR retrievals generally fall between the two radar estimates of integrated rain mass for the first precipitation cell. All of the microwave retrieved rain masses are too low for the second cell, because of the perhaps inexplicably low 10 GHz brightness temperatures. The passive microwave retrieved integrated ice mass agrees relatively well with the radar derived mass, except for the Rutledge and Hobbs microphysics case. This case has much greater integrated ice mass in the first cell because of a large amount of ice retrieved near the freezing level (that compensates for less above). The two retrievals with fixed mean particle size agree closely even though the average ice diameter is different by 20% (1.00 mm and 1.20 mm). Because of the assumptions concerning size distribution and particle density made for the radar retrieval of ice mass it is not wise to consider the radar to be truth in this case. Fig. 5.34 shows the integrated hydrometeor mass for the retrievals with two different forward distributions widths ($\sigma = 10$°K and $\sigma = 5$°K). The retrieval that fits more closely to the data has more rain in the first cell and less in the second cell than the standard retrieval. The integrated ice mass trace is clearly less smooth for the $\sigma = 5$°K case.

Turning now to the nadir track in the 2059Z dataset over land, Fig. 5.35 shows the reflectivity image comparison. The reflectivity is overestimated by the AMPR retrieval in the light precipitation area before scan 17. In the strong convection the reflectivity in the lower ice layers is modeled fairly well, but is too low for the higher ice layers. The AMPR derived reflectivity for rain in the two heavy precipitation cells is far too low compared with the actual CP-2 observations. For retrievals over land most of the information about the rain comes from its correlation with the ice mass above in the prior probability distribution since the rain is not sensed directly. Thus the prior distribution used here probably does not have the desired correlation. Since the retrieval method operates on vertical columns, it also has difficulty with the slanted precipitation cells observed by the radar. The large decrease in reflectivity seen around pixel 30 is seen as relative small brightness temperature warming at 37 and 85 GHz. Over land the change in 10 GHz brightness temperature from rain generally cannot be separated from surface emissivity changes, and here the retrieval of emissivity (not shown) closely follows the 10 GHz channel.

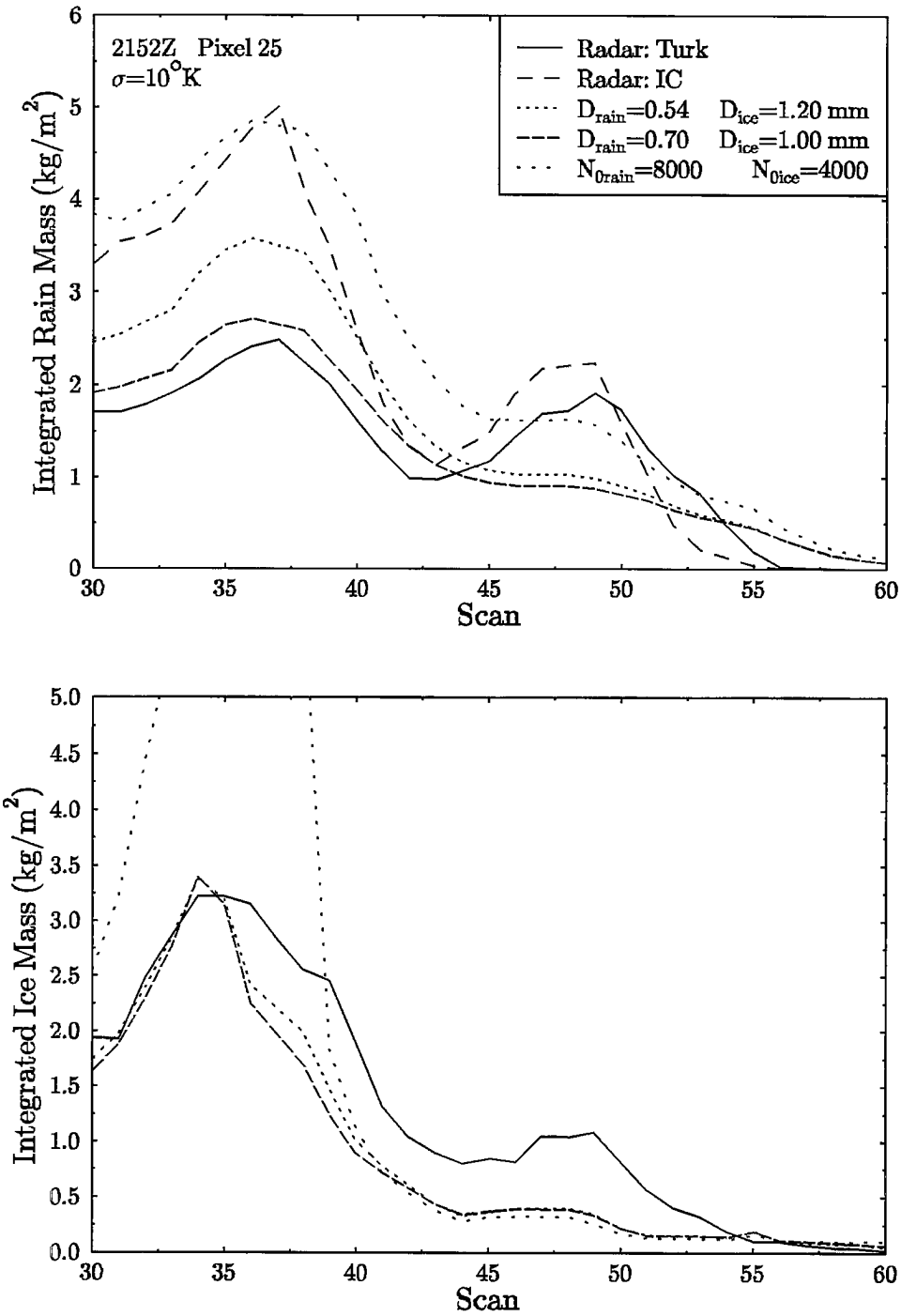


Figure 5.33: Vertically integrated rain and ice mass content derived from CP-2 radar and retrieved from AMPR data pixel 25 in the 2152Z dataset. Three different microphysical assumptions made for the microwave retrieval are shown. The Turk radar method is that in Turk et al. (1993) and the IC method is from Illingworth and Caylor (1989).

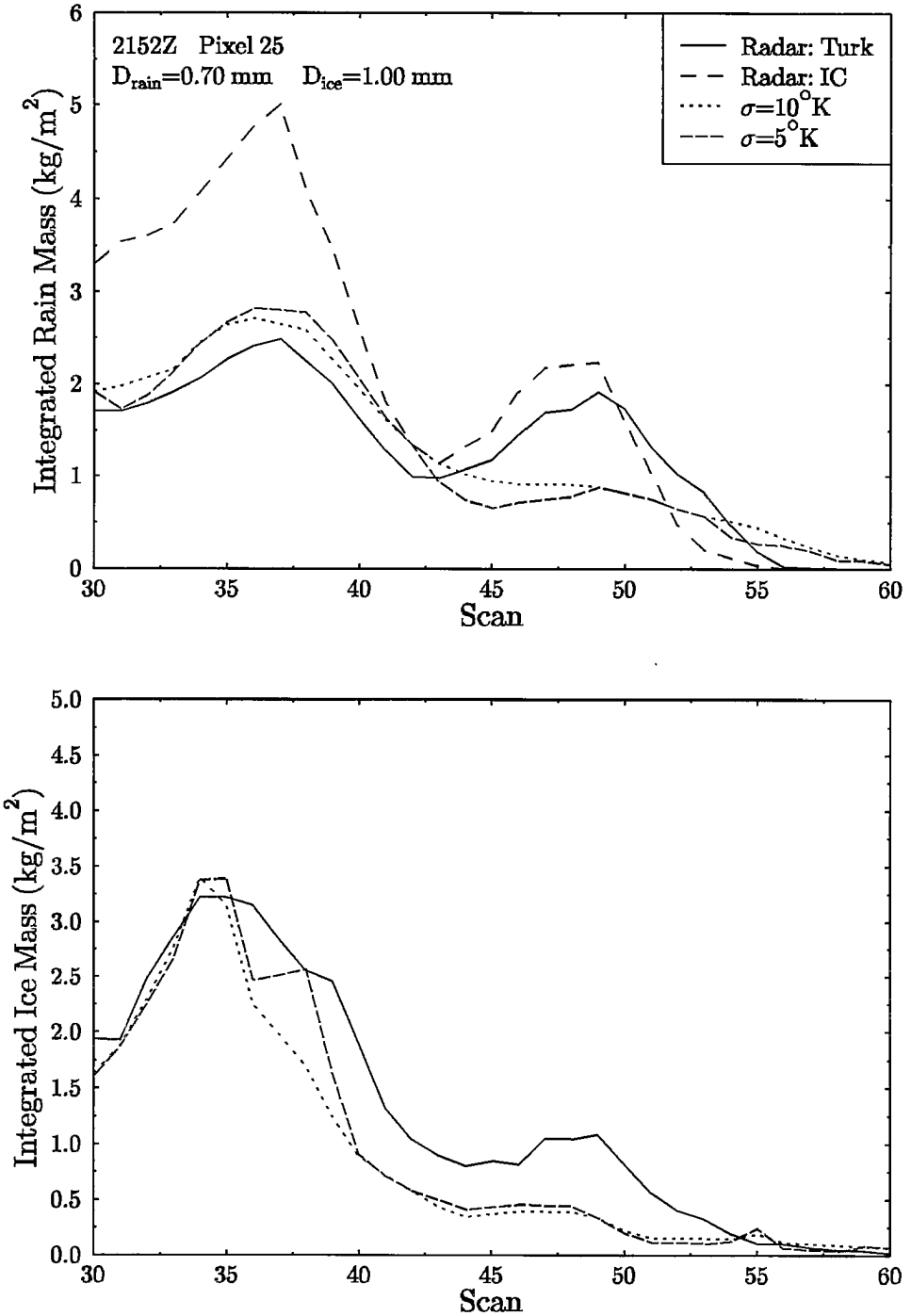


Figure 5.34: Vertically integrated rain and ice mass content derived from CP-2 radar and retrieved from AMPR data pixel 25 in the 2152Z dataset. Two different forward distribution widths used for the microwave retrieval are shown.

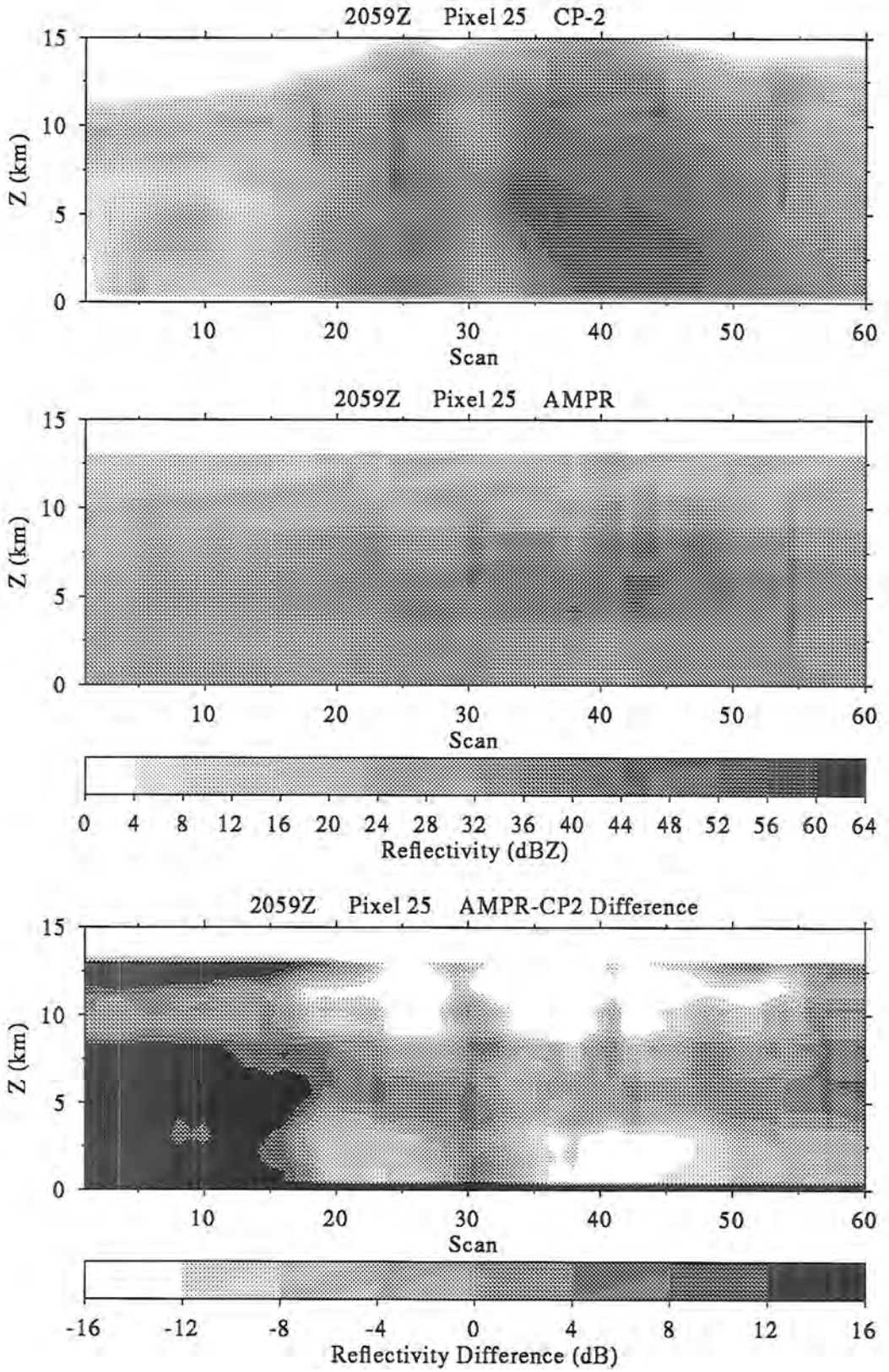


**Figure 5.35: Images of the reflectivity observed by CP-2 and reflectivity simulated from hydrometeor profiles retrieved from AMPR data for pixel 25 (nadir) in the 2059Z (land) dataset.**

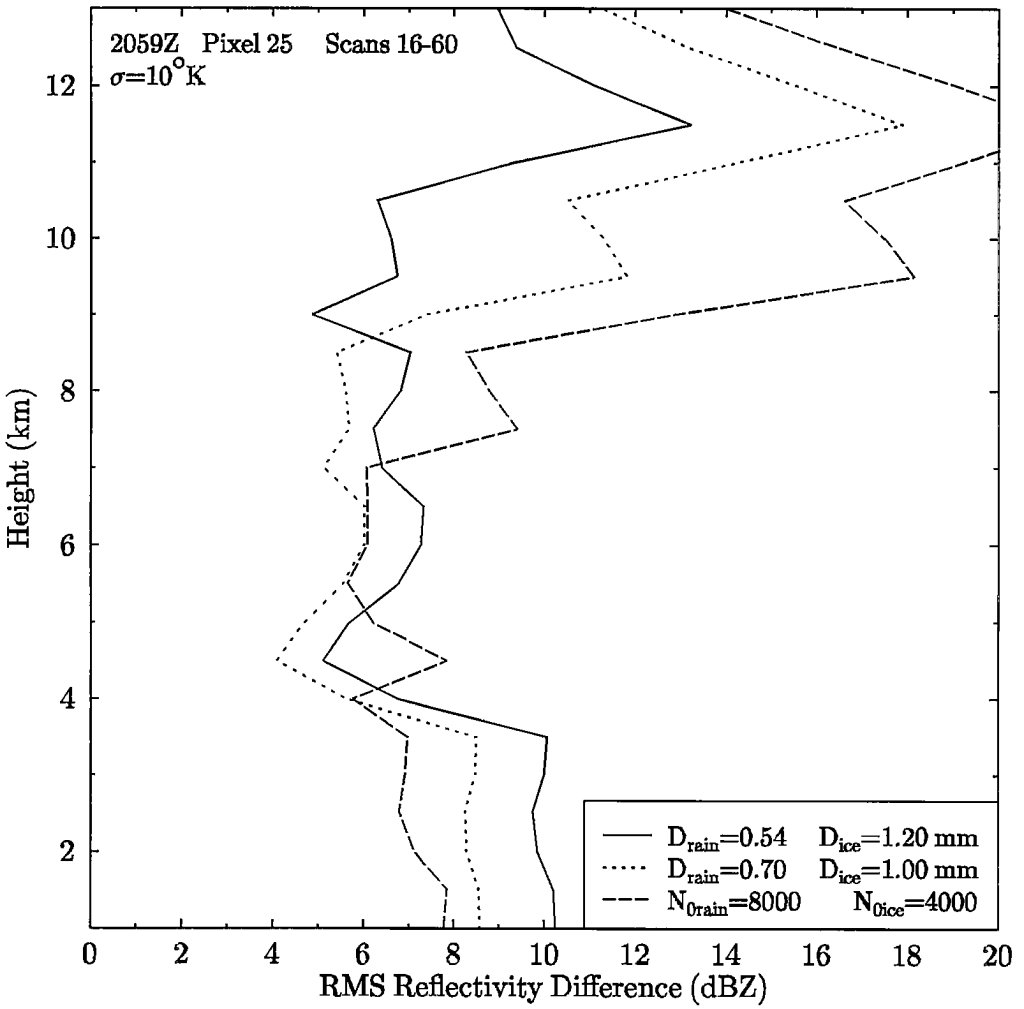


Figure 5.36: RMS difference between the observed CP-2 reflectivity and the AMPR derived reflectivity for the 2059Z dataset. Three different microphysical assumptions made for the microwave retrieval are shown.

Fig. 5.36 shows the rms reflectivity difference for retrievals with different microphysical assumptions. In the rain layer the fixed intercept assumption is somewhat better, while the smaller mean diameter (0.54 mm) case has even lower reflectivity than the standard case and has significantly more error. For the lower ice layers the retrieval with the smaller ice particles agrees better. Higher up, where the retrieved reflectivity is too low, the larger ice assumption has, of course, closer reflectivity. For this land case the retrieved reflectivity is further from the observed than for the ocean case. The standard assumption has rms reflectivity errors of around 8 dB in the rain layer and 6 dB in the lower ice levels. Fig. 5.37 shows the rms reflectivity difference for three sets of forward probability distribution widths. The different observation widths have equivalent reflectivity error except for midlevel ice layers where the larger width is better.

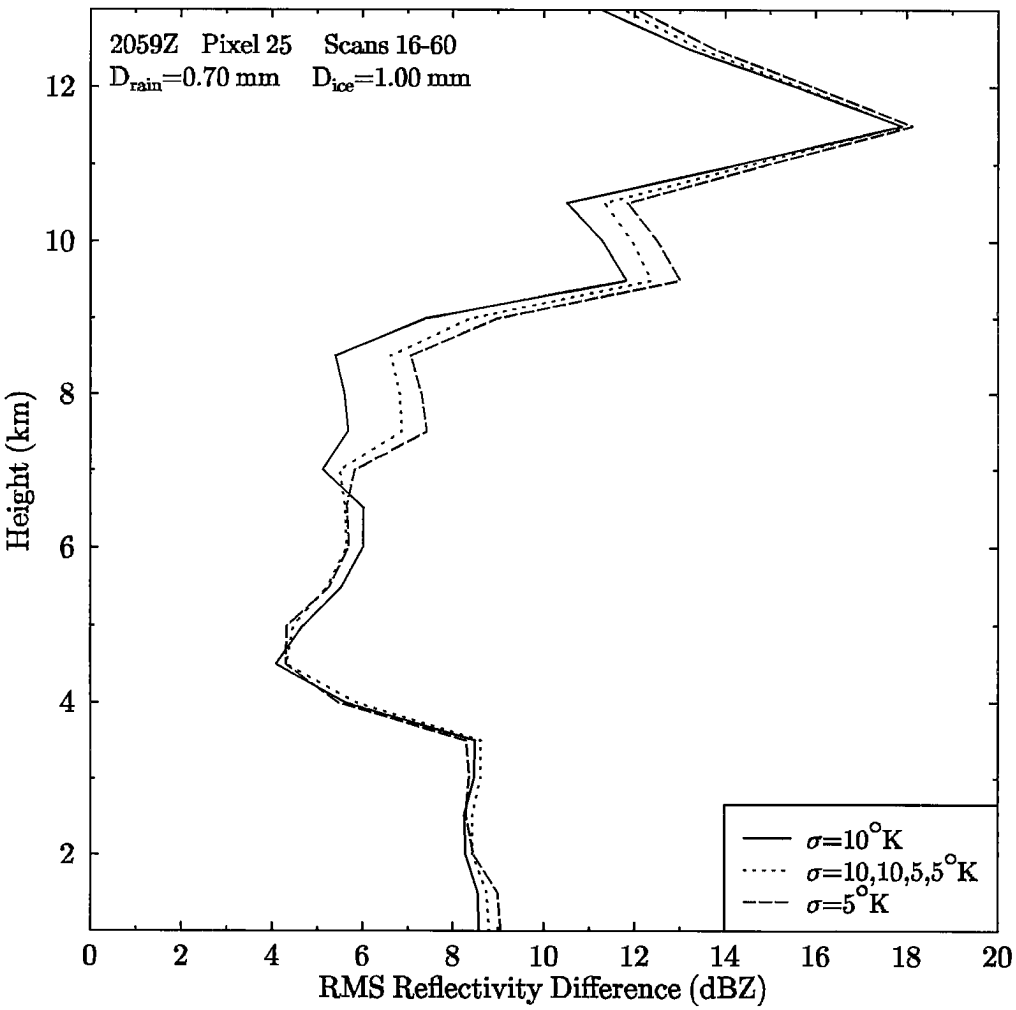


Figure 5.37: RMS difference between the observed CP-2 reflectivity and the AMPR derived reflectivity for the 2059Z dataset. Three different forward distribution widths used for the microwave retrieval are shown.

Comparisons of CP2 radar and AMPR microwave derived integrated hydrometeor mass contents are shown in Figs. 5.38 and 5.39. All three microphysical assumptions for the microwave retrieval grossly underestimate the integrated rain mass. The Illingworth and Caylor (1989) radar inversion method for rain mass was heavily contaminated by ice (low $Z_{DR}$ in high $Z_H$) and the maximum $N_0$ technique of correcting leaves this estimate of rain mass fairly uncertain. The fixed mean diameter AMPR retrieval results follow the radar derived ice mass reasonably well, though falling short in the most intense cell. Fitting the data more closely with $\sigma = 5°$K gives slightly higher rain mass and ice mass in some areas, although the difference is not really significant. Even though variable cloud liquid water is in the precipitation structure, virtually none is retrieved over land, although very small amounts (0.02 kg/m$^2$) are retrieved over the ocean. When the forward distribution width is set to $\sigma = 5°$K, then there are some pixels that have substantial amounts ($\geq 1$ kg/m$^2$) of cloud water, but in an obviously incorrect pattern.

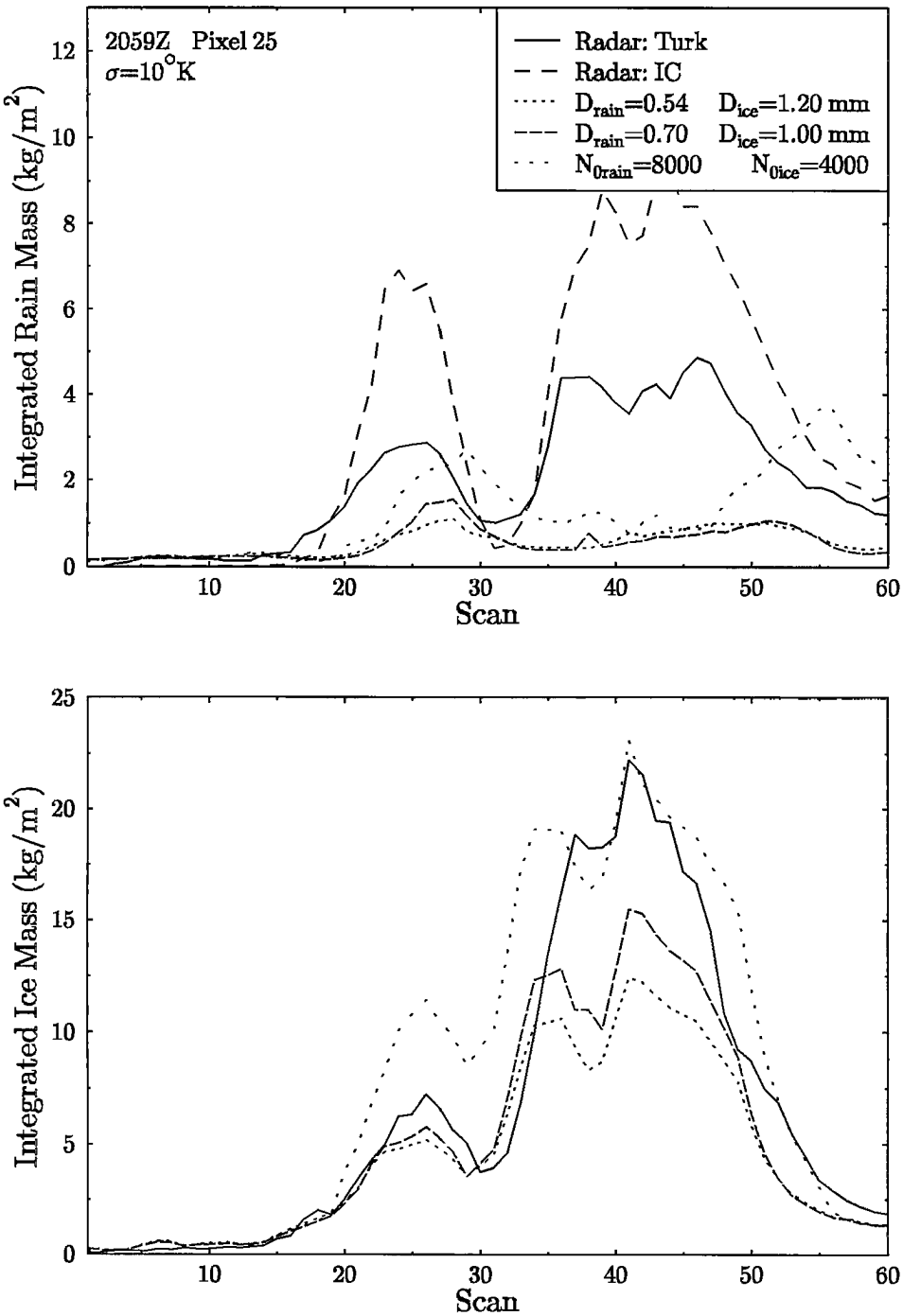


Figure 5.38: Vertically integrated rain and ice mass content derived from CP-2 radar and retrieved from AMPR data pixel 25 in the 2059Z dataset. Three different microphysical assumptions made for the microwave retrieval are shown.

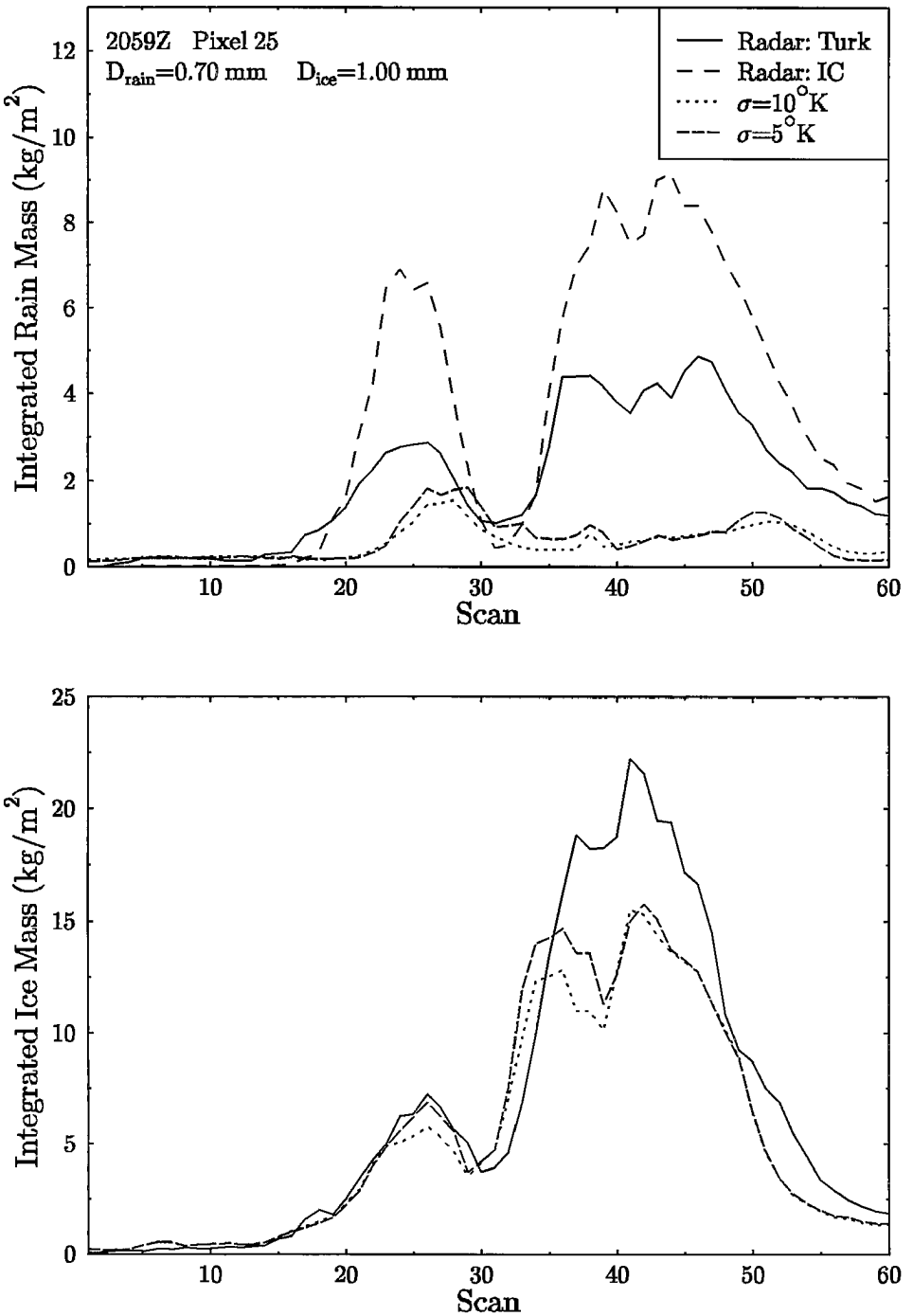


Figure 5.39: Vertically integrated rain and ice mass content derived from CP-2 radar and retrieved from AMPR data pixel 25 in the 2059Z dataset. Two different forward distribution widths used for the microwave retrieval are shown.

The reflectivity image comparison for the other two pixel tracks of the ocean dataset (2152Z) are shown in Figs. 5.40 and 5.41. The two tracks are 5 pixels (9 degrees in angle) away from the nadir track, which is greater than the largest beamwidth of the AMPR channels. The microwave retrieval for these tracks is rather poor. The CP-2 reflectivity image shows that there is only light rainfall, in some places not even reaching the ground. For pixel 20 from scan 40 to 60 the 19 GHz and 37 GHz channels are indicating light rain that the method retrieves as such, even though the radar indicates no rainfall. For pixel 30 the cells at scans 40 and 44 are seen in the 19 and 37 GHz channels, but again the retrieval indicates more rain than the radar sees. One plausible reason for the large discrepancy between the observed and retrieved rain layer reflectivities is that these tracks are on the edge of the precipitation cell where the hydrometeor fields are changing rapidly. The coarser resolution of the lower frequencies compared with the radar would cause the AMPR retrieved rain amounts to be higher. The reflectivity in the high level ice is retrieved fairly well because of the high resolution 85 GHz channel. The integrated hydrometeor mass contents for these two tracks are shown in Figs. 5.42 and 5.43. The rain mass is fairly low, but nonetheless overestimated substantially by the AMPR retrieval as compared with the radar retrieved mass. The integrated ice mass agrees well outside the first cell. The ice mass retrieved from the AMPR data follows the 85 GHz channel quite closely.

Figs. 5.44 and 5.45 show the reflectivity image comparison for the two off nadir pixel tracks of the land dataset (2059Z). The AMPR retrieval, as indicated by the simulated reflectivity, behaves similarly for these two tracks as for the nadir track over land. The simulated reflectivity is lower in the rain layers than the lower ice layers. While usually wrong, this happens to be correct for pixel 20, which has an rms reflectivity difference (scans 6 to 60) of under 8 dB up to 9 km. The AMPR derived reflectivity is again too high in the light or no rain regions. Where the observed reflectivity is higher above than below, the microwave retrieval greatly overestimates the reflectivity in the lower region (e.g. scans 25 to 40 for pixel 30). This is to be expected since the upwelling microwave radiation is much more sensitive to the integrated amount of ice than to its vertical structure. Figs. 5.46 and 5.47 compare the integrated hydrometeor mass for two tracks. The integrated rain retrieved from the microwave data is much less than the radar derived rain mass for pixel 20, but too high for much of the domain for pixel 30. The retrieved integrated ice masses do agree closely, except for a small region in the pixel 20 track in which the radar is spuriously high.

One possibility for improving the agreement between the microwave retrievals and the corresponding radar hydrometeor inversion is to average over the size of the beamwidths of the low frequency channels. The averaging is done with the integrated hydrometeor traces, and not with the input microwave brightness temperatures or radar reflectivities. The retrievals are run for pixels 24 through 27 (2 on each size of nadir) and averaged in the pixel direction. Then a four point moving average in the scan direction is applied.

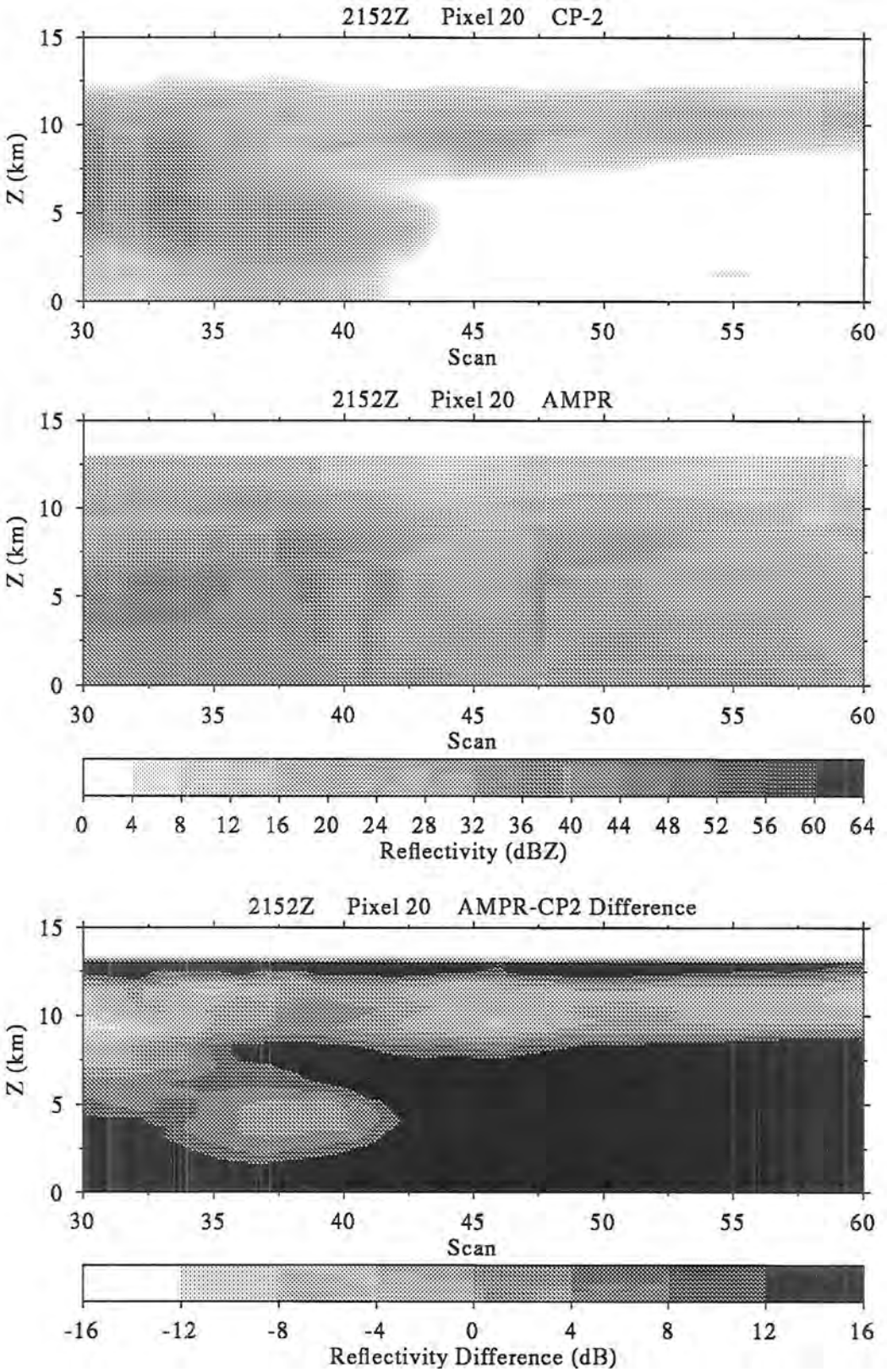


Figure 5.40: CP-2 observed and AMPR retrieved reflectivity for pixel 20 in the 2152Z dataset.

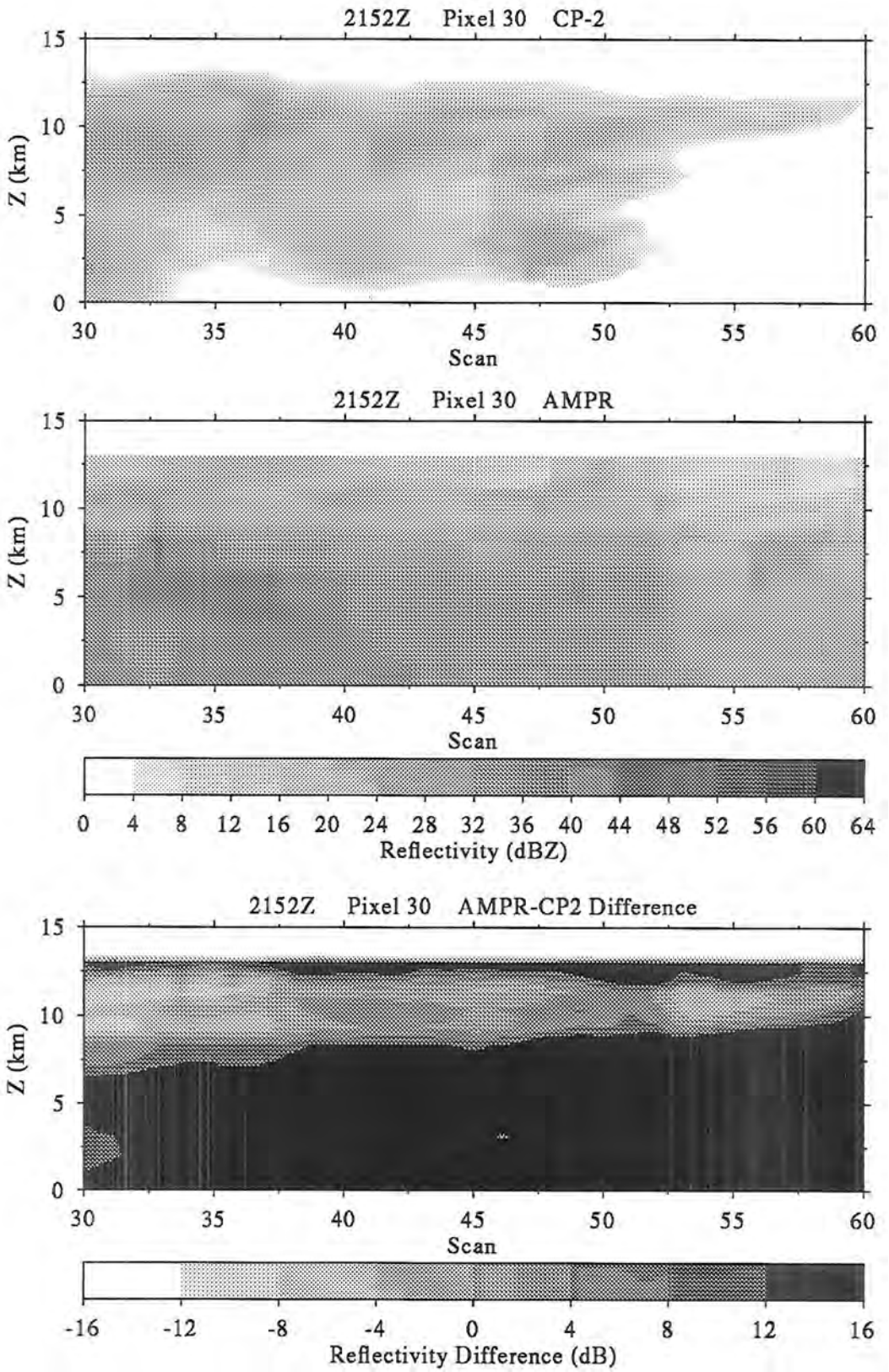


**Figure 5.41: CP-2 observed and AMPR retrieved reflectivity for pixel 30 in the 2152Z dataset.**

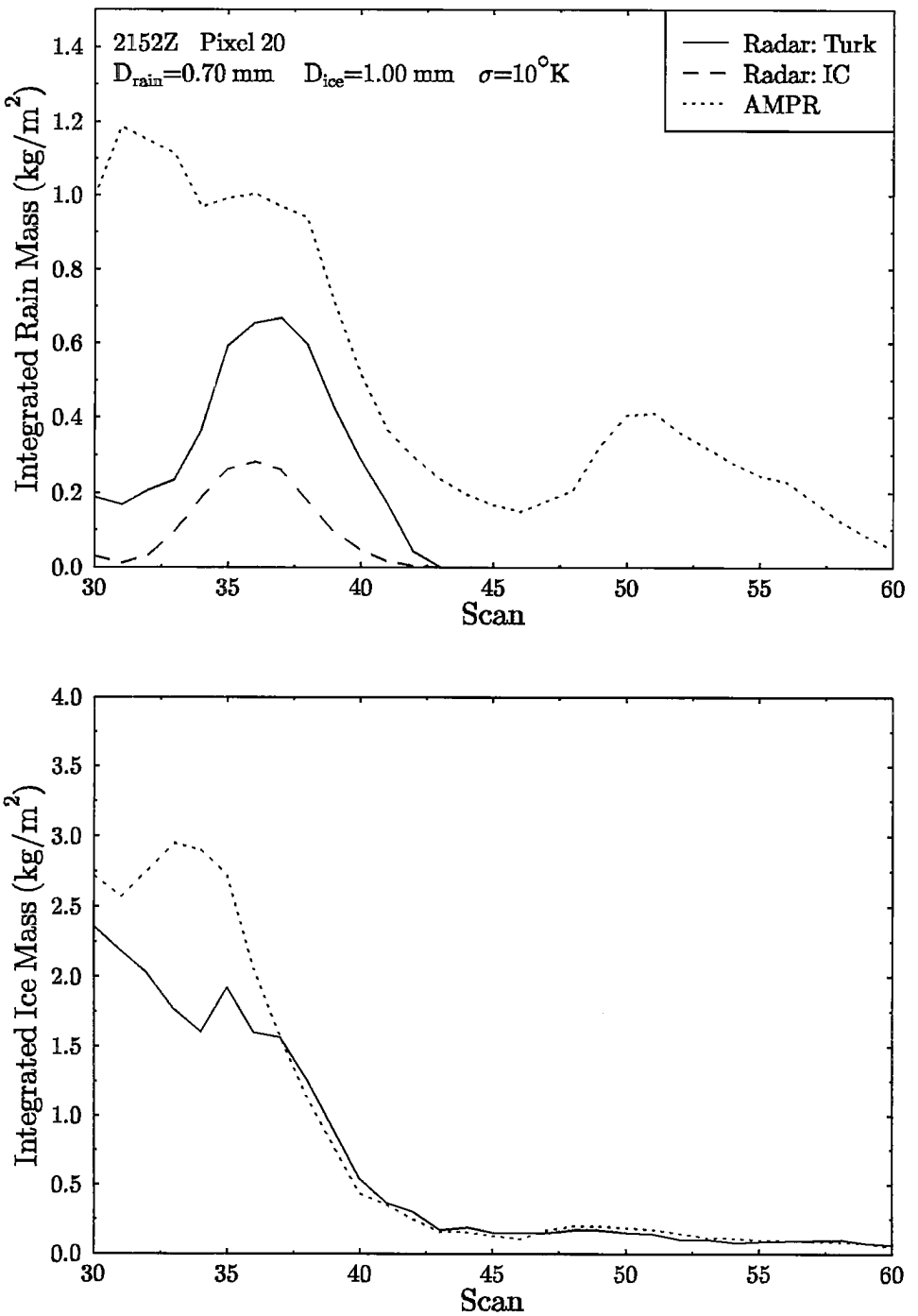


Figure 5.42: Vertically integrated rain and ice mass content derived from CP-2 radar and retrieved from AMPR data for pixel 20 in the 2152Z dataset.

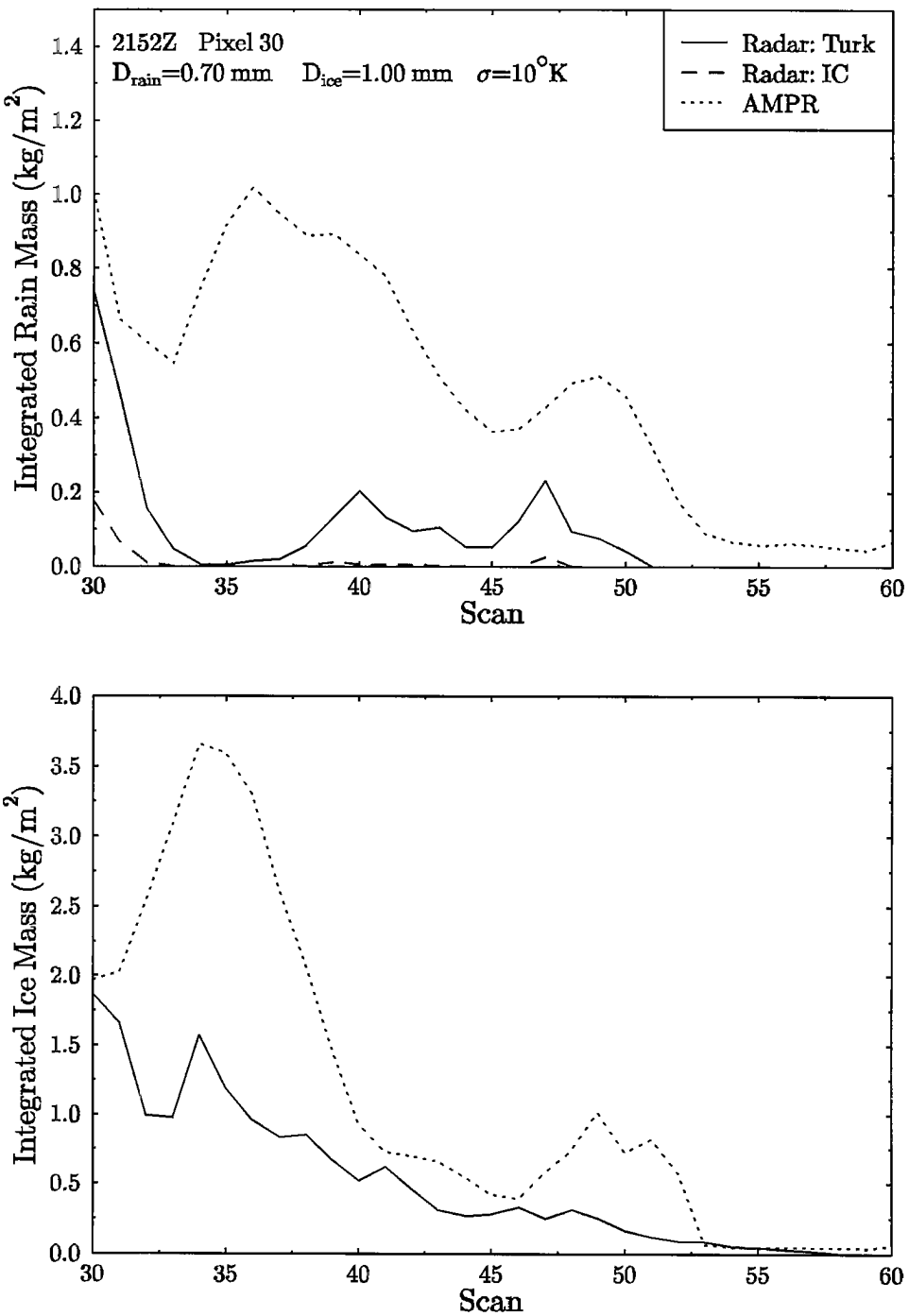


Figure 5.43: Vertically integrated rain and ice mass content derived from CP-2 radar and retrieved from AMPR data for pixel 30 in the 2152Z dataset.

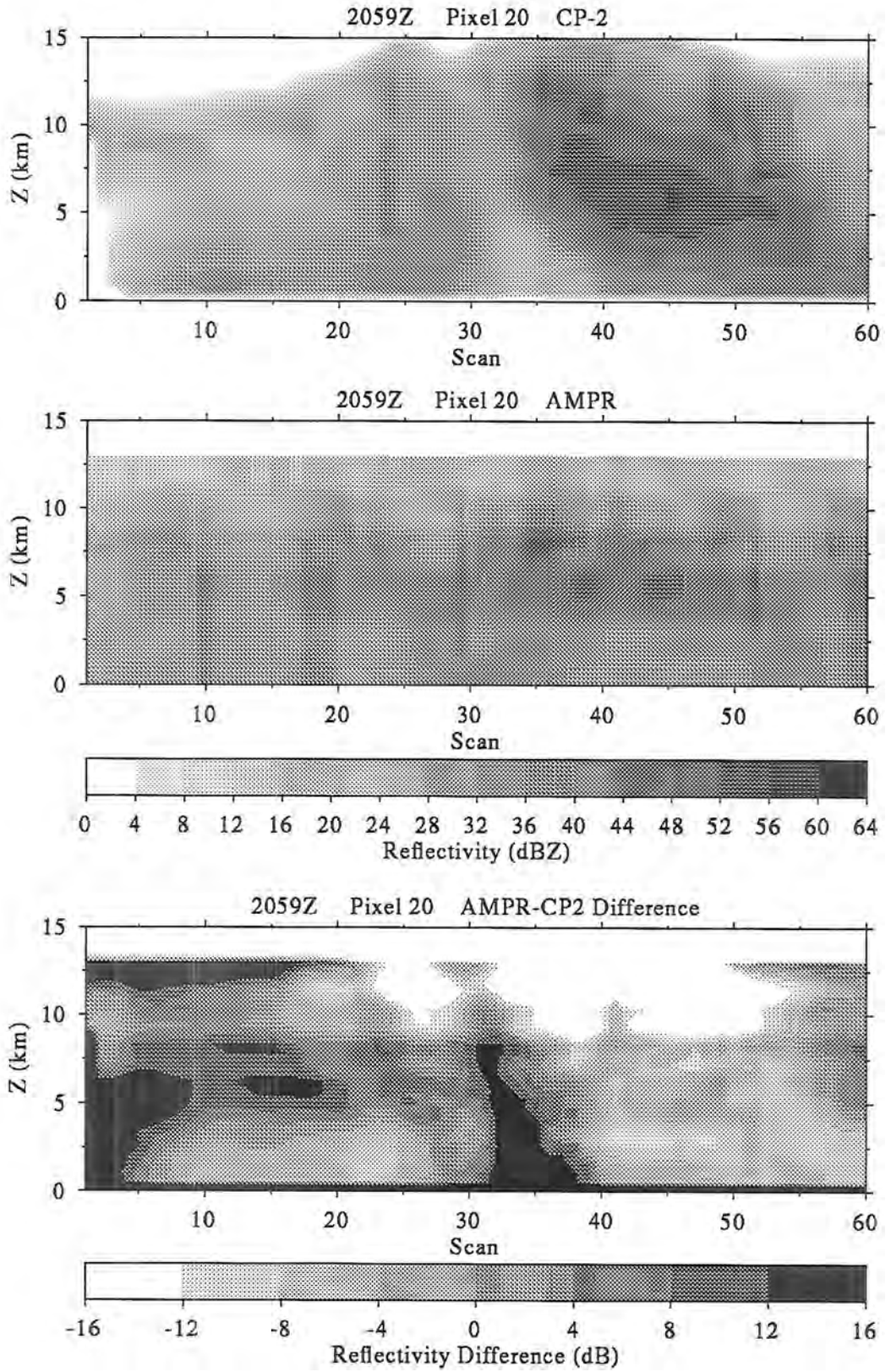


Figure 5.44: CP-2 observed and AMPR retrieved reflectivity for pixel 20 in the 2059Z dataset.

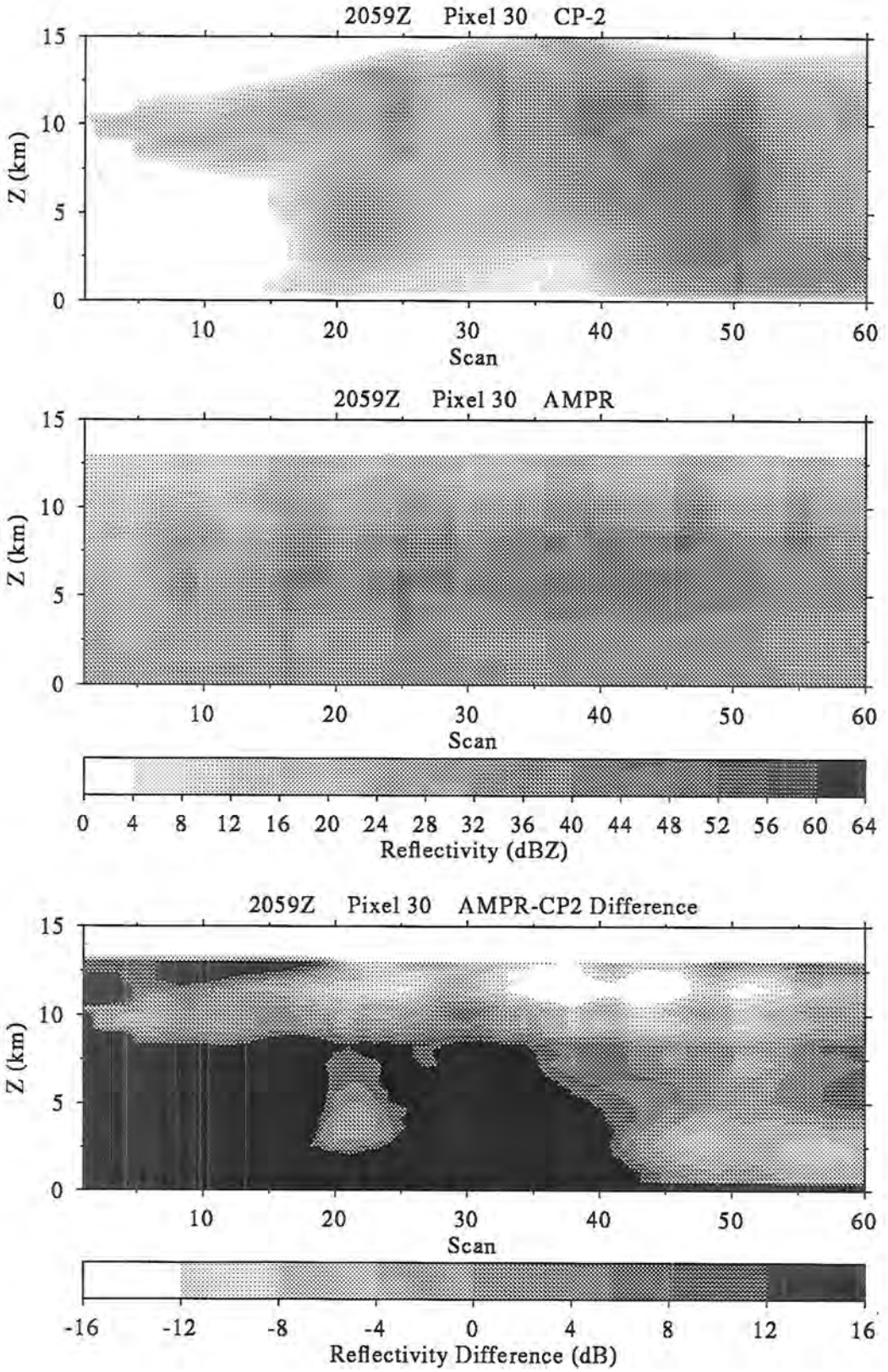


**Figure 5.45: CP-2 observed and AMPR retrieved reflectivity for pixel 30 in the 2059Z dataset.**

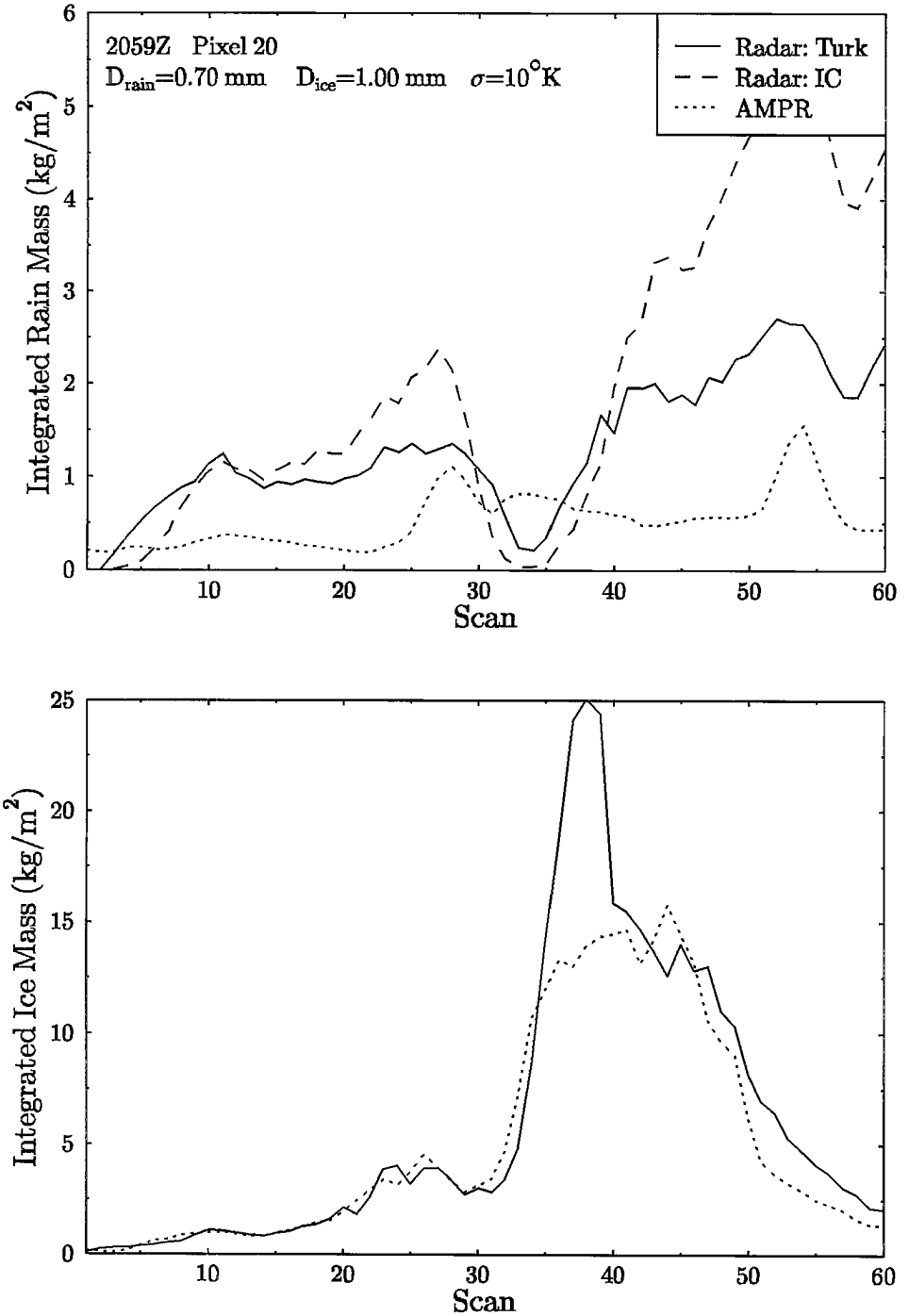


Figure 5.46: Vertically integrated rain and ice mass content derived from CP-2 radar and retrieved from AMPR data for pixel 20 in the 2059Z dataset.

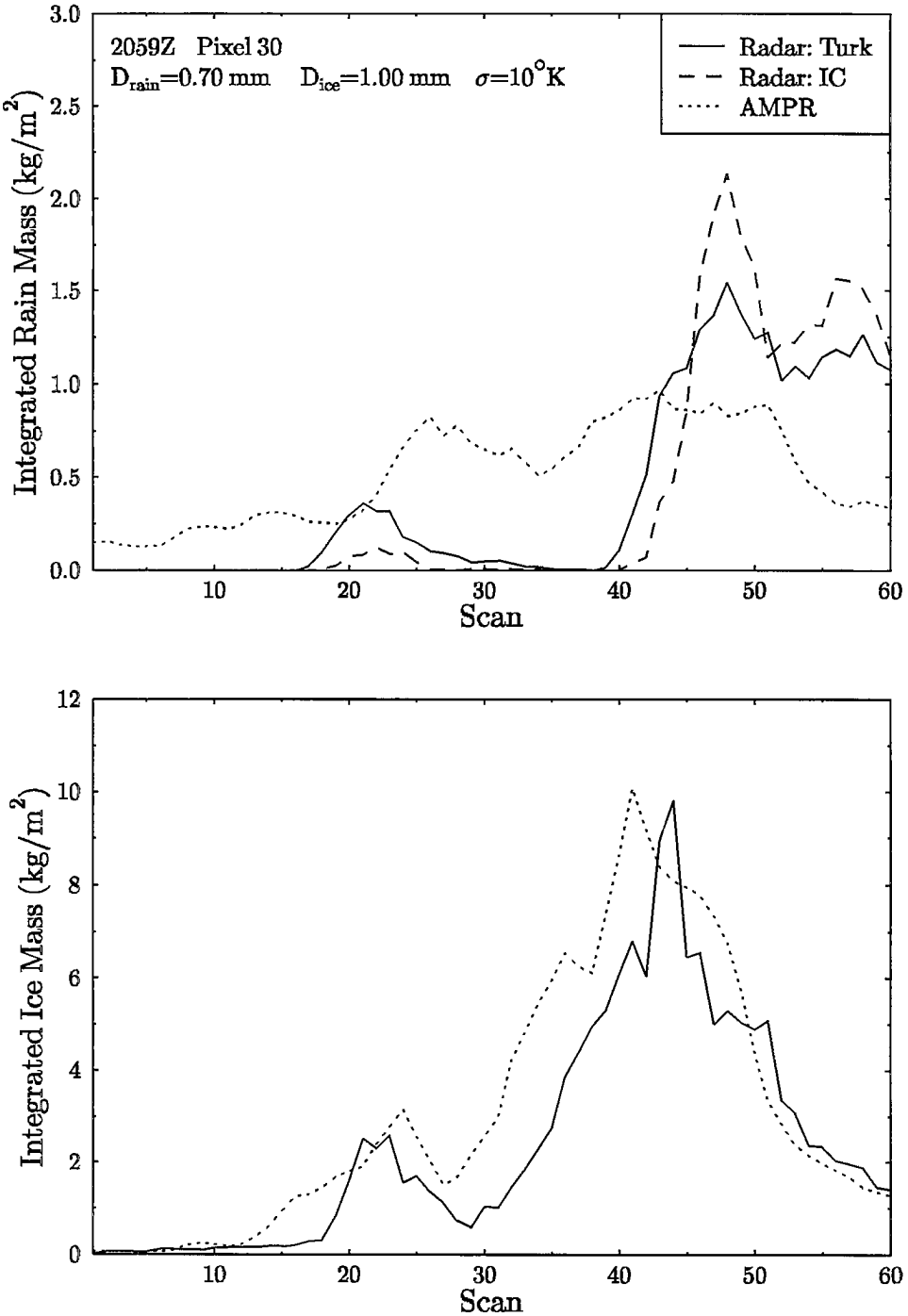


Figure 5.47: Vertically integrated rain and ice mass content derived from CP-2 radar and retrieved from AMPR data for pixel 30 in the 2059Z dataset.

Figs. 5.48 and 5.49 show the results of this averaging process. Besides being smoother there is not much difference in the comparison between the AMPR retrieved hydrometeors and the radar derived ones. Such an averaging process may be of more help in regions where the hydrometeor fields are changing rapidly.

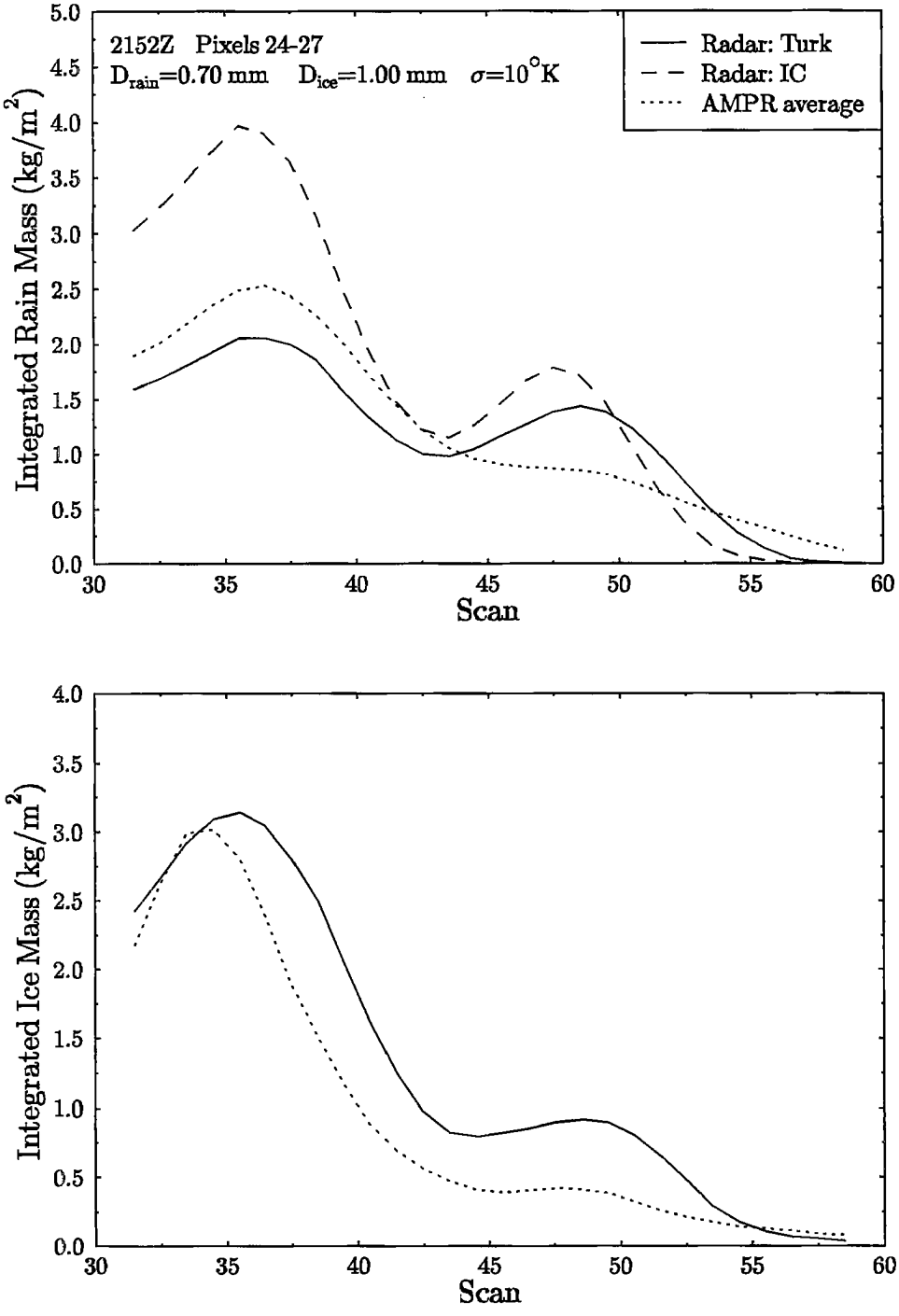


Figure 5.48: Vertically integrated rain and ice mass content derived from CP-2 radar and retrieved from AMPR data averaged over pixels 24-27 in the 2152Z dataset. A four point moving average is also done in the scan direction.

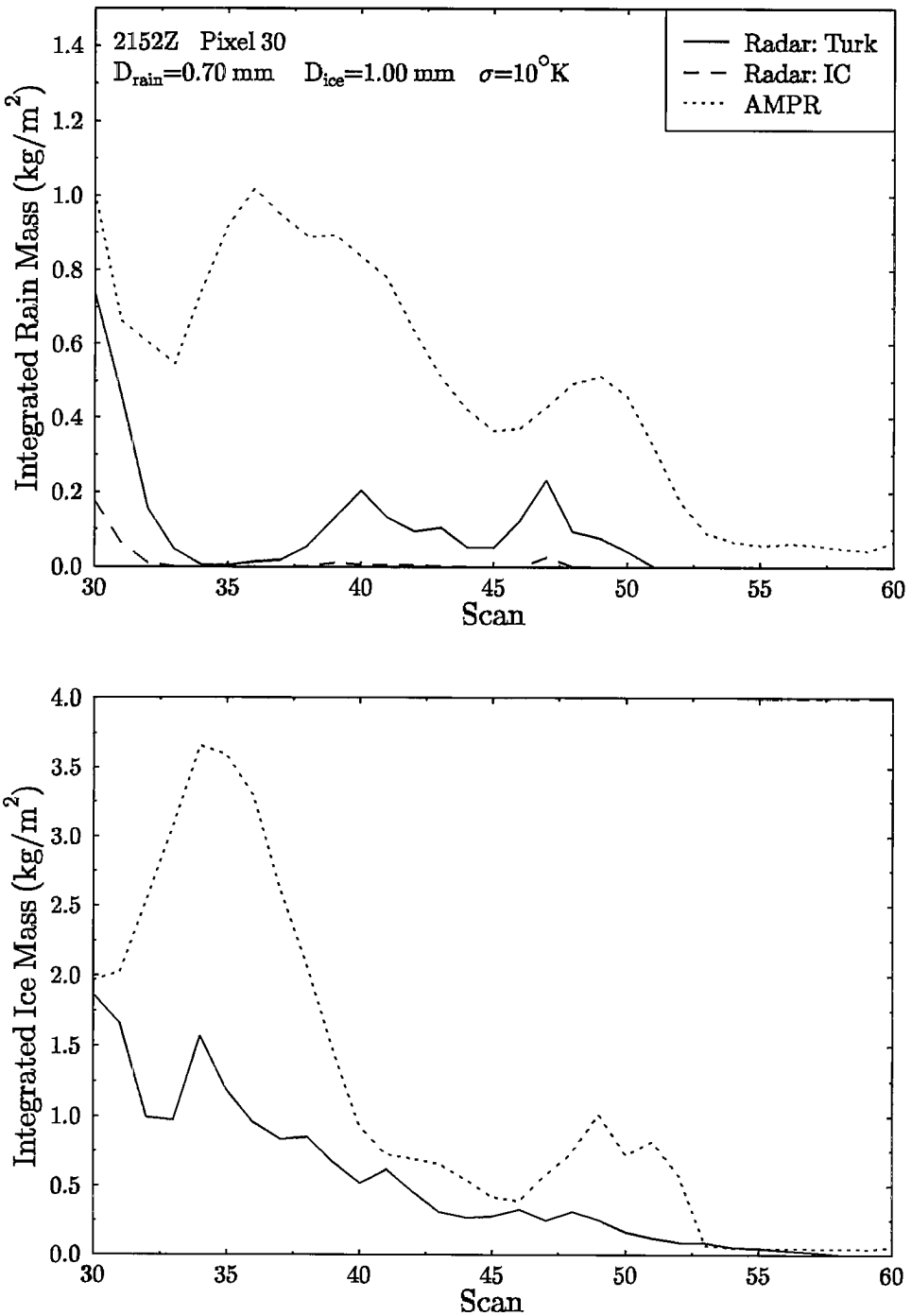


Figure 5.49: Vertically integrated rain and ice mass content derived from CP-2 radar and retrieved from AMPR data averaged over pixels 24-27 in the 2059Z dataset. A four point moving average is also done in the scan direction.

### 5.2.7 Discussion of retrieval results

The AMPR retrievals made with the Bayesian method agree most closely with the radar results for the vertically integrated hydrometeors. For land and water background surfaces the microwave retrieved integrated ice mass content is fairly close to the radar derived ice mass. The integrated rain mass content retrieved over the ocean is comparable to the radar derived rain mass, but the amount of rain retrieved over land is generally much lower than the radar values. Experimental retrievals with two ice categories (aggregate and graupel) did retrieve substantially greater rain mass over land. It should be remembered that there are significant uncertainties of perhaps a factor of two in the radar derived hydrometeor mass, which limit accuracy of the validation. Other sources of error in the comparisons are the differing resolutions of the AMPR channels and the CP-2 radar and possible misnavigation of the AMPR data. The surface rainrate is not explicitly computed with a rain fallout model, because it not directly relevant to the validation process.

The microwave retrieval of hydrometeor profiles as verified by the simulated radar reflectivity is much poorer than the integrated quantities. When the actual hydrometeor structure follows the profile expected from the prior information the agreement can be good, but variations from the expected structure are not captured. This is to be expected from the physics of microwave radiative transfer through hydrometeors profiles. Microwave brightness temperatures are primarily sensitive to the integrated mass of ice or rain, depending on frequency, until the optical depth reaches the saturation level. Across the microwave spectrum there are too few independent observations to retrieve a detailed vertical structure. Thus much of the profile structure information must come from the prior distribution. The high sensitivity of the 10 GHz channel to surface properties means that over land there is little direct information about the rain mass in the microwave measurements.

For these reasons we don't expect the single pixel retrievals of hydrometeor profiles to be particularly accurate. It still makes sense to retrieve profiles, rather than surface rain alone, because various parts of the hydrometeor profiles are what the microwave radiation directly senses. The instantaneous surface rainfall cannot be measured accurately with microwave radiometers. The vertical profile of hydrometeors is important in its own right for its connection to the latent heating profile. Work with the Monte Carlo integration approach to Bayesian precipitation retrieval show that the single pixel hydrometeor mass error bars, obtained from the second moment of the posterior distribution, are quite large. Sufficient accuracy in hydrometeor profiles and surface rainfall will come about only by averaging many single pixel retrievals to find the climatological mean over a region. Of course single pixel retrievals can provide some useful information as to the likely rain intensity. But over land there may be little rainfall underneath ice canopies that cause large brightness temperature depressions at the scattering channels, just as there may be

no rain below a thick cirrus shield causing low infrared brightness temperatures. So there are inherent limits to the accuracy of instantaneous microwave precipitation retrievals. This does not mean, however, that the retrieval results shown here cannot be improved upon significantly.

One advantage of the Bayesian framework is that one can examine explicitly the assumptions made in order to determine why the method behaved as it did and find ways to improve it. There are three parts to the Bayesian precipitation retrieval: the forward probability distribution, the prior probability distribution, and choosing the retrieved profile from the posterior distribution. The most important aspect to consider for the forward distribution are the errors in the radiative transfer modeling. There are uncertainties in modeling the scattering properties of low density ice. The index of refraction mixing rule method gives less scattering for larger size parameters than does the equivalent volume sphere method, though they are equivalent for small size parameters. The issue of how to model low density ice particles, as well as that of the effects of nonspherical shapes of precipitating hydrometeors could be investigated with discrete dipole approximation calculations. The assumptions made to derive particle size distributions from hydrometeor mass contents are the largest source of uncertainty. The reflectivity comparison results showed that the fixed intercept assumption is poor for determining the size distribution of ice. The mass of rain retrieved over the ocean is related to the assumed mean raindrop size. Of course, there will always be uncertainty in hydrometeor size distributions, but one can do better than the one size fits all approach used here. It would be desirable to have a cloud model predict the two parameters of exponential size distributions to provide correct information about how size distributions vary vertically. With this prior information both the mass content and the mean diameter of the hydrometeor size distributions could be variable in the retrieval process.

Another area of radiative transfer modeling error is from the surface emissivity. Here very simple emissivity models are used: a single variable emissivity for land and a fixed Fresnel surface for water. The flat ocean assumption probably underestimates the surface emissivity leading to light rain retrieved in nonraining areas. The retrievals for land let the surface emissivity be variable over a large range, which probably reduced further the limited usefulness of the 10 GHz channel. The water emissivity model could be improved by using a model that depends on surface wind speed (e.g., Schluessel and Luthardt, 1991), though there is considerable uncertainty in these types of models. The wind speed could then be retrieved, perhaps with the help of prior information connecting surface wind speed and area rain intensity. The land emissivity is much more difficult to model, but a model based on a variable wetness parameter along with a known soil or vegetation type might be possible. Using prior information to relate the soil moisture to rainfall could be done, but the problem of the storm path history is rather difficult.

The effects of horizontal variability on radiative transfer is another source of error. Two aspects of this are relating the footprint average brightness temperatures to the average hydrometeor profile and the effects of horizontal variability on the upwelling radiation. The plane-parallel model used for the retrieval does not deal with three-dimensional variability, for example, increased brightness temperature caused by radiation scattering through the sides of a thick ice core. The footprint filling problem is not likely to be much of a problem for this AMPR retrieval, at least for the nadir track, because of the small footprints. In the future, the footprint filling problem could be dealt with by considering a distribution of precipitation intensities described by one or two parameters. These parameters could be related to the type or intensity of precipitation through three dimensional cloud modeling, but an efficient way to perform the forward modeling would have to be developed. That the retrieval with the larger forward probability distribution width ($\sigma = 10°$K) agreed better in terms of simulated radar reflectivity implies that there are substantial forward modeling errors. In light of all the possible errors in the radiative transfer modeling it does not make sense to fit the modeled brightness temperatures exactly to the observations.

Much of the reason for the errors in the profile retrievals can be explained by examining the cloud model output and prior distributions derived from it. There are two possible sources of error in the prior distributions. The first is the simplicity of the assumed functional form, i.e. the multivariate lognormal distribution. The second is incorrectness or unrepresentativeness of the hydrometeor profiles produced by the cloud model. This issue is investigated by examining scatterplots of the 1680 hydrometeor profiles that went into making the prior distribution used in the retrievals. Fig. 5.50 shows the relationship between the rain mass contents in the two lower layers and also between the lowest layer rain mass and the ice mass from 5 to 7 km. Along with the scatterplot shown on the log-log plots is the one sigma ellipse derived from the covariance matrix that indicates the shape of the prior distribution. The two rain layers are well, but not completely, correlated. The correlation between the 0-2 km rain mass and the 5-7 km ice mass is quite low, as indicated by the angle and axial ratio of the ellipse. The distribution of ice is clearly not lognormal, since it is not symmetric on this plot. The correlation between 2-4 km rain and cloud water is very low (Fig. 5.51). The cloud liquid water has a bimodal distribution which may be unphysical. The cloud water in RAMS is predicted by determining what water mass is left after the conversion processes have run. The result is that the log mean cloud water content is 0.002 g/m$^3$, which leads to very low retrieved cloud water contents. The 5-7 km ice mass content and that at 9-11 km is moderately correlated, but the lognormal distribution is not representing the functional form of the scatter of points at all well. The scatterplot indicates that when there is a large amount of ice up high (strong updraft) then there is also much ice below, but there also can be a lot of ice in the lower region without much above. The underestimate of higher level ice in the land retrieval is caused

by this poor match between the form of the prior and the cloud model output. Fig. 5.52 breaks the ice category down into the aggregate and graupel categories simulated in the RAMS run. As one would expect from microphysics the correlation between rain and graupel is much higher than between rain and aggregate. However, the log-space mean of graupel mass is 70 times smaller than that of aggregate mass; this is why it was necessary to use the aggregate category. As a result there is a low correlation between rain and ice, leading to the large underestimate of rainfall for the land retrieval.

Improvements in the microphysical parameterizations in cloud models used to generate the prior probability distribution should lead to improved hydrometeor retrievals with the Bayesian method. Bulk microphysical parameterizations that predict two parameters of the hydrometeor size distribution, and perhaps the ice density as well, are needed. Having a water coated ice particle category might be a useful addition as well. The most important aspect of improved cloud modeling is that the microphysical parameterizations be tested for their effect on those aspects of hydrometeor distributions that are important for microwave radiation. Statistical validation of the parameterizations should be done using radar and passive microwave observations.

The algorithm validation with CaPE data performed here has shown some of the limitations of the simple multivariate lognormal form for the prior distribution. The lognormal distribution, while approximately correct, can lead to occasional large overestimates of quantities because of its long tail. The symmetry of the distribution in log-space means that the very small values in the cloud model output can greatly effect the high end of the distribution through their influence on the distribution width. A simple modification of the lognormal distribution with another parameter may resolve these problems. A method better than using the log-mean and log-variance to estimate the parameters of the prior distribution could be found. A more flexible way to describe the relationship between variables in the prior distribution should be found. Such a functional form obviously will require more parameters, and thus more cloud model data than the simple form used here. Close examination of cloud model output and measurements of hydrometeors could lead to a better functional form for the prior distribution.

Once the prior and forward distributions are determined, there is still the matter of how to choose the retrieved profile from the posterior distribution. The maximum of the probability density function depends in which space that function is measured. The current log-space density function may not be optimal and is fairly arbitrary. Other ways to use the posterior distribution, besides maximizing probability, should be developed, especially for estimating area and time averages of precipitation.

The Bayesian precipitation retrieval method can be made more efficient. For the standard retrievals done for the CaPE validation an average of 14000 posterior probability evaluations were made for each pixel. Each function evaluation takes four (the number of channels) two-stream radiative transfer computations. A minimum of five optimization

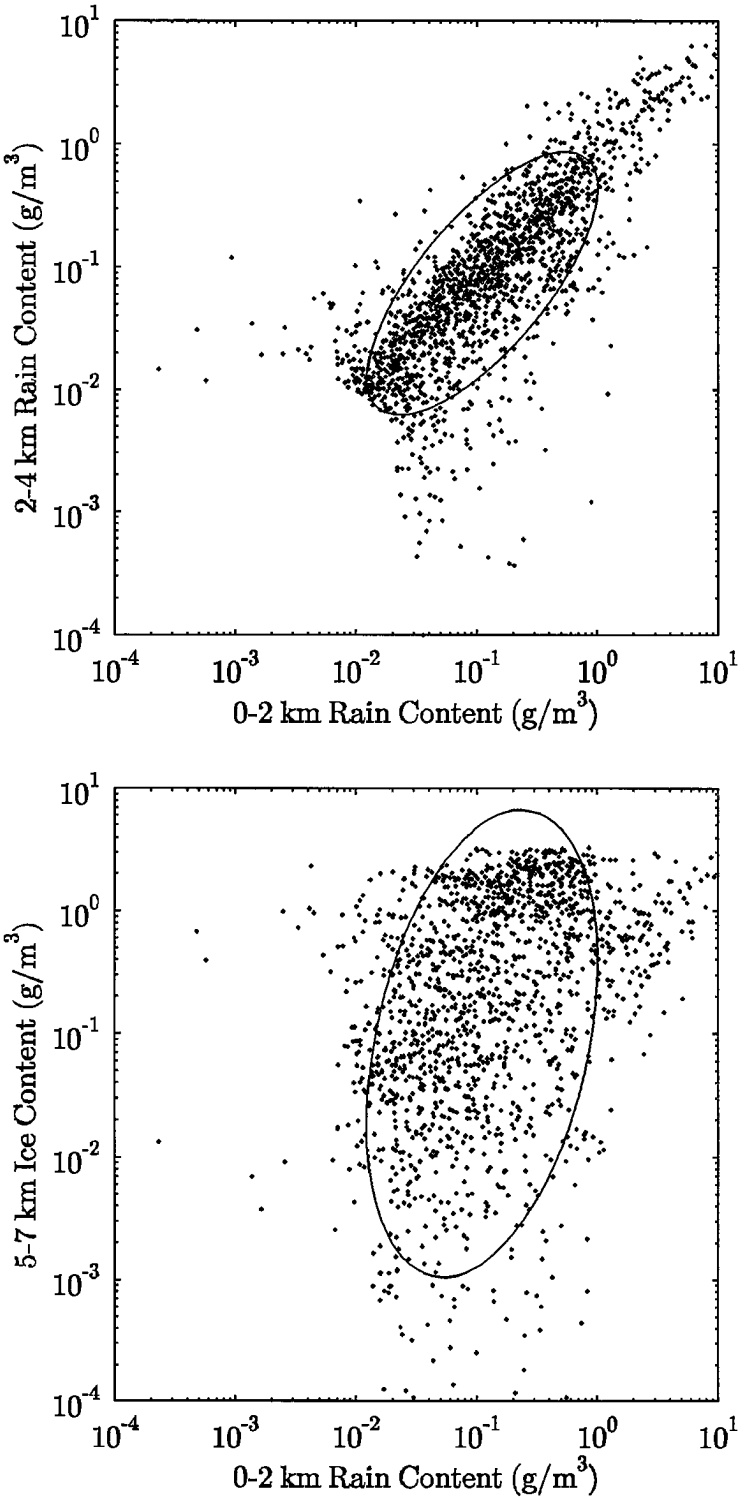


Figure 5.50: Scatter plot of the hydrometeor mass contents produced by the RAMS simulation for various layers in the precipitation structure. Also shown is the one sigma ellipse indicating the lognormal prior distribution fit to the points. The top panel shows the rain mass for two layers, and the bottom panel shows the lowest layer rain and midlevel ice. The raining pixel cutoff eliminates the points in the lower left corner of the top panel.

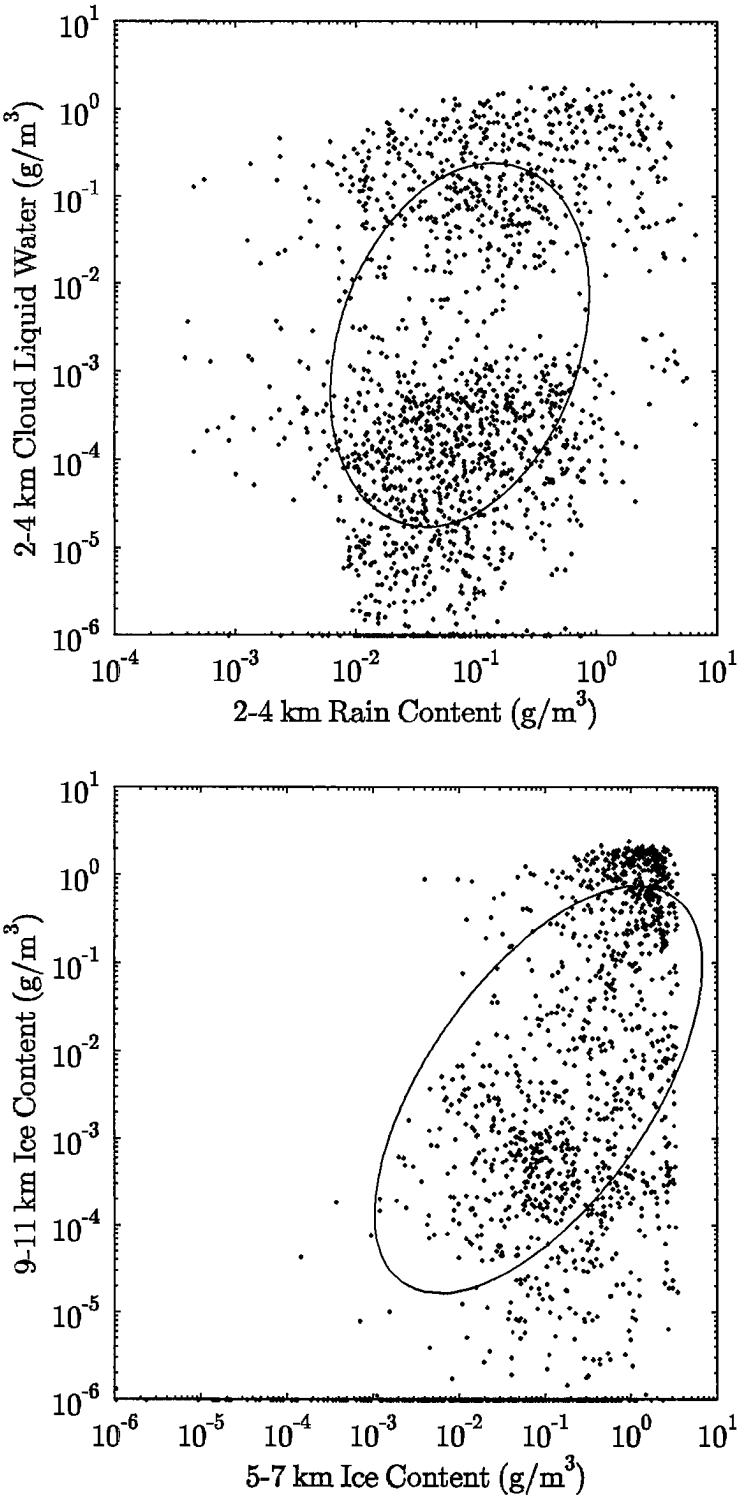


Figure 5.51: Scatter plot of the hydrometeor mass contents produced by the RAMS simulation.The top panel shows the rain and cloud mass for one layer, and the bottom panel shows the ice mass for two layers.

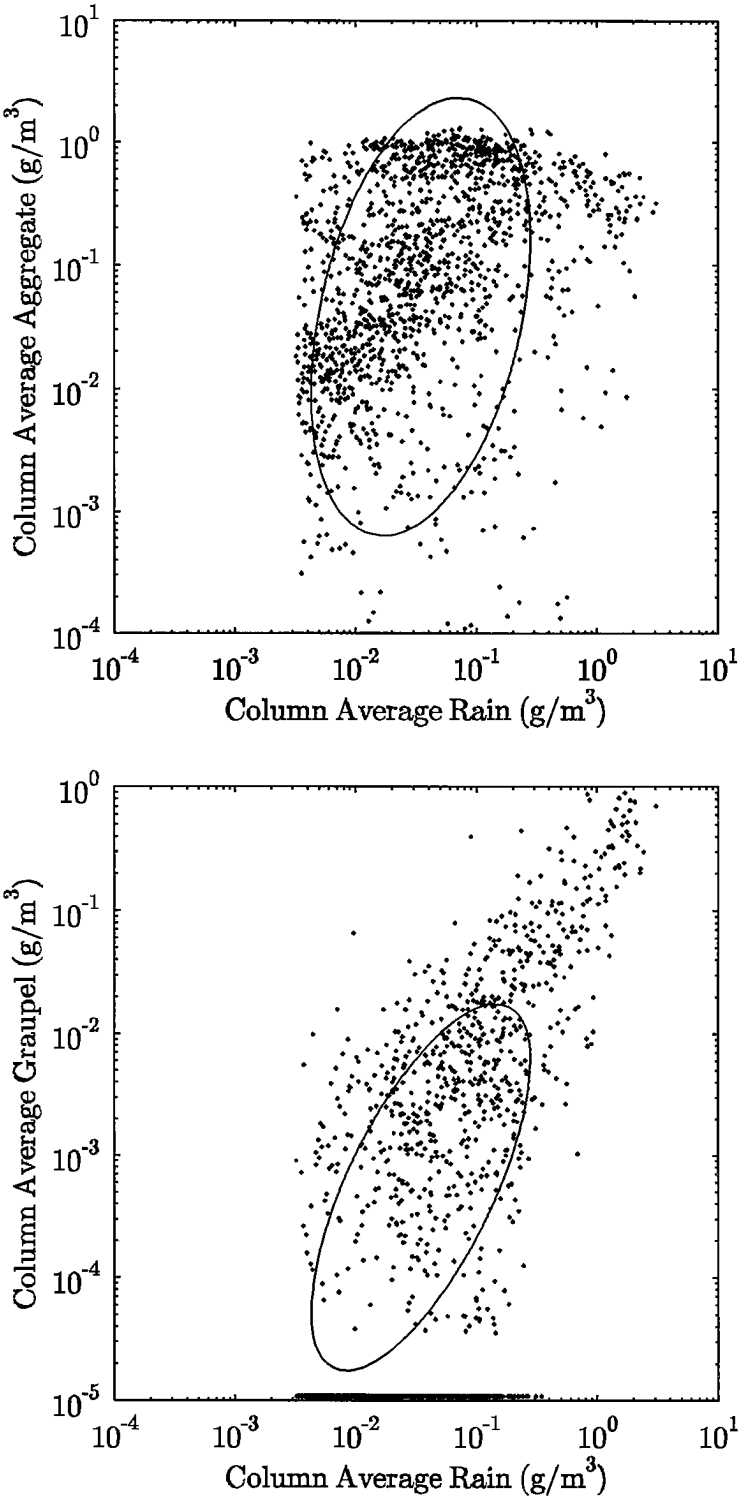


Figure 5.52: Scatter plot of the hydrometeor mass contents produced by the RAMS simulation. The top panel shows the column average rain and aggregate mass, and the bottom panel shows the column average rain and graupel mass.

tries was required for these retrievals, but the five tries nearly always got the same results, indicating that a single optimization would be adequate for 2800 function evaluations. The number of function evaluations made by the optimization method goes as the square of the number of variables. The search for matching observations to initialize the optimization could be made much faster by using a method more intelligent than sequential searching. It may also be possible to find a faster optimization method and speed up the radiative transfer computation.

This validation with AMPR microwave and CP-2 radar data has shown that the Bayesian precipitation retrieval algorithm is an effective way of combining prior information about hydrometeor structure from cloud models with forward radiative transfer modeling to retrieve hydrometeor profiles from microwave radiometer data. No passive microwave profiling algorithm can retrieve single pixel hydrometeor structures with high accuracy, but this method often produced approximately correct profiles. The validation experiment found why certain retrieval mistakes were made and how the retrieval method and input data from cloud models could be improved. The validation effort should be considered only preliminary because of the small amount of data and limited range of conditions. In addition to improvements to the existing algorithm, further work comparing hydrometeor profile retrievals with radar observations is needed.

# Chapter 6

# SUMMARY

This dissertation describes the development of passive microwave remote sensing algorithms for two parts of the hydrological cycle important to the climate system. Modeling studies were carried out to determine the feasibility of and possible methods for high frequency microwave remote sensing of the ice water path of cirrus clouds. A microwave precipitation remote sensing algorithm that retrieves profiles of hydrometeors was developed and tested.

## 6.1 Summary of Microwave Cirrus Remote Sensing

While there are data from programs such as ISCCP on the optical properties of cirrus clouds, the global distribution of cirrus ice water path (IWP) is very uncertain. Now that general circulation models are beginning to predict the mass content of various hydrometeor species it is important to be able to remotely sense cirrus IWP. High frequency microwave radiometry has the advantage that the brightness temperature depression is proportional to the IWP for visible optically thick clouds and does not depend on the cloud temperature. The difficulty is that the proportionality constant between the brightness temperature depression and the IWP depends on the ice particle size distribution and the particle shape. These issues are investigated with theoretical modeling of the scattering properties and radiative transfer of a number of shapes and size distributions.

### 6.1.1 Model development

The discrete dipole approximation (DDA) was used to compute the scattering properties of irregularly shaped particles. This method divides the particle into cubes that are small compared with the wavelength and computes the dipole field interaction between all pairs of cubes in the particle. For a particular incident field the complex electric field at each dipole is found by solving the linear system representing this dipole-dipole interaction. The far field scattering properties are then found by summing over the contributions from each dipole. The DDA approach of Goedecke and O'Brien (1988) was implemented for this work and added to by computing those quantities necessary for radiative transfer. In addition an FFT solution method that allows larger particles to be solved was developed. Tests comparing the DDA scattering results with Mie theory for spheres and with

ECBM for oblate spheroids show the DDA method to be accurate to 1 to 5% for the range of parameters used here.

A polarized monochromatic plane-parallel radiative transfer model was developed to compute the upwelling polarized brightness temperatures from the scattering properties output by the DDA model. The radiative transfer model represents the polarization state of the radiation field with Stokes parameters and the zenith angle dependence with discrete quadrature angles. For thermally emitting plane-parallel atmospheres the radiation field is azimuthally symmetric and only the $I$ and $Q$ Stokes parameters (equivalent to vertical and horizontal polarizations) are nonzero. The interaction of the radiation with the medium is described in terms of reflection and transmission matrices and source vectors, and the doubling and adding method is used to solve the radiative transfer of the whole atmosphere. The surface reflection is modeled either by a Lambertian surface for land or a Fresnel surface for flat water. The Rayleigh-Jeans assumption is not used because of the high frequencies considered. Absorption by oxygen and water vapor is computed with Liebe's MPM92 model.

### 6.1.2 Microwave scattering by cirrus

The scattering properties of realistic distributions cirrus ice crystals are computed with the DDA at the atmospheric window frequencies of 85.5, 157, 220, and 340 GHz. Five particle shapes are modeled: solid columns, hollow columns, hexagonal plates, four-bullet planar rosettes, and equivalent volume spheres (volume going as $D^{-2.5}$) with the aspect ratios varying according to empirical formulae. The long axes of the ice particles are randomly oriented in the horizontal plane. The scattering properties are computed at 16 zenith angles for 13 discrete sizes (maximum particle diameter from 30 microns to 2 mm). The discrete sizes are used to make 18 gamma size distributions ($N = aD^{\alpha}e^{-(\alpha+3.67)D/D_m}$), with $D_m = 70, 100, 150, 250, 400, 700\mu$m ($D_m$ is the median of the third moment) and $\alpha = 0, 1, 2$. Tests with many sizes of spheres show that the gamma distribution can be accurately represented by these 13 sizes.

Plots of extinction as a function of particle size show that there are three regimes: absorption going as the particle volume for the smallest particles, Rayleigh scattering going as the square of the volume, and beyond the Rayleigh regime where the scattering goes up more slowly with size. The range in extinction for size distributions with the same IWC over the five shapes is up to a factor of three with rosettes having the least and solid columns the most extinction. The extinction is usually greater for nadir angles because the particles present the largest cross section to the radiation. The ratio of extinction at the two polarizations is a measure of the polarizing effect of the non-spherical particles. Plates are the thinnest and most polarizing shape, followed by planar rosettes, and then columns. Larger sizes generally have more polarizing effect, but beyond the Rayleigh regime the polarization ratio oscillates with size. The single scattering albedo has a simple behavior

with particle size, being near zero for the smallest size and smoothly increasing to near unity for the largest size. The particle size at which the transition happens increases with frequency, so that the higher frequencies are more scattering. The single scattering albedo is higher for distributions of columns than for rosettes or equivalent volume spheres because columns have more volume for a given size. The amount of forward scattering increases with particle size and aspect ratio; plates have forward scattering equal to backscattering for nadir view.

To make the results of the DDA calculation easily available, the scattering properties are fit to functions of particle size using 14 coefficients for each outgoing angle, polarization, shape, and frequency. The fit quantities are designed for use with a simple first order radiative transfer model. The upwelling brightness temperatures computed using the scattering fits with the first order model agree closely with those from the multi-stream model for most relevant situations where reflection from below the cirrus cloud can be ignored.

### 6.1.3 Microwave radiative transfer in cirrus

Radiative transfer simulations are done for cirrus clouds composed of the various shapes and size distributions in standard tropical and midlatitude winter atmospheres. In the tropical atmosphere there is little or no transmission from the surface for the three higher frequencies. At typical heights of cirrus clouds and above there is virtually no gaseous emission at these frequencies. The radiative transfer simulations are done for 3 km thick clouds at appropriate heights over land and water surfaces. The brightness temperatures at nadir and near 49° are used in the analysis. Since cirrus clouds at microwave wavelengths will usually be in the linear radiative transfer regime, a natural quantity to consider is the ratio of the brightness temperature depression to ice water path ($\Delta T_b/IWP$), which here is called the sensitivity.

The range of linearity is about a factor of ten from a detectable limit of a brightness temperature depression of 3°K to around 30°K. A test with cirrus clouds at different heights in the tropical atmosphere shows that the sensitivity is independent of temperature except for the smallest size distributions and lowest frequencies where there is significant emission. A test of placing the same temperature cirrus cloud in the two different atmospheres shows that the sensitivity is independent of the underlying atmosphere for higher frequencies and larger size distributions.

The brightness temperature depression depends most strongly on the "average" size of the distribution as indicated by $D_m$. There is a factor of ten in sensitivity between $D_m = 100\mu$m and $D_m = 400\mu$m. The width of the gamma distribution has a much smaller effect of at most 20% over the range of $\alpha$ considered. The range in sensitivity from particle shape is typically a factor of 2 for the same size distribution. Of course, the sensitivity increases dramatically with frequency. The higher frequencies should be able

to detect moderate values of cirrus IWP: at 340 GHz for $D_m = 250\mu$m an IWP of 60 g/m$^2$ generates a nadir brightness temperature depression of 3 to 6°K depending on shape.

Given the wide range in sensitivities it is important to be able to infer the average particle size and shape in order to relate a brightness temperature depression to an IWP. Because the sensitivity varies differently with particle size for different frequencies, ratios of brightness temperature depressions at two adjacent frequencies contain information about the size distribution. The most relevant ratio available in this study ($\Delta T_b(340)/\Delta T_b(220)$) is multivalued, i.e. a single ratio can mean either small or large particles, so other information about the size distribution may be needed. If even higher frequencies are used, the frequency ratio becomes less multivalued because more of the size distributions lie on a single branch. Higher frequencies are also more sensitive to cirrus mass and less to the size distribution.

The ratio of brightness temperature depressions at the two polarizations has information about particle shape. The polarization ratio depends mostly on the particle aspect ratio as well as average size. The probable random attachment of bullets in rosettes complicates the problem of determining their shape from the polarization ratio. The ratio of brightness temperature depressions at the two angles considered here contains information much like the polarization ratio. The range in sensitivity due to particle shape is significantly reduced by using vertical polarization at 49° and expressing the size of the distribution by a characteristic size based on the square of the particle volume.

A specific cirrus microwave remote sensing algorithm is not presented here because it would depend on the particular experimental setup. Instead, some guidelines are given for how to use the above results for a remote sensing method. The brightness temperature depression, which is the signal proportional to cirrus IWP, can be found from a brightness temperature image by differencing clear or thin cirrus pixels from the thicker cirrus pixels. This assumes that the subcirrus layer is homogeneous, but perhaps the lower frequencies could be used to detect and correct for inhomogeneities. Information about average particle size can come from $\Delta T_b$ frequencies ratios or from multichannel infrared retrievals. Information about particle shape might be obtained from polarization ratios or assumptions using environmental conditions such as temperature. Having the size and shape information allows one to use the correct sensitivity to convert the measured brightness temperature to cirrus IWP. These idea will be tested and developed in the future using data from NASA's Millimeter-Wave Imaging Radiometer.

While microwave radiometry cannot provide information on the vertical structure of cirrus clouds, it should be able to measure integrated properties such as ice mass and characteristic particle size. Since cirrus clouds are optically thin at microwave frequencies, the radiative transfer is linear, and the brightness temperature depression for spatial inhomogeneities or particle mixtures is simply the appropriate average. The effects of cirrus particle shape can be modeled accurately at microwave wavelengths (using the

discrete dipole approximation), unlike at the shorter wavelengths in the infrared and visible. The scattering based microwave method of cirrus retrieval has properties, such as cloud temperature independence, that are different from the emission based infrared methods. The microwave cirrus retrieval approach is complementary to, and perhaps best used in conjunction with, the window infrared emission and near IR reflectance techniques.

## 6.2 Summary of Bayesian Precipitation Retrieval

Passive microwave radiometers on spacecraft instruments are either sensitive primarily to the upper parts of precipitating hydrometeor structures or are influenced strongly by the surface in addition to the rain layer. Thus effective use of the multiple channels available requires the retrieval of hydrometeor profiles rather than the surface rain rate, because the surface rainfall is not uniquely related to the rest of the profile. The vertical structure of rain and ice particles is related to the latent heating profile, which is important for its dynamical effect. The major difficulty in microwave precipitation retrieval is that even multiple frequency measurements do not uniquely define the hydrometeor profile. Thus additional information is needed to constrain the retrieval to the most physically reasonable profile. In the method developed here the extra information is provided by hydrometeor output from cloud models that have bulk microphysical parameterizations.

### 6.2.1 Description of precipitation retrieval method

The retrieval of profiles is done by combining the information from cloud models with forward microwave radiative transfer modeling using Bayes theorem. Bayes theorem computes the posterior probability distribution of the hydrometeor profile given an observation by multiplying the prior distribution times the forward conditional distribution. The prior probability distribution of the hydrometer profile contains the additional information from cloud model output. The forward distribution is the probability of an observation vector given a particular hydrometeor distribution, and is computed from the radiative transfer model. A profile is retrieved for an observation by finding the hydrometeor structure that maximizes the posterior probability density function.

The hydrometeor profile is represented as a horizontally homogeneous column with any number of layers. There are up to four species of hydrometeors: rain, two types of ice particles, and a water coated particle (not used for this work). The particles are assumed to be spherical and have exponential size distributions. The parameters that describe each layer are layer top temperature, water vapor mass content, cloud liquid water content, mass content ($M$) and mean drop diameter ($\overline{D}$) for rain, and $M$, $\overline{D}$, and density $\rho$ for the ice particles. In addition there are surface temperature and emissivity parameters. A precipitation structure specifies the number of layers and which parameters within each layer are variable for the retrieval. Those parameters that are not chosen to vary (e.g.

temperature and water vapor) are fixed at climatological values obtained from the cloud model output. Only the mass content of the hydrometeor distributions is allowed to vary for this work.

The prior probability function is a multivariate lognormal distribution. Actual hydrometeor mass contents are approximately lognormal. The multivariate aspect of the prior distribution is what provides the crucial information on the correlation between various hydrometeor species at a number of levels. The parameters of the prior distribution are found by computing the mean vector and covariance matrix of the precipitation profile vector computed for each raining pixel in a range of times from the cloud model output.

The forward conditional probability distribution is an independent normal distribution around the simulated observation vector obtained from the radiative transfer model for a given hydrometeor structure. The width of the normal distribution is specified for each microwave channel, and this governs the tradeoff between fitting the model closer to the data or relying more on the prior information. The appropriate forward distribution width should be chosen based on the accuracy of the forward model.

The forward model is designed to compute upwelling brightness temperatures from the precipitation structure very rapidly. The scattering properties of the rain and ice distributions are found from interpolation in tables prepared from Mie calculations. The two-dimensional tables are functions of average particle size and temperature (for rain) or density (for ice particles). Since here the average size is not a variable, the average particle size may be fixed or be computed from the mass content assuming a fixed distribution intercept. The absorption by water vapor and cloud liquid water is computed with the MPM92 model. The upwelling brightness temperatures are computed from the layer scattering information and surface properties with an Eddington approximation model. The surface properties are assumed to be either Lambertian (for land) or Fresnel (for calm water). The Fresnel surface is the only source of polarization in the model.

Two methods are described for finding the retrieved profile from the high dimensional posterior probability distribution. The first performs Monte Carlo integration over the hydrometeor profile space to find the first and second (logarithmic) moments. This is appropriate for estimating the parameters of the hydrometeor probability distribution from a number of observations, but not for the single pixel retrievals done here. The second method finds the maximum of the posterior probability density function with an optimization technique. Simulated observations (i.e. $T_b$ pixels) are precomputed and stored for large number of profiles. For each observation the Powell optimization algorithm is started off with those profiles that have simulated observations close to the actual observation and have the highest prior probability function. A number of Powell optimization runs can be done to help make sure the global maximum is found.

### 6.2.2 Theoretical tests

Because the Bayesian precipitation retrieval system is very flexible and complex a number of theoretical tests were done to discover how it behaves and help decide among the many ways to configure the system. Synthetic brightness temperature observations are computed from cloud model fields, and input to the precipitation retrieval system. The theoretical tests allow one to compare the retrieved hydrometeor fields with the known "truth". The tests are done with output from a 2D simulation of a tropical squall line during GATE using the Goddard Cumulus Ensemble model (Tao and Simpson, 1989). The simulation provides fields of cloud liquid water, rain, snow, and graupel. Three regions containing a total of 300 pixels from different model times are used. The forward radiative transfer is done with a more accurate scattering and radiative transfer model. The Rutledge and Hobbs microphysical scheme determines the rain and ice size distributions and ice particle densities. An observation angle of 53° and frequencies of 10.7, 19.4, 37.0, and 85.5 GHz are simulated. The tests are done by varying one aspect at a time of the retrieval system inputs. The basic results of the tests are the rms difference between true and retrieved surface rain and integrated rain and ice content.

One test is to determine the best type of precipitation structure to use for the retrievals. Ten precipitation structures ranging in complexity from 2 layers to 11 layers and from 2 variables to 27 variables are tried. The results show that simple two or three layer structures do not perform as well as a five layer structure, but that structures more complicated than this are not necessary. Having cloud water in the structure is important for retrieving integrated ice mass or for rain over land. Variable snow, water vapor, or temperature does not improve the accuracy of the retrieval. Thus a five layer structure with variable cloud water, rain, and graupel (11 variables in all) appears to work well and is the structure used in the remaining tests.

The width of the forward probability distribution is another choice to be made. A test examined the accuracy of the retrievals with the observation widths for all channels varied from 1°K to 8°K. Retrievals with the 1°K width are noisier (less stable) and sometimes have worse rms errors than 2°K widths. This occurs because fitting to model error can cause bad retrievals. The rms error also increases as the observation widths become large because the retrieval relaxes toward the climatological value of the prior distribution. A fairly large range of observation widths give basically the same results. The width of the forward distribution should be chosen to be comparable to the size of the forward modeling errors, which for real data will be substantially larger than for this test.

A set of microphysical assumptions must be used to derive the particle size distributions and densities from the variable mass content. A test is done to see the effect of using microphysical schemes for the retrieval that are different than that used for the forward simulation. Besides the fixed intercept approach of the Rutledge and Hobbs scheme

($N_{0rain} = 8000$ mm$^{-1}$m$^{-3}$, $N_{0ice} = 4000$ mm$^{-1}$m$^{-3}$, $\rho_{graup} = 0.4$ g/cm$^3$), two fixed average size schemes were used: the default in RAMS ($\overline{D}_{rain} = 0.54$ mm, $\overline{D}_{graup} = 1.00$ mm, $\rho_{graup} = 0.9$ g/cm$^3$), and a modification ($\overline{D}_{rain} = 0.54$ mm, $\overline{D}_{graup} = 0.8$ mm, $\rho_{graup} = 0.4$ g/cm$^3$). The larger raindrops of the two fixed size schemes causes much lower rain mass to be retrieved. The scheme with the larger solid graupel has very high errors for integrated ice because much less ice amount is retrieved. This test shows that large errors can be expected from incorrect microphysical assumptions.

Another test investigates the effects of changes in how the prior distribution is made. Ignoring the covariance information is quite detrimental to the rain retrieval, but less so for the integrated ice mass. Using a lower raining pixel cutoff for the prior distribution results in considerably worse rms error for rain retrieval over land because this increases the width of the prior distribution, allowing much larger retrievals of rain. Having the prior distribution made from cloud model times close to the times of the simulated data did improve the retrievals, but not dramatically.

The final test looked into the effects of using less than the full complement of four frequencies. The 10 GHz channel is needed for retrieving rain accurately over a water surface, as 19 GHz gets contaminated by ice scattering. The 85 GHz channel is very useful for determining ice content, but has high error if used alone. In general, having all four channels greatly improves the retrieval as compared with having just one or two channels.

### 6.2.3 Validation experiment with CaPE data

A preliminary validation is done with data from the CaPE experiment in Florida in August 1991. Passive microwave observations made with the Advanced Microwave Precipitation Radiometer mounted on the ER-2 aircraft flying at 20 km altitude are used. The AMPR is a cross track scanning instrument with single channels at 10.7, 19.4, 37.1, and 85.5 GHz. The resolutions at the ground of 0.6 to 2.8 km greatly lessen the problems of sub-footprint variability. The CP-2 multiparameter radar provides the ground truth for the hydrometeor profiles. Rather few coincident AMPR and CP-2 datasets were produced during CaPE so only two datasets, one over land and one over the ocean, are analyzed for this experiment. The land case has stronger convection with AMPR brightness temperatures dropping to 105°K at 37 and 85 GHz and radar reflectivities over 55 dBZ, compared with 85 GHz $T_b$'s down to 160°K for the ocean dataset. The prior information for the retrieval is from a simulation performed with the Regional Atmospheric Modeling System (RAMS) of Florida sea breeze initiated convection. The 2D simulation was a modification of one performed by Nicholls et al. (1991).

The two datasets are about 100 km from the CP-2 radar resulting in too much attenuation at X band, so only the reflectivity $Z_H$ and differential reflectivity $Z_{DR}$ at S band are available. The retrieved hydrometeor profiles are compared with radar data

either by simulating radar reflectivity from the profiles or by inverting the radar data to provide hydrometeor mass content. Two methods of radar inversion are used. Turk et al. (1993) finds rain, mixed particle, and ice particle distributions from the reflectivity. A method from Illingworth and Caylor (1989) computes only the rain distribution from reflectivity and $Z_{DR}$.

A seven layer precipitation structure with variable cloud water, rain, and a single high density ice category (graupel) is used for the microwave precipitation retrieval. Low density ice (aggregate) is not included because it does not produce large enough brightness temperature depressions for the distributions of aggregate and graupel obtained from the cloud model. There are 14 or 15 variables in the precipitation structure (the surface emissivity is retrieved over land). The integrated rain mass retrieved over the ocean agrees relatively well with the radar rain mass, though the amount of rain retrieved depends on the microphysical assumptions made. There is uncertainty in making the comparison between AMPR and CP-2 rain mass because there is more than a factor of two difference between the two radar derived integrated rain masses in some areas. There is far too little integrated rain mass retrieved in the strong convection area in the land case. This is from too low a correlation between total ice mass and rain in the cloud model output, because the prior distribution is providing most of the information about rain over land. In general there is too much rain retrieved in no or very low rain areas. This is probably caused by the prior distribution applying only to raining pixels and problems with the surface emissivity models. Excluding the nonraining areas the reflectivity profiles for the rain layers have an rms difference of better than 4 dB for the water case and 9 dB for the land case. The integrated ice mass retrieved from the microwave data agrees well with that from radar. If the vertical distribution of ice is significantly different from that expected by the prior information then the profiles of reflectivity do not agree well. The retrieved vertical distribution of ice falls off too quickly in the strong land convection because the form of the prior distribution is unable to capture the correct relationship between lower and higher level ice mass. The rms reflectivity difference for ice is about 6 dB at lower levels and increases to above 12 dB at higher levels for the land case, and has approximately the opposite behavior for the water case.

A number of areas in which the Bayesian precipitation retrieval could be improved are found by investigating the effects of different microphysical assumptions on the validation results and looking at the cloud model source of prior information. The forward radiative transfer modeling could be improved by implementing realistic surface emissivity models. Two parameter size distribution information from cloud models would allow both the mass content and mean diameter to be variable thus eliminating the need for dubious microphysical assumptions concerning size distributions. The prior distribution could be improved by a more general functional form than the lognormal multivariate distribution

used here. Most important are improved cloud model microphysical parameterizations that have been verified with passive and active microwave observations.

The Tropical Rain Measuring Mission (TRMM) has a requirement for a passive microwave hydrometeor profile retrieving algorithm, and a number of such methods are under development. The Bayesian precipitation retrieval algorithm, while too inefficient in its current form, contains a number of concepts that could aid in the development of the best microwave profiling scheme for TRMM. One is using a mathematical framework for incorporating statistical microphysical information from cloud models to constrain the nonunique inversion problem. The Bayesian framework also provides a way to estimate the uncertainty of each retrieved parameter by determining the width of posterior distribution. The issue of how to combine data from the multiple sensors on TRMM is another for which the Bayesian method provides a potential solution. While not pursued in this work, it is simple to extend the Bayesian method to incorporate data from the TRMM precipitation radar, and perhaps visible and infrared sensors, along with data from the microwave imager. This would provide a single retrieval of hydrometeor profiles that is consistent with all the available data and with prior information about precipitation structure.

## Bibliography


Acton, F. S., 1990: *Numerical Methods that Work.* Mathematical Association of America.

Adler, R. F. and A. J. Negri, 1988: A satellite infrared technique to estimate tropical convective and stratiform precipitation. *J. Appl. Met.*, **27**, 31–50.

Adler, R. F., A. J. Negri, N. Prasad, and W.-K. Tao, 1989: Cloud model-based simulations of satellite microwave data and their applications to an SSM/I rain algorithm. In *Fourth Conference on Satellite Meteorology and Oceanography*, None, editor.

Adler, R. F., H.-Y. M. Yeh, N. Prasad, W.-K. Tao, and J. Simpson, 1991: Microwave simulations of a tropical rainfall system with a three-dimensional cloud model. *J. Appl. Met.*, **30**, 924–953.

Arkin, P. A., 1979: The relationship between fractional coverage of high cloud and rainfall accumulations during GATE over the B-scale array. *Mon. Wea. Rev.*, **107**, 1382–1387.

Atlas, D. and C. W. Ulbrich, 1990: Early foundations of the measurement of rainfall by radar. In *Radars in Meteorology*, Atlas, D., editor. American Meteorological Society, Boston, 86-97.

Barber, P. and C. Yeh, 1975: Scattering of electromagnetic waves by arbitrary shaped dielectric bodies. *Appl. Optics*, **14**, 2864–2872.

Barton, I. J., 1983: Upper-level cloud climatology from an orbiting satellite. *J. Atmos. Sci.*, **40**, 435–447.

Bohren, C. F. and D. R. Huffman, 1983: *Absorption and Scattering of Light by Small Particles.* John Wiley & Sons, 530 pp.

Bringi, V. N. and A. Hendry, 1990: Technology of polarization diversity radars for meteorology. In *Radars in Meteorology*, Atlas, D., editor. American Meteorological Society, Boston, 153-190.

Cotton, W. R., M. A. Stephens, T. Nehrkorn, and G. J. Tripoli, 1982: The Colorado State University three dimensional cloud/mesoscale model, 1982, II: An ice parameterization. *J. Rech. Atmos.*, **16**, 295–320.

Cotton, W. R., G. J. Tripoli, and R. M. Rauber, 1986: Numerical simulation of the effects of varying ice crystal nucleation rates and aggregation processes on orographic snowfall. *J. Clim. Appl. Met.*, **25**, 1658–1680.

DeMaria, M., 1985: Linear response of a stratified tropical atmosphere to convective forcing. *J. Atmos. Sci.*, **42**, 1944–1959.

Draine, B. T., 1988: The discrete dipole approximation and its application to interstellar graphite grains. *Astrophys. J.*, **333**, 848–872.

Dungey, C. E. and C. F. Bohren, 1993: Backscattering by nonspherical hydrometeors as calculated by the coupled-dipole method: An application in radar meteorology. *J. Atmos. Ocean. Tech.*, **10**, 526–532.

Evans, K. F., 1990: Polarized radiative transfer modeling: An application to microwave remote sensing of precipitation. Master's thesis, Colorado State University.

Evans, K. F., 1993: Two-dimensional radiative transfer in cloudy atmospheres: The spherical harmonic spatial grid method. *J. Atmos. Sci.*, **50**, 3111–3124.

Evans, K. F. and G. L. Stephens, 1991: A new polarized atmospheric radiative transfer model. *J. Quant. Spectosc. Radiat. Transfer*, **46**, 412–423.

Evans, K. F. and G. L. Stephens, 1992: A theoretical basis for passive microwave remote sensing of cirrus. In *Proceedings of Specialist Meeting on Microwave Radiometry and Remote Sensing Applications*, Westwater, R., editor.

Evans, K. F. and J. Vivekanandan, 1990: Multiparameter radar and microwave radiative transfer modeling of nonspherical atmospheric ice particles. *IEEE Trans. Geosci. Remote Sensing*, **28**, 423–437.

Flatau, P. J., 1990: Light scattering by rectangular solids in the discrete-dipole approximation: A new algorithm exploiting the block-Toeplitz structure. *J. Opt. Soc. Am.*, **7**, 593–600.

Fowler, L. D., D. A. Randall, and S. A. Rutledge, 1993: Liquid and ice cloud microphysics in the CSU GCM. Part I: Model description and results of a baseline simulation. *J. Atmos. Sci.* To be Submitted.

Fulton, R. and G. M. Heymsfield, 1991: Microphysical and radiative characteristics of convective clouds during COHMEX. *J. Appl. Met.*, **30**, 98–116.

Gasiewski, A. J., 1992: Numerical sensitivity analysis of passive EHF and SMMW channels to tropospheric water vaper, clouds, and precipitation. *IEEE Trans. Geosci. Remote Sensing*, **30**, 859–870.

Gill, A. E., 1982: *Atmosphere-Ocean Dynamics.* Academic Press.

Goedecke, G. H. and S. G. O'Brien, 1988: Scattering by irregular inhomogeneous particles via the digitized Green's function algorithm. *Appl. Optics*, **27**, 2431–2437.

Goodman, J. J., B. T. Draine, and P. Flatau, 1991: Application of fast-Fourier-transform techniques to the discrete-dipole approximation. *Optics Lett.*, **16**, 1198–1200.

Grant, I. P. and G. E. Hunt, 1969: Discrete space theory of radiative transfer. *Proc. Roy. Soc. London*, **A313**, 183–197.

Hartmann, D. L., H. H. Hendon, and J. Robert A. Houze, 1984: Some implications of the mesoscale circulations in tropical cloud clusters for large-scale dynamics and climate. *J. Atmos. Sci.*, **41**, 113–120.

Heymsfield, A., 1972: Ice crystal terminal velocities. *J. Atmos. Sci.*, **29**, 1348.

Heymsfield, A. J. and C. M. R. Platt, 1984: A parameterization of the particle size spectrum of ice clouds in terms of the ambient temperature and the ice water content. *J. Atmos. Sci.*, **41**, 846–855.

Illingworth, A. J. and I. J. Caylor, 1989: Polarization radar estimates of raindrop size spectra and rainfall rates. *J. Atmos. Ocean. Tech.*, **6**, 939–949.

Inoue, T., 1985: On the temperature and effective emissivity determination of of semi-transparent cirrus clouds by bispectral measurements in the 10 $\mu$m window region. *J. Meteorol Soc. Japan*, **63**, 88–98.

Intrieri, J. M., G. L. Stephens, W. L. Eberhard, and T. Uttal, 1993: A method for determining cirrus cloud particle sizes using lidar and radar backscatter technique. *J. Appl. Met.*, **32**, 1074–1082.

Joseph, J. H., W. J. Wiscombe, and J. A. Weinman, 1976: The delta-Eddington approximation for radiative flux transfer. *J. Atmos. Sci.*, **33**, 2452–2459.

Joss, J. and A. Waldvogel, 1990: Precipitation measurement and hydrology. In *Radars in Meteorology*, Atlas, D., editor. American Meteorological Society, Boston, 577-606.

Kedem, B., L. Chiu, and G. North, 1990: Estimation of mean rain rates: Application to satellite observations. *J. Geophys. Res.*, **95**, 1965–1972.

Kosarev, A. L. and I. P. Mazin, 1989: Empirical model of physical structure of the upper level clouds of the middle latitudes. In *Radiation Properties of Cirrus Clouds*, 29-52.

Kropfli, R. A., S. Y. Matrosov, T. Uttal, B. W. Orr, A. S. Frisch, K. A. Clark, B. W. Bartram, and J. B. Snider, 1993: Studies of cloud microphysics with millimeter wave radar. *Atmos. Res.* Submitted.

Kummerow, C., I. M. Hakkarinen, H. F. Pierce, and J. A. Weinman, 1991: Determination of precipitation profiles for airborne passive microwave radiometric measurements. *J. Atmos. Ocean. Tech.*, **8**, 148–159.

Kummerow, C., R. A. Mack, and I. M. Hakkarinen, 1989: A self-consistency approach to improve microwave rainfall rate estimation from space. *J. Appl. Met.*, **28**, 869–884.

Kummerow, C. D., 1993: On the accuracy of the Eddington approximation for radiative transfer in the microwave frequencies. *J. Geophys. Res.*, **98**, 2757–2765.

Larson, H. J., 1982: *Introduction to Probability Theory and Statistical Inference.* John Wiley & Sons, 637 pp.

Liebe, H. J., 1985: An updated model for millimeter wave propagation in moist air. *Radio Sci.*, **20**, 1069–1089.

Liebe, H. J. and G. A. Hufford, 1993: Models for atmospheric refractivity and radio-wave propagation at frequencies below 1 THz. *Int. J. Infrared and Millimeter Waves.* In press.

Liou, K.-N., 1986: Influence of cirrus clouds on weather and climate processes. *Mon. Wea. Rev.*, **114**, 1167–1199.

Liu, G. and J. A. Curry, 1992: Retrieval of precipitation from satellite microwave measurements using both emission and scattering. *J. Geophys. Res.*, **97**, 9959–9974.

Marzano, F. S., A. Mugnai, E. A. Smith, X. Xiang, J. Turk, and J. Vivekanandan, 1993: Active and passive microwave remote sensing of precipitating storms during CaPE. Part II: Intercomparison of precipitation retrievals over land from AMPR radiometer and CP-2 radar. *Met. and Atmos. Phys.* Accepted.

Matrosov, S. Y., B. W. Orr, R. A. Kropfil, and J. B. Snider, 1993: Retrieval of vertical profiles of cirrus cloud microphysical parameters from doppler radar and IR radiometer measurements. *J. Atmos. Sci.* Submitted.

Matrosov, S. Y., T. Uttal, J. B. Snider, and R. A. Kropfli, 1992: Estimation of ice cloud parameters from ground-based infrared radiometer and radar measurements. *J. Geophys. Res.*, **97**, 11567–11574.

Meador, W. E. and W. R. Weaver, 1980: Two-stream approximations to radiative transfer in planetary atmospheres: A unified description of existing methods and a new improvement. *J. Atmos. Sci.*, **37**, 630–643.

Minnis, P., P. W. Heck, and D. F. Young, 1993b: Inference of cloud cirrus properties using satellite-observed visible and infrared radiances. Part II: Verification of theoretical cirrus radiative properties. *J. Atmos. Sci.*, **50**, 1305–1322.

Minnis, P., K.-N. Liou, and Y. Takano, 1993a: Inference of cloud cirrus properties using satellite-observed visible and infrared radiances. Part I: Parameterization of radiance fields. *J. Atmos. Sci.*, **50**, 1279–1304.

Mugnai, A., H. J. Cooper, E. A. Smith, and G. J. Tripoli, 1990: Simulation of microwave brightness temperature of an evolving hailstorm at SSM/I frequencies. *Bull. Amer. Meteor. Soc.*, **71**, 2–13.

Mugnai, A. and E. A. Smith, 1988: Radiative transfer to space through a precipitating cloud at multiple microwave frequencies. Part I: Model description. *J. Appl. Met.*, **27**, 1055–1073.

Mugnai, A., E. A. Smith, and G. J. Tripoli, 1993: Foundations for statistical-physical precipitation retrieval from passive microwave satellite measurements. Part II: Emission-source and generalized weighting-function properties of a time-dependent cloud-radiation model. *J. Appl. Met.*, **32**, 17–39.

Mugnai, A. and W. J. Wiscombe, 1986: Scattering from nonspherical Chebyshev particles. I: Cross sections, single-scattering albedo, asymmetry factor, and backscattered fraction. *Appl. Optics*, **25**, 1235–1244.

Nicholls, M. E., R. A. Pielke, and W. R. Cotton, 1991: A two-dimensional numerical investigation of the interaction between sea breezes and deep convection over the Florida peninsula. *Mon. Wea. Rev.*, **119**, 298–332.

O'Brien, D. M., 1992: Accelerated quasi monte carlo integration of the radiative transfer equation. *J. Quant. Spectosc. Radiat. Transfer*, **48**, 41–59.

O'Brien, S. G. and G. H. Goedecke, 1988: Scattering of millimeter waves by snow crystals and equivalent homogeneous symmetric particles. *Appl. Optics*, **27**, 2439–2444.

Olson, W. S., 1989: Physical retrieval of rainfall rates over the ocean by multispectral microwave radiometry: Application to tropical cyclones. *J. Geophys. Res.*, **94**, 2267–2280.

Ono, A., 1969: The shape and riming properties of ice crystals in natural clouds. *J. Atmos. Sci.*, **26**, 138.

Ou, S. C., K. N. Liou, W. M. Gooch, and Y. Takano, 1993: Remote sensing of cirrus cloud parameters using advanced very-high-resolution radiometer 3.7- and 10.9-$\mu$m channels. *Appl. Optics*, **32**, 2171–2180.

Parol, F., J. C. buriez, G. Rogniez, and Y. Fouquart, 1991: Information content of AVHRR channels 4 and 5 with respect to the effective radius of cirrus cloud particles. *J. Appl. Met.*, **30**, 973–984.

Petty, G. W. and K. B. Katsaros, 1990: Precipitation observed over the south China sea by the Nimbus-7 scanning multichannel microwave radiometer during winter MONEX. *J. Appl. Met.*, **29**, 273–287.

Pilewskie, P. and S. Twomey, 1987: Discrimination of ice from water in clouds by optical remote sensing. *Atmos. Res.*, **21**, 113–122.

Platt, C. M. R., 1979: Remote sounding of high clouds. I: Calculation of visible and infrared optical properties from lidar and radiometer measurements. *J. Appl. Met.*, **18**, 1144–1150.

Platt, C. M. R., 1981: The effect of cirrus of varying optical depth on the extraterrestrial net radiative flux. *Quart. J. R. Met. Soc.*, **1981**, 671–678.

Platt, C. M. R., N. L. Abshire, and G. T. McNice, 1978: Some microphysical properties of an ice cloud from lidar observation of horizontally oriented crystals. *J. Appl. Met.*, **17**, 1220–1224.

Prabhakara, C., G. Dalu, G. L. Liberti, J. J. Nucciarone, and R. Suhasini, 1992: Rainfall estimation over oceans from SMMR and SSM/I microwave data. *J. Appl. Met.*, **31**, 532–552.

Prabhakara, C., R. S. Fraser, G. Dalu, M. L. C. Wu, R. J. Curran, and T. Styles, 1988: Thin cirrus clouds: Seasonal distribution over oceans deduced from Nimbus-4 Iris. *J. Appl. Met.*, **27**, 379–399.

Pruppacher, H. R. and J. D. Klett, 1980: *Microphysics of Clouds and Precipitation.* Reidel, Dordrecht, Holland, 714 pp.

Purcell, E. M. and C. R. Pennypacker, 1973: Scattering and absorption of light by nonspherical dielectric grains. *Astrophys. J.*, **186**, 705–714.

Ray, P. S., 1972: Broadband complex refractive indices of ice and water. *Appl. Optics*, **11**, 1836–1843.

Riehl, H. and J. S. Malkus, 1958: On the heat balance in the equatorial trough zone. *Geophysica (Helsinki)*, **6**, 503–538.

Rossow, W. B., F. Mosher, E. Kinsella, A. Arking, M. Desbois, E. Harrison, P. Minnis, E. Ruprecht, G. Sèze, C. Simmer, and E. Smith, 1985: ISCCP cloud algorithm intercomparison. *J. Clim. Appl. Met.*, **24**, 877–903.

Rossow, W. B. and R. A. Schiffer, 1991: ISSCP cloud data products. *Bull. Amer. Meteor. Soc.*, **72**, 2–20.

Rutledge, S. A. and P. V. Hobbs, 1984: The mesoscale and microscale structure and organization of clouds and precipitation in midlatitude cyclones, XXI: A diagnostic modeling study of precipitation development in narrow cold-frontal rainbands. *J. Atmos. Sci.*, **41**, 2949–2972.

Sassen, K., 1974: Depolarization of laser light backscattered by artificial clouds. *J. Appl. Met.*, **13**, 923–933.

Sassen, K., C. J. Grund, J. D. Spinhirne, M. M. Hardesty, and J. M. Alvarez, 1990: The 27-28 October 1986 FIRE IFO cirrus case study: A five lidar overview of cloud structure and evolution. *Mon. Wea. Rev.*, **118**, 2288.

Schluessel, P. and H. Luthardt, 1991: Surface wind speeds over the north sea from special sensor microwave/imager observations. *J. Geophys. Res.*, **96**, 4845–4853.

Seliga, T. A. and V. N. Bringi, 1976: Potential use of radar differential reflectivity measurements at orthogonal polarizations for measuring precipitation. *J. Appl. Met.*, **15**, 69–76.

Simpson, J., R. F. Adler, and G. R. North, 1988: A proposed tropical rainfall measuring mission (TRMM) satellite. *Bull. Amer. Meteor. Soc.*, **1988**, 278–295.

Singham, M. K., S. B. Singham, and G. C. Salzman, 1986: The scattering matrix for randomly oriented particles. *Journal of Chemical Physics*, **85**, 3807–3815.

Singham, S. B. and C. F. Bohren, 1987: Light scattering by an arbitrary particle: A physical reformulation of the coupled dipole method. *Opt. Let.*, **12**, 10–12.

Smith, E. A. and A. Mugnai, 1988: Radiative transfer to space through a precipitating cloud at multiple microwave frequencies. Part II: Results and analysis. *J. Appl. Met.*, **27**, 1074–1091.

Smith, E. A., A. Mugnai, H. J. Cooper, G. J. Tripoli, and X. Xiang, 1992: Foundations for statistical-physical precipitation retrieval from passive microwave satellite measurements. Part I: Brightness-temperature properties of a time-dependent cloud-radiation model. *J. Appl. Met.*, **31**, 506–531.

Smith, W. L., X. L. Ma, S. A. Ackerman, H. E. Revercomb, and R. O. Knuteson, 1993: Remote sensing cloud properties from high spectral resolution infrared observations. *J. Atmos. Sci.*, **50**, 1708–1720.

Spencer, R. W., H. M. Goodman, and R. E. Hood, 1989: Precipitation retrieval over land and ocean with the SSM/I: identification and characteristics of the scattering signal. *J. Atmos. Ocean. Tech.*, **6**, 254–273.

Spencer, R. W., R. E. Hood, F. LaFontaine, and E. A. Smith, 1993: High resolution microwave imaging of the Earth with the advanced microwave precipitation radiometer. Part I: System description and sample imagery. *J. Atmos. Ocean. Tech.* In Press.

Spencer, R. W., D. W. Martin, B. B. Hinton, and J. A. Weinman, 1983: Satellite microwave radiances correlated with radar rain rates over land. *Nature*, **304**, 141–143.

Spinhirne, J. D. and W. D. Hart, 1990: Cirrus structure and radiative parameters from airborne lidar and spectral radiometer observations: The 28 October 1986 FIRE study. *Mon. Wea. Rev.*, **118**, 2329.

Stackhouse, P. W. and G. L. Stephens, 1991: A theoretical and observational study of the radiative properties of cirrus: Results for FIRE 1986. *J. Atmos. Sci.*, **48**, 2044–2059.

Stephens, G. L. and P. J. Webster, 1981: Clouds and climate: Sensitivity of simple systems. *J. Atmos. Sci.*, **38**, 235–247.

Tao, W.-K. and J. Simpson, 1989: Modeling study of a tropical squall-type convective line. *J. Atmos. Sci.*, **46**, 177–202.

Tao, W. K., J. Simpson, S. Lang, M. McCumber, R. Adler, and R. Penc, 1990: An algorithm to estimate the heating budget from vertical hydrometeor profiles. *J. Appl. Met.*, **29**, 1232–1244.

Thiele, O. W., 1987: On requirements for a satellite mission to measure tropical rainfall. Technical report, NASA, 49 pp.

Tripoli, G. J. and W. R. Cotton, 1982: The Colorado State University three dimensional cloud/mesoscale model, 1982, I: General theoretical framework and sensitivity experiments. *J. Rech. Atmos.*, **16**, 185–220.

Turk, J., J. Vivekanandan, F. S. Marzano, R. E. Hood, R. W. Spencer, and F. J. LaFontaine, 1993: Active and passive microwave remote sensing of precipitating storms during cape. Part I: Advanced microwave precipitation radiometer and polarimetric radar measurements and models. *Met. and Atmos. Phys.* Accepted.

van de Hulst, H. C., 1963: A new look at multiple scattering. Technical report, Goddard Institute for Space Studies, NASA, New York, NY.

van de Hulst, H. C., 1981: *Light Scattering by Small Particles.* Dover, 470 pp.

Vivekanandan, J., J. Turk, and V. N. Bringi, 1993: Advanced microwave precipitation radiometer (AMPR) and multiparameter radar comparisons of precipitation. *IEEE Trans. Geosci. and Rem. Sensing.* Accepted.

Vivekanandan, J., J. Turk, G. L. Stephens, and V. N. Bringi, 1990: Microwave radiative transfer studies using combined multiparameter radar and radiometer measurements during COHMEX. *J. Appl. Met.*, **29**, 561–585.

Vonder Haar, T. H., W. E. Shenk, and D. W. Graul, 1986: Passive microwave radiometer experiment for GOES-NEXT. In *Second Conference on Satellite Meteorology/ Remote Sensing and Applications*, None, editor. May 12-16, 1986, Williamsburg, Virginia.

Warren, S. G., 1984: Optical constants of ice from the ultraviolet to the microwave. *Appl. Optics*, **23**, 1206–1225.

Warren, S. G., C. J. Hahn, J. London, R. M. Chervin, and J. L. Jenne, 1986: Global distribution of total cloud cover and cloud type amounts over land. NCAR Tech. Note NCAR/TN-273+STR, National Center for Atmospheric Research, Boulder, CO.

Warren, S. G., C. J. Hahn, J. London, R. M. Chervin, and J. L. Jenne, 1988: Global distribution of total cloud cover and cloud type amounts over ocean. NCAR Tech. Note NCAR/TN-317+STR, National Center for Atmospheric Research, Boulder, CO.

Webster, P. J., 1972: Response of the tropical atmosphere to local, steady, forcing. *Mon. Wea. Rev.*, **100**, 518–541.

Weinman, J. A. and R. Davies, 1978: Thermal microwave radiances from horizontally finite clouds of hydrometeors. *J. Geophys. Res.*, **83**, 3099–3107.

Weinman, J. A. and P. J. Guetter, 1977: Determination of rainfall distributions from microwave radiation measured by the Nimbus 6 ESMR. *J. Appl. Met.*, **16**, 437–442.

Weng, F., 1992: *Vector Radiative Transfer Model: Application to Rainfall Retrieval with Microwave Radiometric Data.* Dissertation, Colorado State University, Fort Collins, CO 80523.

Wielicki, B. A., J. T. Suttles, A. J. Heymsfield, R. M. Welch, J. D. Spinhirne, M.-L. C. Wu, D. O. Starr, L. Parker, and R. F. Arduini, 1990: The 27-28 October 1986 FIRE IFO cirrus case study: Comparison of radiative transfer theory with observations by satellite and aircraft. *Mon. Wea. Rev.*, **118**, 2356–2376.

Wilheit, T. T. and A. T. C. Chang, 1991: Retrieval of monthly rainfall indices from microwave radiometric measurements using probability distrtibution functions. *J. Atmos. Ocean. Tech.*, **8**, 118–136.

Wilheit, T. T., A. T. C. Chang, M. S. V. Rao, E. B. Rodgers, and J. S. Theon, 1977: A satellite technique for quantitatively mapping rainfall rates over the oceans. *J. Appl. Met.*, **16**, 551–560.

Williams, S. F., K. Caesar, and K. Southwick, 1992: The convective and precipitation/electrification (CaPE) experiment: Operations summary and data inventory. Technical document, National Center for Atmospheric Research, Boulder, Colorado, 425.

Wiscombe, W. J., 1976: Extension of the doubling method to inhomogeneous sources. *J. Quant. Spectosc. Radiat. Transfer*, **16**, 637–658.

Woodbury, G. E. and M. P. McCormick, 1983: Global distributions of cirrus clouds determined from SAGE data. *Geophys. Res. Letters*, **10**, 1180–1183.

Woodbury, G. E. and M. P. McCormick, 1986: Zonal and geographical distributions of cirrus clouds determined from SAGE data. *J. Geophys. Res.*, **91**, 2775–2785.

Wu, M.-L., 1987: Determination of cloud ice water content and geometrical thickness using microwave and infrared radiometric measurements. *J. Clim. Appl. Met.*, **26**, 878–884.

Yeh, H.-Y. M., N. Prasad, R. A. Mack, and R. F. Adler, 1990: Aircraft microwave observations and simulations of deep convection from 18 to 183 GHZ. Part II: Model results. *J. Atmos. Ocean. Tech.*, **7**, 392–410.

Yung, Y. L., 1978: Variational principle for scattering of light by dielectric particles. *Appl. Optics*, **17**, 3707–3709.

## Appendix A

## THE DDA FFT SOLUTION METHOD

The Greens function solution for the electric field (2.1) may be written as

$$\mathbf{E}^{\text{in}}(\mathbf{r}) = S^{-1}(\mathbf{r})\mathbf{p}(\mathbf{r}) - \int G((\mathbf{r}-\mathbf{r}')\mathbf{p}(\mathbf{r}')d^3\mathbf{r}' \ . \tag{A.1}$$

This equation is implemented on a uniform discrete grid of $N$ points, which forms the discrete dipoles making up the particle. The scalar dipole self interaction term ($S$) depends only on the susceptibility and the dipole size. The three-by-three Greens function matrix ($G$) is convolved with the vector dipole polarization ($p$). The FFT solution method performs this convolution using Fast Fourier Transforms and the conjugate gradient method.

The discretized linear system from (A.1) may be put in matrix form as

$$Ap = b \qquad A = 1 - SG \quad b = SE^{in} \ , \tag{A.2}$$

where $p$ and $b$ are vectors with $3N$ complex elements and $A$ is a $3N \times 3N$ complex matrix. Multiplication by $A$ is done by an FFT convolution by $G$ followed by a multiplication by the diagonal operator $S$. The simple conjugate gradient method used here requires that the system be positive definite, so the objective function to be minimized is set to

$$f = \frac{1}{2}|Ap - b|^2 \ , \tag{A.3}$$

and the gradient of the objective function is

$$\nabla f = A^{\dagger}(Ap - b) \ . \tag{A.4}$$

The adjoint ($\dagger$) operation of transposing and complex conjugating becomes just conjugating for the Greens function operator which is invariant under transpose, giving $A^{\dagger} = 1 - G^*S^*$. Starting with the noninteracting dipole solution $p_1 = b = SE^{in}$, the initial gradient vector is $g_1 = -A^{\dagger}(Ap_1 - b)$, and the inital step direction is $h_1 = g_1$. Then the conjugate gradient iterations proceed as follows:

$$\begin{aligned} c_n &= A^{\dagger}Ah_n \\ \lambda &= \frac{g_n \cdot h_n}{c_n \cdot h_n} \\ p_{n+1} &= p_n + \lambda h_n \\ g_{n+1} &= g_n - \lambda c_n \\ \gamma &= \frac{|g_{n+1}|^2}{|g_n|^2} \\ h_{n+1} &= g_n + \gamma h_n \quad . \end{aligned} \tag{A.5}$$

The iterations are stopped when the stopping criterion $|g_{n+1}|/|b|$ becomes less than some specified limit.

The memory space required by the FFT solution method is dominated by the size of the FFT arrays. To avoid aliasing the convolutions must be done in arrays twice as large in each dimension as the number of dipoles in the particle (a factor of eight in memory). The vector to be convolved has three complex elements per dipole ($24N$), where $N$ is the number of grid points (dipoles) in the box that circumscribes the particle. The Greens function matrix has six unique elements per dipole, but it has symmetry around the origin which allows its storage to be cut almost by two to $24N$. There are also five complex vector arrays and two scalar complex arrays with a size of the number of dipoles. So the memory requirements are about $65N$ complex numbers.

The CPU time of the algorithm is dominated by the FFT's in the two convolutions per conjugate gradient iteration. The Greens function is transformed before the iterations start so only two FFT's are required per convolution. The vector to be convolved is put in the FFT work array, padded with zeros to the full size, and FFTed. In Fourier space the complex vector (3 elements) is multiplied by the Greens function matrix (3x3), and then transformed back. The convolution is speeded up by 20% by avoiding transforms of the zero padded region. The number of floating point operations per convolution is about $240N log_2 8N$.

## Appendix B

# DEVELOPMENT OF THE EDDINGTON RADIATIVE TRANSFER MODEL

Simple radiative transfer models are often used in microwave precipitation retrieval where speed is essential (Kummerow et al., 1989). The Bayesian precipitation retrieval method uses Eddington's second approximation (Weinman and Davies, 1978). In this model the Eddington two-stream model is solved first. From the Eddington fluxes the scattering source term is derived. The radiative transfer equation is then integrated over optical depth at the desired observation angle. The two polarizations (horizontal and vertical) are treated separately with no interaction.

### B.1 Eddington flux model

The appropriate radiative transfer equation for passive microwave applications is plane-parallel, azimuthally symmetric with only thermal sources.

$$\mu \frac{dI}{d\tau} = -I + \frac{\omega}{2} \int_{-1}^{+1} P(\mu, \mu') I(\mu') d\mu' + (1-\omega)T \ , \tag{B.1}$$

where $I$ is the radiation intensity expressed in brightness temperature, $P$ is the phase function, $\omega$ is the single-scatter albedo, $T$ is the environment temperature, and the Rayleigh-Jeans approximation is used. The optical depth $\tau$ increases downward, and $\mu$ is positive downward.

The Eddington approximation expands the radiance field to first order in the cosine of the zenith angle ($I = I_0 + I_1\mu$). Using the notation of Meador and Weaver (1980) (except for the sign of $\mu$) the radiance field may be expressed as a function of the fluxes $I^+$ (downward) and $I^-$ (upward):

$$I(\pm\mu) = \frac{1}{2}\left[(2 \pm 3\mu)I^+ + (2 \mp 3\mu)I^-\right] \ . \tag{B.2}$$

The phase function is also expanded to first order

$$P(\Theta) = 1 + 3g\cos\Theta = 1 + 3g\mu\mu' \ , \tag{B.3}$$

where $g$ is the asymmetry parameter. Substituting these forms for the radiance and phase function and integrating over $\mu$ from 0 to 1 gives

$$\pm\frac{dI^{\pm}}{d\tau} = -\left(1 \pm \frac{3}{4}\right) I^+ - \left(1 \mp \frac{3}{4}\right) I^- + \omega\left[(I^+ + I^-) \pm \frac{3}{4} g\,(I^+ - I^-)\right] + (1-\omega)T \ , \tag{B.4}$$

which may be rearranged into a two-by-two matrix equation for the fluxes:

$$\begin{aligned} \frac{d}{d\tau}\begin{pmatrix} I^+ \\ I^- \end{pmatrix} &= \begin{pmatrix} -t & -r \\ r & t \end{pmatrix}\begin{pmatrix} I^+ \\ I^- \end{pmatrix} + \begin{pmatrix} +\beta \\ -\beta \end{pmatrix} \\ r &= [1-\omega(4-3g)]/4 \\ t &= [7-\omega(4+3g)]/4 \\ \beta &= (1-\omega)T \ . \end{aligned} \tag{B.5}$$

For a uniform layer, where the coefficients $r$ and $t$ are constant, the two-stream radiative transfer equation may be solved analytically to get solutions in terms of exponentials. The eigenvalues for the matrix operator are

$$\lambda = \pm\sqrt{t^2-r^2} \ = \ \pm\sqrt{3(1-\omega)(1-\omega g)} \tag{B.6}$$

and the eigenvectors are

$$\begin{pmatrix} -r \\ t+\lambda \end{pmatrix} , \quad \begin{pmatrix} t+\lambda \\ -r \end{pmatrix} \tag{B.7}$$

where $\lambda$ is the positive eigenvalue. The homogeneous solution, the solution for no source, is then

$$\begin{aligned} I_h^+ &= -rC^+e^{\lambda\tau} + (t+\lambda)C^-e^{-\lambda\tau} \\ I_h^- &= (t+\lambda)C^+e^{\lambda\tau} - rC^-e^{-\lambda\tau} \ , \end{aligned} \tag{B.8}$$

where $C^{\pm}$ are constants that depend on the boundary conditions. The full solution requires that the particular solution for the source term be added to the homogeneous solution. If the temperature is linear in optical depth ($T = T_0 + T'\tau$) then the particular solution is

$$\begin{aligned} I_p^+ &= -\frac{T'}{3(1-\omega g)} + \frac{1}{2}(T_0 + T'\tau) \\ I_p^- &= +\frac{T'}{3(1-\omega g)} + \frac{1}{2}(T_0 + T'\tau) \end{aligned} \tag{B.9}$$

The constants $C^+$ and $C^-$ may be derived from the boundary conditions, i.e. the fluxes incident on the layer. First, the particular solution is subtracted off,

$$I_{h1}^+ = I_1^+ - I_{p1}^+ \ , \qquad I_{h2}^- = I_2^- - I_{p2}^- \ , \tag{B.10}$$

and then the homogeneous solution is rearranged to give

$$\begin{aligned} C^+ &= \frac{(t+\lambda)I_{h2}^- + re^{-\lambda\Delta\tau}I_{h1}^+}{(t+\lambda)^2e^{\lambda\Delta\tau} - r^2e^{-\lambda\Delta\tau}} \\ C^- &= \frac{(t+\lambda)e^{\lambda\Delta\tau}I_{h1}^+ + rI_{h2}^-}{(t+\lambda)^2e^{\lambda\Delta\tau} - r^2e^{-\lambda\Delta\tau}} \ . \end{aligned} \tag{B.11}$$

For multiple layers the boundary conditions of all the layers must be simultaneously satisfied.

## B.2 Deriving single layer properties

The constants $C^+$ and $C^-$ that determine the radiation inside a layer depend on the flux incident on the boundaries of the layer. In a multi-layer atmosphere the constants for the layers are coupled together in a penta-diagonal system. The coupled system may be transformed to tri-diagonal by expressing the equations in terms of the reflection $R$, transmission $T$, and internal source $S$ for each layer. The reflection and transmission due to a single layer can be derived from the interaction principle

$$\begin{aligned} I_1^- &= RI_1^+ + TI_2^- + S^- \\ I_2^+ &= RI_2^- + TI_1^+ + S^+ \,, \end{aligned} \tag{B.12}$$

in which the plus superscript refers to downward quantities and the subscripts refer to the layer boundary. The upper boundary (1) is at $\tau = 0$ while the lower boundary (2) is at $\tau = \Delta\tau$. $R$ and $T$ are found by substituting the homogeneous Eddington solution (zero internal source) into the above equation and setting $I_2^- = 0$, giving

$$I_1^- = RI_1^+, \qquad I_2^+ = TI_1^+. \tag{B.13}$$

The resulting $T$ and $R$ in terms of the intrinsic layer properties are

$$\begin{aligned} T &= \frac{2\lambda}{(\lambda+t)e^{\lambda\Delta\tau} + (\lambda-t)e^{-\lambda\Delta\tau}} \\ R &= \frac{-r(e^{\lambda\Delta\tau} - e^{-\lambda\Delta\tau})}{(\lambda+t)e^{\lambda\Delta\tau} + (\lambda-t)e^{-\lambda\Delta\tau}} \,. \end{aligned} \tag{B.14}$$

The downwelling and upwelling source terms, $S^\pm$ can be found by considering the case of no incident radiation, $I_1^+ = I_2^- = 0$.

$$\begin{aligned} I_1^+ = 0 \rightarrow \quad & I_{h1}^+ = -I_{p1}^+ \quad S^+ = I_{h2}^+ + I_{p2}^+ \\ I_2^- = 0 \rightarrow \quad & I_{h2}^- = -I_{p2}^- \quad S^- = I_{h1}^- + I_{p1}^- \end{aligned} \tag{B.15}$$

Which allows the constants $C_S^\pm$ to be solved for,

$$\begin{aligned} C_S^+ &= -\frac{re^{-\lambda\Delta\tau}I_{p1}^+ + (t+\lambda)I_{p2}^-}{(t+\lambda)^2e^{\lambda\Delta\tau} - r^2e^{-\lambda\Delta\tau}} \\ C_S^- &= -\frac{(t+\lambda)e^{\lambda\Delta\tau}I_{p1}^+ + rI_{p2}^-}{(t+\lambda)^2e^{\lambda\Delta\tau} - r^2e^{-\lambda\Delta\tau}} \,. \end{aligned} \tag{B.16}$$

The particular fluxes at the boundaries ($n = 1, 2$) are

$$I_{pn}^\pm = \mp\frac{T'}{3(1-\omega g)} + \frac{1}{2}T_n \,, \tag{B.17}$$

where $T_1$ and $T_2$ are the top and bottom temperatures. The final expressions for the source terms are best left in terms of the $C_S^\pm$ and the $I_p$ above,

$$\begin{aligned} S^+ &= -rC_S^+e^{\lambda\Delta\tau} + (t+\lambda)C_S^-e^{-\lambda\Delta\tau} + I_{p2}^+ \\ S^- &= (t+\lambda)C_S^+ - rC_S^- + I_{p1}^- \end{aligned} \tag{B.18}$$

### B.3 Two stream tri-diagonal structure

The layer boundary fluxes $I^{\pm}$ are related to the source terms $S^{\pm}$ through a tri-diagonal matrix whose elements include the reflection and transmission terms $R$ and $T$ of the layers. The isotropic boundary radiances, $B^{+}_{top}$ and $B^{-}_{bottom}$ (expressed as emitting temperatures), enter in to the expression as extra source terms. For each internal layer, there are two equations which follow directly from the interaction principle:

$$\begin{aligned} I^{-}_{n-1} - R_n I^{+}_{n-1} - T_n I^{-}_{n} &= S^{-}_{n} \\ -T_n I^{+}_{n-1} - R_n I^{-}_{n} + I^{+}_{n} &= S^{+}_{n} \, . \end{aligned} \tag{B.19}$$

At the lower boundary, layer $N$, there is an extra equation involving reflection from the ground ($R_g$):

$$\begin{aligned} I^{-}_{N-1} - R_N I^{+}_{N-1} - T_N I^{-}_{N} &= S^{-}_{N} \\ -T_N I^{+}_{N-1} - R_N I^{-}_{N} + I^{+}_{N} &= S^{+}_{N} \\ I^{-}_{N} - R_g I^{+}_{N} &= B^{-}_{bottom}/2 \, . \end{aligned} \tag{B.20}$$

At the top of the atmosphere there is no reflection so the incident flux is combined with the interaction principle for the first layer to get

$$\begin{aligned} I^{-}_{0} - R_1 I^{+}_{0} - T_1 I^{-}_{1} &= S^{-}_{1} + R_1 B_{top}/2 \\ -T_1 I^{+}_{0} - R_1 I^{-}_{1} + I^{+}_{1} &= S^{+}_{1} + T_1 B_{top}/2 \, . \end{aligned} \tag{B.21}$$

$B_{top}$ is set to the brightness temperature of the downwelling radiance incident on the top of the atmosphere (the cosmic background radiation), while $B_{bottom}$ is set to the diffuse surface emissivity times the surface temperature. These equations represent a tri-diagonal system of $M = 2N + 1$ equations, which is solved by calling a tri-diagonal solver that runs in order $M$ operations to provide all the layer interface Eddington fluxes $I^{\pm}_{n}$.

### B.4 Integrating the radiative transfer equation

The second part of the Eddington model is to use the Eddington fluxes to calculate the the source terms and integrate the radiative transfer equation. The integral is done analytically for each layer, so that the radiance exitting a layer is computed from the transmission of the radiance entering the layer plus a contribution from that layer. The source function has thermal emission and scattering components:

$$J(\tau, \mu) = (1 - \omega) T(\tau) + \frac{\omega}{2} \int_{-1}^{1} P(\mu, \mu') I_{edd}(\mu') d\mu' \, , \tag{B.22}$$

which for the Eddington approximation becomes

$$J(\tau, \mu) = (1 - \omega)(T_0 + T'\tau) + \omega(I^{+} + I^{-}) + \frac{3}{2} \omega g \mu (I^{+} - I^{-}) \, . \tag{B.23}$$

Using the Eddington solution, the sum and difference of the fluxes may be written in terms of the layer constants $C^+$ and $C^-$ as

$$I^+ + I^- = (t+\lambda-r)C^+e^{\lambda\tau} + (t+\lambda-r)C^-e^{-\lambda\tau} + (T_0 + T'\tau) \quad \text{(B.24)}$$

$$I^+ - I^- = -(t+\lambda+r)C^+e^{\lambda\tau} + (t+\lambda+r)C^-e^{-\lambda\tau} - \frac{2}{3}\frac{T'}{1-\omega g} \quad \text{(B.25)}$$

The source function's dependence upon $\tau$ for a single layer can be made more explicit by introducing the coefficients $B_0, B', D^+$ and $D^-$,

$$J(\tau,\mu) = B_0 + B'\tau + D^+e^{\lambda\tau} + D^-e^{-\lambda\tau} \; . \quad \text{(B.26)}$$

The coefficients are determined to be

$$B_0 = T_0 - \frac{T'\omega g}{1-\omega g}\mu \qquad B' = T'$$

$$D^\pm = C^\pm\left[\omega(t+\lambda-r) \mp \frac{3}{2}\omega g(t+\lambda+r)\mu\right] \; , \quad \text{(B.27)}$$

where $T_0$ is the temperature at the top of the layer, and $T_0 + T'\Delta\tau$ is the temperature at the bottom of the layer.

The radiance at the bottom of a layer ($\tau = \Delta\tau$) is found by integrating the source term (B.26) for positive $\mu$,

$$I(\Delta\tau,\mu) = I(0,\mu)e^{-\Delta\tau/\mu} + \frac{1}{\mu}\int_0^{\Delta\tau} J(\tau,\mu)e^{-(\Delta\tau-\tau)/\mu}d\tau \; . \quad \text{(B.28)}$$

In terms of the coefficients, the radiance at the bottom of the layer is

$$I(\Delta\tau,\mu) = I(0,\mu)e^{-\Delta\tau/\mu} + B_0[1-e^{-\Delta\tau/\mu}] + B'[\Delta\tau - \mu(1-e^{-\Delta\tau/\mu})] \quad \text{(B.29)}$$
$$+ \frac{D^+}{1+\lambda\mu}[e^{\lambda\Delta\tau} - e^{-\Delta\tau/\mu}] + \frac{D^-}{1-\lambda\mu}[e^{-\lambda\Delta\tau} - e^{-\Delta\tau/\mu}] \; .$$

The radiance at the top of the layer ($\tau = 0$) is found by integrating for negative $\mu$,

$$I(0,\mu) = I(\Delta\tau,\mu)e^{\Delta\tau/\mu} - \frac{1}{\mu}\int_0^{\Delta\tau} J(\tau,\mu)e^{\tau/\mu}d\tau \; ; \quad \text{(B.30)}$$

which in terms of the coefficients is

$$I(0,\mu) = I(\Delta\tau,\mu)e^{\Delta\tau/\mu} + B_0[1-e^{\Delta\tau/\mu}] - B'[(\Delta\tau-\mu)e^{\Delta\tau/\mu} + \mu] \quad \text{(B.31)}$$
$$- \frac{D^+}{1+\lambda\mu}[e^{\lambda\Delta\tau}e^{\Delta\tau/\mu} - 1] + \frac{D^-}{1-\lambda\mu}[e^{-\lambda\Delta\tau}e^{\Delta\tau/\mu} - 1]$$

The procedure to compute the upwelling radiance starts with computing the reflection, transmission, and source terms of the tri-diagonal system from the layer optical depth $\Delta\tau$, single scattering albedo $\omega$, asymmetry factor $g$, and layer interface temperatures using (B.14) and (B.18). The tri-diagonal solver computes the Eddington fluxes $I^\pm$ from the

layer reflection, transmission, and source terms along with the boundary conditions. The particular solution is subtracted off the Eddington fluxes (B.9) and then the layer constants $C^{\pm}$ are computed from (B.11). The $D^{\pm}$ constants are computed from (B.27) and used to find the contribution to the radiance integral from each layer, first for the downward integration (B.30) and then for the upward integration (B.32). The upwelling radiance at the bottom of the atmosphere is the thermal emission plus the reflected downwelling radiance (for a specular Fresnel surface) or the reflected downwelling Eddington flux (for a Lambertian surface). The radiance at the top and bottom of the atmosphere is computed by summing the contributions from each layer taking into account the attenuation from the layers.